

INFORMATION TO USERS

This manuscript has been reproduced from the microfilm master. UMI films the text directly from the original or copy submitted. Thus, some thesis and dissertation copies are in typewriter face, while others may be from any type of computer printer.

The quality of this reproduction is dependent upon the quality of the copy submitted. Broken or indistinct print, colored or poor quality illustrations and photographs, print bleedthrough, substandard margins, and improper alignment can adversely affect reproduction.

In the unlikely event that the author did not send UMI a complete manuscript and there are missing pages, these will be noted. Also, if unauthorized copyright material had to be removed, a note will indicate the deletion.

Oversize materials (e.g., maps, drawings, charts) are reproduced by sectioning the original, beginning at the upper left-hand corner and continuing from left to right in equal sections with small overlaps. Each original is also photographed in one exposure and is included in reduced form at the back of the book.

Photographs included in the original manuscript have been reproduced xerographically in this copy. Higher quality 6" x 9" black and white photographic prints are available for any photographs or illustrations appearing in this copy for an additional charge. Contact UMI directly to order.

UMI

A Bell & Howell Information Company
300 North Zeeb Road, Ann Arbor, MI 48106-1346 USA
313/761-4700 800/521-0600

Experimental Study of the Thermophoretic Force and Evaporation Rates for Single
Microparticles in the Knudsen Regime

by

Wanguang Li

A dissertation submitted in partial fulfillment
of the requirements for the degree of

Doctor of Philosophy

University of Washington

1995

Approved by *E. James Davis*
Chairperson of Supervisory Committee

Program Authorized
to Offer Degree *Department of Chemical Engineering*

Date *December 8, 1995*

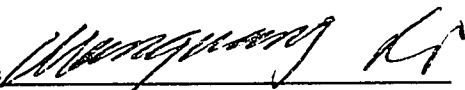
UMI Number: 9616636

UMI Microform 9616636
Copyright 1996, by UMI Company. All rights reserved.

This microform edition is protected against unauthorized
copying under Title 17, United States Code.

UMI
300 North Zeeb Road
Ann Arbor, MI 48103

In presenting this dissertation in partial fulfillment of the requirements for the Doctoral degree at the University of Washington, I agree that the Library shall make its copies freely available for inspection. I further agree that extensive copying of this dissertation is allowable only for scholarly purposes, consistent with the "fair use" as prescribed in the U.S. Copyright Law. Requests for copying or reproduction of this dissertation may be referred to University Microfilms, 1490 Eisenhower Place, P.O. Box 975, Ann Arbor, MI 48106, to whom the author has granted "the right to reproduce and sell (a) copies of the manuscript in microform and/or (b) printed copies of the manuscript made from microform."

Signature 

Date 12/8/95

University of Washington

Abstract

Experimental Study of the Thermophoretic Force and Evaporation Rates for Single
Microparticles in the Knudsen Regime

by Wanguang Li

Chairperson of the Supervisory Committee: Professor E. James Davis

Department of Chemical Engineering

Elastic and inelastic light scattering techniques were used to explore the processes of Knudsen evaporation, thermophoresis and gas/droplet reaction related to single microparticles. The reaction between single titanium ethoxide (TTE) droplets with water vapor was investigated. It was found that the fast surface reaction led to the formation of a coated microsphere consisting of a TiO_2 shell and an unreacted core.

The thermophoretic force was measured over a wide range of Knudsen number ($\text{Kn} = \lambda/a$) for dioctyl phthalate (DOP) droplets and microspheres of polystyrene latex (PSL), glass and nickel in air, helium and carbon dioxide. The data in the transition regime were used to examine existing theories for the thermophoretic force. It was found that the numerical solutions of Loyalka (1992) and the theory of Brock (1962) are in good agreement with measurements in air and carbon dioxide. The results in helium were found to be somewhat higher than most theoretical solutions for monatomic gases.

The effects of the thermal properties of the gases and particles on the thermophoretic force were also investigated. It was found that the force strongly depends on the thermal conductivity of gas and weakly on the thermal conductivity of particle. The effects of surface charge on force were studied in this research for the first time. Negatively-charged particles receive a larger force than those positively-charged.

Knudsen evaporation measurements were made for single dioctyl phthalate droplets in air in the temperature regime 263 - 302 K. The evaporation rates near room temperature

(297.7K) were used to evaluate the theories of Loyalka *et al.* (1989), Fuchs and Sutugin (1970) and Sitarski and Nowakowski (1979). The agreement between the measurements and the solutions of Loyalka *et al.* (1989) and Fuchs and Sutugin (1970) was good for all values of Kn, but the solution of Sitarski and Nowakowski (1979) did not agree with the experiments at large Kn.

TABLE OF CONTENTS

LIST OF FIGURES	v
LIST OF TABLES	xiii
NOMENCLATURE	xv
CHAPTER 1	
INTRODUCTION	1
CHAPTER 2	
LIGHT SCATTERING BY A SPHERE	
2.1 Introduction.....	6
2.2 Elastic scattering by a homogenous sphere	7
2.2.1 Phase function.....	9
2.2.2. Optical resonance spectrum	11
2.3 Elastic scattering by an inhomogenous sphere	14
2.4 Inelastic scattering: Raman spectroscopy	17
CHAPTER 3	
REVIEW OF THERMOPHORESIS AND EVAPORATION	
3.1 Introduction.....	23
3.2 Theory of thermophoresis	25
3.2.1 Slip flow.....	28
3.2.2 Free-molecule regime	32
3.2.3 Knudsen regime	34
3.3 Prior experiments of thermophoretic force	40

3.3.1 Millikan's chamber.....	41
3.3.2 Deflection of the particle	43
3.3.3 Slit method.....	44
3.3.4 Discussion of the measurement methods.....	45
3.4 Theory of droplet evaporation/condensation	46
3.5 Prior experiments of droplet evaporation	52
3.6 Summary	53

CHAPTER 4

EXPERIMENTAL APPARATUS AND MEASUREMENT PRINCIPLE

4.1 Introduction.....	54
4.2 Electrodynamic Balance	55
4.2.1 Principle of EDB.....	55
4.2.2 Principle of particle trapping	61
4.2.3 The EDB power supply	65
4.2.4 Electrical discharge and ring design	66
4.3 Vacuum apparatus and gas introduction	69
4.4 Optics and photodetectors.....	74
4.5 Constant temperature cells.....	77
4.6 Measurement technique	80
4.6.1 Gravimetric measurements	80
4.6.2 Particle sizing via light scattering measurement	82
4.6.3 Particle sizing via marginal-stability measurement.....	84
4.6.4 Raman spectroscopy	87
4.7 Particle generation and experimental procedures	87

CHAPTER 5

A STUDY OF THE FORMATION OF TiO₂-COATED MICROSHERE BY LIGHT SCATTERING

5.1 Introduction.....92
5.2 Chemical reaction between single TTE droplets and water vapor95
5.3 Determination of physical properties.....103
5.4 Raman scattering112
5.5 Conclusion119

CHAPTER 6

MEASUREMENTS OF THE THERMOPHORETIC FORCE: MICROSPHERES IN AIR

6.1 Experimental materials121
6.2 Experiment.....122
6.3 Results and discussion128
 6.3.1 Temperature jump at thermal plate surfaces.....128
 6.3.2. Comparison among experiments and theory133
6.4. Conclusion141

CHAPTER 7

EFFECTS OF THE THERMAL PROPERTIES OF GAS AND PARTICLE ON THE THERMOPHORETIC FORCE

7.1 Effects of temperature jump142
7.2 Comparison of theory and experiment144
7.3 Effects of temperature gradient and particle size146
7.4 Effects of particle thermal conductivity148
7.5 Effects of gas thermal conductivity151
7.6 Effects of particle charge153
7.7 Conclusion157

CHAPTER 8

AEROSOL EVAPORATION IN THE TRANSITION REGIME

8.1 Evaporation of single DBP droplets in air159

 8.1.1 Estimation of evaporation rate161

 8.1.2 Determination of vapor pressure164

 8.1.3 Comparison between experiment and theory168

8.2 Effects of PMMA polymer on DBP evaporation174

8.3 Evaporation study of tin catalyst droplet177

8.4 Conclusion182

CHAPTER 9

CONCLUSION184

REFERENCE.....187

APPENDIX A

Schematic Diagram of the Vacuum Chamber198

APPENDIX B

FORTTRAN program "MIE_COATED_OPTIMUM1.FOR201

APPENDIX C

Raw Data for the Measured Thermophoretic force212

LIST OF FIGURES

<u>Figure</u>	<u>Page</u>
Figure 2.1 Coordinate system for Mie scattering	7
Figures 2.2 A calculated phase function from Mie theory for a DOP droplet with $X = 300$ and $\phi = 90^\circ$	10
Figure 2.3 A plot of the size parameters of DOP droplets versus the number of peaks showing the linear relationship of them	11
Figure 2.4 The optical resonance spectrum of a DOP droplet calculated from Mie theory with $\phi = 90^\circ$ and $\theta = 45^\circ$	12
Figure 2.5 Comparison of the phase functions between (a) a coated particle consisting of TTE core and TiO_2 shell, and (b) a pure TTE droplet.	16
Figure 2.6 A schematic diagram showing the Stokes and anti-Stokes Raman scattering.	21
Figure 3.1 Comparison among the solutions of Phillips (1972), Dwyer (1967) and Brock (1962) based upon unity accommodation coefficients and $k_g/k_p = 1$	33
Figure 3.2 Comparison of the theory of Brock and of Ivchenko and Yalamov for $k_g/k_p = 1$ and $\alpha_t = 0.1$ and 1.0	36
Figure 3.3 Numerical results of Sone and Aoki (1983) for $k_p = \infty$, Yamamoto and Ishihara (1988) for $k_p/k_g = 598$ corresponding to the nickel/helium system, and Loyalka for $k_p/k_g = 100$, all based upon unity coefficient.	39
Figure 3.4 Description of the thermophoresis problem	40

Figure 3.5 A schematic diagram of modified Millikan's apparatus used to measure the thermophoretic force by Rosenblatt and LaMer (1946) and others	42
Figure 3.6 Experimental setup used by Davis and Adair (1975) and Tong (1975) for the measurement of thermophoretic force.	43
Figure 3.7 A comparison among the solutions of Loyalka <i>et al.</i> (1989), Sitarski and Nowakowski (1979), and the equation of Fuchs-Sutugin (1970) for $Z = 10$	51
Figure 4.1 A schematic diagram of the bihyperboloidal EDB and peripheral equipment (called "Fulton's balance" or "Apparatus A")	55
Figure 4.2 A schematic diagram of the electrodynamic balance coupled with Raman facilities, also called "Apparatus B"	56
Figure 4.3 Systematic overview of the apparatus used to measure the thermophoretic force and droplet evaporation in the Knudsen regime, also called "Apparatus C"	57
Figure 4.4 Configurations of electrodynamic balance (a) three-plates by Straubel (1955), (b) spherical void by Arnold and Folan (1987) and (c) double-ring by Buehler (1991)	60
Figure 4.5 Geometry and construction of ring-electrodes.	62
Figure 4.6 The first marginal stability envelope for the double-ring electrodynamic balance and experimental data for DOP droplets.	65
Figure 4.7 The circuit diagram for superposing DC and AC potentials applied to the ring-electrodes.	66
Figure 4.8 The breakdown voltage V_s of air as a function of the products of pressure P and separation distance d (data were taken from Hirsh and Oskam).....	68

Figure 4.9 A cross view of the vacuum chamber showing the thermal plates and electric feedthroughs.....	70
Figure 4.10 Top view of the main chamber showing the positions of the ports in the midplane.....	71
Figure 4.11 Schematic diagram of the vacuum system associated with the double-ring balance.....	72
Figure 4.12 Diagram of the gas introduction system for the double-ring balance.	73
Figure 4.13 A cross section of the optical components used for collecting elasticity scattered light.....	76
Figure 4.14 Measured temperatures of various vertical positions between the top and bottom thermal cells (center square denotes ring positions).....	79
Figure 4.15 Measured phase functions for an evaporating DOP droplet at various times.....	83
Figure 4.16 Comparison among the theoretical MDRs and the experimental MDRs obtained for an evaporating droplet of DBP at $T = 278$ K in the free-molecule regime.	85
Figure 4.17 A Stoke's Raman spectrum in the wavenumber range $250 - 1600 \text{ cm}^{-1}$ for a reacting droplet of titanium ethoxide.	88
Figure 5.1 Phase functions obtained at different times during an experiment with a reacting droplet of TTE.	97
Figure 5.2a A resonance spectrum obtained for a reacting TTE droplet at the beginning of the experiment	98
Figure 5.2b A resonance spectrum obtained for a reacting TTE droplet after a solid shell of TiO_2 began to form	99

Figure 5.2c A resonance spectrum obtained for a reacting TTE droplet after a solid shell of TiO ₂ had formed at long times	100
Figure 5.3 The levitation DC voltage as a function of reaction time for a reacting TTE droplet.....	102
Figure 5.4 A comparison among (a) a "raw" phase function, (b) the FFT-smoothed phase function corresponding to (a), and (c) the "best fit" computed from the solution of Aden and Kerker (1951).....	104
Figure 5.5 The effect on the phase function by changing the shell thickness by 10%.....	106
Figure 5.6 The outer radii of two different reacting droplets and the core radius of the smaller droplet determined by analysis of the measured phase function	107
Figure 5.7 Shell thickness of TiO ₂ estimated by the "best fit" of measured elastic scattering data, and the bulk density determined from the shell thickness and DC voltage.....	108
Figure 5.8 A plot of particle radius square, a_t^2 , versus V_{dc}/a_t used to determine the particle surface charge, q	110
Figure 5.9 The shell density determined from the shell thickness, core and overall particle mass.	111
Figure 5.10 Comparison among the Raman spectrum obtained in this work for a reacting TTE microparticle (coated), and the spectra obtained by Payne and Berglund for bulk TTE and ethanol.....	115
Figure 5.11 Raman spectra obtained at different times for an reacting TTE droplet in the wavenumber range 250-1000 cm ⁻¹	116

Figure 5.12 A series of Raman spectra obtained for an reacting TTE droplet in the wavenumber range 2500-4000 cm^{-1}	117
Figure 5.13 Raman spectra obtained during CO_2 laser heating for a reacting TTE microparticle compared with the results of She and Hsu for the thin films of TiO_2 on a silicon substrate.....	118
Figure 6.1 Experimental and theoretical phase functions for a DOP droplet with a = 23.9 μm	124
Figure 6.2 Measured phase function for a PSL sphere with a = 10.56 μm	125
Figure 6.3 Ratio of the thermophoretic force to the particle weight for five DOP droplets levitated in air at $298 \pm 3\text{K}$	126
Figure 6.4 Data for thermophoretic force (shown in Fig. 6.3) normalized by $a^2 \nabla T_\infty$ compared with Waldmann's theory for the free-molecule regime.....	127
Figure 6.5 Comparison among the data for DOP in air, the data of Schmitt (1959) for silicone oil in argon, the data of Schadt and Cadle (1961) for tricresylphosphate in air, and the theory of Waldmann (1950) for the free-molecule regime.....	129
Figure 6.6 The schematic diagram showing the "effective" separation distance of two thermal plates in the transition regime accounting for the temperature jump	130
Figure 6.7 Experimental data for Run 0510d replotted as $(1+2C_t \text{Kn}_2) F_{\text{th}} / a^2 \nabla T_\infty$ versus Kn for three values of the thermal accommodation coefficient for the air/copper system.	133
Figure 6.8 Comparison among experimental data of 0510d and the theories of Brock (1962), Phillips (1975) and Dwyer (1967) using unit accommodation coefficient for DOP/ air.	134

Figure 6.9 Comparison among the data for DOP and PSL spheres and the solutions of Loyalka (1992) for $k_g/k_p = 0.1$ and of Waldmann (1959).....	135
Figure 6.10 Comparison among the data for glass and nickel spheres in air with the solutions of Loyalka (1992) for $k_g/k_p = 0.01$ and of Waldmann (1959)	136
Figure 6.11 Data for DOP droplets in air in the slip flow regime compared with the solutions of Epstein (1929), Brock (1962) and Derjaguin and Yalamov (1965) using $\alpha_t = \alpha_m = 1.0$	138
Figure 6.12. Adjusted and normalized force of experiment 0510d compared with the solutions of Brock (1967a) for the transition regime at $\alpha_t = 0.5, 0.75$ and 1.0	139
Figure 6.13 Adjusted and normalized force of experiment 0510d compared with the solutions of Ivchenko and Yalamov (1970) for $\alpha_t = 0.5, 0.75$ and 1.0	140
Figure 7.1 Thermophoretic force for a PSL sphere in helium normalized by $a^2\nabla T_\infty$ and replotted as $(1+2C_tKn_2)F_{th}/a^2\nabla T_\infty$ for $\alpha_t = 0.33$ and $\alpha_t = 0.05$ showing the effects of temperature slip.....	143
Figure 7.2 Comparison among experimental data for nickel and glass spheres in helium and various theoretical results.	145
Figure 7.3 Comparison among experimental data for PSL and glass spheres in CO_2 and various theoretical results.	147
Figure 7.4 Effects of the temperature gradient on the thermophoretic force for glass and PSL spheres in helium compared with the solutions of Brock.	148
Figure 7.5 Effects of the particle radius on the thermophoretic force for DOP droplet in air.....	149
Figure 7.6 Thermophoretic force for DOP, PSL, glass and nickel spheres in helium	150

Figure 7.7 Thermophoretic force for DOP, PSL, glass and spheres in carbon dioxide.	151
Figure 7.8 Effects of surrounding gas on the thermophoretic force for glass spheres.	152
Figure 7.9 Effects of the charge polarity on the thermophoretic force for DOP droplets in air.	154
Figure 7.10 Effects of charge polarity on the thermophoretic force for DOP droplets in helium.	156
Figure 7.11 Effects of charge polarity on the thermophoretic force for PSL spheres in helium.	157
Figure 8.1 radius of an evaporating DBP droplet at six system pressures.	161
Figure 8.2 Plot of droplet radius versus time for an evaporating DBP droplet at $P = 12.69$ kPa ($Kn = 0.0064$) and $T = 296.4$ K, the slope is used to determine the evaporation rate	162
Figure 8.3 Comparison among the droplet radius of DBP determined from MDRs, DC voltage and phase function, respectively.	164
Figure 8.4 Comparison among the vapor pressure of DBP reported by Ray <i>et al.</i> (1979) and the results of this work estimated from the evaporation rate in the free-molecule regime.	167
Figure 8.5 Flux ratio at various Kn based upon the measured flux in the free-molecule limit compared with the theories of Loyalka <i>et al.</i> (1989), Sitariski and Nowakowski (1979) and Fuchs and Sutugin (1970).....	172

Figure 8.6 Flux ratio at various Kn based upon the flux calculated from Eq. (3.33) for the free-molecule limit compared with the theories of Loyalka <i>et al.</i> (1989), Sitarski and Nowakowski (1979) and Fuchs and Sutugin (1970).....	173
Figure 8.7 A sequence of resonance spectra obtained in the free-molecule regime and T = 284 K for an evaporating droplet, initially consisting of DBP and 0.986 wt% PMMA polymer	176
Figure 8.8 Mass flux measured in the free-molecule regime for evaporating droplets consisting of DBP and polymer at various concentration of polymer and various temperatures.	177
Figure 8.9 Comparison among the Raman spectrum of microdroplet of EHA and the spectrum of bulk sample by Sadtler (1973)	179
Figure 8.10 Raman spectra obtained at different times of evaporation for a droplet of catalysis consisting of EHA and SNO.....	180
Figure 8.11 A Raman spectrum (a) for the remaining material of an evaporating droplet of tin catalysis and the infrared spectrum (b) for bulk SNO by Sadtler (1966).....	181
Figure A1 A front view of the vacuum chamber used for the measurements of the thermophoretic force and evaporation rates in the Knudsen regime	198
Figure A2 A diagram for the mating flange for Port 7 showing the holes for electrical feedthrough, inlet and outlet ports for constant temperature fluids	199
Figure A3 A diagram for the mating flange for Port 8 showing the holes for electrical feedthrough, inlet and outlet ports for constant temperature fluids	200

LIST OF TABLES

<u>TABLES</u>	<u>Pages</u>
Table 4.1. Correlation determined from Mie theory for the particle size parameter, X, and the number of peaks, N_p , in the X range of 25 - 200.	84
Table 5.1. Estimated parameters for a layered TiO ₂ /TTE microsphere for large reaction times.	112
Table 6.1. Physical properties of the four materials: DOP, PSL, nickel and glass, together with three gases: helium, air and CO ₂ at T = 298 K and 1 atmosphere pressure	122
Table 6.2. Experimental conditions for particle/air thermophoretic force measurements.	123
Table 7.1. Surface charge density for DOP droplets and PSL spheres.....	155
Table 8.1. Measured mass flux and vapor pressure of DBP at different temperatures.	166
Table 8.2 Comparison among the diffusivities of DBP in air estimated from the flux measurements, and the values determined from theories	177
Table C1. Thermophoretic force data for system DOP/air and Run 0409b	213
Table C2. Thermophoretic force data for system DOP/air and Run 0501a.....	214
Table C3. Thermophoretic force data for system DOP/air and Run 0510d	215
Table C4. Thermophoretic force data for system DOP/air and Run 0510e.....	216
Table C5. Thermophoretic force data for system DOP/air and Run 0518h	217

Table C6. Thermophoretic force data for system DOP/air and Run OT94A	217
Table C7. Thermophoretic force data for system DOP/air and Run 1011j	218
Table C8. Thermophoretic force data for system DOP/air and Run 1011k	219
Table C9. Thermophoretic force data for system DOP/helium and Run 0519h	220
Table C10. Thermophoretic force data for system DOP/helium and Run 0519h	221
Table C11. Thermophoretic force data for system DOP/CO ₂ and Run OT94C	223
Table C12. Thermophoretic force data for system PSL/air and Run 0905a.....	224
Table C13. Thermophoretic force data for system PSL/air and Run 0905b	225
Table C14. Thermophoretic force data for system PSL/CO ₂ and Run SE94H2	226
Table C15. Thermophoretic force data for system PSL/CO ₂ and Run SE94H5	226
Table C16. Thermophoretic force data for system PSL/helium and Run 1005c	227
Table C17. Thermophoretic force data for system PSL/helium and Run 1005c	228
Table C18. Thermophoretic force data for system PSL/helium and Run 0524j	229
Table C19. Thermophoretic force data for system nickel/air and Run 0726a.....	230
Table C20. Thermophoretic force data for system nickel/helium and Run SE94C	231
Table C21. Thermophoretic force data for system glass/air and Run 0927a.....	233
Table C22. Thermophoretic force data for system glass/air and Run 0927b	233
Table C23. Thermophoretic force data for system glass/helium and Run JA95Y1	234

Table C24. Thermophoretic force data for system glass/CO₂ and Run SE95F1 235

Table C25. Thermophoretic force data for system glass/CO₂ and Run SE95F2 236

NOMENCLATURE

<u>Symbol</u>	<u>Definition</u>
a	particle radius [=] μm
a_c	core radius [=] μm
$a_t, a(t)$	particle radius at any time t [=] μm
\mathbf{a}	acceleration
a'	invariant of the derived polarizability tensor
a_n, b_n	Mie theory light scattering coefficients
A	aerodynamic drag parameter
B	AC field strength parameter
Bi	Biot number
c	speed of light in vacuum [=] m/s
\bar{c}	mean speed of gas molecules
C_m	velocity jump coefficient
C_t	temperature jump coefficient
C_{ts}	thermal slip coefficient
C_p	heat capacity at constant pressure
C_v	heat capacity at constant volume
c_n, d_n	Mie theory internal field coefficients
C_0	geometric balance constant for DC voltage
c_s	vapor concentration at the droplet surface
c_∞	vapor concentration at infinity
D_{AG}	gas phase diffusivity
D_{AL}	liquid phase diffusivity
D_{ij}	gas phase diffusion coefficient of species i in background gas j [=] m^2/s
$D_{ij}^{(0)}$	low-order diffusivity for rigid-sphere molecules [=] m^2/s
$D_{ij}^{(1)}$	first-order diffusivity [=] m^2/s
E_1	Mie theory internal electric field
E	average energy flux; electric field
E_r, E_θ, E_ϕ	r, θ, ϕ components of internal electric field
$E_{ac,z}, E_{ac,r}$	z and r components of AC voltage
$E_{dc,z}, E_{dc,r}$	z and r components of DC voltage

E_0	amplitude of incident electric field
f	Boltzmann distribution function
f^0	Maxwellian distribution function
F_{th}	thermophoretic force
$F_{th, fm}$	thermophoretic force in the free-molecule limit
F_z	axial force
g	gravitational constant [=] m/s^2
H	separation distance of the thermal plates [=] m
H_A	Henry's law constant
i	$\sqrt{-1}$
I	Mie scattering light intensity
I_a	anti-Stokes Raman scattering intensity
I_o	incident light irradiance
I_s	intensity of Stokes Raman
J_k	mass flux at arbitrary Kn [=] $kg/m^2 s$
$J_{k, fm}$	mass flux in the free-molecule regime [=] $kg/m^2 s$
k	imaginary part of refractive index; constant in Eqs. (8.3) and (8.4)
k_1	propagation constant of light, $2\pi m/\lambda$
k_B	Boltzmann constant
k_c	reaction rate constant
k_g	thermal conductivity of gas [=] $W/m K$
$k_{g, tran}$	translational portion of gas thermal conductivity [=] $W/m K$
Kn	Knudsen number, λ/a
Kn_2	Knudsen number, λ/H
k_p	thermal conductivity of particle [=] $W/m K$
m	relative refractive index, mass of particle
M	dipole moment
M	Momentum, molecular weight of gas
M_i	molecular weight of species i, [=] $kg/kmol$,
n	real part of refractive index
N	refractive index of medium surrounding particle
N_{Da}	Damkohler number
N_p	number of peaks in phase function
Nu	Nusselt number
n_i, n_j	number density of species i and j

\mathbf{p}	dipole moment of molecule
P	system pressure
$P_n^1(x)$	associated Legendre function of order 1 and degree n
p_i^0	partial pressure at the droplet surface
p_i^∞	partial pressure at infinity
Pr	Prandtl number
$P_n(\cos\theta)$	associated Legendre function of $\cos\theta$
q	charge on particle surface
q_{Re}	charge of Rayleigh instability limit
Q	charge density [=] C/m
Q_{k0}	normal coordinate of vibration,
r	radial coordinate
R	gas constant
Re	Reynolds number
$Re(N_1)$	real part of refractive index
S	surface area
S_1, S_2	Mie theory scattering amplitude functions
S_{ij}	slope of the plot of radius square vs. time
t	time
T	temperature [=] K
T_0	average gas temperature [=] K
T_p	temperature of particle [=] K
T_g	temperature of gas [=] K
T_s	temperature of particle surface [=] K
T_∞	ambient temperature [=] K
U_∞	gas velocity [=] m/s
v	velocity of gas molecule
V	potential
V_{dc}	DC levitation potential
V_r	relative velocity of the two molecules involved in binary collision
V_t	thermophoretic velocity
V_{ts}	thermal slip velocity
W_t	polymer concentration by weight at any time t
x_k	displacement of vibration
X	Mie theory size parameter, $2\pi a/\lambda$

Z	mass ratio, or molecular weight ratio of vapor molecule to background gas molecule
z_0	half of separation distance of DC electrodes

Greek Symbols

<u>Symbol</u>	<u>Definition</u>
α_e	evaporation coefficient
α_m	momentum accommodation coefficient
α_t	thermal accommodation coefficient
α	polarizability tensor
δ_k	phase factor
ϕ	electric field associated with a charge sphere
λ	mean free path of gas molecules, wavelength of light in medium surrounding sphere
λ_0	wavelength of light in vacuum
∇T_∞	external temperature gradient [=] K/m
∇T_{Kn}	corrected temperature gradient in the Knudsen regime [=] K/m
γ	vibrational frequency in unit cm^{-1} ; ratio of heat capacity
γ	invariant of the derived polarizability tensor
ε	angle between the plane of the orbit and the fixed plane passing through the initial velocity vector (Eq. (3.3))
ε_{ij}	Lennard-Jones molecular interaction parameter
ε_0	permittivity of free space
ϕ	azimuthal angle
Δ	distance in the order of one mean free path
μ	viscosity of gas
$\tilde{\nu}_0$	wavenumber of incident light
$\tilde{\nu}_k$	wavenumber of Raman shifted light
π_n, τ_n	Mie theory angular scattering functions
θ	polar angle
ρ	density of gas [=] kg/m^3
ρ_t	density of particle [=] kg/m^3
σ	surface tension [=] mN/m ; molecule diameter [=] Angstrom

σ_{ii}, σ_{ij}	molecule diameter of like- and unlike-molecules [=] Angstrom
Ψ	group constant (in Eqs. 4.19 and 4.20)
Ψ_n, ξ_n	Ricatti-Bessel functions
$\Omega_{D,ij}$	collision integral
ω_k	circular frequency of the k-th model vibration
ω_0	circular frequency of the incident light

ACKNOWLEDGMENTS

The author is greatly indebted to his research advisor, Professor E. James Davis, for his financial support and superior guidance of this project. He would also like to extend thanks to his committee members: Prof. John C. Berg, Prof. Eric M. Stuve, Prof. Lewis E. Wedgewood and Prof. Mike J. Pilat for their time and helpful suggestions. Thanks should be also given to the staff and technicians in the Department of Chemical Engineering of University of Washington. A special thanks should be made to the author's research group members: Dr. Mark F. Buehler, Dr. Scott D. Rassat, Willard R. Foss, Dr. Theresa M. Allen, Christopher L. Aardahl, John F. Wildmann, and Michelle Shulman for their friendship and technical support. Finally, the author like to acknowledge his family for their support, especially his brother Dr. Wancheng Li.

INTRODUCTION

Aerosols, consisting of solid particles or droplets suspended in a gas, are commonly encountered in nature and in the life of human beings. They range from submicrometer to micrometer in size and are of great importance in atmospheric phenomena and industrial applications. Typical examples are the formation of the clouds in nature, atmospheric pollution by aerosols produced by natural and industrial processes, and applications of aerosol technology to manufacture high performance materials.

The necessity of studying individual microparticles is apparent since microparticles often behave significantly differently from bulk samples. For example, the rates of formation of sulfuric acid via oxidation of SO_2 in aqueous droplets have been found to be significantly larger than those in bulk solutions (Hansen *et al.*, 1991; Freiberg and Schwartz, 1981). The experimental study of aerosols is complicated by the difficulty of measuring the number density and size distribution of particles. This can be avoided by studying single particles. One advantage of examining single particles is that they experience very short transients, and the processes of heat and mass transfer can usually be regarded as quasi-steady state.

Three techniques have been developed to suspend a single particle, which are electrostatic, electrodynamic and optical levitation. Optical levitation was introduced by Ashkin (1970), and Ashkin and Dziedzic (1977). It allows a neutral particle to be trapped by radiation pressure in a high intensity laser beam operating in the Gaussian mode. Such trapping is not robust, and any imperfection of the laser beam profile as well as motion of the surrounding gas may induce instability.

The electrodynamic balance (EDB) is a widely used apparatus for single particle trapping. It was derived from the electrostatic levitation. Its principles and applications have been reviewed by Davis (1992). The classic EDB (Wuerker *et al.*, 1959) consists of

middle-ring electrode and top and bottom endcaps. An AC source is connected to the ring electrode, and positive and negative DC potentials are imposed on the endcap electrodes. A charged particle can be trapped robustly in the EDB by the combined AC and DC electric forces. AC field centers the particle radially and any vertical forces acting on the particle can be balanced by the DC field. The vertical forces include gravity, the aerodynamic force, radiation pressure, phoretic force and others. The advantage of trapping using the EDB is that one can vary the initial DC potential as well as the amplitudes and frequency of the AC voltage to trap a particle with a desired size. Particles or droplets in the size range of 1-100 μm are routinely trapped in our laboratory.

Since no time-averaged AC electric force is exerted on the suspended particle, the EDB can be used as a gravimetric analyzer to measure vertical forces associated with the particle. For example, Davis and his associates (1992) have studied the drag force and radiation pressure on the particle from the measurements of DC levitation potential. If the EDB is combined with facilities for light scattering measurements, a variety of processes and phenomena can be studied. Light scattering is an effective tool which can be used to measure the physical properties of the particle, such as size and refractive index, and the particle chemistry.

It is the objective of this research to isolate a single particle electrostatically and utilize the technique of light scattering to experimentally explore gas/droplet reactions, droplet evaporation and thermophoresis.

Thermophoresis is the motion of a particle in a gas having an external temperature gradient. When a particle is exposed to the non-equilibrium gas, gas molecules impinging from the hot side of the particle have greater momentum than molecules from the cold side. The difference in momentum transferred by the gas molecules drives the particle toward the cold side. The resulting velocity and associated force are defined as the thermophoretic velocity and the thermophoretic force, respectively.

Thermophoresis can be observed in our daily life and is practically important. For example, one can see the blacking of a glass globe of a kerosene lantern. This is caused by the temperature gradient between the flame and globe which causes the burned particles to deposit on the globe. The principle of thermophoresis has been used for sampling aerosols, and in the optical fiber industry the thermophoretic force is applied to deposit semi-conductive particles on a substrate (Walker *et al.*, 1979). The so-called "modified chemical vapor deposition (MCVD)" is based upon thermophoresis (Nagel, *et al.*, 1982). On the other hand, thermophoresis can cause some undesirable effects. A typical example is the deposition of dusty particles on the cold walls of boilers or heat exchangers, lowering the efficiency of heat transfer.

Evaporation is another phenomenon related to the droplets. Evaporation and condensation are two processes affecting the dynamics of the clouds, dust and smoke. In terms of transport processes, droplet condensation is similar to thermophoresis. The former involves mass transfer of vapor molecules to the droplet surface, and the latter deals with momentum transfer between the particle and the non-equilibrium gas. The mechanics of momentum and mass transfer determined by the ratio of the mean free path of gas to the particle size, which is called Knudsen number, $Kn = \lambda/a$. Here a is the radius of the particle and λ is the mean free path of gas. In the continuum regime ($Kn \ll 1$) the two processes can be described by the macroscopic equations of motion and diffusion. In the free-molecule regime ($Kn \gg 1$) the kinetic theory of gases can be applied to develop expressions for evaporation rate and thermophoresis. In the intermediate or called "Knudsen" regime, the analysis of rate processes faces great mathematical challenges. Approximate solutions based on the Boltzmann equation have been proposed, but theoretical work must be supplemented by experiments to determine accommodation coefficients. Definition and discussion of the accommodation coefficients are given in Chapter 3.

The literature related to thermophoresis and evaporation/condensation is large since both processes are theoretically interesting and practically important. Most of the studies performed so far are theoretical, and experimental work is scarce. Available data for the thermophoretic force or thermophoretic velocity mainly fall in the continuum and near-continuum regimes due to measurement limitations, and the reported data in the continuum, intermediate and free-molecule regimes are insufficient to evaluate recently proposed theories of thermophoresis. Therefore, further measurements of the thermophoretic force are highly desired (Bakanov, 1995).

Experimental studies of droplet evaporation in the transition regime have also been scarce. Numerous measurements have been made in the continuum regime, but accurate data covering the transition regime are unavailable.

Besides making measurements of thermophoretic force and evaporation rates, some studies of gas/droplet reactions were also carried out in this research by means of light scattering. Aerosol reactions are often encountered in the atmosphere and can be used to manufacture materials with unique optical, electric and magnetic properties. The hydrolysis of titanium ethoxide droplets to produce TiO_2 has been examined. The initial purpose of the TiO_2 work was to generate solid microsphere for thermophoresis studies. Prior experiments showed that theories of thermophoresis significantly underpredicted the thermophoretic force for particles with high thermal conductivity k_p . Liquid droplets are spherical, but the thermal conductivity is relatively low, except mercury droplets, and cubic particles of sodium chloride were used in prior experimental studies (Schadt and Cadle, 1961; Jacobsen and Brock, 1965). There is a large uncertainty involved in the size estimation of nonspherical particles. Furthermore, the theory of thermophoresis is based on spheres, so a rigorous test of the theory requires the measurements using spheres with high k_p . Although TiO_2 has a relatively large thermal conductivity, the spheres produced by chemical reactions were found to be chemically inhomogeneous. Light scattering

measurements were used to determine the optical and physical properties of the TiO_2 particle.

In summary, this research experimentally explored gas/droplet reactions and transport processes in the Knudsen regime by means of light scattering. The dissertation is organized according to the following: Chapter 2 provides a brief description of the theory of light scattering. The theory of elastic light scattering for a sphere, now called Mie theory, was developed by Mie (1908), Lorenz (1890) and Debye (1909). Interpreting the measured elastic light scattering data according to Mie theory yields the particle size, which is crucial for the study of thermophoretic force and droplet evaporation, as will be shown in later chapters. The theoretical work and prior experimental studies on thermophoretic force and droplet evaporation will be outlined in Chapter 3.

A newly developed apparatus and the measurement principles used are described in Chapter 4. The history of the EDB is also briefly reviewed in this chapter. The experimental results for the gas/droplet reaction and droplet evaporation are presented in Chapter 5 and 8, respectively. The results for the thermophoretic force are shown in Chapter 6 and 7. The data were used to validate and compare the theories of the thermophoretic force and evaporation. The main achievements of this research are briefly summarized in Chapter 9.

CHAPTER 2

LIGHT SCATTERING BY A SPHERE

2.1 Introduction

When an electromagnetic wave interacts with a particle, the applied electric fields will induce an oscillatory motion for electric charges within the molecules of the particle (electrons, protons and etc.). According to the classical radiation theory, the accelerated charges radiate electromagnetic energy in all directions. This second radiation is described as scattering. At the same time, the electric charges may transfer part of the incident electric energy into other forms, a process called absorption. The scattering process is considered to be elastic if the second radiation has the same frequency of the incident wave. The incident radiation can also cause molecular excitations which lead to a wavenumber shift of the emitted radiation. The shifted radiation in wavenumber with respect to the incident radiation is termed inelastic scattering.

The elastic scattering by objects with a size small compared with the incident wavelength, like gas molecules, is referred to as Rayleigh scattering in memory of Rayleigh, who developed the scattering theory to explain the blue of sky in 1871. The more general theory describing the scattering from spheres with a size order of the incident wavelength was made by Mie (1908) in seeking an understanding of the absorption properties of a gold suspension in water. The same problem was also investigated by Lorenz (1890) and Debye (1909). One of the inelastic phenomena is Raman scattering, which was predicted theoretically by Smekal in 1923, and experimentally observed in liquids five years later by Indian scientists Raman and Krishnan.

The Raman effect and elastic scattering were employed to explore transport processes and droplet reactions in this research. Single particles of micrometer size isolated electrostatically were illuminated by a visible laser beam, and the elastic scattering is

described by Mie theory. Therefore, Mie theory, as well as the principles of Raman scattering, are presented in this chapter. Mie's solution was developed for a homogeneous sphere, and the theory of elastic scattering by an inhomogeneous or "coated" sphere was given by Aden and Kerker (1951). The latter solution, which was used to interpret the light scattering data from a TiO_2 -coated sphere, is also reviewed here.

2.2 Elastic Scattering by a Homogenous Sphere

Consider a homogeneous sphere with radius a which is situated at the origin of a spherical coordinate system (Fig. 2.1), and is illuminated in the z -direction by a linearly polarized monochromatic wave with a wavelength λ and an electric vector \mathbf{E} vibrating in the x -direction. The scattering intensity far away from the particle surface can be obtained from the Maxwellian electromagnetic equations along with the appropriate boundary conditions.

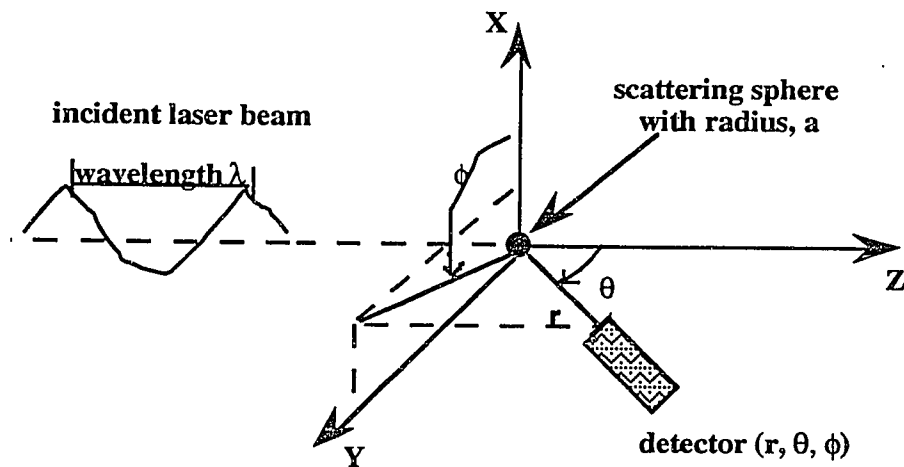


Fig. 2.1 Coordinate system for Mie scattering

The full process for the solution is given in several textbooks (van De Hulst, 1957; Kerker, 1969; Bohren and Huffman, 1983). The final results for the scattering intensity, I , may be written as

$$I = \frac{\lambda^2 I_0}{4\pi^2 r^2} [|S_1|^2 \sin^2 \phi + |S_2|^2 \cos^2 \phi], \quad (2.1)$$

where I_0 is the intensity of incident light, λ is the wavelength of incident beam in vacuum, r represents the radial position of the detector, ϕ is the azimuthal angle for the detector, and S_1 and S_2 are the scattering amplitude functions perpendicular to and parallel with the incident \mathbf{E} vector, respectively. They have the forms

$$S_1 = \sum_{n=1}^{\infty} \frac{2n+1}{n(n+1)} [a_n(m, X)\pi_n(\cos\theta) + b_n(m, X)\tau_n(\cos\theta)] \quad (2.2)$$

and

$$S_2 = \sum_{n=1}^{\infty} \frac{2n+1}{n(n+1)} [a_n(m, X)\tau_n(\cos\theta) + b_n(m, X)\pi_n(\cos\theta)], \quad (2.3)$$

where θ is the polar angle or scattering angle defined by the propagation vector and the position of the detector. The scattering coefficients a_n and b_n are defined by

$$a_n = \frac{m\psi_n(mX)\psi'_n(X) - \psi'_n(mX)\psi_n(X)}{m\psi_n(mX)\xi'_n(X) - \psi'_n(mX)\xi_n(X)} \quad (2.4)$$

and

$$b_n = \frac{\Psi_n(mX)\Psi'_n(X) - m\Psi'_n(mX)\Psi_n(X)}{\Psi_n(mX)\xi'_n(X) - m\Psi'_n(mX)\xi_n(X)}, \quad (2.5)$$

in which Ψ_n and ξ_n are Riccati-Bessel functions, and the prime represents differentiation with respect to the arguments in the associated brackets, m is the ratio of refractive index of the particle to the surrounding medium, which consists of a real number, n , and imaginary part, k , that is, $m = n + ik$, where $i = \sqrt{-1}$. The values of n and k depend on the materials and also vary with the incident wavelength. The imaginary part k determines the absorption of incident electromagnetic energy by the particle, and X is a dimensionless parameter called the particle size parameter, defined by

$$X = \frac{2\pi a}{\lambda}. \quad (2.6)$$

The angular dependence of the scattering intensity is expressed by

$$\pi_n = \frac{P_n^{(1)}(\cos\theta)}{\sin\theta}, \quad (2.7)$$

and

$$\tau_n = \frac{d}{d\theta} P_n^{(1)}(\cos\theta) \quad (2.8)$$

where $P_n^{(1)}$ is the associated Legendre polynomial of order 1 and degree n .

2.2.1 Phase Function

The intensity of the scattered light is determined by four variables: m , X , θ and ϕ . Phase function refers to the scattering intensity as a function of scattering angle, θ , at given

values of X , m and ϕ . A calculated phase function from Mie's solution is shown in Fig. 2.2. It consists of numerous oscillatory peaks. The fine structure of a phase function depends on the size parameter and refractive index of the particle, but the global structure (the number of peaks) is found to be moderately insensitive to the refractive index, m . Davis and Periasamy (1985) performed extensive calculations of phase functions for solids and droplets having different m and X from Mie theory, and recognized that the number of peaks in a defined scattering angle range depends on m weakly, but is proportional to the size parameter of the particle, that is, to the radius of the particle.

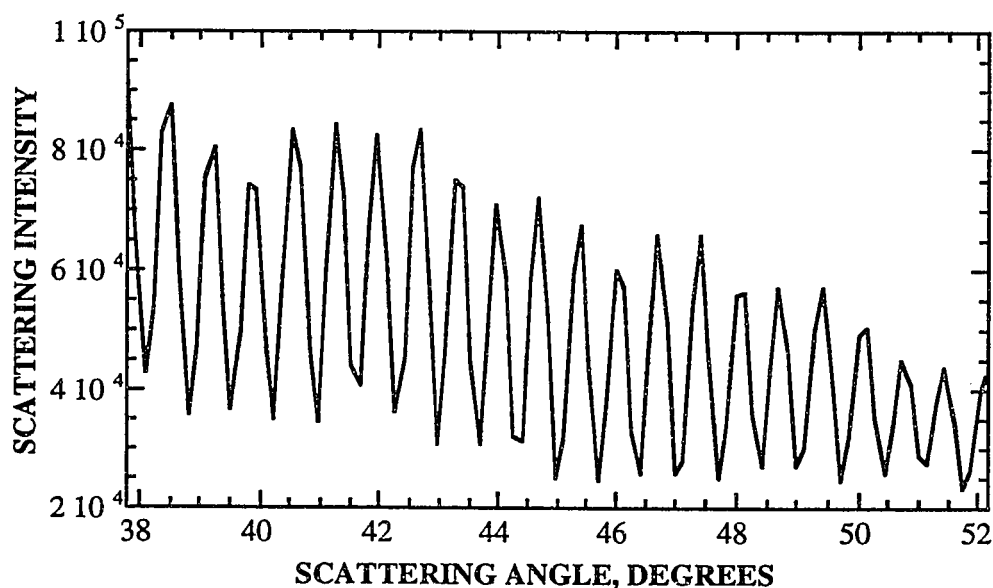


Figure 2.2 A calculated phase function from Mie theory for a DOP droplet with $X = 300$ and $\phi = 90^\circ$.

Figure 2.3 is a plot of the particle size parameter, X , versus the number of peaks counted from the calculated phase functions for DOP droplets in the angle range $37.85^\circ \leq \theta \leq 52.15^\circ$. A linear relationship can be obtained from such a plot, and the

interpolation formula may be used to determine the particle size from the measured phase functions over the same scattering angle range.

Phase functions can be used to determine the particle size and refractive index with a high accuracy. For example, Ray *et al.* (1990) demonstrated that comparing a carefully measured phase function with Mie theory could yield the particle size and refractive index with an accuracy of 2 parts in 10^4 .

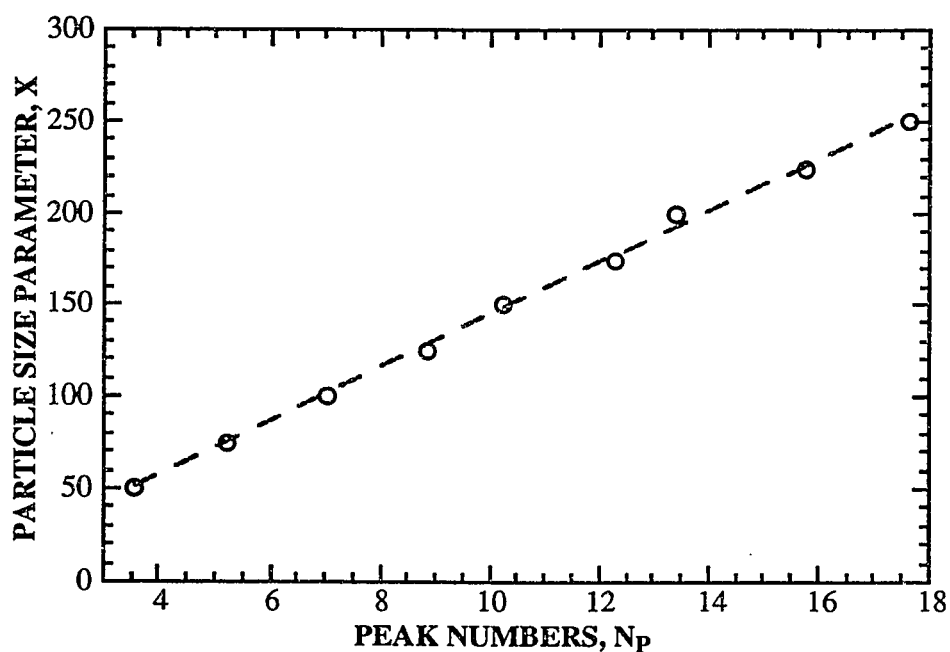


Figure 2.3 A plot of the size parameters of DOP droplets versus the number of peaks showing the linear relationship of them.

2.2.2 Optical Resonance Spectrum

The optical resonance spectrum is a result of "morphology dependent resonances" (MDRs) and describes the change of light scattering intensity with X and/or m for the particle at fixed values of θ and ϕ . Phase functions and MDRs are two useful tools for determining the size and refractive index of a particle. Calculated MDRs from Mie's

solution are shown in Fig. 2.4. The structure of MDRs is characterized by periodical and sharp spikes superimposed on the broad, round "lobes". The sharp resonance occurs because at specific combinations of X and m , the refracted and reflected rays from the droplet interfere constructively and the droplet behaviors like a resonant cavity under these conditions.

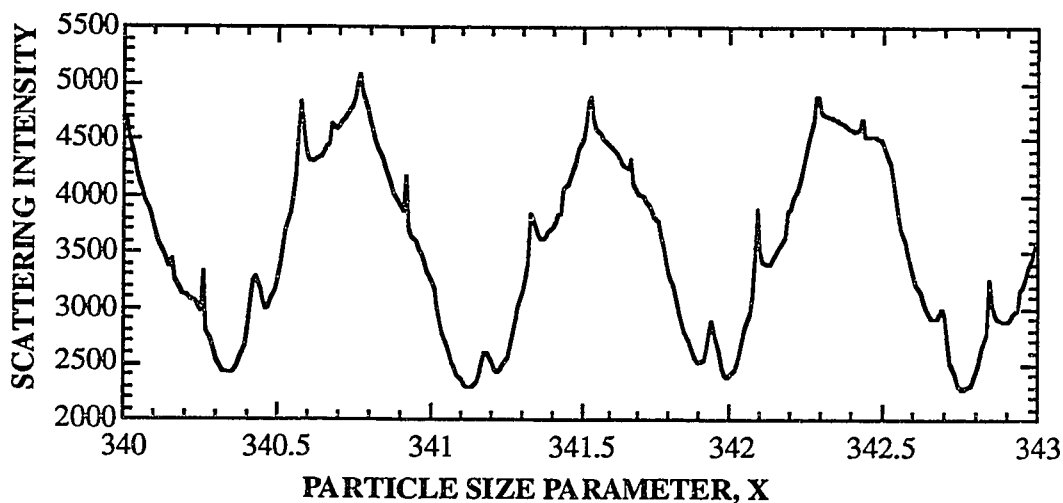


Figure 2.4 The optical resonance spectrum of a DOP droplet calculated from Mie theory with $\phi = 90^\circ$ and $\theta = 45^\circ$.

The MDRs were first recognized experimentally by Ashkin and Dziedzic (1977) in their investigation of radiation pressure for an optically levitated droplet. Theoretically, the appearance of an optical resonance is attributed to the poles of the scattering coefficients a_n and b_n , as discussed by Conwell *et al.* (1984). At certain values of particle size and refractive index, the denominators of a_n and b_n vanish which causes a dramatic increase in the scattering functions S_1 and S_2 defined by Eq. (2.2) and (2.3). The resonance is called a transverse magnetic mode or TM resonance if it is produced by the complex zero in the

denominator of a_n . Otherwise, it is referred to as transverse electric mode or TE resonance, corresponding to the poles of b_n .

On resonance the internal electromagnetic fields of the particle are also substantially increased since the scattered fields and internal fields are related to each other. The components of the internal fields for a sphere shown in Fig. 2.1 may be expressed by

$$E_r = \frac{\cos\phi}{k_1 r^2} E_0 \sum_{n=1}^{\infty} i^{n-1} (2n+1) d_n \pi_n \Psi_n(k_1 r) \sin\theta \quad (2.9)$$

$$E_\theta = \frac{\cos\phi}{k_1 r} E_0 \sum_{n=1}^{\infty} i^{n-1} \frac{(2n+1)}{n(N+1)} [d_n \tau_n \Psi'_n(k_1 r) + i c_n \pi_n \Psi_n(k_1 r)] \quad (2.10)$$

and

$$E_\phi = \frac{-\sin\phi}{k_1 r} E_0 \sum_{n=1}^{\infty} i^{n-1} \frac{(2n+1)}{n(N+1)} [d_n \pi_n \Psi'_n(k_1 r) + i c_n \tau_n \Psi_n(k_1 r)]. \quad (2.11)$$

in which $k_1 = 2\pi m/\lambda_0$, and the coefficients c_n and d_n are given by

$$c_n = \frac{m i}{\Psi_n(mX) \xi'_n(X) - m \Psi'_n(mX) \xi_n(X)} \quad (2.12)$$

and

$$d_n = \frac{m i}{m \Psi_n(mX) \xi_n(X) - \Psi'_n(mX) \xi'_n(X)}. \quad (2.13)$$

One may note that the denominators of the expansion coefficient c_n and d_n are, respectively, the same as the denominators of the scattering coefficients b_n and a_n . On

resonance the increased internal electric field will not only increase the elastic scattering intensity, but it may also increase the intensity of Raman scattering. This effect was observed by Thurn and Kiefer (1984) and others in the study of Raman spectra of single microdroplets. It complicates the quantitative interpretation of Raman spectra since the measured height or area of a Raman peak on a resonance is significantly increased without corresponding to a change of concentrations of a Raman-active chemical within the particle (Buehler, 1991).

The MDRs are extremely sensitive to the size parameter and the refractive index of the particle. A measurement accuracy of approximately one part in 10^5 has been reported by Chylek *et al.* (1983). However, it is difficult to make an unambiguous comparison of measured MDRs with theory since the fine structure of MDRs vary significantly with the scattering angle θ . This requires that the position of a detector is known very accurately. Normally, an average of MDRs over a small range of scattering angles is measured, and theoretical solutions integrated over the same scattering angle range are used in the comparison. Another limitation in using MDRs is that the initial particle size for a measured MDR spectrum is not known, *a priori*, so it requires a trial and error matching procedure to identify the correct initial particle size. This limitation may be overcome if phase functions are recorded in the experiments along with the MDRs, for the sizes determined from the phase functions can be incorporated into the comparison of MDRs. Also, it provides an consistent check on the size measurements.

Because of the high accuracy of measurement, optical resonance spectra have been widely used to explore physical and chemical processes and phenomena for single microparticles. The applications were reviewed by Davis (1992).

2.3 Elastic Scattering by an Inhomogeneous Sphere

Let the particle shown in Fig. 2.1 be a coated sphere consisting of a core with a radius, b , and refractive index, m_1 , with respect to the surrounding gas, and of a shell with a refractive index, m_2 , and with a thickness $a-b$. This boundary value problem of light scattering was solved by Aden and Kerker (1951). The results were summarized by Bohren and Huffman in their textbook (1983). The expression for the scattered intensity is the same as that for the homogeneous sphere expressed by Eq. (2.1), except that the scattering coefficients a_n and b_n are more complicated, having the forms

$$a_n = \frac{\psi_n(Y)[\psi'_n(m_2Y) - A_n\chi'_n(m_2Y)] - m_2\psi'_n(Y)[\psi_n(m_2Y) - A_n\chi_n(m_2Y)]}{\xi_n(Y)[\psi'_n(m_2Y) - A_n\chi'_n(m_2Y)] - m_2\xi'_n(Y)[\psi_n(m_2Y) - A_n\chi_n(m_2Y)]} \quad (2.14)$$

and

$$b_n = \frac{m_2\psi_n(Y)[\psi'_n(m_2Y) - B_n\chi'_n(m_2Y)] - \psi'_n(Y)[\psi_n(m_2Y) - B_n\chi_n(m_2Y)]}{m_2\xi_n(Y)[\psi'_n(m_2Y) - B_n\chi'_n(m_2Y)] - \xi'_n(Y)[\psi_n(m_2Y) - B_n\chi_n(m_2Y)]}, \quad (2.15)$$

in which A_n and B_n are defined by

$$A_n = \frac{m_2\psi_n(m_2X)\psi'_n(m_1X) - m_1\psi'_n(m_2X)\psi_n(m_1X)}{m_2\chi_n(m_2X)\psi'_n(m_1X) - m_1\chi'_n(m_2X)\psi_n(m_1X)} \quad (2.16)$$

and

$$B_n = \frac{m_2\psi_n(m_1X)\psi'_n(m_2X) - m_1\psi'_n(m_2X)\psi_n(m_1X)}{m_2\chi'_n(m_2X)\psi_n(m_1X) - m_1\psi'_n(m_1X)\chi_n(m_2X)}. \quad (2.17)$$

Here $X (= 2\pi b/\lambda)$ is the size parameter of the core, $Y (= 2\pi a/\lambda)$ is the size parameter of the sphere, and Ψ and χ are the Riccati-Bessel functions.

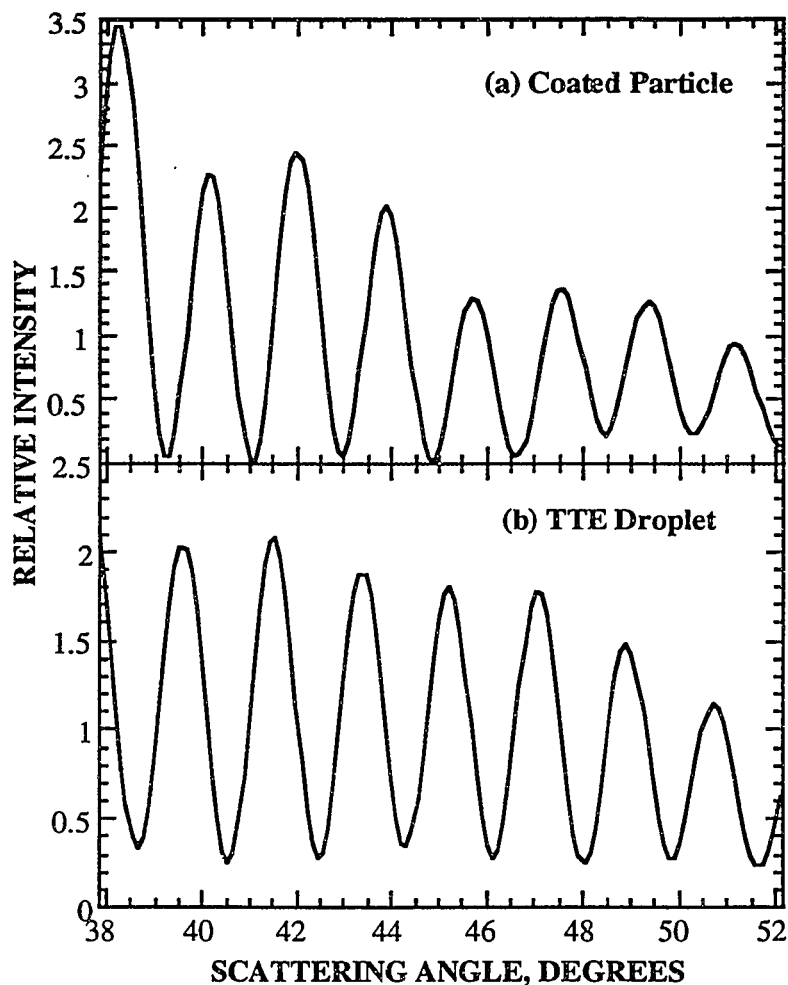


Figure 2.5 Comparison of the phase functions between (a) a coated particle consisting of TTE core and TiO_2 shell, and (b) a pure TTE droplet.

Figure 2.5 presents a phase function determined from the solution of Aden and Kerker for a titanium ethoxide (TTE) droplet ($X = 100$) coated with a shell of TiO_2 ($Y = 110$). Also shown in the figure is the phase function for a pure TTE droplet with the size parameter 110. It can be seen that the scattering intensity and the positions of peaks and troughs are different, although the outer sizes of both particles are the same. The difference in phase functions between coated and pure particles indicates that one may estimate the

shell thickness from the measured phase functions. Measurements of the light scattering by a coated particle were made by Hightower *et al.* (1988), and Ray *et al.* (1991) examined the coating of dioctyl phthalate vapors on the droplet of glycerol via elastic light scattering. The solution of Aden and Kerker was also employed by Li, *et al.* (1994) to study the chemical reaction of titanium ethoxide and water vapor (Chapter 5).

2.4 Inelastic Scattering — Raman Spectroscopy

Raman scattering has been treated by numerous investigators since its discovery. A good survey was made by Schweiger (1990) for Raman scattering by single microparticles, and a full theoretical treatment can be found in books by Bhagavantam (1942) and Long (1970). A brief explanation of the Raman effect will be made here.

When an incident electromagnetic wave interacts with a polarizable molecule, the applied electric field induces a dipole moment in the molecule. The dipole moment, \mathbf{M} , can be related to the incident electric field \mathbf{E} by a power series

$$\mathbf{M} = \alpha \cdot \mathbf{E} + \mathbf{M}^{(2)} + \mathbf{M}^{(3)} + \dots, \quad (2.18)$$

in which α is a second-order polarizability tensor. It represents the ability of electrons to be displaced by the applied electric field to produce an electric dipole. The molecular polarizability depends on the motion of electron clouds and on the intermolecular distance as well as other factors. Moments $\mathbf{M}^{(2)}$ and $\mathbf{M}^{(3)}$ are higher-order dipole moments associated with the incident electric fields. The first term in Eq. (2.18) represents a linear relationship between the dipole moment, \mathbf{M} , and the incident electric field, \mathbf{E} . The higher-order terms corresponding to nonlinear scattering processes are generally many orders of magnitude smaller than the first-order term, and they cannot be observed in the experiments

without a high intensity radiation source (pulsed laser). Thus, Eq. (2.18) may be simplified to

$$\mathbf{M} = \alpha \cdot \mathbf{E}. \quad (2.19)$$

The polarizability may be altered by molecular rotations and vibrations. For a k-th normal vibration with a frequency ω_k , one may express the polarizability by a Taylor series with respect to the equilibrium position, $\mathbf{x}_{k,0}$

$$\alpha = \alpha_0 + \left(\frac{\partial \alpha}{\partial \mathbf{x}_k} \right) \mathbf{x}_k, \quad (2.20)$$

in which α_0 is the polarizability at the equilibrium position, \mathbf{x}_k is the displacement of vibration at the circular frequency ω_k .

Suppose the vibration of the k-th model is harmonic and the motion may be expressed by

$$\mathbf{x}_k = \mathbf{x}_{k,0} \cos(\omega t + \delta_k), \quad (2.21)$$

in which δ_k is a phase factor, and let the incident electric field, \mathbf{E} , be

$$\mathbf{E} = \mathbf{E}_0 \cos(\omega t). \quad (2.22)$$

Then, one can obtain the following expression for the induced dipole moment $\mathbf{M}^{(1)}$ from Eq. (2.19) - (2.22)

$$\begin{aligned}
\mathbf{M}^{(1)} = & \alpha_0 \cdot \mathbf{E}_0 \cos(\omega_0 t) + \left(\frac{\partial \alpha}{\partial \mathbf{x}_k} \right) \cdot \mathbf{E}_0 \mathbf{x}_{k,0} \cos[(\omega_0 + \omega_k)t + \delta_k] \\
& + \left(\frac{\partial \alpha}{\partial \mathbf{x}_k} \right) \cdot \mathbf{E}_0 \mathbf{x}_{k,0} \cos[(\omega_0 - \omega_k)t + \delta_k].
\end{aligned} \tag{2.23}$$

It is noted that Eq. (2.23) has three terms including three distinctive frequencies: the first term, having the same frequency as the incident radiation, accounts for the elastic scattering, and the second and third terms having higher and lower radiation frequencies compared with the incident radiation. The latter frequencies correspond to the anti-Stokes Raman and Stokes Raman, respectively.

Derivations based upon the classic theory of radiation give the intensity ratio of anti-Stokes scattering to Stokes scattering by

$$\frac{I_a}{I_s} = \frac{(\nu_0 + \nu_k)^4}{(\nu_0 - \nu_k)^4} \tag{2.24}$$

with

$$I_s = \frac{\pi^2 I_0 N}{\epsilon_0^2} (\nu_0 - \nu_k)^4 \left\{ (\alpha'_{yy})_k^2 + (\alpha'_{zy})_k^2 \right\} Q_{k0}^2 \tag{2.25}$$

Here, I_0 is the intensity of the incident radiation, I_s and I_a are the Stokes and anti-Stokes Raman intensities, ϵ_0 is the permittivity of free space, α'_{yy} and α'_{zy} are components of the derived polarizability tensor, Q_{k0} is the normal coordinate of vibration, ν is related to the vibrational frequency and is in energy units of wavenumber (cm^{-1}), which is commonly used as the abscissa of Raman spectra. It is related to the circular frequency, ω , by

$$\nu = \frac{\omega}{2\pi c} \quad (2.26)$$

in which c is the speed of light in vacuum.

The results from the classic radiation theory are adequate to qualitatively illustrate the characteristics of Raman scattering, but the dependence of the intensity ratio I_a/I_s on the scatterer temperature, which is observed in experiments, is not revealed in Eq. (2.24). To treat the scattering intensity ratio correctly, the principles of the quantum mechanics are required.

In the treatments of quantum mechanics, the incident photons are usually regarded as being absorbed, and the same amount of photons are created by molecules. Suppose some molecules initially reside in a certain vibrational energy level of the ground electronic state (Fig. 2.6), and then are excited to some virtual electronic state after absorbing the incident photons. The excited electrons are unstable and rapidly (10^{-15} s) return to the ground state by scattering new photons. The energy associated with the released photons is determined by the vibrational energy state in which electrons fall. If the electrons return to the same energy level initially occupied, there is no energy exchange involved and the scattering process is elastic. If electrons fall into higher vibrational energy level than the initial one, some of the incident photon energy is transferred to the molecules, and the scattered photons have lower energy (Stokes Raman). However, if electrons are already vibrating or in an upper energy level, and they fall back to a lower energy level after the excitation, part of their vibrational energy will be transferred to the scattered photons, and the anti-Stokes Raman appears. Thus, the scattered photons carry information about the molecular vibrations.

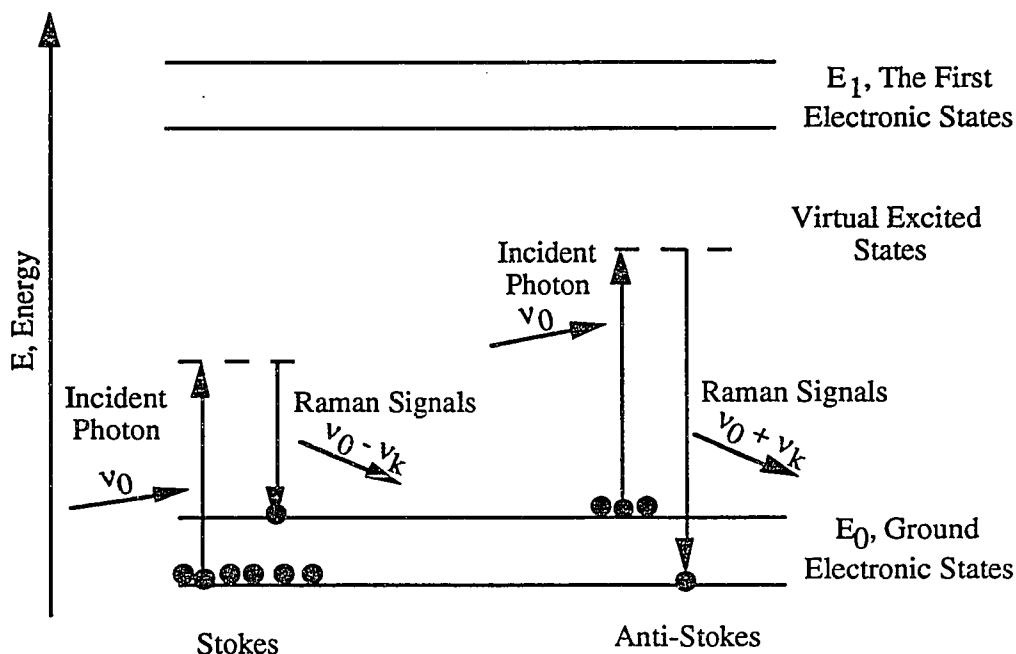


Figure 2.6 A schematic diagram showing the Stokes and anti-Stokes Raman scattering.

At room temperature large numbers of molecules remain in the ground electronic state, and the intensity of Stokes Raman is stronger than the anti-stokes Raman. According to Long's analysis, the relative magnitude of the intensity of the Stokes scattering to the anti-Stokes scattering is

$$\frac{I_a}{I_s} = \frac{(\nu_0 + \nu_k)^4}{(\nu_0 - \nu_k)^4} \exp(-h\nu_k / k_B T), \quad (2.27)$$

Here k_B is the Boltzmann constant, T is the absolute temperature. The dependence of Raman scattering on the temperature is explicitly shown in Eq. (2.27). By measuring the intensity of Stokes Raman and anti-Stokes Raman, the absolute temperature may be determined.

Compared with bulk samples, the Raman effect from a droplet is complicated by the appearance of MDRs as pointed out earlier. On resonance the enhanced internal electric field increases the scattering field significantly. Theoretical considerations of the effects of the internal field, size and refractive index of the sphere on the intensity of Raman spectra have been made by Chew *et al.* (1976, 1978), by Schweiger (1990) and by Kerker and his associates (1978, 1979). These effects have also been experimentally observed by Owen *et al.* (1981a, b), Thurn and Kiefer (1984), Buehler (1991) and others

In addition to Raman scattering, fluorescence is another inelastic phenomenon. Fluorescence involves molecular transitions from the ground to higher electronic states (such as the first electronic state; see Fig. 2.6), while Raman scattering is caused by electronic excitations between the ground electronic state and some virtual energy states, falling below the first excited state. The intensity of fluorescence is much stronger and the process is much slower (10^{-5} to 10^{-9} s) than Raman scattering (10^{-15} s).

CHAPTER 3

REVIEW OF THERMOPHORESIS AND EVAPORATION

3.1 Introduction

The processes of thermophoresis and evaporation depend on the Knudsen number, $Kn = \lambda/a$, where λ is the mean free path of gas phase molecules, and a is radius of the spherical particle or droplet. For arbitrary Kn , the thermophoretic force, F_{th} , can be calculated from the net momentum transfer by gas molecules to the particle through the following expression:

$$F_{th} = \int dS \cdot \sum_{\pm} \int_{\pm} m \mathbf{v} \mathbf{v} f^{\pm} dv, \quad (3.1)$$

and the mass flux, J_k , can be determined from the number of vapor molecules evaporated from the droplet surface by

$$J_k = \int dS \cdot \sum_{\pm} \int_{\pm} \mathbf{v} f^{\pm} dv, \quad (3.2)$$

in which + and - denote quantities for molecules incidented on and reflected from the particle surface, respectively, f is molecular velocity distribution function, \mathbf{v} is molecular velocity, dv represents the element volume of the velocity space, $dS = 2\pi a^2 n \sin\theta d\theta$, \mathbf{n} is the unit vector and θ is the polar angle.

The velocity distribution functions included in Eqs. (3.1) and (3.2) are govern by the Boltzmann integro-differential equation, which has the form:

$$\frac{\partial f}{\partial t} + \mathbf{v} \cdot \frac{\partial f}{\partial \mathbf{r}} + \mathbf{a} \cdot \frac{\partial f}{\partial \mathbf{v}} = \int_{-\infty}^{\infty} d\mathbf{v} \int_0^{2\pi} d\epsilon \int_0^{\infty} db [(ff_1 - f'f'_1)b\mathbf{V}_r]. \quad (3.3)$$

Equation (3.3) was derived based upon the binary molecular collisions. Here f is the distribution function of the gas velocity for the incident stream of molecules, f_1 is the distribution function for the target molecules, f' and f'_1 are respectively the distribution functions for the incident and the target molecules after the collision, \mathbf{a} is the acceleration, b is the impact parameter, \mathbf{V}_r is the relative velocity of the two molecules involved in the binary collision, ϵ is the angle between the plane of the orbit and the fixed plane passing through the initial velocity vector.

The Boltzmann equation cannot be solved unless simplified (linearized) because of the complicated right-side term, called "collision term". Various approximate methods and mathematical models have been developed to simplify the collision term. A model developed by Bhatnagar, Gross and Krook (1954), called BGK model, is relatively simple and widely used. The basic idea behind the BGK model is to rewrite the complicated collision term by

$$\int_{-\infty}^{\infty} d\mathbf{v} \int_0^{2\pi} d\epsilon \int_0^{\infty} db [(ff_1 - f'f'_1)b\mathbf{V}_r] = \omega(f - f^0). \quad (3.4)$$

in which ω is called the collision frequency and f^0 is the Maxwellian distribution function for the equilibrium state.

In addition to the BGK approximation, a number of semi-theoretical approaches have been employed to develop expressions for the two processes. In the continuum regime ($Kn \ll 1$), the macroscopic transport equations and "slip" model were used, and in the so-called "free-molecule" limit ($Kn \gg 1$), the kinetic principles of gases are applied. At the

intermediate regime ($Kn \sim O(1)$) or called "Knudsen regime", Fuchs (1934) proposed the "matching" method to determine the rate of droplet evaporation, and Springer (1970) generalized the Shermann correlation (1963) for heat transfer and shear in a rarefied gas to fit the data for thermophoretic force (TF). Experimental correlations were also developed by Schmitt (1959) and by Jacobsen and Brock (1965) to predict TF at $0.2 < Kn < \infty$.

The theoretical results for thermophoresis and evaporation based upon the linearized BGK equation and the solutions derived from other approximations are reviewed in this chapter. Prior experimental studies of droplet evaporation and thermophoresis are also discussed.

3.2 Theory of Thermophoresis

Early theoretical analyses of thermophoresis were made by Einstein (1924) and Cawood (1936). They applied the elementary kinetic theory of gases to derive expressions for particles with small size compared with the mean free path of gas, that is $Kn \gg 1$. Waldmann (1959) and Derjaguin and Bakanov (1959) improved the analyses of the free-molecule regime.

A primary uncertainty in theoretical analyses is the state of molecules after colliding with a surface. Maxwell (1879) recognized and addressed this problem and introduced the concept of partial accommodation of gas molecules with a surface. Momentum and energy are exchanged by molecular collisions. The characteristics of the molecules leaving a surface can be represented by accommodation coefficients, which are defined by

$$\alpha_m = \frac{M_i - M_e}{M_i - M_s} \quad (3.5)$$

and

$$\alpha_t = \frac{E_i - E_e}{E_i - E_s}. \quad (3.6)$$

Here M represents the average tangential component of momentum of the molecules, and E is the average energy flux. Subscripts e , i and s refer, respectively, to molecules emerging from the surface, incident molecules, and molecules leaving the surface in Maxwellian equilibrium with the surface.

Two special cases related to the momentum and energy exchange processes are respectively called specular reflection and diffuse emission. The former case, corresponding to zero accommodation coefficient, physically represents no change of tangential momentum or energy during the collision. In the latter case a molecule is considered to be absorbed and then re-evaporated from the surface with an energy and momentum independent of its energy and momentum prior to collision, so the accommodation coefficients are unity.

The first analysis of the thermophoretic force in the near-continuum regime was performed by Epstein (1929). He solved the Navier-Stokes equations and incorporated the concept of "thermal slip flow" into the gas/particle boundary condition. Thermal slip flow was introduced by Maxwell (1879). In seeking an understanding of the radiometric force, Maxwell investigated the motion of gas around an unequally heated surface and concluded that a discontinuity in the gas phase velocity distribution should exist. It was called the "thermal slip flow". Maxwell obtained the following expression for the velocity of thermal slip:

$$V_{ts} = -\frac{3}{4} \frac{\mu}{\rho T_0} \nabla T_\infty, \quad (3.7)$$

where μ is the gas viscosity, ρ the gas density, ∇T_∞ is the external temperature gradient, and T_0 is the average gas temperature. The constant $3/4$ is called "thermal slip coefficient" denoted by C_{ts} . The solution for thermophoretic force based upon above gas/particle boundary condition may be written

$$F_{th} = -9\pi a \frac{\mu^2}{\rho T_0} Kn \left(\frac{k_g / k_p}{1 + 2k_g / k_p} \right) \nabla T_\infty, \quad (3.8)$$

where k_g and k_p are respectively the thermal conductivities of gas and particle. For polyatomic gases the translational thermal conductivity should be used, which is related to viscosity by

$$k_{g,tran} = \frac{15}{4} \mu R, \quad (3.9)$$

based upon the kinetic theory of gases. Here R is the gas constant. (Based upon most theoretical studies and all experimental work so far, the directions of thermophoretic force and thermophoretic velocity should be opposite to the external temperature gradient, so the vector signs for F_{th} and V_{ts} are ignored in Eqs. (3.7) and (3.8), and will be ignored in the following discussion).

Epstein's result, which is to first order in Kn shown in Eq. (3.8), was found to agree reasonably with measurements of Schadt and Cadle (1961) for particles with low k_p , but for high k_p the theory predicts a vanishing force, which contradicts experiments. For example, Schadt and Cadle showed that the measured thermophoretic force for a particle of sodium chloride is about two orders of magnitude larger than the prediction.

It should be pointed out that the thermal slip coefficient $3/4$ obtained by Maxwell is only a rough approximation, and the results based upon the BGK approximation show that

C_{ts} depends on the thermal accommodation coefficient α_t . The calculated values from different methods vary from 0.75 to 1.2. The correlation of Ivchenko and Yalamov (1971), who solved the BGK approximation using the ellipsoidal statistical method, was recommended by Talbot *et al.* (1980) to calculate C_{ts} as a function of α_t . It may be written

$$C_{ts} = \frac{3}{2} \left(\frac{0.6264 + 0.3736\alpha_t}{1.2528 + 0.0306\alpha_t} \right). \quad (3.10)$$

Other correlations for C_{ts} were reviewed by Annis (1972) and Bakanov (1991).

Epstein's pioneer work on the thermophoretic force in the near-continuum regime led to numerous analyses. The methods involved in these analyses can be categorized as (i) application of continuum theory with slip and jump boundary conditions, (ii) moment-approximate solutions to the Boltzmann equation, (iii) application of the principles of irreversible thermodynamics, and (iv) numerical solutions of the linearized BGK Boltzmann Equation. The following review is classified according to the three Kn regimes: slip flow (near-continuum), Knudsen (intermediate) and free-molecule regimes.

3.2.1 Slip Flow

Recognizing that the measurements for particles with high k_p disagreed with Epstein's theory, Brock (1962) extended the hydrodynamic analysis to include the tangential temperature jump and normal velocity slip boundary conditions, which may be expressed as

$$T_g - T_p = C_t \lambda \left(\frac{\partial T_g}{\partial r} \right) \Big|_{r=a}, \quad (3.11)$$

and

$$V_{\theta} = C_m \lambda \left[r \frac{\partial}{\partial r} \left(\frac{V_{\theta}}{r} \right) + \frac{1}{r} \frac{\partial V_r}{\partial r} \right] + C_{ts} \frac{\mu}{\rho T_0} \left(\frac{\partial T_g}{\partial \theta} \right), \quad (3.12)$$

Here, T_0 is the average gas temperature, and C_t and C_m are respectively the temperature jump coefficient and the velocity jump coefficient. The first term of the right side in Eq. (3.12) represents the normal velocity jump, and the second term is the tangential thermal slip velocity, which is similar to Eq. (3.7) except that the $3/4$ is replaced by C_{ts} .

The jump coefficients C_t and C_m can be determined from the kinetic theory of gases (Kennard, 1938) to yield

$$C_m = \frac{2 - \alpha_m}{\alpha_m}, \quad (3.13)$$

and

$$C_t = \frac{2 - \alpha_t}{\alpha_t} \frac{2}{\gamma + 1} \frac{k_g}{\mu C_v} = \frac{2 - \alpha_t}{\alpha_t} \frac{2\gamma}{\gamma + 1} \frac{1}{Pr}. \quad (3.14)$$

Here γ is the ratio of the heat capacity at constant pressure, C_p , to the heat capacity at constant volume, C_v , μ is gas viscosity and Pr is the Prandtl number. For a monatomic ideal gas, kinetic theory gives $\gamma = C_p/C_v = 5/3$ and $k_g/\mu C_p = Pr^{-1} = 1.5$, Eq. (3.14) can be simplified to:

$$C_t = \frac{15}{8} \frac{2 - \alpha_t}{\alpha_t}. \quad (3.15)$$

The coupled transport equations and the jump and slip boundary conditions were solved by Brock applying a perturbation method. The solution may be written

$$F_{th} = -12\pi C_{ts} a \frac{\mu^2}{\rho T_0} \left\{ \frac{k_g / k_p + C_t Kn}{(1 + 3C_m Kn)(1 + 2k_g / k_p + 2C_t Kn)} \right\} \nabla T_\infty. \quad (3.16)$$

Brock's result reduces to Epstein's expression for small Kn using $C_{ts} = 3/4$. Brock compared Eq. (3.16) with experimental data, and found the agreement was better than Epstein's solution for the particles of low k_p , but the discrepancy was still high for particles with high k_p . Later, Jacobsen and Brock (1967) developed an expression using the flux expression obtained from the third approximation to the Boltzmann equation. The final results can only be used to fit experimental data, but not to predict the force *a priori*, for it contains an unknown constant.

Brock's solution based on the macroscopic hydrodynamic equations and slip boundary conditions should be valid in the continuum and near-continuum regimes. Talbot *et al.* (1980) suggested the use of Eq. (3.16) to fit the experimental data for arbitrary Kn. Note that Eq. (3.16) approaches $(C_{ts}/C_m)F_{th,fm}$ at large Kn. Here, $F_{th,fm}$ is Waldmann's free-molecule limit given by Eq. (3.21). Thus, if the ratio C_{ts}/C_m is close to unity, Brock's theory approaches Waldmann's free-molecule limit.

An alternative analysis for thermophoresis in the slip-flow regime was introduced by Derjaguin and Yalamov (1965) based upon irreversible thermodynamics and Onsager's reciprocity relations. The principles were first used to study the problem of thermomolecular pressure drop in a capillary, and then extended to the study of the thermophoretic velocity, V_t . The details were described by Derjaguin *et al.* (1972). The earlier results were found to be incomplete by Derjaguin *et al.* (1976). The final solution for the thermophoretic velocity may be written

$$V_t = -3 \frac{\mu}{\rho T_0} \frac{(k_g / k_p + C_t Kn)}{(1 + 2k_g / k_p + C_t Kn)} \nabla T_\infty. \quad (3.17)$$

The thermophoretic force can be determined from the Basset relationship for drag force and velocity valid in the near-continuum regime, which gives

$$F_{th} = -18a\pi \frac{\mu^2}{\rho T_0} \left(\frac{k_g / k_p + C_t Kn}{1 + 2k_g / k_p + C_t Kn} \right) \nabla T_\infty. \quad (3.18)$$

Measured results of thermophoretic velocities by Derjaguin *et al.* (1976) showed that the factor 3 in Eq. (3.18) has to be revised downward to 2.2, which corresponds to $C_{ts} = 1.1$, a value falling in the range of theoretical predictions. The effect of the temperature jump on velocity and force is represented by the coefficient C_t , but no information on the velocity jump and thermal slip effects is included in Eq. (3.18). Equation (3.18) agrees with Brock's solution if $C_{ts} = 1.5$ is assigned in Eq. (3.16) and if the term $(1+3C_m Kn)$ is ignored.

Grad's 13-moment solution of the Boltzmann equation was first used by Dwyer (1967) to derive expressions for the thermophoretic force on a sphere, which was claimed to be applicable over the whole Kn regime. The expression, including the third-order term in Kn, may be written

$$F_{th} = -\frac{16}{15} \pi a^2 k_g \frac{\nabla T_\infty}{c} \left(C_t Kn^2 + \left[\frac{1 + 2k_g / k_p}{C_m (12Kn + \alpha_t)} + \frac{k_g}{k_p} - 1 \right] Kn + \frac{2C_t Kn^2}{12C_m Kn + 1} \right) / \left(\frac{6C_t}{15} Kn^3 + \left(\frac{1}{5} - \frac{3R\mu}{2k_p} \right) Kn^2 + \frac{1}{3} \left(1 + 2\frac{k_g}{k_p} + 2Kn\pi C_t \right) \left(\frac{3C_m Kn + 1}{12C_m Kn + 1} \right) \right), \quad (3.19)$$

in which R is the gas constant.

Phillips (1975) presented an expression for the thermophoretic force using the modified two-stream distribution function of Chapman-Enskog and the first four-moment solutions of the Boltzmann equation. The final result may be written

$$F_{th} = -9\pi a \frac{\mu^2 \nabla T_\infty}{\rho T_0} \left(\frac{k_g / k_p}{1 + 2k_g / k_p} \right) \left(\frac{1 + N_1 Kn + N_2 Kn^2}{1 + D_1 Kn + D_2 Kn^2 + D_3 Kn^3} \right), \quad (3.20)$$

in which N_1 , N_2 , D_1 , D_2 and D_3 are terms related to the thermal and momentum accommodation coefficients along with the thermal conductivities of the particle and the gas.

Equations (3.16), (3.19) and (3.20) are presented in Fig. 3.1 for the case of diffuse accommodation ($\alpha = 1.0$) and $k_g/k_p = 1.0$. The force is normalized by Waldmann's free-molecule limit $F_{th,fm}$ given by Eq. (3.21). It is noted that solutions of Dwyer and Phillips almost overlap at $Kn < 1.0$, but after that Phillips' solution approaches Waldmann's free-molecule limit, while Dwyer's solution reaches a maximum then decreases dramatically with Kn . It is interesting that both solutions give "negative forces" around $Kn = 0.1$. More will be said on the negative thermophoretic force later. It is noted that Brock's solution provides the dependence of force on Kn significantly different from other two solutions.

3.2.2 Free Molecule Regime

Waldmann (1959) and Bakanov and Derjaguin (1959) applied the Chapman-Enskog distribution function to calculate the thermophoretic force or velocity, assuming that the presence of the particle does not distort the distribution function. According to Waldmann, the expression for thermophoretic force can be written

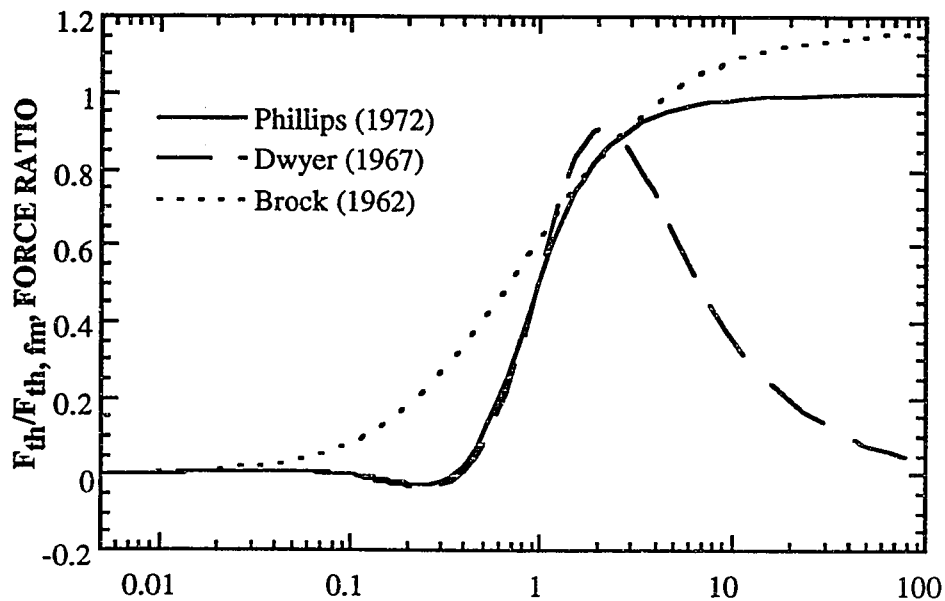


Figure 3.1 Comparison among the solutions of Phillips (1972), Dwyer (1967) and Brock (1962) based upon unity accommodation coefficients and $k_g/k_p = 1$.

$$F_{th, fm} = -\frac{32}{15} a^2 \frac{k_g}{\bar{c}} \nabla T_\infty, \quad (3.21)$$

in which \bar{c} is mean speed of gas given by

$$\bar{c} = \left(\frac{8RT}{\pi M} \right)^{1/2}. \quad (3.22)$$

Here M is gas molecule weight.

The same problem was also investigated by Mason and Chapman (1962) using the dusty gas model, which treats the suspended particles as large molecules of a second species. They assumed that a fraction q of gas molecules was reflected diffusely and the remaining $(1-q)$ reflected specularly. The diffuse collisions were modeled as elastic collisions in which the relative speed is unchanged, but the directions of the molecular

velocities may be accommodated, which is different from Waldmann's assumption that the diffusely reflected molecules have a Maxwellian velocity distribution. The final result is $(1 + 4q/9)$ times of Waldmann's solution. It is interesting that Waldmann's solution indicates that TF is independent of the gas-particle interaction, although they considered it in their analysis. Experimental data favor the results of Waldmann.

Later, Talbot *et al.* (1980) reconsidered the problem using a boundary condition slightly different from Waldmann's, and a second term representing the gas-particle interaction was added to the Waldmann's solution. The corrected formula is

$$F_{th} = -\frac{32}{15} a^2 \frac{k_g}{\bar{c}} \nabla T_\infty \left[1 + \frac{5\pi}{32} (1 - \alpha_t) \right]. \quad (3.23)$$

3.2.3 Knudsen Regime

Analytical solutions for TF in this regime were proposed by Brock (1967a), and Ivchenko and Yalamov (1970). Both solutions are based on the BGK approximation. The difference lies in the methods used to solve the BGK equation for the velocity distribution function. Brock obtained the velocity distribution function f^- for the striking molecules from the solution of the BGK equation. The distribution function f^+ for the reflecting gas molecules was specified by introducing the thermal accommodation coefficient α_t . He assumed that a fraction $(1 - \alpha_t)$ of gas molecules was specularly reflected and the remaining fraction α_t evaporated in equilibrium with the particle surface. Therefore, f^+ can be expressed by:

$$f^+ = \alpha_t f^{0+} + (1 - \alpha_t) f^- \quad (3.24)$$

where f^{0+} represents the Maxwell distribution function for leaving molecules from the particle surface in equilibrium with the particle.

Brock chose the frequency ω in the BGK model to make the Chapman-Enskog viscosity agree with that given by the collision model for Maxwellian molecules. Constant mass and energy flux were specified at the gas-particle interface. The final solution may be written

$$\frac{F_{th}}{F_{th,fm}} = \left\{ 1 - \frac{0.06 + 0.37\alpha_t - 0.28\alpha_t^2 k_g / k_p}{Kn} \right\}, \quad (3.25)$$

where $F_{th,fm}$ is Waldmann's free-molecule limit. Brock's analysis was based upon monatomic gas molecules.

Slightly different from Brock's method, Ivchenko and Yalamov attempted to obtain the two distribution functions, f^+ and f^- , from the BGK equation using a perturbation technique. The frequency ω in the BGK equation was selected to make the distribution function far from the particle the same as that of Chapman-Enskog for a non-equilibrium gas. The thermal accommodation coefficient, α_t , was introduced for the gas/particle interface. The result for the thermophoretic force may be written as:

$$\begin{aligned} \frac{F_{th}}{F_{th,fm}} = \frac{5\pi}{16} \{ & 1 + 0.491(1 - \alpha_t) - [0.267\alpha_t(1 - \frac{1}{2}\alpha_t \frac{k_g}{k_p}) \\ & + 0.0672 - 0.0015\alpha_t - 0.0679(1 - \alpha_t)^2] / Kn \}. \end{aligned} \quad (3.26)$$

The solution of Ivchenko and Yalamov is plotted in Figure 3.2 together with Eq. (3.25) for $\alpha_t = 0.1$ and 1.0 . It is noticed that the theory of Ivchenko and Yalamov usually gives a higher force than Brock's solution for the same gas/particle interface. Brock's solution approaches Waldmann's prediction for any value of the accommodation coefficient, but Ivchenko and Yalamov's solution approaches Waldmann's prediction only for complete accommodation ($\alpha_t = 1$). In other cases the force approaches a value which is

$(1.491-0.491\alpha_t)$ times Waldmann's solution. Both solutions predict that TF increases with decreasing α_t , and the direction of the force reverses at $Kn < 0.2$.

In addition to the analytical solutions proposed for TF in the transition regime, the linearized BGK equation was numerically solved by Lea and Loyalka (1982) to obtain the velocity profile and the drag force for a sphere at various pressures. Their approach was extended by Law and Loyalka (1986) to study TF. They relaxed the assumption made by Lea and Loyalka that the temperature profile within the Knudsen layer was constant. Their calculations were performed for $k_g/k_p = 0, 0.004$ and 0.135 over the Kn range $0.1 \leq Kn \leq 20$. The convergence of the method was found unsatisfactory for small Kn . Recently, Loyalka (1992) recalculated the linearized Boltzmann equation for rigid-sphere molecules using the so-called "S_N method". Data for several Kn numbers were obtained for $k_g/k_p = 0.1$ and 0.01 , which are tabulated in the paper.

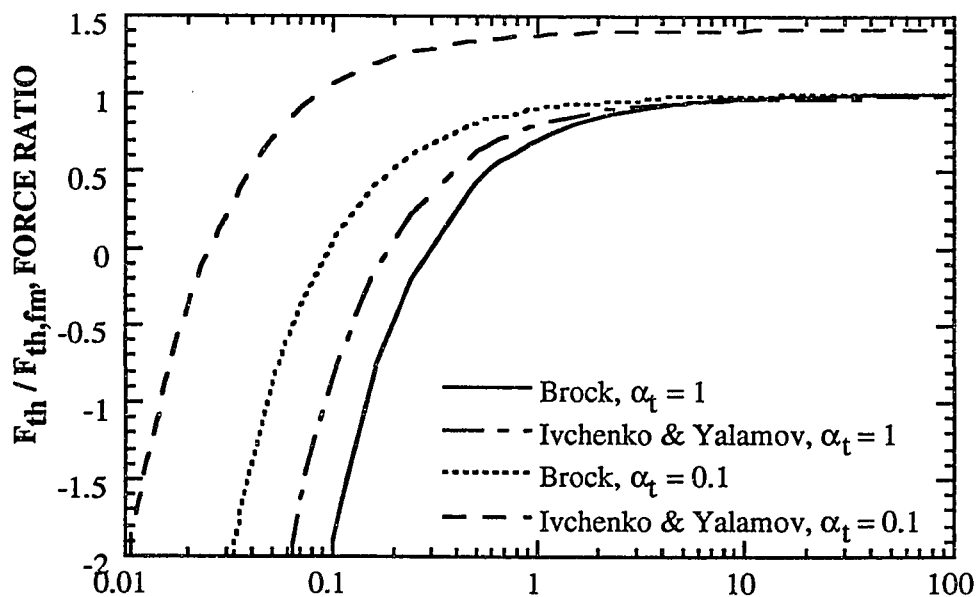


Figure 3.2 Comparison of the theory of Brock (1967a) and of Ivchenko and Yalamov (1970) for $k_g/k_p = 1$ and $\alpha_t = 0.1$ and 1.0 .

Based on the linearized BGK equation, Yamamoto and Ishihara (1988) performed numerical calculations applying a method different from the perturbation technique of Loyalka *et al.*. They divided the gas around the particle into a "Knudsen region", which is on the order of one mean free path from the particle surface, and a "Stokes' region", which is beyond that distance. In the Stokes region the velocity and temperature of the gas are described by Stokes's equations. In the Knudsen region the solution was appropriately organized so that it approaches Stokes's solution as the distance from the particle surface goes to infinity. The unknown parameters embodied in the solution were determined from the boundary conditions. The matching process of the two solutions was accomplished numerically, and the solutions for TF were obtained for thermal conductivity ratios k_g/k_p of 0.01-100 for $0.01 \leq Kn \leq 50$. The results can be expressed as

$$\frac{F_{th}}{F_{th,fm}} = \frac{2}{\sqrt{\pi}} [A_w H_0 - A_0 (H_w + C)] / (H_w + C) \quad (3.27)$$

in which A_w , A_0 , H_w and H_0 are numerical values tabulated in their paper for various Kn numbers, and $C = 5(\pi)^{1/2} Kn k_p / 4k_g$. This theory reasonably agreed with experimental data of Schmitt (1959) in the slip flow regime. A negative thermophoretic force was clearly seen when $k_g/k_p = 0.01$ around $Kn = 0.1$, and also a maximum force appears for $Kn \sim O(1)$ when $k_g/k_p > 1.0$.

Numerical solution of the linearized BGK equation was also considered by Gorelov (1976) for $k_g/k_p = 0.2$ and $k_g/k_p = 0.002$ in $0.1 \leq Kn \leq \infty$. The results of the first case, where the thermal conductivity of particle is low, showed that TF increases monotonically with Kn, and eventually approaches Waldmann's solution. But for the second case, corresponding to high thermal conductivity of the particle, the direction of the force is first reversed around $Kn = 0.1$, and it eventually reaches Waldmann's free-molecule limit.

The "negative" thermophoretic force encountered in the study of BGK equation was also found by Sone and his associates. Sone and Aoki (1980, 1983) analyzed the problem using the linearized BKW (Boltzmann-Krook-Welander) model of the Boltzmann equation, and a negative force was predicted for particles with high thermal conductivity at $Kn < 0.2$. Earlier Sone (1972) proposed an explanation of the negative force by a mechanics different from thermal slip flow. He concluded that a new kind of flow, which is called "thermal stress slip flow" by the author, occurs for a particle with uniform temperature in a nonisothermal gas. This differs from the thermal creep flow induced around a nonuniformly heated surface by a non-equilibrium gas. Therefore, a negative TF exists for high k_p particles which have a negligible internal temperature gradient. The negative force was also confirmed by Ohama and Sone (1992), who obtained the Grad-Hilbert expansion of the Boltzmann equation for a rigid-sphere molecular gas.

The negative thermophoresis encountered in the numerical solutions of the linearized Boltzmann equation has also been predicted by Dwyer's 13-moment solution for particles of high thermal conductivity, but it has never been observed in experiments. For example, Jacobsen and Brock (1965) presented measurements for six sodium chloride particles in the near-continuum regime, where the negative forces should appear according to the results of Dwyer (1967), of Sone and Aoki (1983) and of Yamamoto and Ishihara (1988). The force was found to be always positive, that is, the force is in opposite direction of the external temperature gradient. The theories predict that a small negative force exists around $Kn \sim 0.1$, except those of Brock (1967a) and of Ivchenko and Yalamov (1970), whose solutions give large negative forces, as shown in Fig. 3.2. It may be difficult to observe such a small effect in experiments, for other effects such as natural convection can dominate the small force. It is probably that the errors involved in the BGK model and in the moment approximation may contribute to the negative force, as commented by Loyalka (1992).

The numerical solutions of Loyalka (1992), Sone and Aoki (1983), and Yamamoto and Ishihara (1988) are plotted in Fig. 3.3. Three results presented are based upon complete accommodation and large k_p ($k_p/k_g = 100$ for Loyalka's results, $k_p = \infty$ for Sone and Aoki's analysis, and $k_p/k_g = 598$ for Yamamoto and Ishihara's theory). The latter value corresponds to a nickel sphere in helium. The results of Sone and Aoki are directly taken from the figures in the paper.

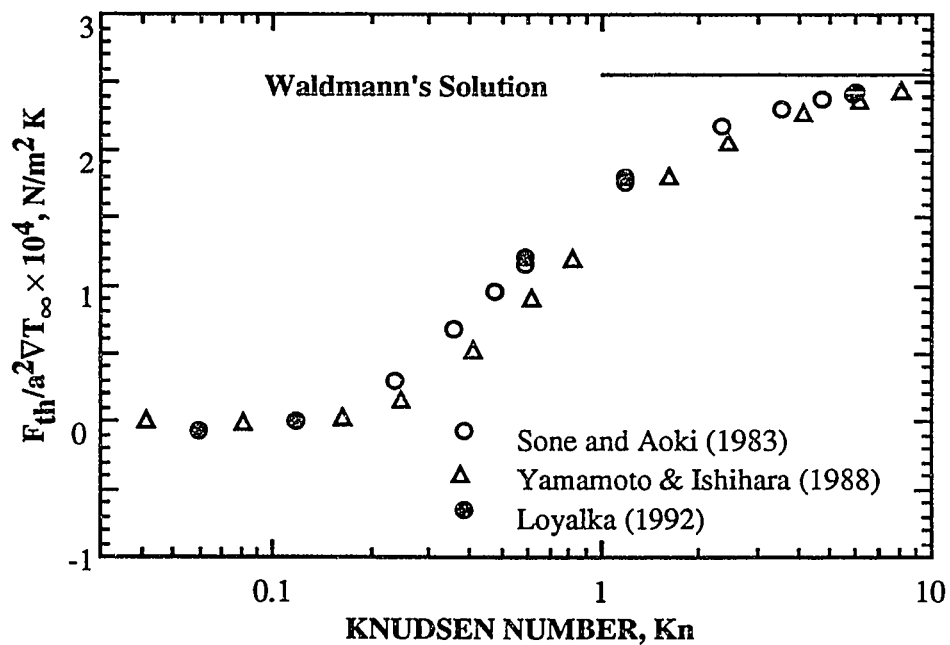


Figure 3.3 Numerical results of Sone and Aoki (1983) for $k_p = \infty$, Yamamoto and Ishihara (1988) for $k_p/k_g = 598$ corresponding to the nickel/helium system, and Loyalka for $k_p/k_g = 100$, all based upon unity coefficient.

It is assumed in the above analyses that the external temperature gradient extends to infinity, so edge effects on the velocity distribution function can be ignored. In experimental studies the dimensions of the apparatus introduce edge effects. Another Kn number is required to explain the results, which is based upon the separation distance of the thermal plates. Consider a single particle suspended in the system shown in Figure 3.4.

Two parallel, infinite plates with temperatures T_h and T_c are separated from the particle center by distances H_1 and H_2 , respectively. The thermophoretic force (TF) on the sphere in such a system is determined by the λ/H_1 and λ/H_2 as well as by Kn (λ/a). Normally, H_1 and H_2 are selected to be equal. As the gas pressure is reduced, Kn_2 ($= \lambda/H_1$) may fall in the slip flow regime, which involves temperature jump and slip conditions near the surfaces of the thermal plates. The jump effects can alter the external temperature gradient, and consequently change the thermophoretic force.

It is quite difficult to consider the two Kn numbers simultaneously. Independent study of the effect of Kn_2 on the thermophoretic force was made by Brock (1965) for the limit $Kn, Kn_2 \rightarrow \infty$, a case where the chamber is extremely rarefied. Based upon elementary kinetic theory, Brock concluded that the force is proportional to the square of the particle size and inversely proportional to the system pressure. In another study of the effect of Kn_2 , Phillips (1972) examined the case where the particle size is much less than the separation distance H and the mean free path of gas. He applied the modified Chapman-Enskog distribution function and the four-moment solutions of Boltzmann equation. The final result was expressed as a function of Kn_2 and the accommodation coefficients of the particle and the thermal plates. The wall effects on the thermophoretic force were also considered by William (1987, 1988), who studied a sphere in a plane and showed that the force increases as the sphere-to-plane distance decreases.

3.3 Prior Experiments of Thermophoretic Force

To date, three experimental techniques have been developed to measure the thermophoretic force or the thermophoretic velocity: (i) Millikan's chamber, (ii) deflection of a particle suspended by a tiny wire, and (iii) the slit method.

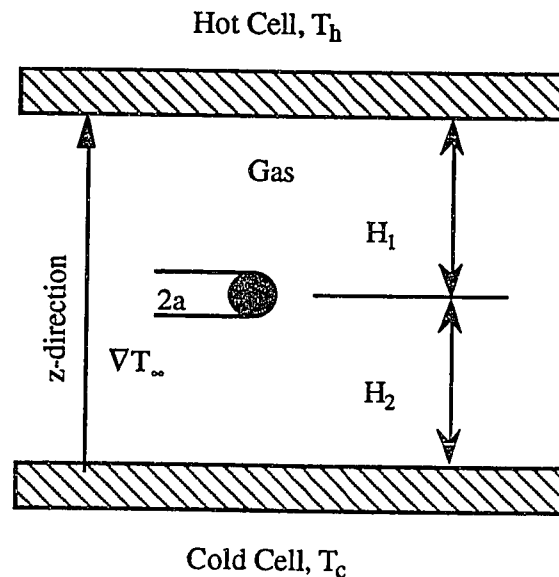


Figure 3.4 Description of the thermophoresis problem

3.3.1 Millikan's Chamber

The basic configuration for the Millikan's chamber is shown in Figure 3.5. It consists of two metal plates on which a DC potential is imposed, and the particle is suspended by the DC electrical field. The apparatus was modified by Rosenblatt and LaMer (1946) for the measurement of thermophoretic force by heating and cooling the top and bottom plates, respectively. The charged particle was introduced to the chamber by means of a gas flow, and the gravitational force was balanced by adjusting the DC voltage. A metal rod was inserted near the upper plate to generate an inhomogeneous electrical field to center the particle. A beam of light illuminated the particle, and its motion was observed with a microscope. There were three horizontal crosshairs in the microscope. The force can be determined from the DC voltage needed to balance the particle, and the velocity was obtained from the time needed to pass through the crosshairs after shorting the DC voltage. A mechanical pump was used to vary the chamber pressure.

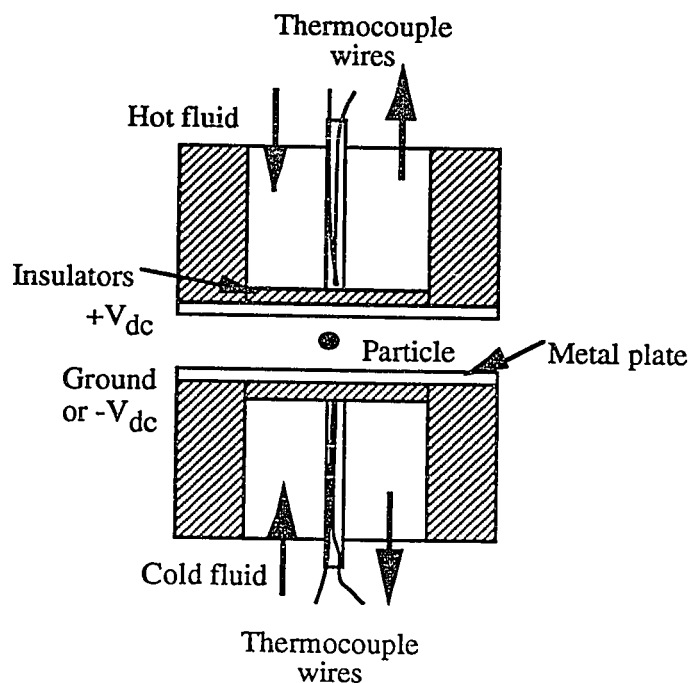


Figure 3.5 A schematic diagram of modified Millikan's apparatus used to measure the thermophoretic force by Rosenblatt and LaMer (1946) and others.

Using the modified Millikan apparatus, Rosenblatt and LaMer measured the thermophoretic force and velocity for tricreszyl phosphate droplets in air, and investigated the dependence of force and velocity on the particle size, on the temperature gradient and on the chamber pressure (that is on the mean free path of gas). The Knudsen number ranged from 0.04 to 1.50. The measured force was about twice Epstein's predictions. The same technique was applied by Schmitt (1959) to measure the silicon oil droplets in N_2 , CO_2 , H_2 and Ar. The data were used to develop interpolation expressions. Schadt and Cadle (1961) investigated the thermophoretic force for particles with high thermal conductivities (mercury and sodium chlorides particles). Comparing their results with Epstein's theory (1929) in the slip flow regime, they found that the measured force was 30 time higher for mercury droplets and 50 time higher for sodium chloride particles. Measurements on

sodium chloride particles were also made by Jacobean and Brock (1965) using the Millikan chamber. They examined Brock's theory (1962) and found the discrepancy was still high.

3.3.2 Deflection of the Particle

The second measurement technique for thermophoresis was the modified version of the digital microstress gauge introduced by Davis and Adair (1975). As shown in Figure 3.6, two parallel metal plates, separated by H , are vertically arranged in a chamber. One plate was heated electrically or by a heat exchanger, and the other was cooled by circulating room temperature water through it. A horizontal temperature gradient was established between the plates. The solid sphere was hung in the chamber by a 0.025 cm diameter quartz rod and positioned in the middle point of the two cells, the equilibrium point. After experiencing a horizontal force exerted by the temperature gradient, the sphere will shift away from the equilibrium position. The displacement was measured with an optical system, and the force was obtained from the displacement and the force constant of the assembly. The whole apparatus was enclosed in a metal chamber, and the chamber was evacuated by mechanical pump and diffusion pump.

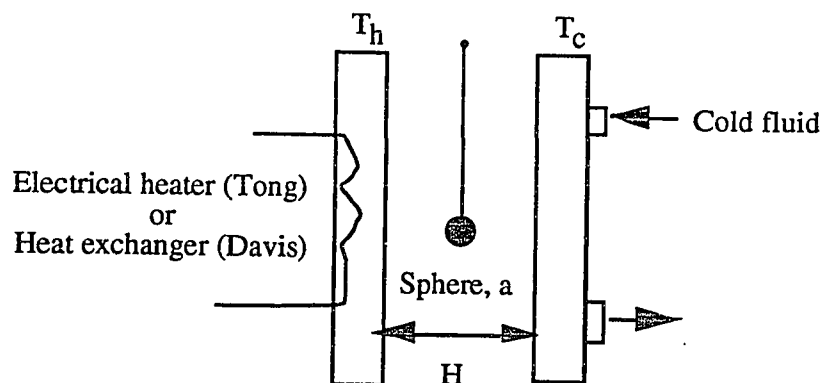


Figure 3.6 Experimental setup used by Davis and Adair (1975) and Tong (1975) for the measurement of thermophoretic force.

Davis and Adair (1975) studied commercial cork balls with a radius of 0.630 ± 0.005 cm in five gases (He, HD, Ne, Ar and N₂). Later, the same technique was used by Tony (1975) to investigate photophoresis and thermophoresis. For thermophoresis, he obtained the force on aluminum and cork spheres in helium and air.

3.3.3 Slit Method

The third method was introduced by Derjaguin *et al.* (1966). Even though more than one design was made to improve the measurement accuracy, the basic measurement principle was almost the same. A slit was drilled in a plate, and the temperatures of the two opposite sides of the slit (the vertical pair or horizontal pair) were arranged to be different. The particles were passed into the center of the slit from an aerosol generator by a gas flow, and the trajectory of one particle was followed by a microscope. The thermophoretic velocity was determined from the measurement of the distance travelled in the direction of temperature gradient divided by the measured time. Also, one can follow more than one particle and average the velocities to decrease the error. Both methods should give the same result since the thermophoretic velocity is independent of particle size. A comprehensive review of this method has been made by Derjaguin and Yalamov (1972).

Derjaguin *et al.* performed extensive measurements on different materials using their design. It was also used by Prodi (1979) and Kousaka *et al.* (1976) to investigate the thermophoretic velocity. Another design similar to the “jet method” was introduced by Talbot *et al.* (1980). Their initial purpose was to measure the velocity profiles in the laminar boundary layer adjacent to a heated flat plate, but a particle-free zone was found near the heated plate within the boundary layer, which gave a zero reading on the particle counter. This was obviously attributed to the thermophoresis, so they turned their attention to a thermophoresis study. They measured the thickness of the particle-free zone which was used to compare with the particle trajectories calculated according to the proposed

theories of the thermophoretic force in the slip flow regime. They found that the calculations based on Brock's theory (1962) agreed with their measurement better than the theory of Derjaguin *et al.* (1965).

3.3.4 Discussion of the Measurement Methods

Among the three measurement techniques, the Millikan chamber is the simplest, most direct and most accurate one used. The ratio of particle diameter to the separation distance, a/H , is typically in the order of 10^{-4} which satisfies the condition that $Kn_2 \rightarrow 0$, so the data can be used to examine the theories directly. Furthermore, one can measure both the velocity and the force using the same apparatus. The difficulty with this method is keeping the particle centered during the experiment. This disadvantage limits the vacuum that can be applied. The other limitation is that only small particles can be studied, for large particles require high DC voltages which can lead to gas ionization. The lowest pressure which was reached in all experiments was 45 Torr. Most data were obtained at a higher pressures. For example, the pressure range in Jacobean and Brock's (1965) experiment was 200 Torr to 800 Torr. Furthermore, natural convection can cause large measurement errors.

The advantage of the method of Davis and Adair is that the separation distance H can be varied to study the effects of Kn_2 on the thermophoretic force. But the vertical arrangement of hot and cold plates gives a horizontal temperature gradient that can cause severe natural convection. In order to minimize natural convection, the initial pressure had to be very low. For example, the upper bound restriction on pressure for a 0.633 cm cork in argon was estimated to be about 0.2 Torr in order to keep the convective flow velocity negligible compared with the thermophoretic velocity. Also, measurements can only be made for solid particles with large sizes (beyond aerosol sizes) due to the way suspension

is achieved. Since a/H was 0.2 (Davis and Adair) or 0.02 - 0.5 (Tong), the data cannot be used to examine most theories, which were derived based upon $a/H \rightarrow 0$.

The slit method and jet method measure the thermophoretic velocity instead of thermophoretic force. The large uncertainty involved in such methods is the measurement of the small distance travelled, especially when particles move close to the plates. Also, the particle sizes were determined from the rate of setting. During the experiment more than one particle was introduced into the chamber. The presence of many particles may alter the local temperature field and the gas velocity distribution, as criticized by Phillips (1975) and Fuchs (1982). Prodi and Tampieri (1988) re-examined this technique and concluded that by appropriate design, no substantial error should be involved in the jet method.

3.4 Theory of Droplet Evaporation/Condensation

Droplet evaporation in the continuum regime ($Kn \ll 1$) is controlled by the diffusion of vapor molecules into the background gas. The theory of evaporation was proposed by Maxwell in an article on "diffusion" written in 1877 for the Encyclopedia Britannica. It was also considered by Langmuir (1918) who followed the theory of Stephan for diffusion. The mass flux, J_k , obtained by Maxwell for the evaporation of a motionless droplet in a static background gas may be written

$$J_k = -\rho_t \frac{da}{dt} = \frac{D_{ij}}{a} (c_s - c_\infty). \quad (3.28)$$

Here, D_{ij} is the diffusivity of vapor species i in the background species j , a is the droplet radius, c_s and c_∞ respectively are the vapor concentrations at the droplet surface and infinity, and ρ_t the density of the droplet.

Assuming that concentration of vapor molecules can be described by the ideal gas law, one can write

$$\rho_t \frac{da}{dt} = -\frac{D_{ij}M_i}{aR} \left(\frac{p_i^0}{T_s} - \frac{p_i^\infty}{T_0} \right), \quad (3.29)$$

in which p_i^0 and p_i^∞ are respectively partial pressures at the particle surface (at temperature T_s) and far from the surface (at bulk gas temperature T_0). For large droplets p_i^0 is equal to the saturation vapor pressure for a flat liquid surface. For small droplets the vapor pressure may be corrected using Kelvin's relationship.

For slow evaporation of a droplet into a large amount of carrier gas containing no vapor ($p_\infty = 0$), the process can be treated as isothermal, and Eq. (3.29) can be integrated to yield

$$a^2 = a_0^2 + S_{ij}(t - t_0), \quad (3.30)$$

where

$$S_{ij} = -2D_{ij}p_i^0M_i / \rho_tRT_s. \quad (3.31)$$

Here a_0 is the droplet radius at time t_0 . In the continuum regime the droplet surface area decreases linearly with time. For fast evaporation such as water droplets in air, Wagner (1982) applied the phenomenological equations for heat and mass transfer to analyze nonisothermal effects on evaporation. The final results contain a number of correction constants.

In the free molecule regime, $Kn \gg 1$, the droplet can be regarded as a large molecule. One can determine the rate of evaporation from the collision frequency of vapor molecules with the droplet surface. The kinetic theory of gases shows the mass flux cross the section area A is

$$J_k = \frac{1}{4} n \bar{c}_i, \quad (3.32)$$

in which n is the number density of gas molecules and \bar{c}_i is the mean speed of vapor molecules given by Eq. (3.22). Equation (3.32) is derived assuming that the collisions of gas/vapor molecules do not distort the Maxwellian distribution function of vapor molecules, and that no evaporated vapor molecules condense on the droplet surface. The "evaporation coefficient" is introduced to account for deviations from classical effusion theory. The rate equation may be written for free-molecule regime as

$$J_{k, \text{fm}} = -\rho_t \frac{da}{dt} = \frac{\alpha_e \bar{c}_i}{4} \frac{M_i p_i^0}{RT_s}, \quad (3.33)$$

where α_e is the evaporation coefficient. Equation (3.33) shows the evaporation rate in the free-molecule regime is a constant.

Analogously to thermophoresis, the theory of droplet evaporation in the Knudsen regime is complicated. The problem was solved semi-theoretically by Fuchs (1934) using the so-called "match method". Fuchs assumed that the evaporating droplet is surrounded by a sphere with a radius $a+\Delta$, where Δ is in the order of mean free path. The transport of molecules from the surface of this imaginary sphere to the gas at infinity is described by diffusion theory, while within the distance Δ Fuchs assumed that the kinetic theory of gases can be applied, since only a small amount of vapor exists within the spherical shell. By matching the mass fluxes for the inner and outer regions at the surface $r = \Delta$, Fuchs obtained

$$\frac{J_k}{J_{k, \text{fm}}} = \frac{1 + \Delta / a}{1 + \Delta / a + a \bar{c}_i \alpha_e / 4D_{ij}}, \quad (3.34)$$

where $J_{k,fm}$ is the mass flux in free-molecule regime given by Eq. (3.33). Fuchs left the evaluation of Δ in an indefinite form. Bradley (1946) and Wright (1960) proposed methods for estimating Δ .

More accurate theories for the droplet evaporation have been developed based upon the BGK equation. Brock (1967c) attempted to solve the linearized Boltzmann equation for droplet evaporation at $Kn \gg 1$. The result was shown to disagree with Kelly and Senegers's solutions (1974), which were based upon the actual solution of the full Boltzmann equation in the free-molecule regime.

Numerical results were obtained by Sahni (1966), who applied the neutron transport theory to droplet evaporation. He considered the evaporation of light vapor molecules in a heavy background gas, that is $M_i/M_j \rightarrow 0$. Here M_i and M_j respectively are the molecular weight of vapor and background gas. The tabulated numerical results were interpolated by Fuchs and Sutugin (1970), who gave

$$\frac{J_k}{J_{k,fm}} = 1.333Kn \left(1 + Kn \frac{1.333Kn + 0.71}{Kn + 1} \right)^{-1}. \quad (3.35)$$

The interpolated solution agrees with the Sahni's numerical data within 2-6%. Equation (3.35) is based on $\alpha_e = 1$. For arbitrary α_e Smirnov (1968) developed an expression of the form

$$\frac{J_k}{J_{k,fm}} = 1.333Kn \left\{ 1 + Kn \left[\frac{1.333Kn + 0.71}{Kn + 1} + \frac{4(1 - \alpha_e)}{3\alpha_e} \right] \right\}^{-1}. \quad (3.36)$$

The linearized Boltzmann equation was solved by Loyalka (1973) applying both variational and boundary methods to obtain the rate of droplet evaporation. The

computations were extended later (Loyalka, 1982) and the solution was generalized. The results may be written in the form of the Fuchs-Sutugin's interpolation formula as

in which ζ_c is a constant. Loyalka determined $\zeta_c = 1.0161$ from the solution of the BGK Boltzmann equation, and Loyalka, Hamoodi and Tomposon (1989) proposed an expression for ζ_c which depends on the molecular weight ratio, $Z (= M_i/M_j)$, given by

$$\zeta_c = 0.9769 - 0.0518z + 0.0018z^2 + 0.0196z^3, \quad (3.38)$$

where $z = \log(1/Z)$. The author claimed that Eq. (3. 37) agreed with Sahni's solution better than the Fuchs-Sutugin's expression.

The effects of M_i/M_j on the evaporation rate appear explicitly in the results of Sitarski and Nowakowski (1979), who applied Grad's 13-moment method to solve the Boltzmann equation. The results are

$$\frac{J_k}{J_{k,fm}} = \frac{Kn[1 + \frac{3\beta(1+Z)^2}{4(3+5Z)} Kn]}{\left\{ \frac{4(9+10Z)}{15\pi(1+Z)^2} + \left[\frac{\beta(1+2Z)}{\pi(3+5Z)} + \frac{1}{2\beta} \right] Kn + \frac{9(1+Z)^2}{8(3+5Z)} Kn^2 \right\}}. \quad (3.39)$$

Here $\beta = \alpha_e/(2-\alpha_e)$, and $Z = M_i/M_j$. As discussed above, Loyalka, Hamoodi and Tomposon (1989) calculated flux for arbitrary Z based upon the linearized equation using the so-called "S_N method". A difference of 1.5% was found for $J_k/J_{k,fm}$ between $Z = 0.1$ and 10 at $Kn = 10$, but there is no significant difference for small Kn .

Evaporation for arbitrary M_i/M_j was also considered by Monchick and Blackmore (1988) using a variational method based upon the theorem of Cercignani. The results are close to the Fuchs-Sutugin formula, and the effects of mass ratio are negligible even for large Z , which supports Loyalka *et al.*'s data (1989).

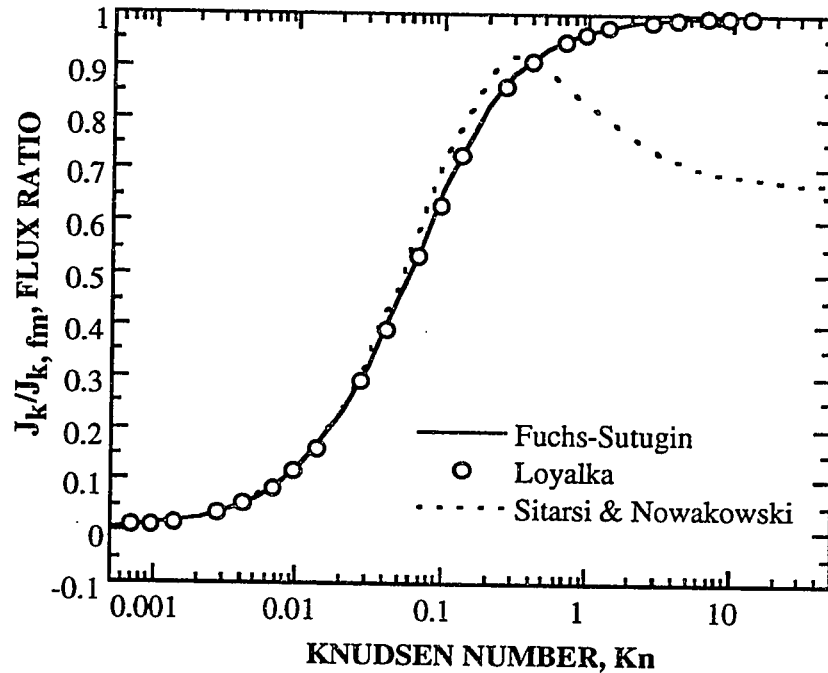


Figure 3.7 A comparison among the solutions of Loyalka *et al.* (1989), Sitarski and Nowakowski (1979), and the equation of Fuchs-Sutugin (1970) for $Z = 10$.

The solutions of Loyalka *et al.* (1989), of Fuchs-Sutugin (1970), and of Sitarski and Nowakowski (1979) are compared in Figure 3.7 for $Z = 10$. The interpolated solution of Loyalka (1983) almost overlap the Fuchs-Sutugin results and are not shown in the figure. It can be seen that Loyalka *et al.*'s solution is very close to Fuchs-Sutugin's results, and only a slight difference can be observed at high Kn . As $Kn \rightarrow \infty$, the 13-moment solution does not approach the free-molecule limit $J_{k, fm}$, but to $(2\beta/3)J_{k, fm}$. It is well-known that

Grad's 13-moment method is intrinsically inaccurate at large Kn , so Eq. (3.39) is mainly valid in the near-continuum regime.

3.5 Prior Experiments of Droplet Evaporation

An experimental study of droplet evaporation was carried out by Bradley and his associates (1946, 1949). They measured evaporation of droplets of di-n-butyl phthalate with an average size of 0.5 mm at pressures in the range 10-0.1 Torr using a microbalance. In their study Kn is less than 0.2. Millikan's chamber was used by Monchick and Reiss (1954) to study the evaporation of diamyl sebecate (DAS). The measurements supported Fuchs-Sutugin's rate expression, but the accuracy was not high enough to validate any theories for the intermediate Kn regime. Davis and his associates (1974, 1977, 1978, 1981) measured the evaporation rate accurately using the Differential II instrument of Science Spectrum, Inc. equipped with an automatic feedback control system and light scattering capabilities. They measured the evaporation rates of dibutyl sebacate (DBS) in the transition regime, but they were not able to reach the free-molecule regime and the near-free molecule regime with their apparatus.

Ray *et al.* (1988) used electrodynamic levitation to measure evaporation rates of dioctyl phthalate (DOP) for large Kn ($1 \leq Kn \leq 9.6$). They found that the evaporation rate reached the free-molecule regime at Kn near 6.0. They compared their data with Eq. (3.35), and (3.37). At low Kn , the data agree with the theoretical predictions, but for $Kn > 3.8$ the theoretical prediction is consistently lower than the measurements; deviations as high as 10% are observed. Recently, Loyalka *et al.* (1989) recalculated the evaporation rates for DOP /air using the " S_N method". Williams and Loyalka (1991) showed that the agreement with the results of Ray *et al.* (1989) was improved.

Richardson *et al.* (1986b), and Tang and Munkelwitz (1991) used electrodynamic levitation and light-scattering data to determine vapor pressures from the measured

evaporation rates in the free-molecule regime. Richardson *et al.* obtained vapor pressures of sulfuric acid droplet over temperature range 263 K to 303 K. Tang and Munkelwitz reported vapor pressures for methanesulfonic acid (MSA), glycerol, oleic acid and DOP for temperatures ranging from 297 K to 325.3 K. The vapor pressure results for DOP were in good agreement with results obtained by Ray, Davis and Ravindran (1979) from measurements in the continuum regime, and the data for MSA, glycerol and oleic acid were consistent with values reported in the literature.

3.6 Summary

The theories of thermophoretic force may be summarized by a general form:

$$\frac{F_{th}}{F_{th,fm}} = f(Kn, k_g / k_p, \alpha_t, \alpha_m). \quad (3.40)$$

Numerous expressions for $F_{th}/F_{th,fm}$ have been developed, but the theories which should be consistent in the same Kn regime disagree with each other. The disagreement also exists among the theories of droplet evaporation in the Knudsen regime. The theoretical predictions of thermophoretic force require knowledge of accommodation coefficients. Therefore, experimental measurements of thermophoretic force are needed. Prior measurements on thermophoresis are incomplete and not accurate. Further experimental study is required to validate the various expressions for thermophoresis (Bakanov, 1995). Experimental study for droplet evaporation is scarce, and prior measurements were made mainly in the near-continuum and free-molecule regimes. Reliable data ranging the continuum to free-molecule regimes are desired to compare with the theory of evaporation. It was the objective of this research to measure the evaporation rate and the thermophoretic force in the transition regime.

CHAPTER 4

EXPERIMENTAL APPARATUS AND MEASUREMENT PRINCIPLE

4.1 Introduction

The experiments of this research have been carried out in three apparatus. Their overviews are shown in Fig. 4.1, 4.2 and 4.3, and I shall refer to them as apparatus A, B and C, respectively. Apparatus A consists of a bihyperboloidal electrodynamic balance (EDB) and peripheral equipment for elastic scattering measurements. A detailed description of apparatus A was given by Fulton (1985) and Taflin (1988). The measurements of elastic scattering during the reactions of titanium ethoxide (TTE) droplets with water vapor were performed on apparatus A. Apparatus B is more sophisticated. It coupled a double-ring EDB with (i) a double monochromator with photodetectors consisting of a photomultiplier (PMT) and an optical multichannel analyzer (OMA) for measuring Raman scattering, (ii) a video camera for sizing nonspherical particles, (iii) a CO₂ laser heating system used to study chemical reactions at elevated temperatures, and (iv) an argon-ion laser with high intensity required for measurements of weak Raman signals from the particle. Descriptions of apparatus B were provided by Buehler (1991), Allen (1992) and Rassat (1994). Raman scattering was used in this research to monitor the reaction process of TTE droplet with water vapor, and to analyze the evaporation of a mixture of stannous octanoate (SNO) and 2-ethylhexanoic acid.

Apparatus C, shown in Fig. 4.3, was developed in this study to investigate the thermophoretic force and the evaporation of droplets in the transition regime. It consists of four major components: (i) a double-ring electrodynamic balance, (ii) a He-Ne laser and photoelectric detectors, (iii) vacuum equipment, and (iv) constant temperature sources. The design of apparatus C allows one to vary the chamber pressure and to control the temperature of the particle, which cannot be achieved with apparatus A or B.

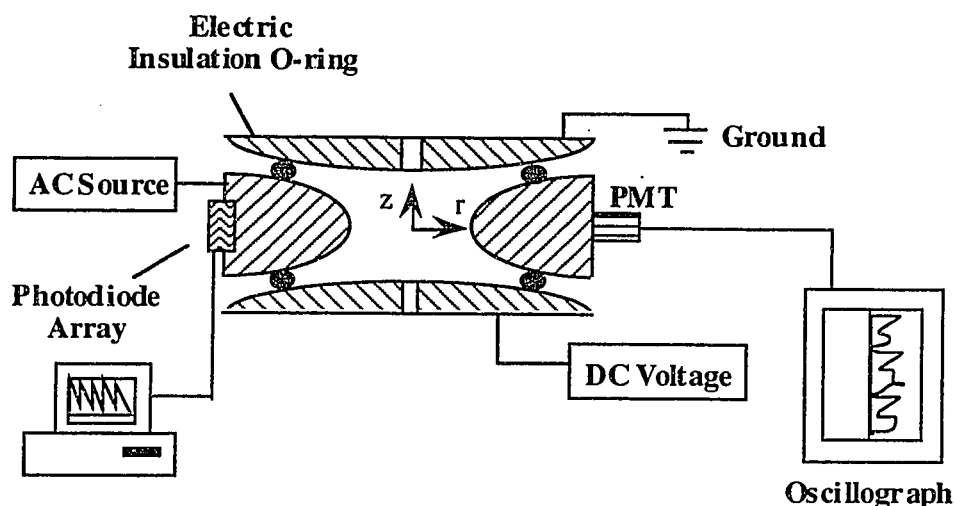


Figure 4.1 A schematic diagram of the bihyperboloidal EDB and peripheral equipment (called "Fulton's balance" or "Apparatus A").

The four components of apparatus C are described in this chapter together with measurement principles. The principles of the EDB are also briefly reviewed here.

4.2 Electrodynamic Balance

Three techniques have been frequently used for isolating single particles: electrostatic, electrodynamic and optical levitation. As discussed in the Introduction, the electrodynamic balance stabilizes the particle more robustly than the other two methods.

4.2.1 Principles of the EDB

The electrodynamic balance evolved from Millikan's chamber, the "electrostatic balance". Millikan's device consists of two parallel metal plates on which DC potentials are imposed. A charged particle is introduced into the chamber and its weight is balanced by a DC electrostatic force. Millikan measured the charge on an electron and, to validate Stokes's equation for the drag on a sphere, the velocities of falling droplets.

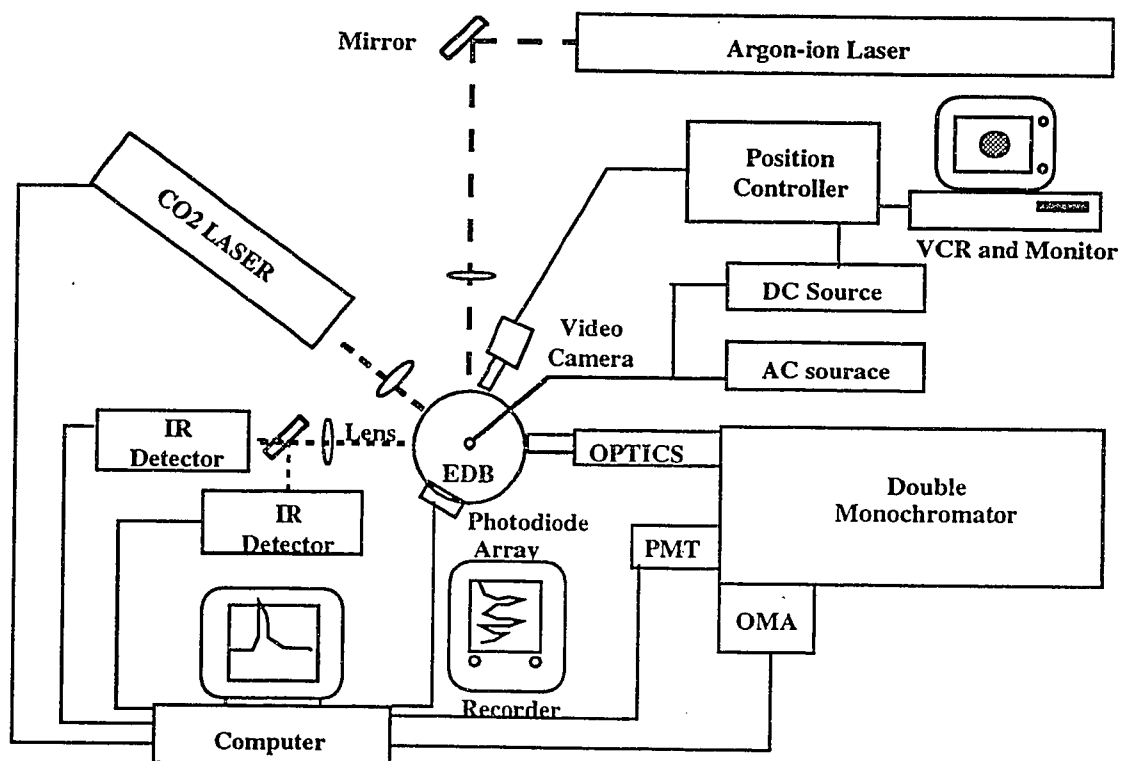


Figure 4.2 A schematic diagram of the electrodynamic balance coupled with Raman facilities, also called "Apparatus B".

The disadvantage of the Millikan apparatus is that no radial restoring forces are exerted on the particle. Motion of gas around the particle can drive the particle away from the original position, and there is no force to move the particle back. This limitation was overcome by Fletcher (1914) who inserted a small metal rod or disk near the top plate. The rod was electrically insulated from the top electrode. When the particle drifted away the chamber center, the two metal electrodes were grounded and at the same time a high potential was applied to the rod. The generated electric field produced a radial restoring

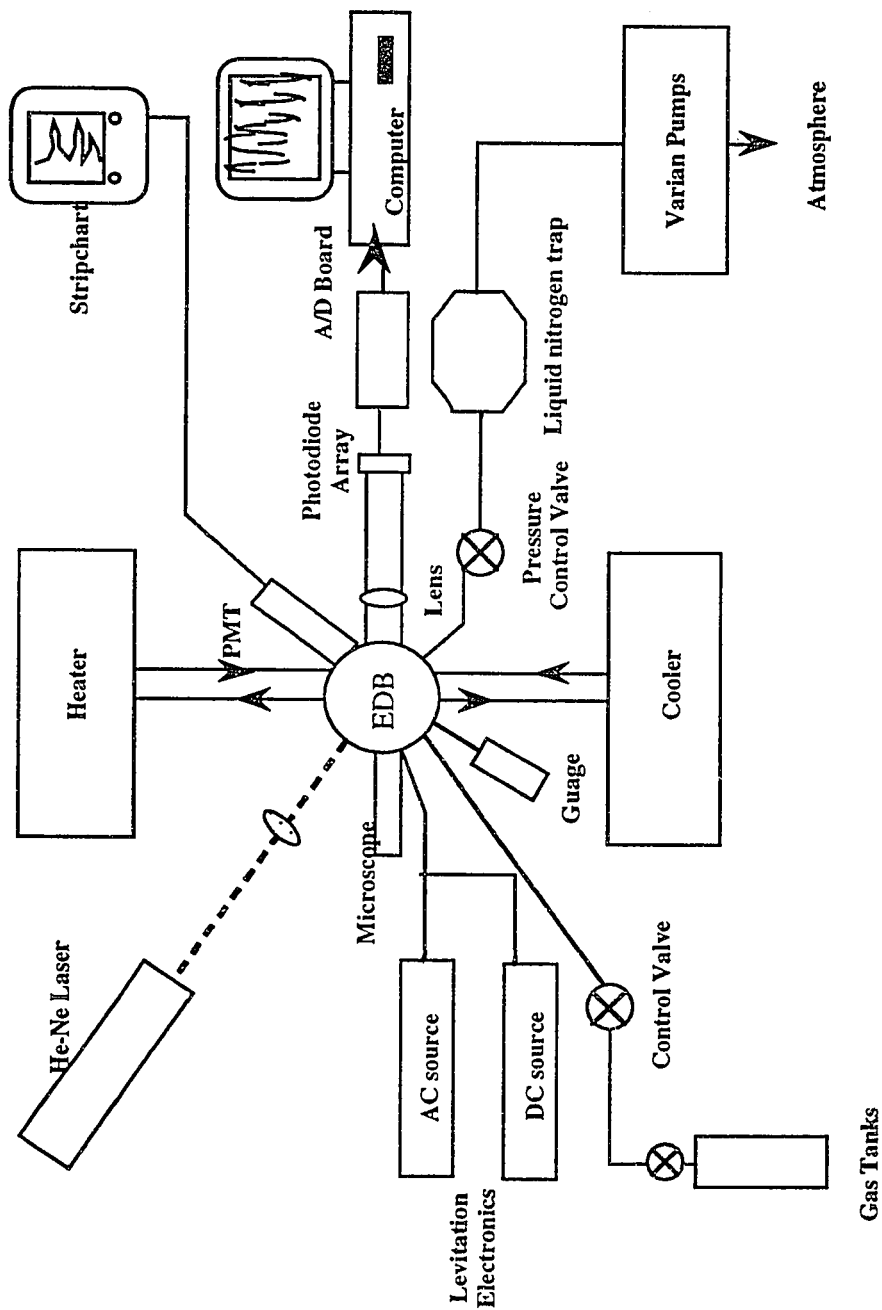


Figure 4.3 Systematic overview of the apparatus used to measure thermophoretic force and droplet evaporation in the Knudsen regime, also called "Apparatus C"

force to drive the particle back to the center. A modified Millikan chamber was used by Rosenblatt and LaMer (1946) to measure the thermophoretic force on single particles, as discussed in Chapter 3. It was also used by Gucker and Egan (1960), who coupled the balance with a photomultiplier (PMT), to study the light scattering from a single particle .

Although the particle can be trapped in the center of the chamber using Fletcher's improvement, one cannot control it vertically. This problem was overcome by Wyatt and Phillips (1972), who developed a commercial instrument called Differential II light scattering photometer of Science Spectrum, Inc.. They integrated an electrostatic balance with an optical-electrical feedback control system for vertical stabilization of the particle. The particle was illuminated by a He-Ne laser and the light scattering from the particle was measured by means of a rotating PMT driven round the particle by a stepper motor. The Differential II is superior to earlier versions of the electrostatic balance, but the particle is not stabilized in the chamber robustly. Convective currents or gas flow through the chamber cannot be tolerated. Furthermore, it takes a long time for the rotating PMT to obtain one phase function over a relatively large range of scattering angles since the movement of the PMT is quite slow. Dynamic processes such as gas/particle chemical reactions cannot be studied with it. These disadvantages can be avoided if the particle is levitated electrostatically.

The concept of electrodynamic trapping was introduced by Paul and Raether (1955) in their development of the electric mass filter. Since then, the evolution of the electrodynamic balance occurred along two paths: the radiofrequency quadrupole developed by Paul *et al.* (1958) for trapping atomic and ions, and the bihyperboloidal device developed by Wuerker *et al.* (1959) to trap micrometer size particles. The bihyperboloidal configuration of Wuerker *et al.*, shown in Fig. 4.1, consists of a ring electrode and two endcap electrodes. For a positively charged particle, the top electrode is grounded or connected to a negative DC source, and a positive DC potential is imposed on the bottom

electrode. The ring electrode is linked to an AC source with variable amplitude and frequency. The particle can be vertically balanced by the DC electric field, and robustly fixed radially by the AC field. The stability characteristics of the bihyperboloidal EDB were discussed by Wuerker *et al.* (1959), Frickel *et al.* (1978), Davis (1985) and Hartung and Avedisian (1992).

A simple configuration of the EDB, consisting of a single washer-shaped ring electrode and two-flat endcaps is shown in Fig. 4.4 (a). It was introduced by Straubel (1955). This design restricts the measurement of light scattering in that the middle ring blocks the light scattered radially. Richardson and his associates (1984, 1986a) combined a cylindrical ring electrode with two hemispherical endcaps in their study of the removal and addition of water vapor from or to the droplets of ammonium sulfate at different relative humidities. This configuration was adopted by Tang *et al.* (1986) to measure the water activity of aqueous solutions of NaCl and KCl.

The bihyperboloidal configuration provides superior stability for a charged particle. For Raman measurements, a large hole in the middle plane of the ring electrode must be drilled to collect enough Raman scattered light. The hole disturbs the electric field and may reduce the stability for the particle. Two other configurations have been found useful for inelastic scattering studies: Arnold and Folan (1987) developed a spherical void electrodynamic levitator (SVEL), and Weiss-Wrana (1983) proposed a double-ring electrodynamic balance. The spherical void balance, shown in Fig. 4.4 (b), consists of a hollow spherical cavity which integrates scattering signals over 4π steradians.

The double-ring configuration is relatively simple. It consists of a pair of parallel rings for the AC electrodes. One can either superimpose the DC potential with the AC source (Rassat, 1994), or apply the DC field with a separated pair of endcap electrodes (Buehler, 1991). The latter case is shown in Fig. 4.4 (c).

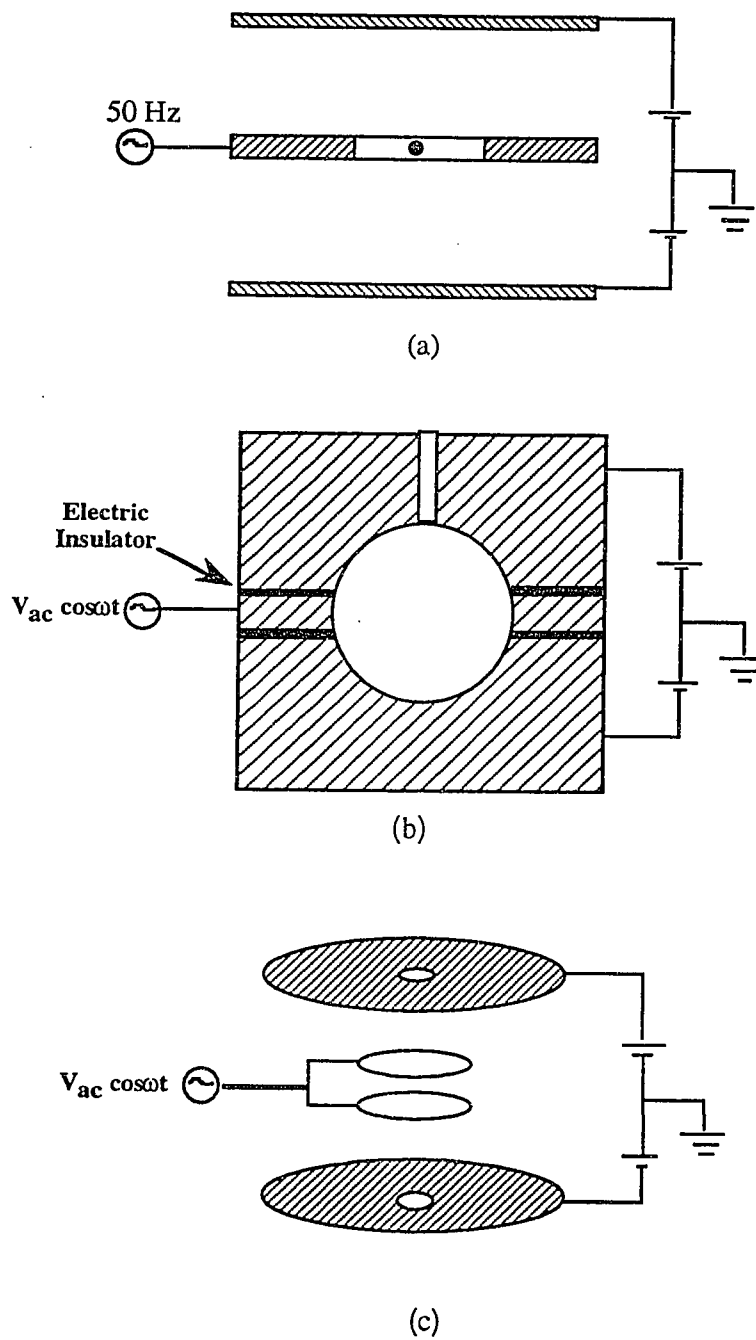


Figure 4.4 Configurations of electrodynamic balance (a) three-plates by Straubel (1955), (b) spherical void by Arnold and Folan (1987) and (c) double-ring by Buehler (1991).

For its simplicity, the double-ring configuration with superimposed AC and DC potentials was selected in this study of thermophoretic force and Knudsen evaporation. The other advantage of using double-ring design is that linear temperature profiles can be easily maintained as shown later, which cannot be achieved conveniently with other kinds of configurations.

4.2.2 Principle of Particle Trapping

A charged particle is trapped in the EDB by the combined AC and DC electric forces. Consider a negatively charged particle suspended in the double-ring EDB shown in Fig. 4.5. The superimposed potentials $(-V_{dc} + V_{ac}\cos\omega t)$ and $(+V_{dc} + V_{ac}\cos\omega t)$ are respectively connected to the top and bottom ring electrodes. Here, V_{dc} and V_{ac} are the amplitudes of DC and AC potentials, and the circular frequency of the AC source is ω . The vertical and radial motions of the trapped particle in the EDB are described by

$$m \frac{d^2z}{dt^2} = -mg + 6\pi a\mu \frac{dz}{dt} + qE_{ac,z} + qE_{dc,z} + F_z \quad (4.1)$$

and

$$m \frac{d^2r}{dt^2} = 6\pi a\mu \frac{dr}{dt} + qE_{ac,r} + qE_{dc,r}, \quad (4.2)$$

in which a is the radius of the particle, q is the coulomb charge of the particle, m is the particle mass, z and r represent the vertical and radial displacements with respect to the center of the balance, μ is the viscosity of surrounding gas, $E_{dc,z}$, $E_{dc,r}$, $E_{ac,z}$ and $E_{ac,r}$ are respectively the z and r components of the DC and AC voltages, and F_z represents vertical forces other than gravity and the drag force on the particle.

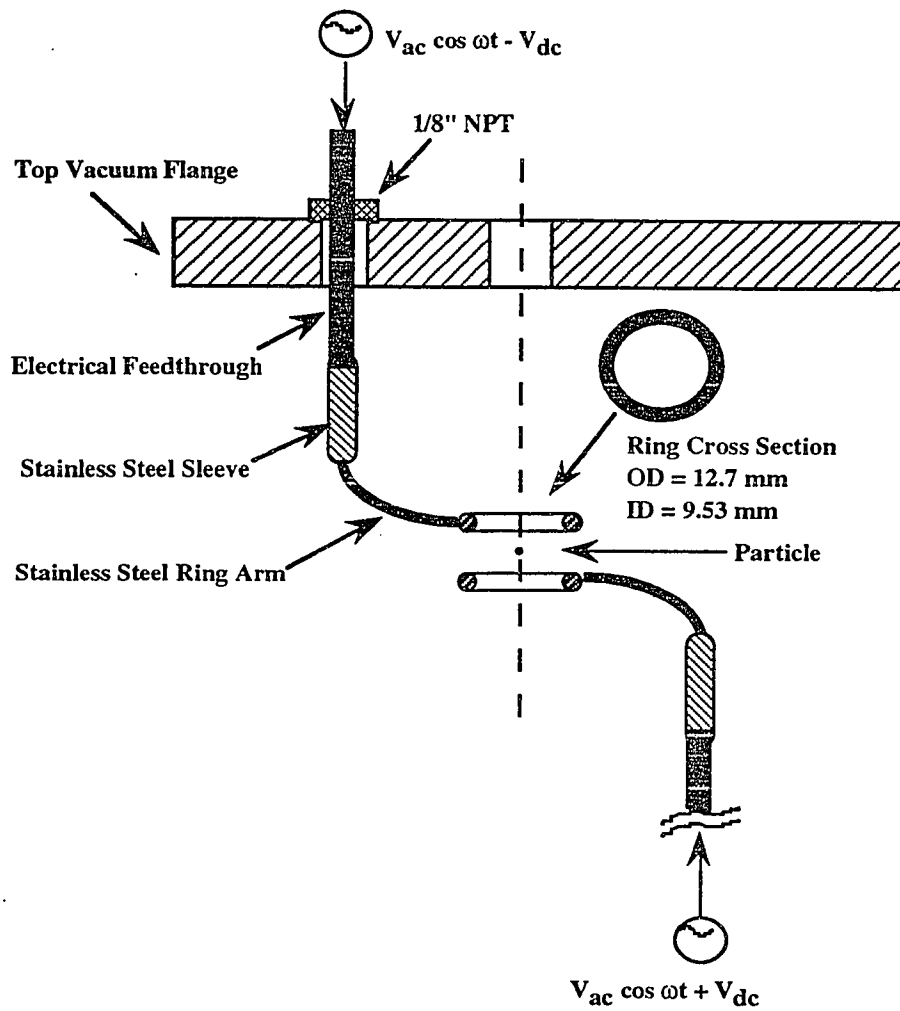


Figure 4.5 Geometry and construction of ring-electrodes.

In order to solve Eq. (4.1) and (4.2), the AC and DC electric fields must be known, which can be obtained by solving Laplace's equation

$$\nabla^2 V = 0, \quad (4.3)$$

along with the appropriate boundary conditions, and by differentiating the voltage with respect to the coordinates z or r ,

$$\mathbf{E} = -\nabla V. \quad (4.4)$$

Approximations for the electric fields for the bihyperboloidal and double-ring EDBs were obtained by Davis (1985, 1992). For example, the vertical component of the AC field for the bihyperboloidal EDB may be written by

$$E_{ac,z} = -(V_b + V_{ac} \cos \omega t) \frac{z}{z_0^2}, \quad (4.5)$$

in which V_b is a DC bias voltage imposed on the AC electrode (usually zero), and $2z_0$ is the separation distance of the DC electrodes at the balance center. Generally, the DC field around the null point may be expressed by

$$E_{dc,z} = -C_0 \frac{V_{dc}}{z_0}, \quad (4.6)$$

where C_0 is a constant accounting for the geometric effects of DC electrodes on the field. For infinite parallel plates, C_0 should be unity, but for the bihyperboloidal configuration, Davis obtained $C_0 = 0.8768$ based on the analytical approximations. Numerical solutions by Sloane and Elmoursi (1987) yielded $C_0 = 0.80$. The measured C_0 for the bihyperboloidal EDB was found to be 0.79 by Taflin (1988).

Equations (4.1) and (4.2) were analyzed by Davis (1992) and Hartung and Avedisian (1992), who found that a necessary but not sufficient condition for particle stability is that the DC voltage must be adjusted to satisfy

$$-mg + qC_0 \frac{V_{dc}}{z_0} + F_z = 0. \quad (4.7)$$

If this condition is met, Eq. (4.1) can be transformed to the form of Mathieu's equation containing two parameters: the aerodynamic drag parameter, A

$$A = \frac{6\pi a\mu}{m\omega}, \quad (4.8)$$

and an AC field strength parameter, B, defined by

$$B = K \frac{qV_{ac}}{m\omega^2}, \quad (4.9)$$

in which K is a constant accounting for the geometric effects on the AC field, similar to the DC geometric constant C_0 .

The stability characteristics of Mathieu's equation have been extensively studied (Abramowitz and Stegun, 1964). The solutions are a set of marginal-stability envelope in a plot of B versus A. The first marginal stability envelope is shown in Fig. 4.6 along with some experimental stability data for DOP droplets (more will be discussed on Fig. 4.6 later). There exists an infinite set of marginal stability envelope.

Stability measurements can be used to determine the AC and DC balance constants, and the particle size may be estimated once the balance constants are known. This technique is especially useful for sizing particles with a low scattering intensity or particles with an irregular shape. More will be explained about this method in the following section.

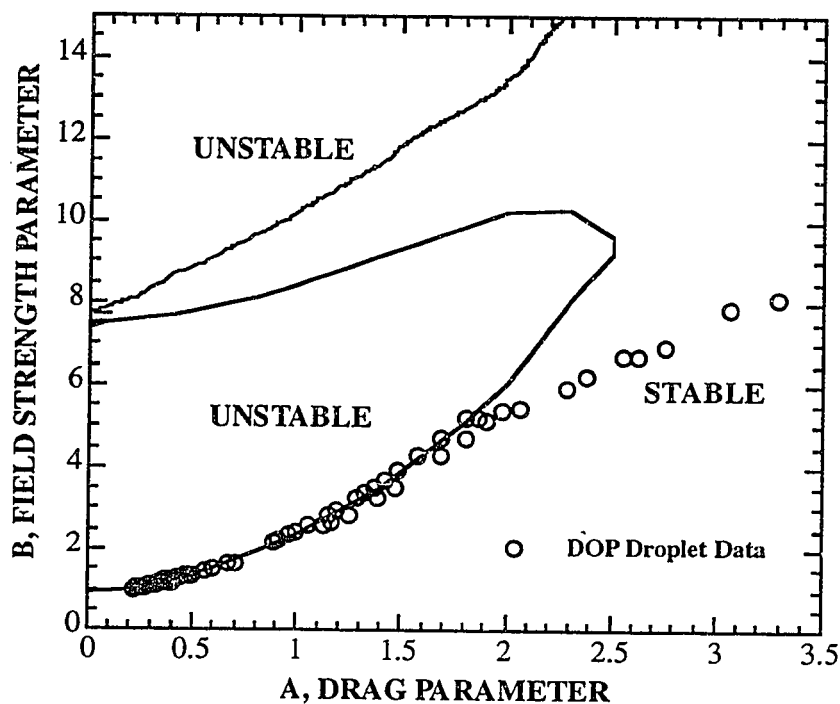


Figure 4.6 The first marginal stability envelope for the double-ring electrodynamic balance and experimental data for DOP droplets.

4.2.3 The EDB Power Supply

The superimposed AC and DC potentials were linked to the ring electrodes through an electrical feedthrough (Insulator Seal Inc.) as shown in Fig. 4.5. The design of the ring-electrode will be discussed in the next section. The feedthrough consisted of a 0.092" nickel rod mounted in the end flange through a 1/8" NPT fitting. The rod is electrically insulated from the flange by ceramic material. The ring electrode was supported by a stainless steel ring arm, and the arm was soldered to a stainless steel sleeve, which tightly fits the feedthrough rod.

The AC and DC power supplies were first coupled by Rassat (1994). The DC potential provided by a Hewlett-Packard model 6209B supply could be varied from -320 V

to 320 V. The AC potential was generated by a Wavetek model 182A function generator with variable frequency of 10-4000 Hz and a maximum peak-to-peak voltage of 20V. The AC potential was amplified by a modified Marantz 4070 audio amplifier along with a 250 turns ratio transformer. The DC potential and the amplified AC voltage were then superimposed in such a way that the potential was $(V_{ac}/2 - V_{dc})$ on the top electrode and $(V_{ac}/2 + V_{dc})$ on the bottom electrode, if the particle was positively charged. The polarity of the DC voltage can be changed from positive to negative. Figure 4.7 is a diagram of DC and AC circuits.

4.2.4 Electrical Discharge and Ring Design

Ring electrodes machined from copper with rectangular cross-sections were used in the initial tests, but the suspended particle was always lost due to ionization of the gas as the chamber pressure was reduced to about 100 Torr. This required the installation of electrodes with circular cross section as shown in Fig. 4.5.

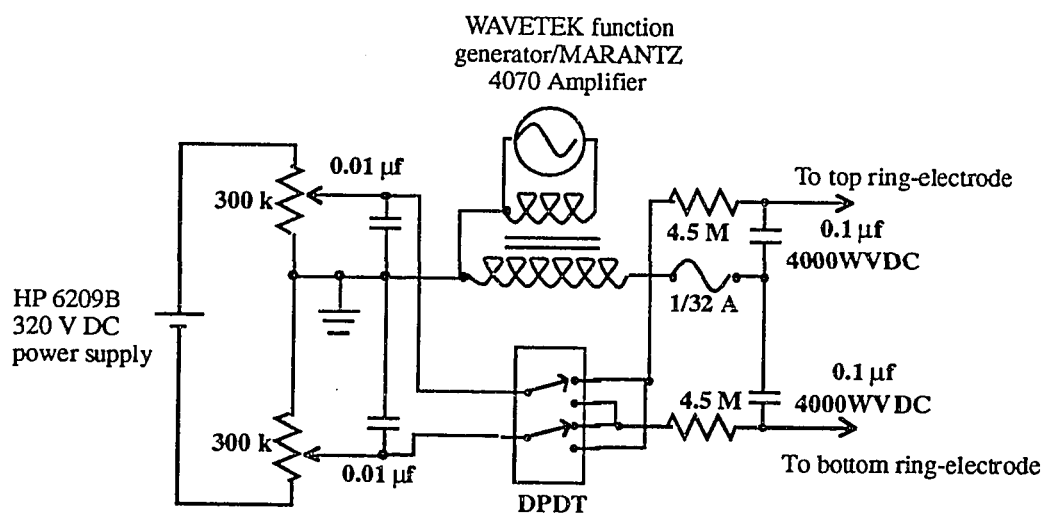


Figure 4.7 The circuit diagram for superposing DC and AC potentials applied to the ring-electrodes.

The electrical discharge (or "electrical breakdown") of gases occurs as a result of the collisions of electrons and/or photons with gas molecules. It is characterized by a rapid transition of gas from a poor electrical conductor with a resistivity of some 10^{14} ohm m to a relatively good conductor with a resistivity dependent on the conditions, typically about 10^3 ohm m for a glow discharge. The potential at which the transition occurs is called the breakdown voltage or spark voltage. It depends on the nature and the density of gas, on the electrode material and geometry, on the surface conditions of the electrode and on any preexisting ionization. The discharge of the low frequency AC ($f < 100$ Hz) potential is nearly identical to that of a DC potential.

Measurements on the DC spark voltage, V_s , have been made for the following electrode configurations: parallel plates, sphere, cylinder, or combinations of them. It was found that V_s depends on the product of the gas pressure and the separation distance, that is, Pd . As shown in Fig. 4.8, a minimum breakdown voltage appears at a specific value of Pd . In this research air, helium and carbon dioxide were chosen to study the effects of gas thermal conductivity on the thermophoretic force. Hirsh and Oskam (1978) found the minimum breakdown voltage for air to be about 350 volt at $Pd \approx 0.06$ N/m. The breakdown voltage is expected to be higher for CO_2 and lower for helium compared with air, since ionization of heavy gas molecules requires a higher voltage than light gas molecules under same conditions. No attempt was made to obtain V_s as a function of pressure for the double-ring electrode configuration; However, no glow discharge was found for the gases used in the pressure range $760 \cdot 10^{-2}$ Torr when the AC voltage was around 200 V. Any discharge can be measured in the EDB since discharge causes a loss of the particle charge.

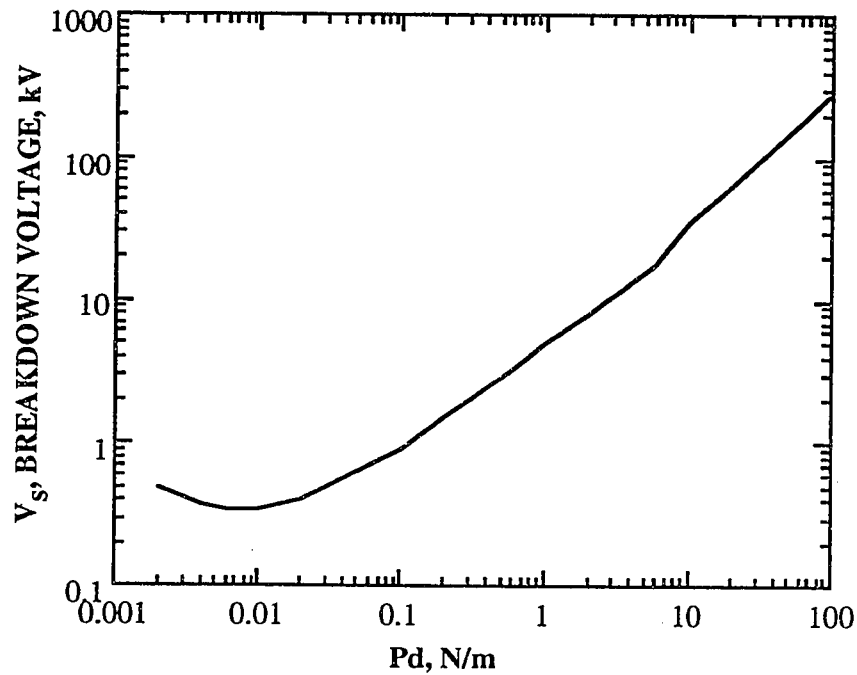


Figure 4.8 The breakdown voltage V_s of air as a function of the products of pressure P and separation distance d (data were taken from Hirsh and Oskam).

The spark voltage slightly varies with electrode materials and surface conditions. Stainless steel was generally found to have a V_s somewhat higher than other metals such as copper and aluminum. In the final design the ring electrodes were machined from stainless steel rod 1.59 mm in diameter to eliminate sharp edges. The sharp edges generate strong local electrical fields and may initiate other types of gas ionization such as corona discharge. Part of the electrical feedthrough, the whole sleeve and ring arms were coated with a layer of Plastic Dip, a type of electrical insulator. The insulated coating is supposed to lower the local electric field.

It should be pointed out that the gas discharge at low pressures cannot be totally eliminated until the applied electrical field is below a critical value. In the measurements of thermophoretic force and droplet evaporation, the AC potential was first set to about 1000

V to trap the particle initially at atmospheric pressure. After a single particle was obtained, the AC was then lowered to 200 V to avoid discharge of gas.

4.3 Vacuum Apparatus and Gas Introduction

A 4 inch stainless steel chamber was designed in this study. It was machined by Nor-Cal Vacuum Company. A crossview of the chamber is shown in Fig. 4.9, and a top view showing the arrangements of the ports is presented in Fig. 4.10. There are eight ports: top and bottom end ports and six midplane ports. Grooves were drilled in port flanges to hold O-rings for vacuum sealing. Port 3 was directly connected to a vacuum gauge, and for other five ports in the middle plane optical windows were placed between the O-ring port flanges and mating flanges to permit passage of the laser beam and the scattered light. The dimensions of the chamber, ports, mating flanges and the size of O-rings are listed in Appendix A.

A pumping system including a Varian 950 mechanical pump and a Varian diffusion pump was used to vary the chamber pressure. The pumps were arranged in such a way that the mechanical pump can either directly pump gas from the main chamber or serve as a backup stage for the diffusion pump by operating the two gas-pneumatic valves V_1 and V_2 of Fig. 4.11. The mechanical pump can evacuate the chamber from atmospheric pressure to about 10^{-3} Torr, which satisfies the pressure requirements for the thermophoretic force and droplet evaporation measurements. The diffusion pump can be used to achieve high vacuum, needed in the future studies. The pumping rate is controlled by a manually-operated Viton Seal Angle valve (Norcal Co.) installed between the exit port of the bottom flange and the PVC tube (Kurt J. Lesker Co.), a plastic tube used to connect the pumps to the chamber. A Varian 325 liquid nitrogen trap (Dunniway Stockroom Corp.) was installed just above the gas input port of the diffusion pump. Any chemical vapors from the main chamber can be condensed in the trap, which prevents the chamber from

becoming contaminated and protects the pump. An on-line thermocouple gauge was mounted near the input port of the mechanical pump to monitor the pressure there. The MKS gauge was used to monitor the pressure in the chamber. It indicates pressures from 110 Torr to 10^{-2} Torr, a range which is adequate for the study of the thermophoretic force and evaporation in the Knudsen regime.

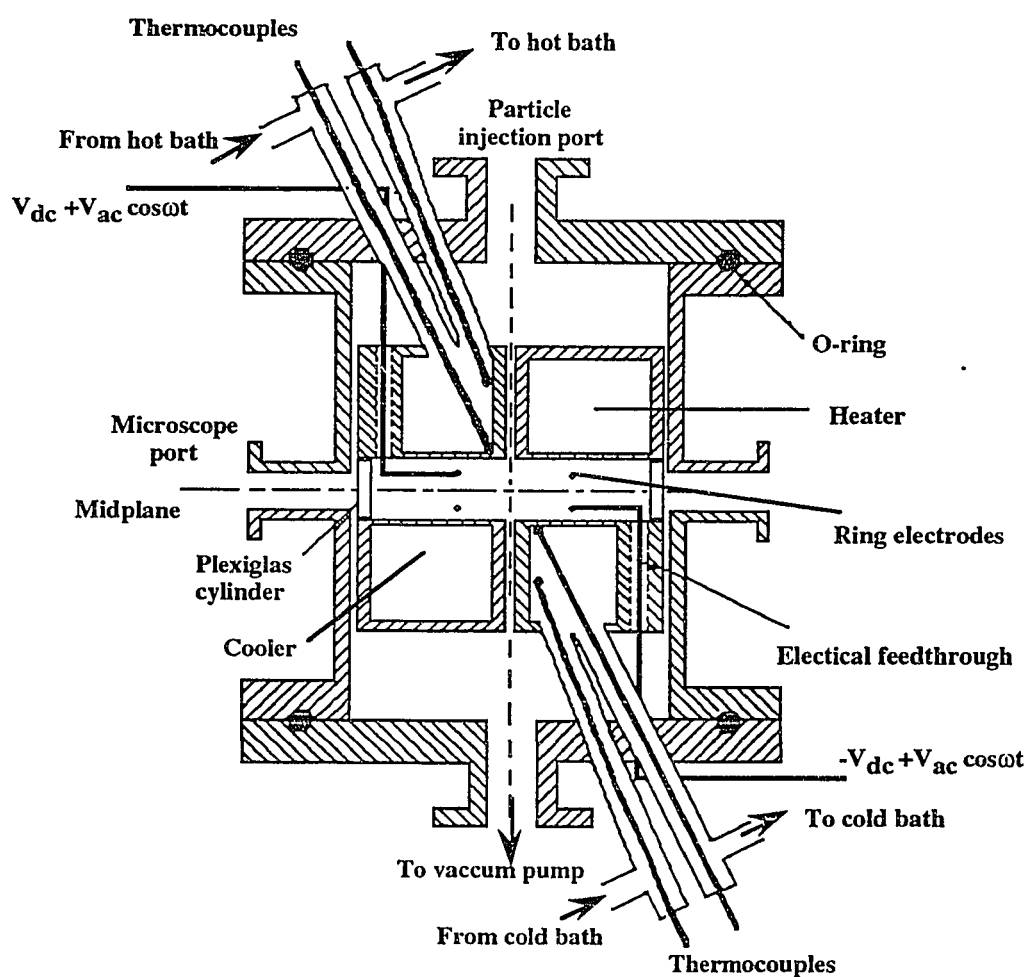


Figure 4.9 A cross view of the vacuum chamber showing the thermal plates and electric feedthroughs.

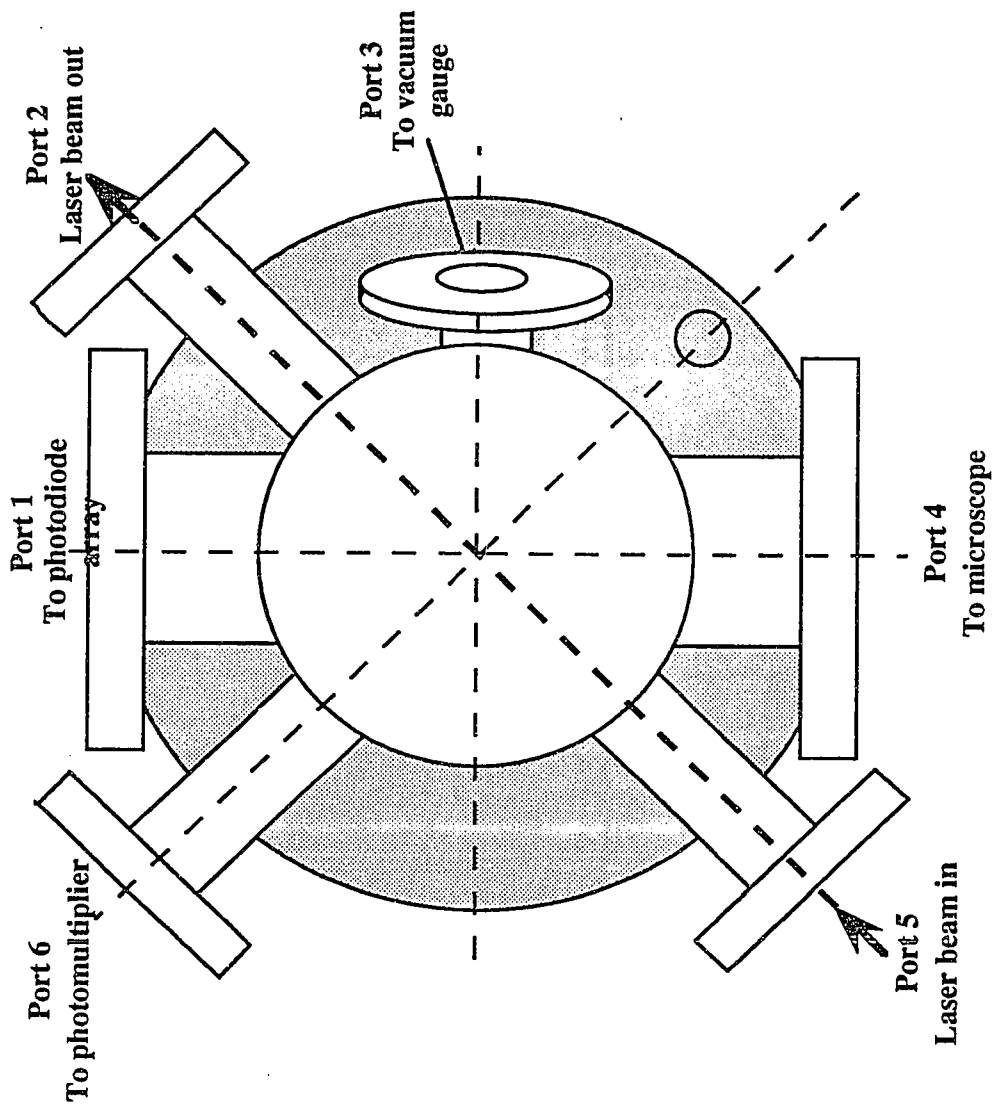


Figure 4.10 Top view of the main chamber showing the positions of the ports in the midplane.

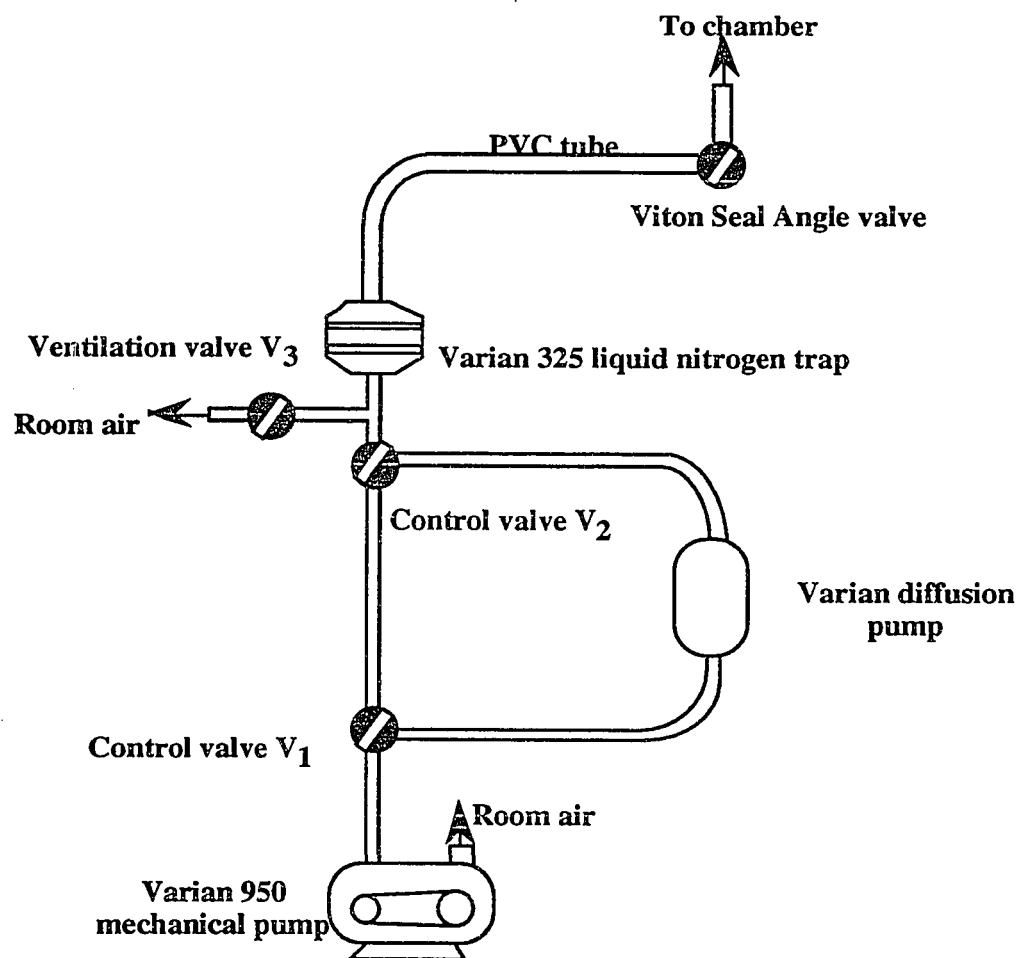


Figure 4.11 Systematic diagram of the vacuum system associated with the double-ring balance.

The calibration of the MKS gauge was achieved by connecting it to a high vacuum system (in Professor Roger's laboratory in Benson Hall of University of Washington) and following the calibration instructions recommended by the company.

A gas introduction system was attached to the vacuum system as shown in Fig. 4.12. Gas from a cylinder could directly flow into the vacuum chamber or be dried first by passing it through a tube filled with a drying agent. Also, gas could be humidified by flowing it through a sintered glass bubbler filled with water. Humidification is not needed in this study, but it may be useful for studies requiring humidified gases or chemical reactions with water vapor as a reactant.

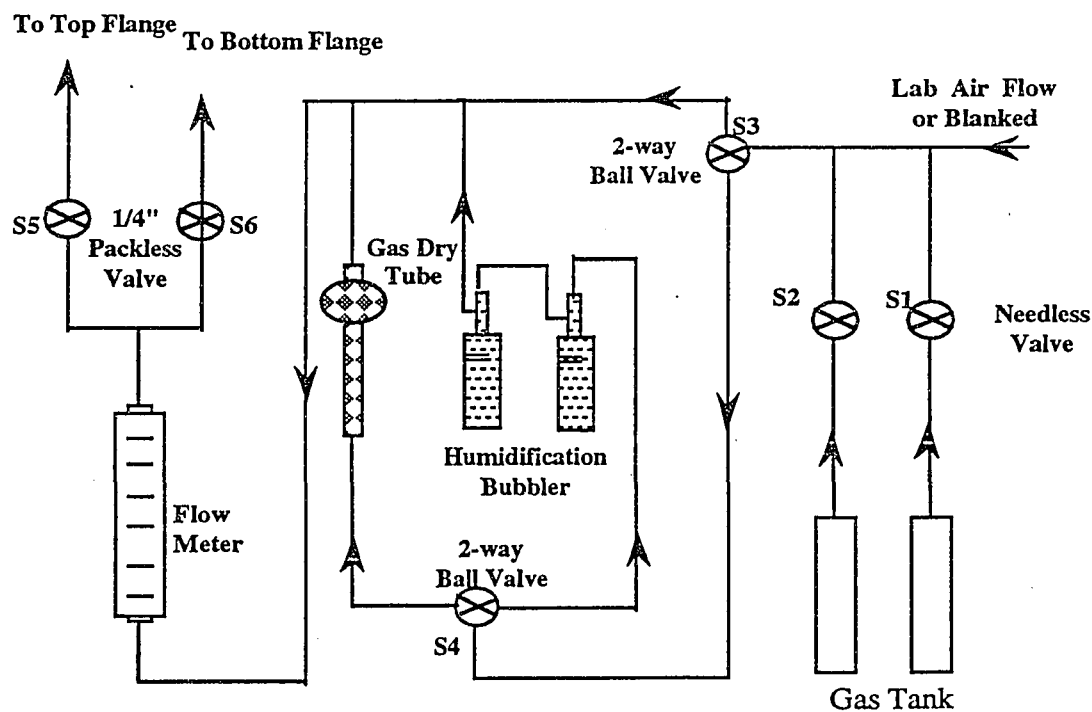


Figure 4.12 Diagram of the gas introduction system for the double-ring balance.

Used as an exit port if the gas passed through the chamber from below at atmosphere pressure. Two 1/4 inch packless valves S5 and S6 (Swagelok Co.) control the flow rates and also provide vacuum sealing. The 1/8 inch stainless steel tubes and appropriate Swagelok fittings were used in the vacuum line construction.

Figure 4.12 Diagram of the gas introduction system for the double-ring balance.

4.4 Optics and Photodetectors

A vertically polarized 15 mW He-Ne laser (Mells Griot Co.) operating at a wavelength of $\lambda = 632.8$ nm was used to illuminate the particle. The output beam was focused by a plane-concave lens with a focal length $\ell = 60$ mm. The laser beam, after it passed through the concave lens, converged and formed a spot, and then diverged. The beam spot was designed to be approximately in the EDB center where the particle is trapped. The minimum beam diameter, depending on the focal length of the plano-concave lens and other factors, is about $150 \mu\text{m}$, which is large enough to allow the particle to be observed easily. For more explanation on the formation of the beam spot and the estimation of beam diameter, one can refer to the catalog of "Optics 6" edited by Meriot Griot, Inc. The image and motion of the particle can be observed by microscope with a 60X magnification.

A Reticon photodiode array (PDA) having 512 elements and a photoelectric-sensitive area of 26.01 mm (ℓ) \times 0.12 mm (w) was used to record the phase function. As shown in Fig. 4.13, scattered light passing through an optical window were first focused by a spherical lens, then refocused by a cylindrical lens ($\ell = 108$ mm) to form a beam sheet in

the x-direction, which was projected on the 512-elements of the PDA. The spherical lens with a diameter of 25.4 mm and a focal length $\ell = 90.9$ mm was mounted one focal length away from the EDB center, so that the trapped particle was positioned at the focal point of the lens. The spherical lens was housed in a copper tube of adjustable length. The PDA was mounted in a stage, and its transverse position (x-direction) could be adjusted for alignment. To fix the range of scattering angles, the optical window for the PDA was blocked by a plate, and a slit was drilled in the plate. The dimension of the slit was 18.4 mm (ℓ) \times 3 mm (w), which just allowed all the elements of the PDA to be illuminated, yielding a scattering angle range of 36.88-52.74 degrees, and $\Delta\phi = 3^\circ$ around the midplane. Light distortion occurs, particularly at the two ends of the photodiode array, for the PDA is not curved but straight. Thus, only the readings from the pixels 30 to 480, corresponding to the scattering angles of 37.85 to 52.15 degrees, were used in data analysis.

The signals from the PDA were first amplified, and then sent to an A/D board and recorded by a 286 IBM/PC computer. A FORTRAN program written by Taflin (seeing Program "DTSCAT. FOR" in the Appendix A.3 of his dissertation, 1988) was slightly modified to collect the data. The data were then transferred to a Macintosh computer for plotting.

A photomultiplier (PMT) was mounted at right angle to the He-Ne laser beam ($\theta = 90^\circ$) to measure the optical resonance spectra. The DC power supply for the PMT could be varied from 120 V to 1300 V, but 900 V was typically used in the experiments. An optical filter was placed before the PMT window to eliminate background noise. The PMT has a high sensitivity and a small amount of reflected light from the stainless steel wall of the chamber could saturate the PMT. So the background signals must be eliminated to obtain good quality optical resonance spectra. Furthermore, a pin hole, with a diameter of about 2 mm giving scattering angles $\Delta\theta \approx 3^\circ$ for the PMT, was drilled in black paper attached to the

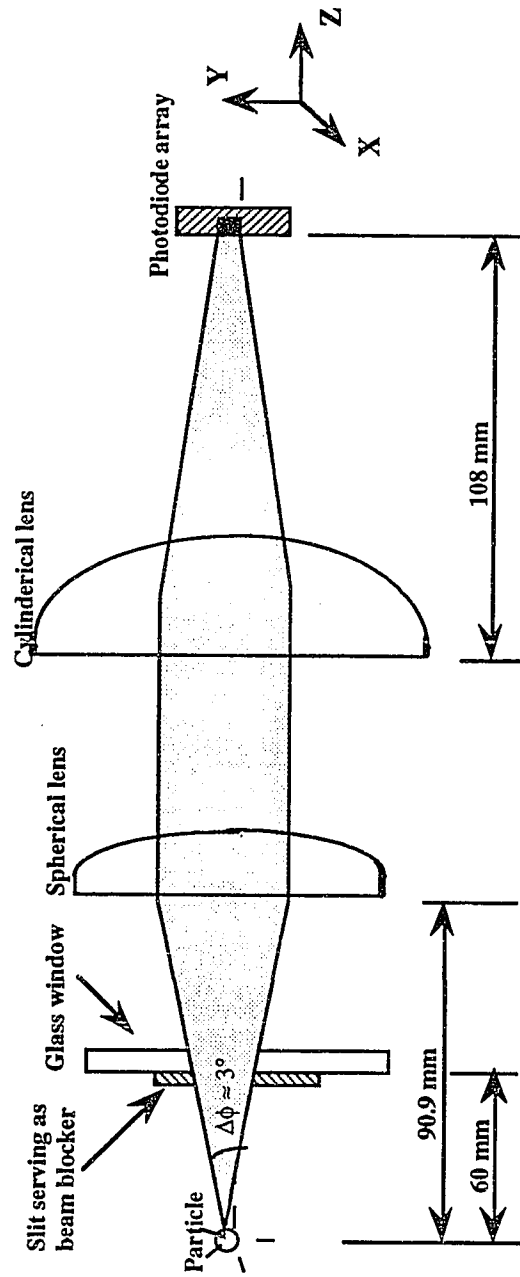


Figure 4.13 A cross section of the optical components used for collecting elastically scattered light.

glass window of the PMT port. The output signals from the PMT were amplified by a current-to-voltage converter. The voltage outputs were displayed on a two-channel oscilloscope. The output could also be connected to an A/D board and recorded by the IBM/PC computer for later data analysis.

4.5 Constant Temperature Cells

Two identical copper cells were machined and inserted in the vacuum chamber to provide temperature gradients for thermophoresis experiments. Hot fluid flowed through one, and cold fluid through the other. These are shown in Figure 4.9. Each cell was attached to the vacuum flange using two 1/4 inch diameter stainless steel tubes. A hole with 1/8 inch diameter was drilled through the center of cell for introducing particles and gas. After the particles were injected, the hole was blocked by a 1/8 inch rod to avoid any possible edge effects on the temperature profile. Another hole with a 1/4 inch diameter was installed for the electrical feedthrough. The outside diameter of the thermal cell was 2.25 inches. The separation distance between cells was about 1 inch. A buffer inside each thermal cell was placed to avoid flow shortcuts.

Natural convection is the main source of error involved in the thermophoretic force measurement. It strongly depends on the gas density, the temperature difference and the geometry of the system, especially the ratio of the plate width to plate spacing. The fluid temperature of the top cell was always higher than the bottom cell to minimize natural convection. Natural convection between two parallel plates, similar to the experimental setup used in this research, was investigated by Paranjpe (1936) who found that convective flow can be totally eliminated if the ratio of the width to spacing is larger than 13. In another study, Ostrach (1972) found that if the temperature of the top plate was higher than that of the bottom and if the side wall was insulated, no natural convection occurred no matter how high the Rayleigh number was. Attempts were made to reduce the separation

distance from 1 inch to 0.5 inch in this research in order to increase the ratio of width to spacing. But when the cells are too close to the ring electrodes, the electrical fields are disturbed and particles cannot be trapped.

To minimize or eliminate natural convection produced because of the glass windows attached to the ports in the midplane of the chamber, a plastic transparent cylinder 2.25 inch in diameter and 1.0 inch in height was placed to enclose the space between the cells. Four 1/8 inch holes and a horizontal groove were drilled in the midplane of the cylinder to pass the He-Ne laser beam and the scattered light. The cylinder functioned like an insulated wall preventing heat loss and blocking natural convection generated at the wall. Smoke was injected to the chamber to examine if natural convection occurred, and no convective motion of the smoke was observed. Indeed, the effect of natural convection can be measured. According to the theory of thermophoresis (Brock, 1962), the ratio of the thermophoretic force to the particle weight is less than 1% at atmospheric pressure for a 10 μm particle (typical in these measurements). Any natural convective currents will exert upward or downward drag forces on the particle which can be measured from the DC levitation voltage. No significant change of the DC voltage was observed as the temperatures of the top and bottom cells were adjusted to vary the temperature gradient. The effects of convection at low pressures cannot be measured since thermophoresis dominates as the pressure is reduced. Since natural convection decreases with decreasing gas density, these effects should be insignificant at low pressures. Most of the measurements were made at pressures below 110 Torr at which natural convection was found negligible by Derjaguin *et al.* (1966) and Tong (1975).

The temperatures of the thermal cells were controlled by circulating glycol and water mixtures from two thermal baths. One could vary the temperature from 0°C to 120°C, the other from -40° C to 120°C. Two K-type grounded thermocouple probes were inserted into the cell inside to measure the fluid temperatures as shown in Figure 4.9. The

measured temperatures were used to calculate the temperature gradient. The temperature drop across the copper cell wall was ignored since the wall was very thin. The outputs of the thermocouples were connected to a digital thermometer which has two input channels. The measurement accuracy of the thermometer is $\pm 0.1^\circ\text{C}$. In order to ensure that the linear temperature profile was not disturbed by the ring electrodes, a 0.05 mm fine bare thermocouple (Omega, Inc.) wrapped with thin Teflon tapes was inserted into the center of chamber to measure the temperatures at different vertical locations. The results are shown in Fig. 4.14. The square indicates the vertical positions between the two rings. The rings did not make a significant disturbance in the linear temperature profile.

In the droplet evaporation experiments, the temperature of the two cells was maintained the same by splitting one flow from one thermal bath into two branches and circulating them through the cells.

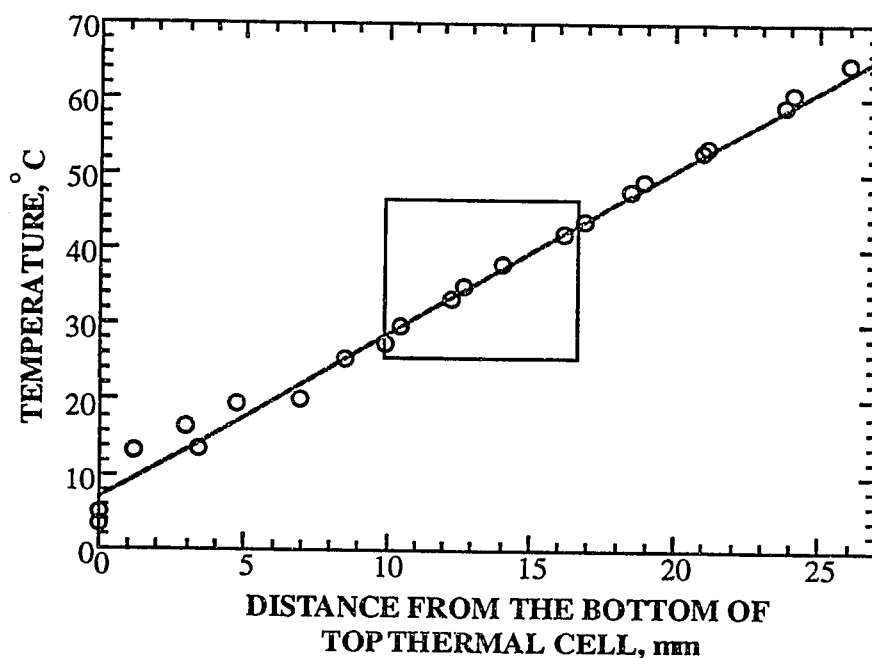


Figure 4.14 Measured temperatures of various vertical positions between the top and bottom thermal cells (center square denotes ring positions).

4.6 Measurement Technique

The measurements included elastic scattering, inelastic scattering (Raman scattering), DC levitation voltages and, in some cases, particle stability. The elastic scattering measurements yielded the particle size, and Raman spectra gave the particle chemistry. The ratio of any vertical force to the particle weight can be determined from the DC levitation voltage. The absolute values of the forces can be estimated from the ratio together with the measured particle size and known particle density. Measurements of particle stability are normally used to determine the balance constant, but such measurements were employed to size the nickel sphere in this study.

4.6.1 Gravimetric Measurements

Vertical forces such as the drag force, thermophoretic force and others., as well as changes of the particle weight caused by chemical reactions, evaporation or other dynamic processes can be determined from the DC voltages.

Suppose no external forces are exerted on the particle except gravity; a vertical force balance gives

$$mg = -q \frac{C_0 V_{dc,0}}{z_0}. \quad (4.10)$$

When the drag force or thermophoretic force acts on the particle, one may write

$$mg - F_t = -q \frac{C_0 V_{dc}}{z_0}. \quad (4.11)$$

Here, F_t represents the upward drag force or thermophoretic force. Therefore, by measuring the DC voltages with and then without an external gas flow or temperature

gradient, the drag force or thermophoretic force can be determined from the following relationship

$$\frac{F_t}{mg} = \frac{V_{dc} - V_{dc,0}}{V_{dc,0}}, \quad (4.12)$$

in which m is the particle mass given by

$$m = \frac{4}{3}\pi a^3 \rho_t \quad (4.13)$$

Here ρ_t is the particle density.

Other quantities such as the charge on a particle and the flow velocity can be determined from the DC measurements. If Stokes flow exists around a droplet, one may write

$$mg = -q \frac{C_0 V_{dc,0}}{z_0} + 6\pi a \mu U_\infty, \quad (4.14)$$

in which U_∞ is the velocity of the gas flow. Using Eq. (4.13), Eq.(4.14) can be rearranged to give

$$a^2 = -\left(\frac{3C_0 q}{4\pi \rho_t g z_0}\right) \frac{V_{dc}}{a} + \left(\frac{9\mu}{2g\rho_t}\right) U_\infty. \quad (4.15)$$

For constant ρ_t and no charge loss, a plot of a^2 versus (V_{dc}/a) yields a line whose slope contains the particle charge, and the intercept is proportional to the velocity of the Stokes flow. So, a simple plot can be used to determine the particle charge, and to examine convective currents in the chamber.

4.6.2 Particle Sizing Via Light Scattering Measurement

As discussed in Chapter 2, phase functions and optical resonance spectra are two effective tools for sizing particles. Applying the method of peak counting (Davis and Periasamy, 1985) to a measured phase function can yield the particle size with an accuracy of 1-3%. Much greater accuracy can be achieved by detailed analysis of the phase functions and resonances.

The photodiode array mounted in Fulton's balance (see apparatus A) has 512 elements. The middle 256 elements, corresponding to a scattering angle range of 34.85° - 54.15° , were used here to determine the particle size. For this angle range, Taflin obtained the following relationship between the number of peaks, N_p , and the size parameter of particle, X , from Mie theory

$$X = 10.07N_p. \quad (4.16)$$

Equation (4.16) is based upon spheres with refractive indices around 1.5, which is typical for organic droplets.

The photodiode array in the new balance was mounted relatively far away from the particle compared with Fulton's balance. The middle 480 elements covering the range $37.85^\circ \leq \theta \leq 52.15^\circ$ were employed to determine the particle size. The corresponding relationships for the peak number and the size parameter of the particle are listed in Table 4.1 for the materials used in this study.

Three phase functions measured at different evaporation times for an dibutyl phthalate (DBP) droplet are shown in Fig. 4.15. The dashed lines are the solutions calculated from Mie theory.

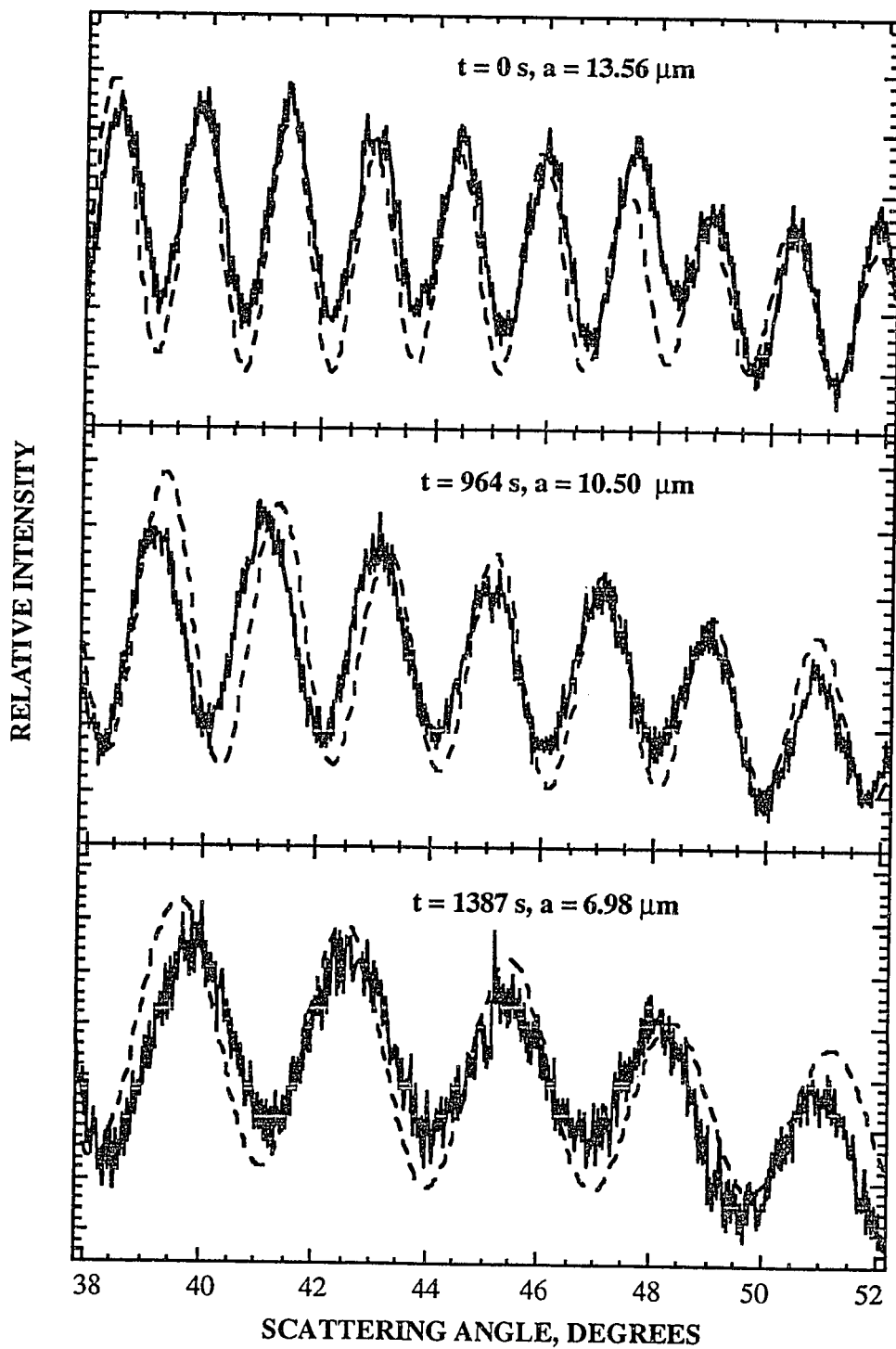


Figure 4.15 Measured phase functions for an evaporating DBP droplet at various times.

Table 4.1 Correlations determined from Mie theory for the particle size parameter, X , and the number of peaks, N_p , in the X range of 25 - 200.

Materials	Refractive Index	Correlation
Dibutyl Phthalate (DBP)	1.492 + 0.00 i	$X = 14.328 N_p - 0.3723$
Diocetyl Phthalate (DOP)	1.486 + 0.00 i	$X = 14.769 N_p - 1.5008$
Polystyrene Latex (PSL)	1.590 + 0.00 i	$X = 14.376 N_p - 0.2088$
Glass Bead	1.510 + 0.00 i	$X = 14.376 N_p - 0.2088$

Morphology dependence resonance (MDRs) offer an alternate method for determining droplet size. An accuracy of 1 part in 10^5 can be achieved by this technique. A portion of one measured MDR for an evaporative DBP droplet at room temperature is presented in Fig. 4.16. The theoretical solution calculated from Mie theory is also shown for a comparison. The calculation is based upon the DBP droplet ($m = 1.492 + 0i$) illuminated by a vertical polarized laser beam ($\phi = 90^\circ$) at $\theta = 90.4^\circ$ with $\Delta\theta = 3^\circ$. The latter corresponds to the subtended scattering angles by the PMT.

4.6.3 Particle Sizing via Marginal-Stability Measurements

An alternative method for sizing a particle is the application of marginal-stability measurements. During the study of the thermophoretic force, it was found that the photodiode array could not detect the elastic scattering from the nickel sphere effectively due to the absorption of the electromagnetic radiation energy and weak scattering by the nickel sphere. Thus, marginal-stability measurements were employed to determine the size of the nickel sphere.

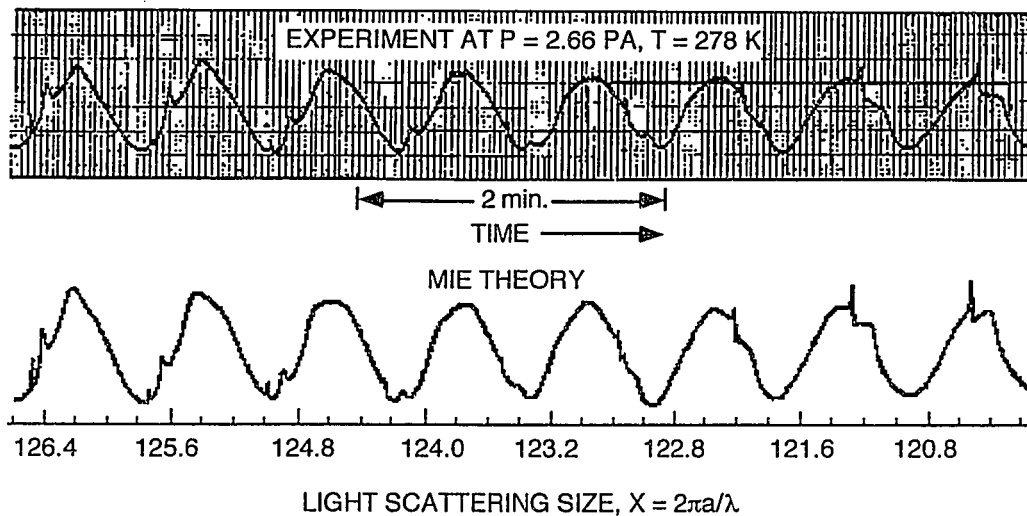


Figure 4.16 Comparison among the theoretical MDRs and the experimental MDRs obtained for an evaporating droplet of DBP at $T = 278$ K in the free-molecule regime.

From the discussion in section 4.2, we know that the particle stability is governed by the aerodynamic drag parameter, A , and the AC field strength parameter, B , which are respectively defined by Eq. (4.8) and (4.9). When B exceeds a critical value, B_{crit} , the particle becomes unstable, which can be achieved by decreasing the frequency of AC potential and/or increasing its amplitude. Using the AC and DC potentials at the marginal stability points, one may determine the particle size once the geometric constants K and C_0 are known.

The ratio q/m in Eq. (4.9) for the AC field parameter may be replaced by

$$\frac{q}{m} = -\frac{gz_0}{C_0 V_{\text{dc}}}. \quad (4.17)$$

Equation (4.17) is obtained from the vertical force balance on the particle. Using Eq. (4.17), the field strength parameter may be written as

$$B = -K \left(\frac{V_{ac}}{V_{dc}} \right) \frac{gz_0}{C_0 \omega^2} \quad (4.18)$$

If the constants in Eq. (4.18) are grouped and the circular frequency is replaced by $\omega = 2\pi f$, then, the AC field parameter becomes

$$B = \Psi \frac{V_{ac}}{V_{dc}} \frac{1}{f^2}, \quad (4.19)$$

with

$$\Psi = \frac{K}{C_0} \frac{gz_0}{4\pi^2}. \quad (4.20)$$

The group constant, Ψ instead of K or C_0 was used in the calculation of particle size. The value of Ψ for the double-ring EDB developed in this study was obtained by measuring the onset of instability for DBP droplets, and performing the best fit of the measured stability data with the solution of Mathieu's equation. The sizes of the DOP droplets included in the calculation of drag parameter A were determined from phase function measurements.

Once the constant Ψ is determined, the size of a nickel sphere can be measured. This is achieved by trapping a nickel sphere at atmospheric pressure and changing V_{ac} and frequency ω until the sphere becomes unstable. At that point B_{crit} is estimated from Eq. (4.19), and the drag parameter A can be determined from the solid line in Fig. 4.6. The size of nickel sphere may be estimated by

$$a = 3 \left(\frac{\mu}{2A\rho_t\omega} \right)^{1/2}. \quad (4.21)$$

The measured stability data for DOP droplets, used to determine the constant Ψ , are presented in Fig. 4.6.

4.6.4. Raman Spectroscopy

Raman scattering measurements were performed with a Spex 1403 0.85 m double-monochromator which was controlled by a Spex CD2A monochromator drive unit. The monochromator consisted of two 1800 groove/mm holographic gratings and two photodetectors: a cooled photomultiplier (PMT) and an optical multichannel analyzer (OMA). The OMA can measure the Raman signals with a wavenumber band of approximate 180 cm^{-1} , but for a wide wavenumber study, the PMT is required. The PMT has high sensitivity, but it takes a long time to take a wide scan since the highest scan rate is $10 \text{ cm}^{-1}/\text{s}$. For example, it requires about 7 minutes to scan a wavenumber range of 4000 cm^{-1} . For the study of fast processes, the OMA is more useful.

As an example, Fig. 4.17 presents an Stokes Raman spectrum obtained for a titanium ethoxide droplet reacting with water vapor. The positions of the individual Raman peaks are related to rotations and vibrations of chemical bonds within the sample molecules. The interpretation of Fig. 4.17 is given in Chapter 5.

4.7 Particle Generation and Experimental Procedures

Particles studied with the three EDBs were generated, charged and introduced into the balance by means of an electrified needle. For liquid samples, the material of interest was sucked into a syringe through a flat-tipped hypodermic needle. The needle passed through a $1/8$ inch hole in the center of the top of the cell and was positioned slightly below the bottom of the upper thermal cell for the thermophoresis experiments. The needle was sheathed with a thin Teflon tube to avoid electric discharge. A short wire was soldered to

the needle and connected to a positive DC power supply whose output could be varied from 0 - 10 kV. A relay switch was installed in the power supply. After a small droplet of liquid was drawn out onto the tip of the needle, a 2500 ~ 6000V DC pulse was applied to the needle by activating the relay switch. The applied electrical force overcomes the surface tension force of the droplet, and the droplet explodes into smaller droplets. Usually, more than one droplet falls into the balance and is trapped by the electrical fields. By adjusting the AC amplitude and/or frequency, a single droplet can be isolated. The DC voltage was then adjusted to balance the weight of the droplet. For solid materials, the sheathing Teflon tube was pushed over the tip of the needle to dislodge the solid particle. A second 5 kV DC power supply was used to negatively charge the particle, so both positively and negatively charged particles were studied.

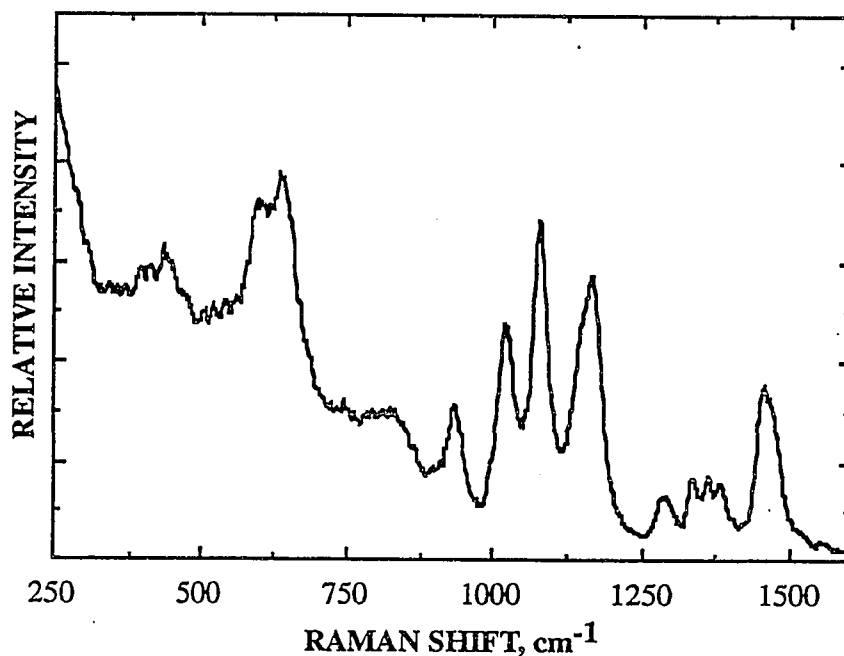


Figure 4.17 A Stoke's Raman spectrum in the wavenumber range 250 - 1600 cm⁻¹ for a reacting droplet of titanium ethoxide.

For measurements at low pressures, the particle was initially trapped in the balance with the AC voltage typically 800 - 1000V. To ensure that no gas discharge occurred, the AC voltage was kept below 200 V during the experiment. Therefore, before evacuating the chamber, the AC voltage was lowered below 200 V to determine whether the particle could be trapped with such a low AC voltage. If the particle met the requirement, the AC voltage and frequency and the DC voltage were recorded. Then, the AC voltage was increased again to prevent particle loss during pumping.

Once a desired particle was trapped, the heater and cooler were turned on and the flow control valves were opened to circulate fluids through the thermal cells. It took about half an hour for temperatures to reach the pre-set values. During the processes of heating and cooling, temperatures of the controllers were adjusted to eliminate any possible convection.

After steady state was reached, the vacuum valve mounted in the bottom flange was slightly opened to evacuate gas from the chamber. The valve was slowly opened as the pressure fell. When the chamber pressure reached 110 Torr, the MKS pressure gauge was used to measure the pressure. At this pressure the valve was closed and the AC voltage was lowered to the value of pre-recorded reference point and kept unchanged during the experiment. The phase function was recorded to obtain the initial particle size, and the DC voltage was adjusted to balance the thermophoretic force. Then, the vacuum valve was reopened to continue evacuation and the DC voltage was readjusted. The whole process was repeated and continued until enough data points were obtained to cover a desired range of Knudsen number. At each point, the pressure and DC voltage were recorded. For the DOP droplet, the phase function was taken every half hour to determine if the size change was negligible during the measurements.

When measurements of the thermophoretic force were made in helium or carbon dioxide, the particle was first trapped in air and the chamber was evacuated to below 10^{-2}

Torr. Then, the vacuum valve was closed and the gas inlet valve (S5 or S6 in Fig. 4.12) was slightly opened to bleed some desired gas into the chamber until the pressure reached 110 Torr. To ensure that only helium or CO₂ remained in the chamber, the chamber was evacuated to 10⁻² Torr one more time and refilled with the desired gas before measurements were started. Usually, it was possible to perform numerous measurements with a particular particle in more than one gas.

The descriptions above were the measurement procedures for the thermophoretic force. The process was similar for the measurements of droplet evaporation, except that the temperatures of the top and bottom cells were kept the same, which was achieved by circulating flows from one cooler through both cells. The whole chamber was wrapped with cotton and thermal insulation tape to reduce the heat exchange between the chamber inside and outside, and to avoid water vapor in the surrounding air from condensing on the outside wall of the chamber. In some measurements the temperatures were less than 0°C.

Normally, in the evaporation experiments DBP droplets were trapped within a couple of trials. If not, the chamber was sealed and evacuated to a pressure of about 10⁻² Torr to remove any accumulated DBP vapor. Once a particle was isolated in the EDB and could be trapped with the lower AC potential, a gas flow was introduced to the chamber to remove DBP vapor in the chamber. Care was taken to keep the amount of DBP in the chamber as small as possible before the start of evaporation to maintain a negligible concentration of vapor in the bulk gas. After the chamber was purged of vapor, the chamber was sealed and gas evacuation proceeded. At the same time, measurements of phase functions and MDRs were initiated. Evaporation rates were determined at a set of discrete pressures, that is, at constant Kn. At a particular pressure, the valve was slightly opened and adjusted to keep the chamber pressure constant. During the measurements, the pressure-control valve S5 (see Fig. 4.12) was slightly opened to leak some air into the chamber to keep the concentration of DBP vapor negligibly small.

The experimental procedures for Raman measurements have been discussed by Allen (1992) and Scott (1994).

CHAPTER 5

A STUDY OF THE FORMATION OF TiO₂-COATED MICROSPHERES BY LIGHT SCATTERING

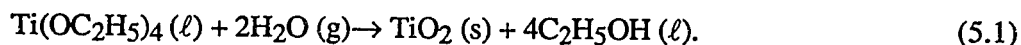
5.1 Introduction

A variety of materials, such as polymers, catalyst and structural, optical and electronic ceramics, can be manufactured via aerosol reaction technology. A typical example is the formation of glassy particles by means of the reaction between various halide vapors (SiCl₄, SiF₄ and etc.) and water droplets. The formed particles are deposited on substrates to manufacture optical fibers for telecommunication. Generally, materials produced via aerosol reactions have high purity since the process is simple and no large volumes of byproducts are involved (Pratsinis and Kodas, 1993).

According to the state of the starting materials, the aerosol processes in material synthesis can be classified into gas-to-particle and droplet-to-particle conversion (Pratsinis and Kodas, 1993). In the former case the precursor gases or vapors react and form small clusters which grow to a powder by means of coagulation and aggregation. In the later route droplets are usually generated by atomizing the precursor solution. Individual droplets can react with another gas or convert to particle by directly pyrolysis in which the solvent evaporates from the solution of precursor. The particles formed from the gas-to-particle conversion have relatively narrow particle size distributions, and are nonporous and spherical, but the size of products cannot be controlled. This limitation can be overcome if the droplet-to-particle process is used, since one can control the final size of the particle by controlling the primary droplet size. The possible undesirable features associated with the product are the chemical and optical inhomogeneity and porosity.

The production of metal oxide spheres via droplet/gas reaction was extensively investigated by Matijević and his coworkers. Visca and Matijević (1979) prepared

spherical narrow size TiO_2 particles by reacting droplets of metal aloxides with water vapor. One example reaction is



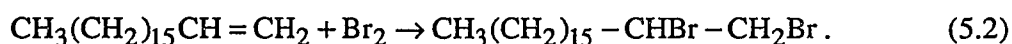
The same procedure was followed by Ingebrethsen and Matijević (1980, 1984) to manufacture oxides of aluminum and titanium from the alkoxides aluminum *sec*-butoxide, titanium tetraethoxide (TTE) and titanium (IV) isopropoxide. They found that partial hydrolysis of the alkoxide led to compounds such as $\text{Ti}_2\text{O}(\text{C}_2\text{H}_5)_6$ and $\text{TiO}(\text{C}_2\text{H}_5\text{O})_2$. The process was modified by Matijević *et al.* (1995) to achieve more uniform dispersions of particle size. Generally, the reaction was found to be fast initially and soon slow down. The decrease in reaction rate was caused by the formation of the solid metal oxide on the droplet surface which lowers the diffusion of water vapor into the particle and/or diffusion of the alcohol product out of the particle. By microtoming the particles and examining them in an electron microscope, the particles were found to be hollow, that is, they consisted of a relatively thin shell of metal oxide around an unreacted core.

The synthesis of metal oxide by Matijević and his associates were made in the aerosol flow reactor in which polydispersed droplets were involved. In the present study attention was paid on the reaction between a single TTE droplet with water vapor described by Eq. (5.1). It is convenient to study the reaction process by following a single droplet process since the effects of the particle size distribution need not be considered. There are a few studies related to the reaction between single particles/droplets with gas reactant in literature. Straubel (1980, 1981), and Straubel and Straubel (1985) investigated chemical reactions of $\text{Na}_2\text{S}_2\text{O}_3 \cdot 5\text{H}_2\text{O}$ particles with HCl vapor. They used the three-plate electrodynamic balance (see Fig. 4.4a) to isolate single $\text{Na}_2\text{S}_2\text{O}_3 \cdot 5\text{H}_2\text{O}$ particles. High concentrations of HCl were initially used and the reaction was found to be complete within

few seconds, which is a short time for quantitative analyses. Later they diluted the HCl concentration and extended the study to the reaction between $\text{ZnCO}_3 \cdot 3\text{Zn(OH)}_2$ particles and water vapors. The changes of particle weight were monitored by the DC levitation voltages, and the diffraction patterns of the reacting particle were photographed.

Rubel and Gentry (1984, 1986, 1987) studied the reaction of phosphoric acid droplets with ammonia gas. Single acid droplets in the size range 42-72 μm were trapped in the bihyperboloidal electrodynamic balance. The partial pressure of gaseous ammonia varied from 11.5 to 100 Pa, and the mass of droplet was monitored by the DC balancing voltage. The reaction was found to be rapid initially, and slow down after the onset of crystallization of the product, ammonium orthophosphate-di-hydrogen. Their data were reanalyzed by Foss and Davis (1995) who theoretically examined the rate of reaction for single aerosol droplets with vapor reactant.

Microparticle reactions were also investigated by Davis and his associates. Using optical resonance spectra, Taflin and Davis (1990) followed the reaction of bromine vapor with 1-octadecene droplets forming 1,2-dibromooctadecane



They were able to determine the concentrations of the product as a function of the reaction time. The same reaction was re-examined by Buehler (1991) using Raman spectroscopy. Following the intensity of Raman peak at 1650 cm^{-1} for C=C bond of the olefin and at 650 cm^{-1} for the C-Br bond of product, he determined the extent of the reaction. The reaction rates obtained by Buehler reasonably agreed with Taflin's results. Raman spectra were also used by Rassat (1994) and by Aardahl (1995) to study the desulfurization reaction of CaO or NaOH microparticles, respectively, and used by Wildmann (1995) to examine the

polymerization of a mixture of 1,6-hexanediol diacrylate and trimethylolpropane ethoxy triacrylate monomers.

The common problem encountered in the syntheses of materials via gas/droplet reactions or spray pyrolysis technique is that the powder produced is hollow or coated. This undesired morphology greatly impedes a wider industrial acceptance and application of the products (Zhang *et al.*, 1990). The hollow characteristic was also found in the present study. Since not much work has been done to characterize coated particles, elastic and inelastic (Raman) scattering were employed to explore the physical and chemical properties of the coated particle, although the original purpose of the present study was to form single TiO₂ spheres *in situ* for the thermophoresis study. It was demonstrated that one can obtain the shell thickness and refractive index from the interpretation of the recorded elastic data using the theoretical solution of Aden and Kerker (1959), and to identify the chemical components within the reacting particle from the Raman spectra. Previous studies of microparticle Raman spectroscopy were made mainly for static droplets and crystalline particles; very little work has been done on the chemically reacting aerosols.

The recorded elastic and inelastic scattering data for the reacting TTE droplets are presented in this chapter. The physical properties estimated from a "best fit" between the raw data and the theory of Aden and Kerker are also listed here.

5.2 Chemical Reaction Between Single TTE Droplets and Water Vapor

Single TTE droplets were generated, charged and introduced into the chamber by means of an electrically charged hypodermic needle, as described in Chapter 4. In order to prevent the sample from reacting with water vapor before they were introduced to the electrodynamic balance, a transparent glass cylinder was placed on the top endcap DC electrode through which dry air was passed. The humidity of air in the glass cylinder was monitored by a probe and the reading approached zero after a period of time. Once zero

humidity reached, TTE sample was sucked into the hypodermic needle and the needle was immediately sealed in the dry air of the cylinder. Before introducing the TTE droplets, the needle was slightly pushed to remove the possibly reacted TTE in the needle tip. High purity TTE is not available, and the titanium ethoxide used, which was purchased from Aldrich Chemical Company, contained approximately 10 wt% ethanol. Ethanol is a highly-volatile organic, and it was assumed to evaporate quickly in the early stage of the reaction.

Once a single TTE droplet was stabilized in the balance, the computer was triggered to collect phase functions for the reacting TTE droplet. Normally, it required approximately 40 ms to record the signals from the 512 pixels of the photodiode array at a time. In the initial stage the reaction was fast and the particle size reduced significantly, so phase functions every one second were collected, but at later times data were taken only occasionally for the particle size did not change significantly. Three "raw" phase functions are presented in Fig. 5.1. These were obtained at different times for a reacting TTE droplet in room air. It is noted that the amplitudes of light scattering intensity, as well as the number of peaks, decreased as the reaction proceeded. Initially, evaporation of TTE and/or ethanol simultaneously occurred with the surface reaction, and both processes caused the reduction of particle size. The measured phase functions can be used to determine the outer size of the particle by means of the peak counting suggested by Davis and Periasamy (1985). Further refinements were made to obtain the shell thickness of TiO_2 and other properties, which will be described in the following section.

The optical resonance spectra or "MDRs" were also recorded simultaneously with the phase functions. Figure 5.2 presents three sections of the MDRs data obtained for a reacting TTE droplet. The time scale on the stripchart starts from the time when the particle was nearly stabilized in the laser beam and the light scattering from the droplet could be detected by the photodiode array and PMT. Normally, two or three seconds elapsed between the time of injection and the time at which the particle was stabilized in the balance.

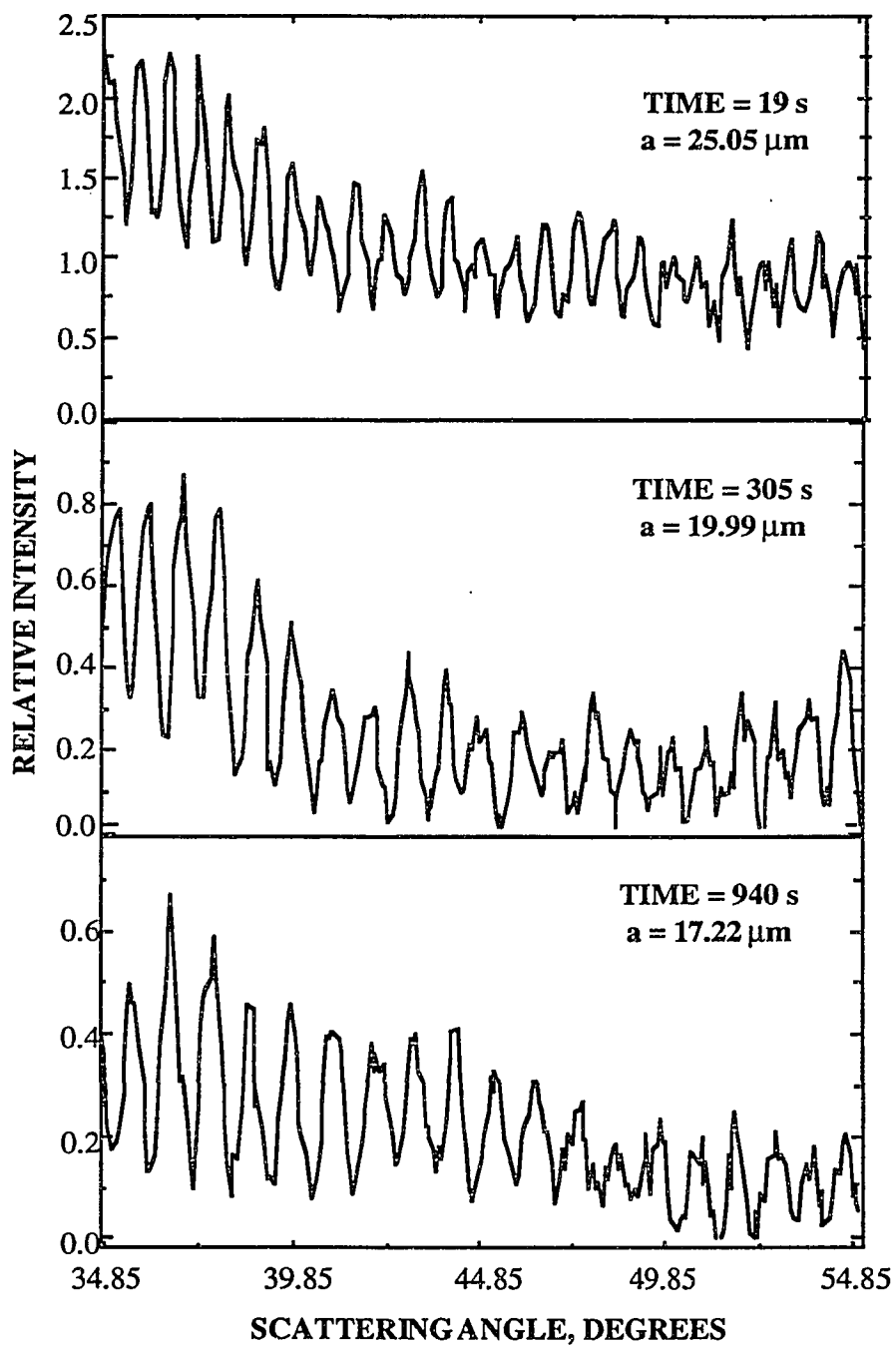


Figure 5.1 Phase functions obtained at different times during an experiment with a reacting droplet of TTE.

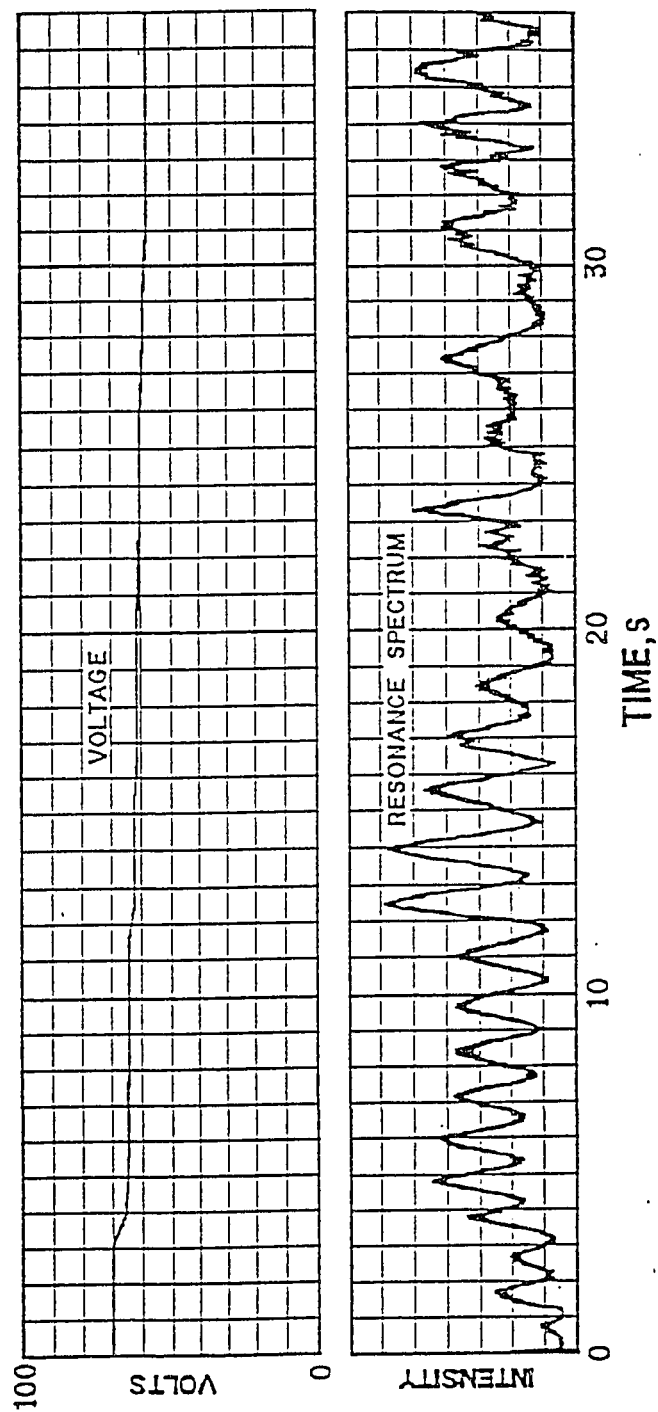


Figure 5.2a. A resonance spectrum obtained for a reacting TTE droplet at the beginning of the experiment.

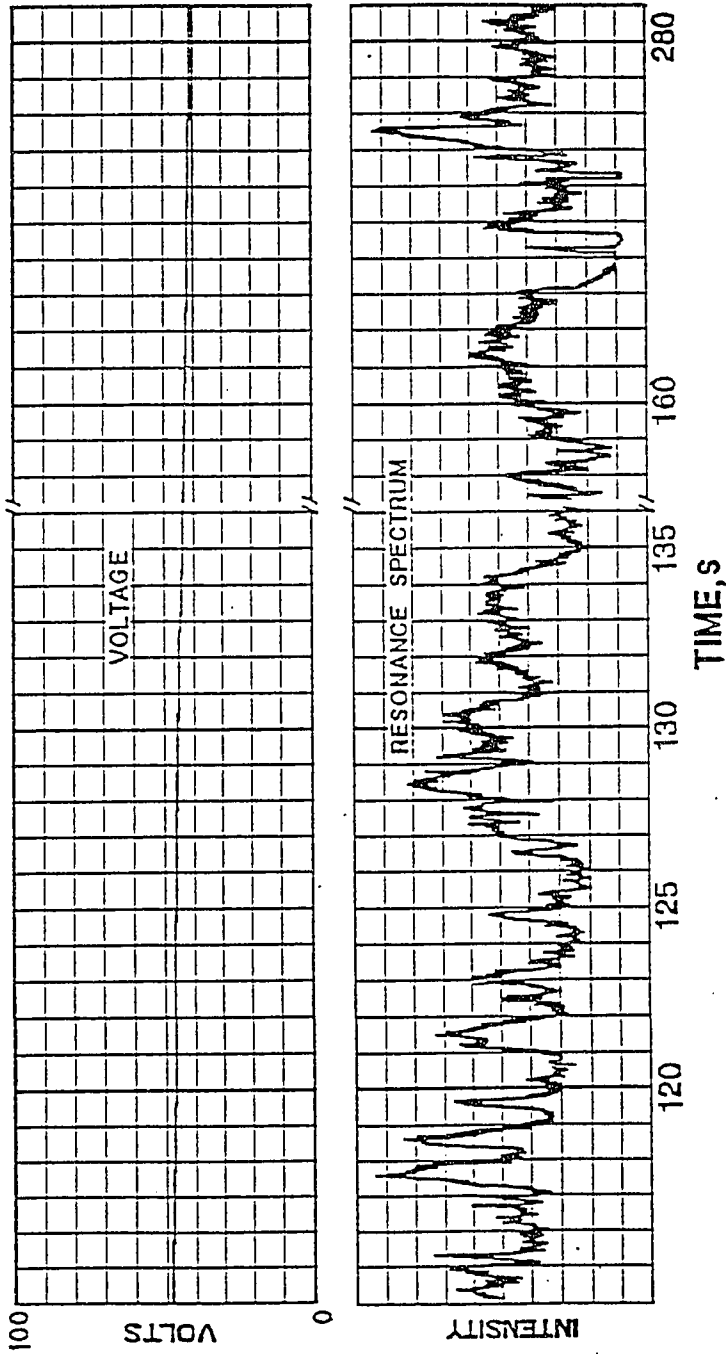


Figure 5.2b. A resonance spectrum obtained for a reacting TTE droplet after a solid shell of TiO₂ began to form.

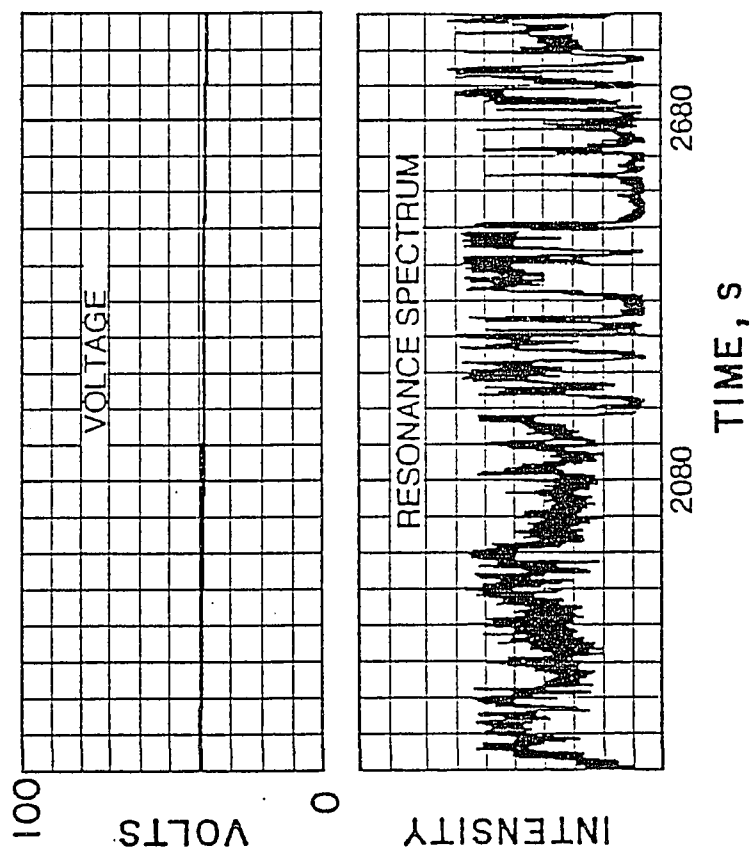


Figure 5.2c. A resonance spectrum obtained for a reacting TTE droplet after a solid shell of TiO₂ had formed at long times.

It is noted that at the outset of reaction, the data are smooth and the peaks are regularly defined, which are typical of resonance spectra corresponding to evaporation and/or chemical reaction of a droplet, but the data became noisy after approximately 20 seconds. At later times, the measured data are chaotic, although the resonant characteristics can still be observed. After several hours the resonance spectra are seen to be very noisy as shown in Fig. 5.2c. The onset of the noise marks the beginning of the formation of an optically rough coated particle, and the chaotic data obtained after a few hundred seconds suggest that a microscopically rough TiO_2 shell had formed. The phase functions also became noisier at large times, but they still retained the wave structure which allowed the outer particle size to be determined.

The DC levitation voltages required to balance the particle weight and other vertical forces were also recorded using the other channel of the stripchart. They are shown in Figs. 5.2a, b and c along with the MDR data. Some of the DC data in Fig. 5.2 are plotted in Fig. 5.3 as a function of time. It is noted that the DC voltages varied significantly in the initial stage of reaction, and a fairly sharp change in the rate of change of the DC voltage occurred at about 100 seconds. The change of the DC voltage was caused by the mass loss of the droplet due to the consumption of TTE and the evaporation of ethanol in the reaction. After about 100 seconds, a TiO_2 shell had formed which reduced the reaction rate by preventing the diffusion of water vapor into the TTE core, and, consequently, lowered the DC rate of change. After a few hours the DC voltage remain constant.

The change of DC voltage was also observed by Rubel and Gentry (1984, 1986) in their study of the reaction between single droplets of phosphoric acid and ammonia vapor. They found that the DC voltages increased rapidly with the reaction time, but the rate of change significantly dropped after a short time. The uptake of ammonia by the phosphoric acid droplet caused the increase in DC voltage. After a shell of the product, ammonium dihydrogen orthophosphate ($\text{NH}_4\text{H}_2\text{PO}_4$), had formed, the reaction rate decreased causing

a decrease in the DC voltage rate of change. They varied the partial pressure of ammonia vapor and found that the reaction rate as measured by the DC voltage decreased with increasing partial pressure of ammonia vapor. This indicates that the higher the concentration of ammonia vapor, the less time it took to form a crystalline shell.

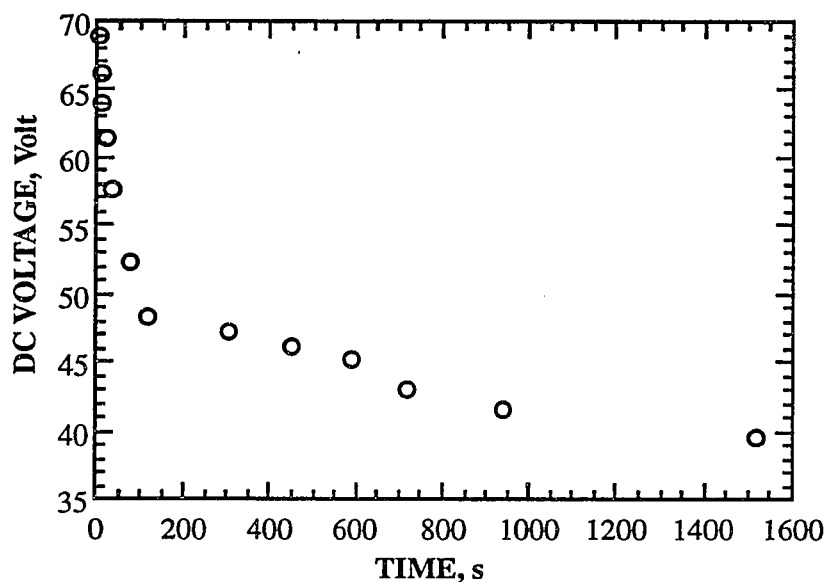


Figure 5.3 The levitation DC voltage as a function of reaction time for a reacting TTE droplet.

Gas/droplet reactions were theoretically examined by Foss and Davis (1995). They formulated and numerically solved the governing equations for the simultaneous diffusion and chemical reaction for a second-order reaction with respect to the dissolved gas and liquid reactant. The problem can be simplified for the initial stage of the reaction when the liquid reactant is in large excess, for the process can be treated as pseudo-first order in the dissolved gas. The two dimensionless parameters that govern the overall process are the Damkohler number, $N_{Da} = k_c a^2 / D_{AL}$, and the Biot number, $N_{Bi} = D_{AG} H_A / D_{AL} R T$, in which k_c is the reaction rate constant, H_A is the Henry's law constant for the vapor reactant, T is the droplet temperature, R is the gas constant, and D_{AG} and D_{AL} are the gas

phase and liquid phase diffusivity of the diffusing species, respectively. Numerical results for various case studies showed that for large N_{Da} , that is, for fast surface reaction, the product will form only near the droplet surface, and the precipitation of the low-solubility product on the droplet surface is expected. For large Biot numbers the reaction rate depends on N_{Da} only when the external resistance to mass transfer vanishes. The vapor concentration near the droplet surface then approaches the bulk concentration of vapor. The numerical results suggest that a homogeneous particle can be formed, if a very low partial pressure of vapor is maintained in the gas phase. This controls the reaction rate by allowing time for diffusion of the solute into the core of the droplet. However, this was not achieved in the present experimental work.

5.3 Determination of Physical Properties

In order to estimate the shell thickness of TiO_2 , a sequence of computations was performed to obtain a "best fit" between the recorded phase functions and the theory of Aden and Kerker (1951) for a coated sphere. The FORTRAN program given by Bohren and Huffman (1983) to calculate the scattered intensity from a coated particle was modified to perform the "best fit". The modified program is listed in Appendix B. Since the measured phase functions became increasingly noisy due to the formation of a TiO_2 shell as the reaction proceeded, the raw data were first smoothed by a fast fourier transform (FFT) procedure discussed by Taflin *et al.* (1988). The scattering data from the middle 128 elements of the photodiode array were used in the "best fit". These correspond to scattering angles in the range 39.87° - 49.87° . Figure 5.4 compares a sample of raw data, the smoothed data and a computed phase function based upon the "best fit".

The calculation of light scattering for the coated particle involves an iterative procedure based on four parameters: the core and outer particle sizes and the indices of refraction of core and shell. The refractive indices of the core, N_c , and of the shell, N_s ,

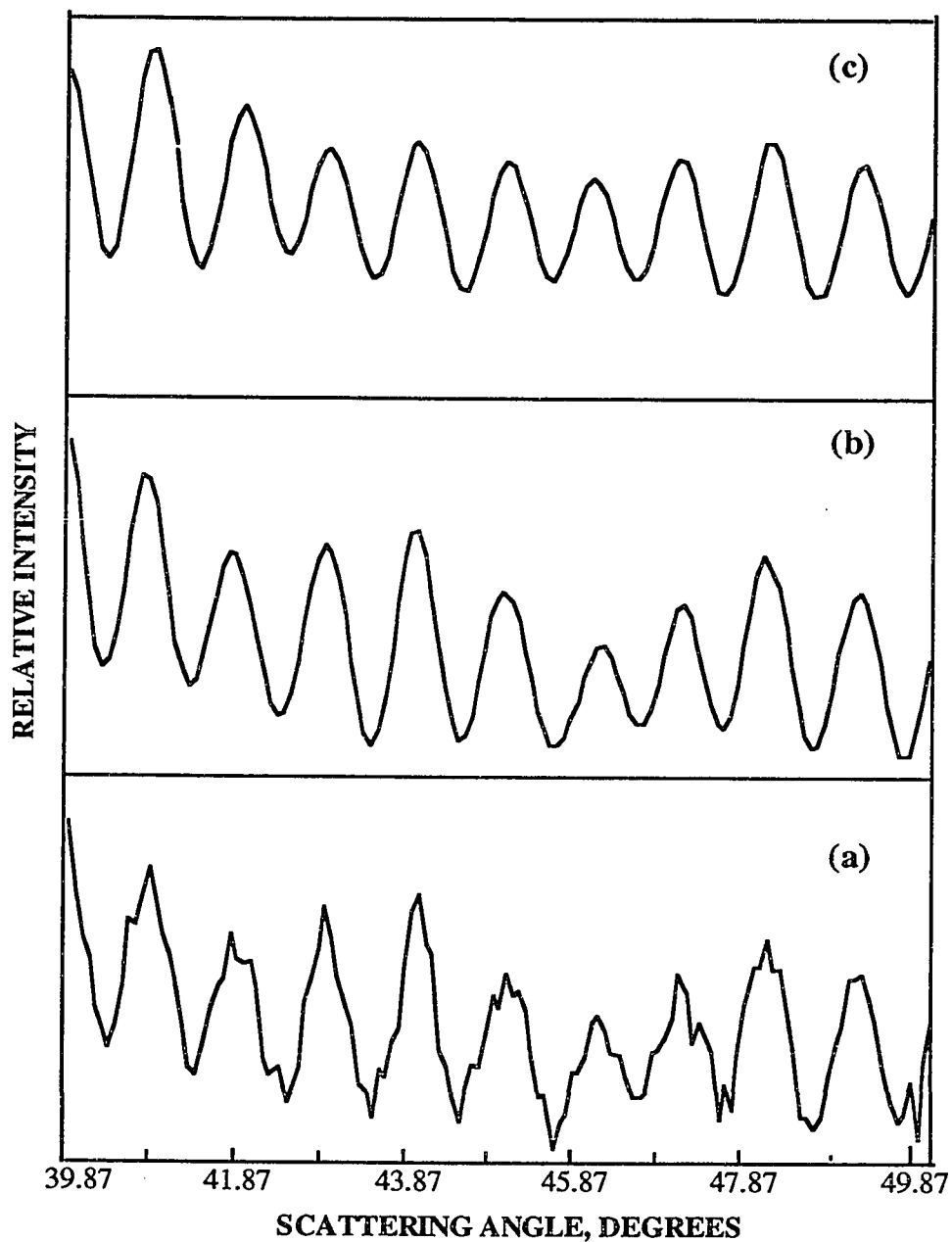


Figure 5.4 A comparison among (a) a "raw" phase function, (b) the FFT-smoothed phase function corresponding to (a), and (c) the "best fit" computed from the solution of Aden and Kerker (1951).

were first assumed to be constant, and the outer size, a , and the shell thickness, $(a-a_c)$, were allowed to change. The refractive indices of titanium ethoxide and TiO_2 , which are respectively 1.508 and 2.586, were assigned for N_c and N_s . These values were reported by Ingebretsen and Matijević (1984).

The assignment of the shell thickness ranged from zero to an upper limit estimated from the change of the DC voltage. As pointed out above, the DC voltage decreased during the reaction due to the consumption of TTE and the evaporation of ethanol. From the decrease of the DC voltage one may estimate approximately how much TiO_2 formed, and then determine the shell thickness based upon the outer particle radius estimated from the number of peaks. The shell thickness estimated from above method was not accurate since part of the ethanol produced could have remained in the particle. The actual DC decrease due to the mass loss by reaction should be larger. Thus, in the "best fit" the assignment for the upper limit of shell thickness was lower than the estimated value because of the ethanol remaining in particle.

At each set of a , $a-a_c$, N_s and N_c the light scattering intensities were calculated using the solution of Aden and Kerker. The outer radius and shell thickness were varied to minimize the rms difference between the measured and computed phase functions. Once the outer and core sizes corresponding to the minimum rms were found, the refractive indices of core and shell were varied around the values for pure components (TTE and TiO_2) to reduce the error. The entire procedure was repeated until a good match between the measured phase function and the theoretical solution was achieved. A unique and precise fit of the four parameters a , a_c , N_c and N_s cannot be made by above procedure, but the "best fit" values are within appropriate bounds, for, as shown later, other properties based upon the estimated core size and shell thickness were found to be within the expected range of values.

One may notice that the relative amplitudes of the peaks presented in Figs. 5.4b and 5.4c are not an exact match, but variations in the trial values of shell thickness make the agreement worse. For example, a variation of 10% in the shell thickness gives the results shown in Fig. 5.5. It is noted that a change of 10% in the shell thickness not only produces a significant change in the peak intensity, but it also causes a slight shift in the angular positions of the peaks.

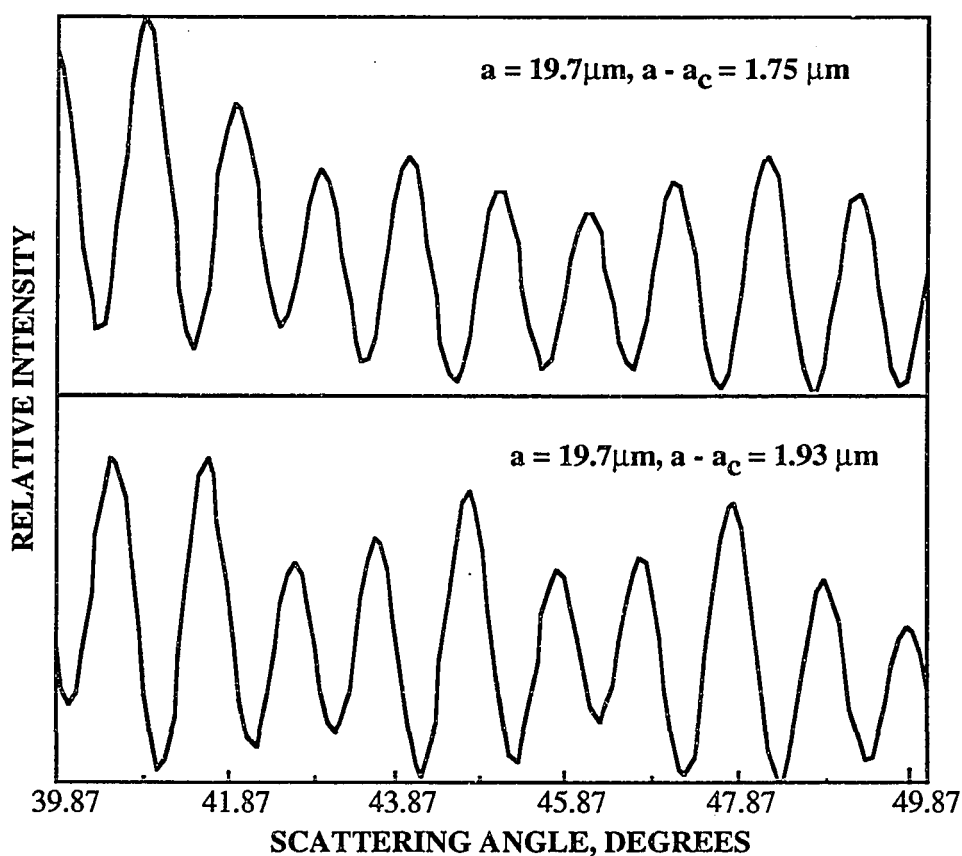


Figure 5.5 The effect on the phase function by changing the shell thickness by 10%.

The "best fit" takes a great deal of computer time, so the data reduction procedure was made only for one full representative sample, although numerous phase functions were measured for several particles. The estimated core and outer dimensions are presented in

Fig. 5.6 as a function of the reaction time. The shell thickness is shown in Fig. 5.7 together with the calculated bulk density of the particle. The outer radii determined from the number of peaks of the phase function for another particle are also plotted in Fig. 5.6 to show the reproducibility of particle size change during the reaction. Both sets of data show a rapid decrease in particle size for about 100 s. After that the particle size decreases almost linearly with time until about 1000 s. The size change vanishes after 1500 s. The size history is similar to that of the DC levitation voltage shown in Fig. 5.3.

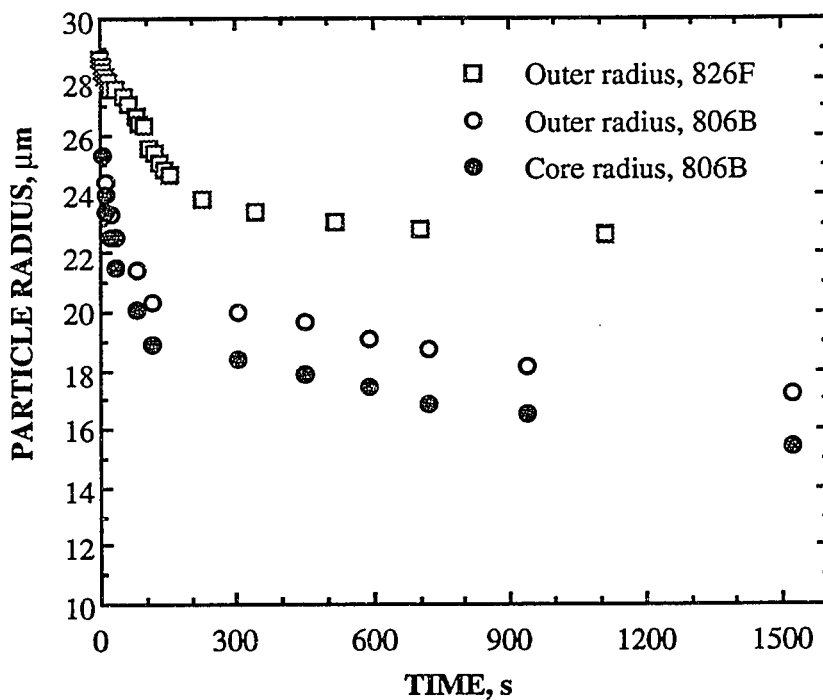


Figure 5.6 The outer radii of two different reacting droplets and the core radius of the smaller droplet determined by analysis of the measured phase function.

In order to examine the accuracy of the shell thickness estimation by the "best fit", the density of shell was determined and compared with values for TiO_2 in literature. The calculation of density requires knowledge of the particle charge, which can be determined

from the slope of the plot of a_t^2 versus (V_{dc}/a_t) . As discussed in section 4.6, a vertical force balance on a trapped particle gives the following relationship:

$$a_t^2 = -A\left(\frac{V_{dc}}{a_t}\right) + B, \quad (5.3)$$

with

$$A = \frac{3C_0q}{4\pi\rho_t z_0 g} \quad (5.4)$$

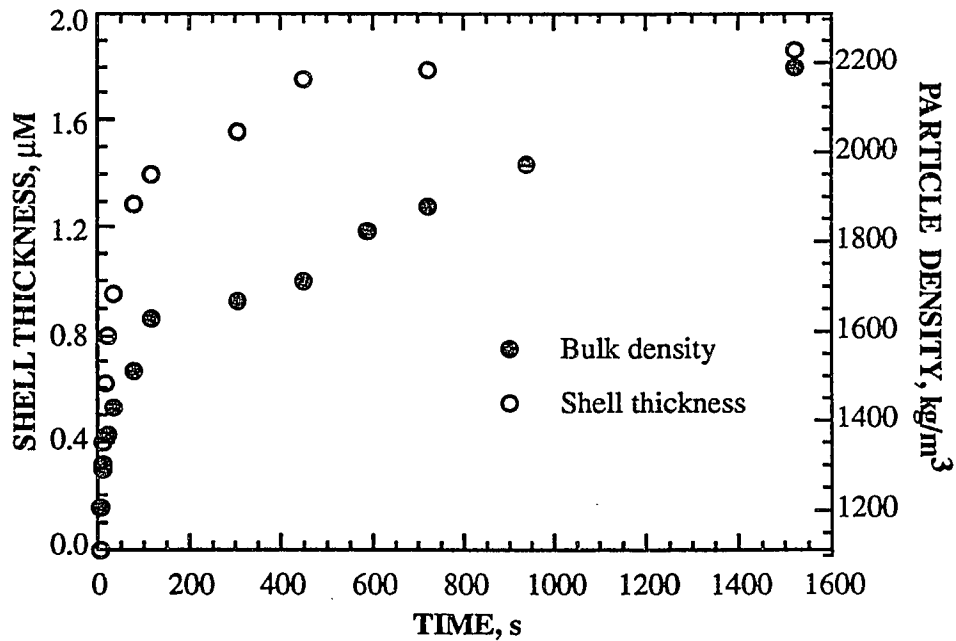


Figure 5.7 The shell thickness of TiO_2 estimated by the "best fit" of measured elastic scattering data, and the bulk density determined from the shell thickness and DC voltage.

and

$$B = \frac{9\mu U_\infty}{2g\rho_t}, \quad (5.5)$$

in which U_∞ is the velocity of convective flow possibly existing around the particle. Figure 5.8 is a plot of a_t^2 versus (V_{dc}/a_t) using the estimated droplet size and the measured DC balancing voltage. It is noted that the data points corresponding to the initial time of reaction (larger values of V_{dc}/a_t) almost fall on a line, and the data at later times are scattered. In the first stage of reaction, the variation of particle size is mainly due to the evaporation of the ethanol contained in the TTE droplet (about 10 wt%), and only a small amount of TiO_2 was formed, so the bulk particle density based upon the total particle mass and volume is almost constant. For constant density the plot of a_t^2 versus (V_{dc}/a_t) should fall on a straight line. At later times, the density of particle continuously increased and the linear relationship between a_t^2 and (V_{dc}/a_t) cannot be expected. For the bihyperboloidal electrodynamic balance, the half separation distance of DC electrodes, z_0 , is 6.5 mm and the DC balance constant was determined by Taflin (1988) to be $C_0 = 0.79$ (Note that the voltage of top DC electrode of bihyperboloidal EDB was not $-V_{dc}$, and the electrode was grounded during the measurements, so 13 mm should be assigned in the calculation of surface charge). The surface charge estimated from the slope of the line with the assumed density of TTE for the particle was 1.89×10^{-13} Coulomb, which is of the same order of magnitude as the values determined by Taflin and Davis (1989).

If no charge loss occurred during the reaction, the bulk density of the particle at arbitrary time, t , can be estimated from the DC levitation voltage by

$$\rho_t = -\frac{3C_0q}{4\pi gz_0} \frac{V_{dc}}{a_t^3} + \frac{9\mu U_\infty}{2ga_t^2}. \quad (5.6)$$

The above relationship is the re-arrangement of Eq. (5.3).

The charge loss of the particle can be attributed to numerous processes such as gas ionization, photo electron emission, etc. Under the present conditions the only mechanism

likely to cause charge loss is that the surface charge reaches the Rayleigh instability limit as the droplet evaporates. The Rayleigh instability limit is given by

$$q_{Re} = 64\pi^2\epsilon_0\sigma a_t^3, \quad (5.7)$$

in which ϵ_0 is the permittivity of free space and σ is the surface tension force of the droplet. For most organics the surface tension is about 30 mN/m. Using 30 mN/m for the surface tension of TTE, one may estimate the critical droplet radius corresponding to the Rayleigh instability limit. It is 1.94 μm based upon the measured charge $q = 1.89 \times 10^{-13}$ Coulomb using Eq. (5.7). This is far below the final size of the particle, so the Rayleigh instability limit is not reached in the reaction process. On the other hand, Taflin and Davis found that charge loss during evaporation or reaction is associated with droplet fissions, which is indicated by a discontinuity in the measured resonance spectra and by a rapid increase in the

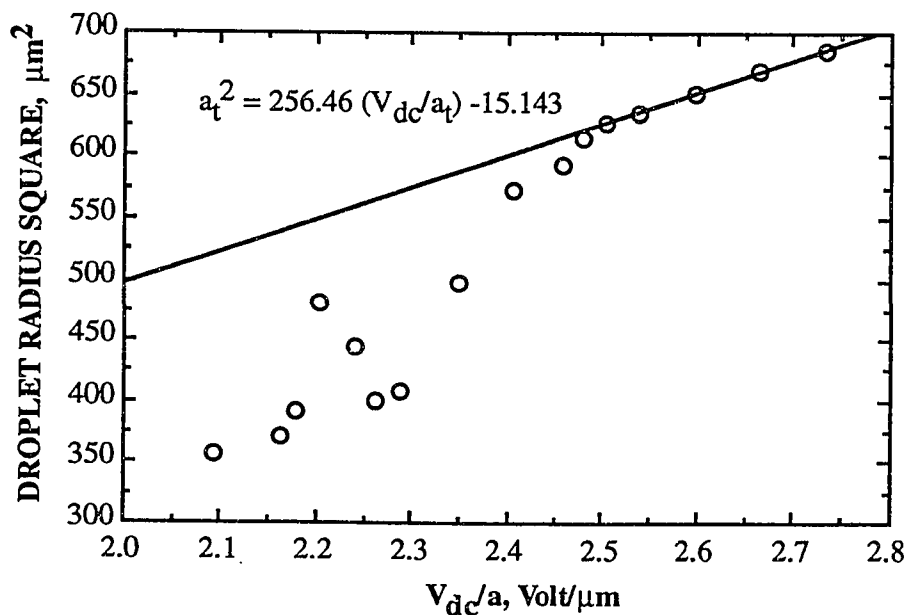


Figure 5.8 A plot of particle radius square, a_t^2 , versus V_{dc}/a_t used to determine the particle surface charge, q .

DC balancing voltage. No such effects can be identified from the MDRs and DC voltage data shown in Fig 5.2, so the particle charge was essentially constant during the reaction.

The estimated bulk density of the particle is plotted in Fig. 5.7 along with the shell thickness. Since the core size of the particle is known, the mass of the core, m_c , can be determined assuming it has the density of TTE ($\rho_{TTE} = 1088 \text{ kg/m}^3$). Then, the shell density can be estimated from the mass ($m_p - m_c$) and shell volume. The estimated shell densities are plotted in Fig. 5.9. They fluctuated around 4200 kg/m^3 . The fluctuation was caused by the inaccuracy of the shell thickness determined by the "best fit". The density is proportional to the reciprocal of the cubic of particle size, so a small error in the shell thickness can cause a large uncertainty in the shell density. The average shell density of 4200 kg/m^3 compares favorably with the reported values of 4260 kg/m^3 for the rutile form of TiO_2 , 3840 kg/m^3 for the anatase form, and 4170 kg/m^3 for the brookite form (Weast,

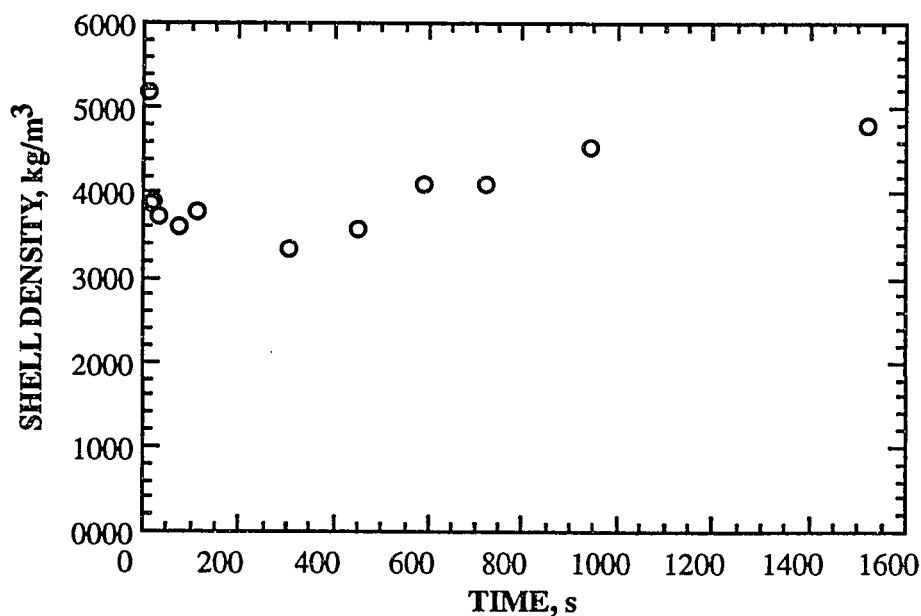


Figure 5.9 The shell density determined from the shell thickness, core and overall particle mass.

1984). This indicates that the shell thickness determined by the "best fit" is entirely reasonable.

Table 5.1 summarizes the results obtained at 1520 s for one experiment. The bulk density at large times averaged 2080 kg/m^3 . The refractive index estimated for the core falls between that of TTE and ethanol. This is reasonable since the droplet core should be mainly the unreacted TTE and small amount of ethanol. The refractive index of the shell is somewhat lower than the values for natural forms of TiO_2 .

Table 5.1 Estimated parameters for a layered TiO_2/TTE microsphere for large reaction times.

Substance	N , Refractive Index	Density, kg/m^3	Dimension, μm
Core	1.484	1088 (assumed)	$a_c = 15.4$
Shell	2.317	4200 (long times)	$a - a_c = 1.75$
Layered Sphere		2080 (bulk density)	$a = 17.2$
TTE	1.508	1088	
Ethanol	1.3611	789.3	
TiO_2 , Brookite	2.586	4170	
TiO_2 , Anatase	2.554	3840	
TiO_2 , Rutile	2.616	4260	

5.4 Raman Scattering

The same reaction was also monitored by the Raman spectra to identify the chemical components within the particle. The experimental apparatus for Raman scattering measurements were briefly described in Chapter 4. During the experiment, single TTE droplets were trapped in the double-ring electrodynamic balance and illuminated from below by an argon-ion laser beam operating at 488 nm. The Raman spectra in the initial stage of the reaction were not obtained since the particle size and other properties changed

significantly in the initial 100 s; a scan of the Raman shift over the region 250-4000 cm^{-1} required several minutes. On the other hand, the droplets experienced numerous resonances as the particle size decreased. Therefore, the Raman data are expected to be complicated by the resonance data and hard to interpret, assuming the gratings in the spectrometer can be rotated fast enough to collect data in the early stage of reaction.

Figure 5.10 presents a Raman spectrum obtained at 300 s during a TTE/ H_2O reaction experiment. Also shown in the figure are the Raman spectra for the pure components TTE and ethanol obtained by Payne and Berglund (1986), who used a UV source at 363.8 nm to avoid fluorescence (the intensity of Raman spectrum is much weaker than that of fluorescence, and it can mask the Raman signals).

Two large peaks at 632 cm^{-1} and 1166 cm^{-1} , shown in the spectra of TTE and the coated particle, correspond to the Ti-O and C-O-Ti vibrational modes of TTE. The product ethanol can be identified by the small peak around 890 cm^{-1} . The peak at 593 cm^{-1} , appearing in the spectrum of the coated particle but not in the data of Payne and Berglund, is associated with the rutile form of TiO_2 and not with ethanol and TTE.

A sequence of Raman data obtained at different reaction times is shown in Fig. 5.11. The spectrum at time 5 minutes is also presented in Fig. 5.10. There exist distinctive changes in the spectra, particularly in the region $\Delta\nu > 1000 \text{ cm}^{-1}$ where several well-defined characteristic peaks of TTE disappeared at long times ($t \gg 300 \text{ min.}$). For example, the peak at 1166 cm^{-1} cannot be identified in the spectrum obtained at 4262 min. Furthermore, the peak associated with TTE at 632 cm^{-1} becomes masked by a broad band in the region 250-1000 cm^{-1} , which is attributed to the amorphous layer of TiO_2 . Within the broad band, however, the peaks at 593 cm^{-1} and 431.7 cm^{-1} associated with rutile TiO_2 still remain identifiable. The disappearance of Raman lines associated with TTE in the spectrum obtained at 4262 min. suggests that the volatile core material, TTE and ethanol,

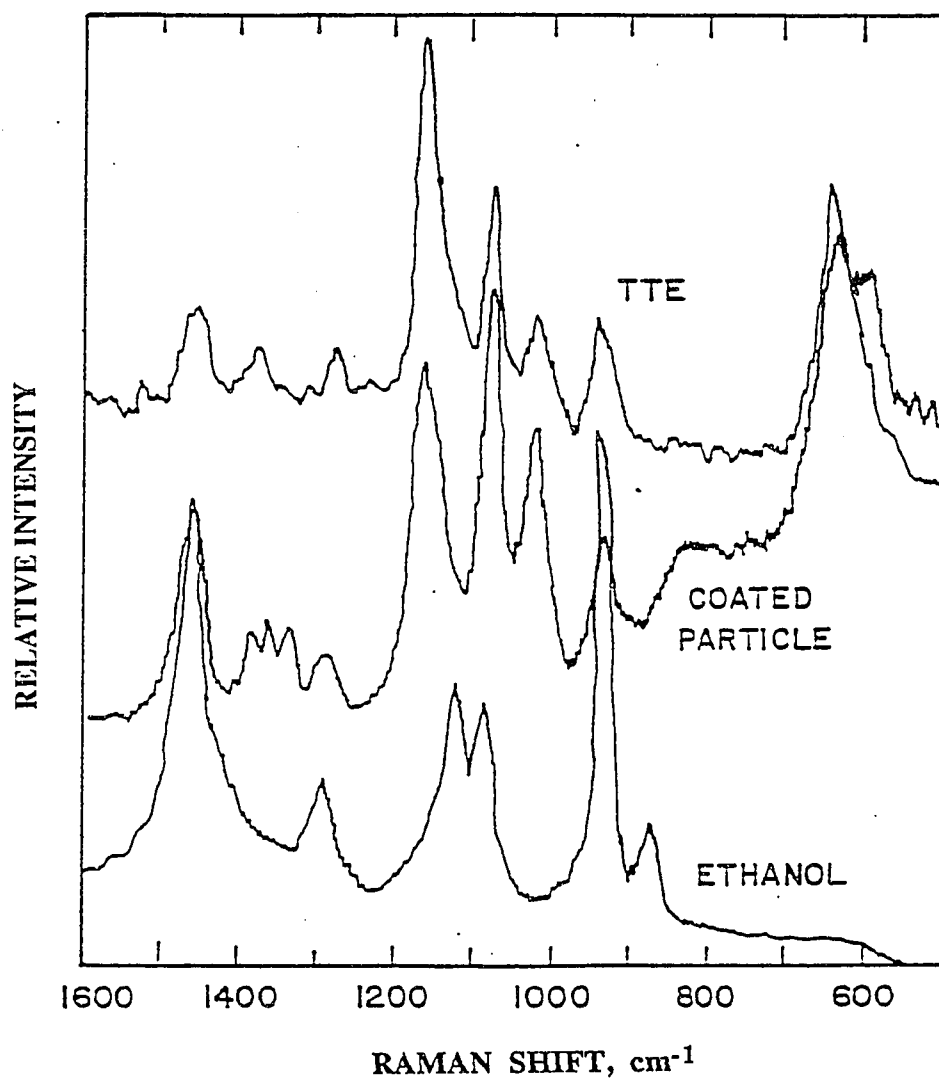


Figure 5.10 Comparison among the Raman spectrum obtained in this work for a reacting TTE microparticle (coated), and the spectra obtained by Payne and Berglund for bulk TTE and ethanol.

diffused through the shell and evaporated during the three days covered by the experiment. It is also possible that the TiO₂ shell masked the Raman emission from the core, but if that is so, a similar effect should have been seen earlier in the experiment, for there is rather little growth of the shell after 1000 s.

The Raman spectra at different reaction times in the wavenumber range 2500-4000 cm⁻¹ are presented in Fig. 5.12. The depletion of TTE and/or the masking of the TTE Raman data can also be seen clearly. The peaks near 2900 cm⁻¹ are associated with C-H bond in TTE. As reaction proceeded, less TTE remained in the particle and the amplitudes of peak gradually decreased. Only a trace of those peaks can be identified after three days. A broad hump in the region 3200-3500 cm⁻¹ developed in the spectra after the first few hours, and this appears to be due to the condensation and/or uptake of water by the microparticle from the air in the balance chamber.

The Raman apparatus was equipped with CO₂ laser heating facilities, so the reacted microparticle could be heated to examine the transitions of the crystal structure of the TiO₂ shell which can occur upon annealing. The CO₂ laser heating facilities were described by Allen (1992). The output power of the laser beam was controlled by a controller which varied the input voltages to the laser from 2.5 to 9.0 V. The output power changed linearly with the input voltage between 0 and 20 W. The infrared laser could be operated in either continuous or pulsed mode.

Figure 5.13 compares the Raman spectra of a coated microsphere under the experiment conditions of (a) no heating, (b) heating for a short time (360 s), and (c) an additional heating for a total time of 542 s. The heating process was made with the input voltage 4.2 V for the CO₂ laser corresponding to the power about 5 W. Figure 5.13a is the spectrum at 4262 s, which is also presented in Figs. 5.11 and 5.12. Except for the removal of some water, there is little effect of heating for the shorter period of heating, but a significant change occurred upon additional heating. First, a broad and intense signal for

$\Delta\nu > 1000 \text{ cm}^{-1}$ was seen in Fig. 5.13c, which can be attributed to fluorescence. The problem of fluorescence was also encountered in the study of Payne and Berglund. Rassat (1994) observed the fluorescence for single microparticles of CaO crystal during the IR heating. He suggested that the fluorescence may be associated with the structural defects in the crystalline product.

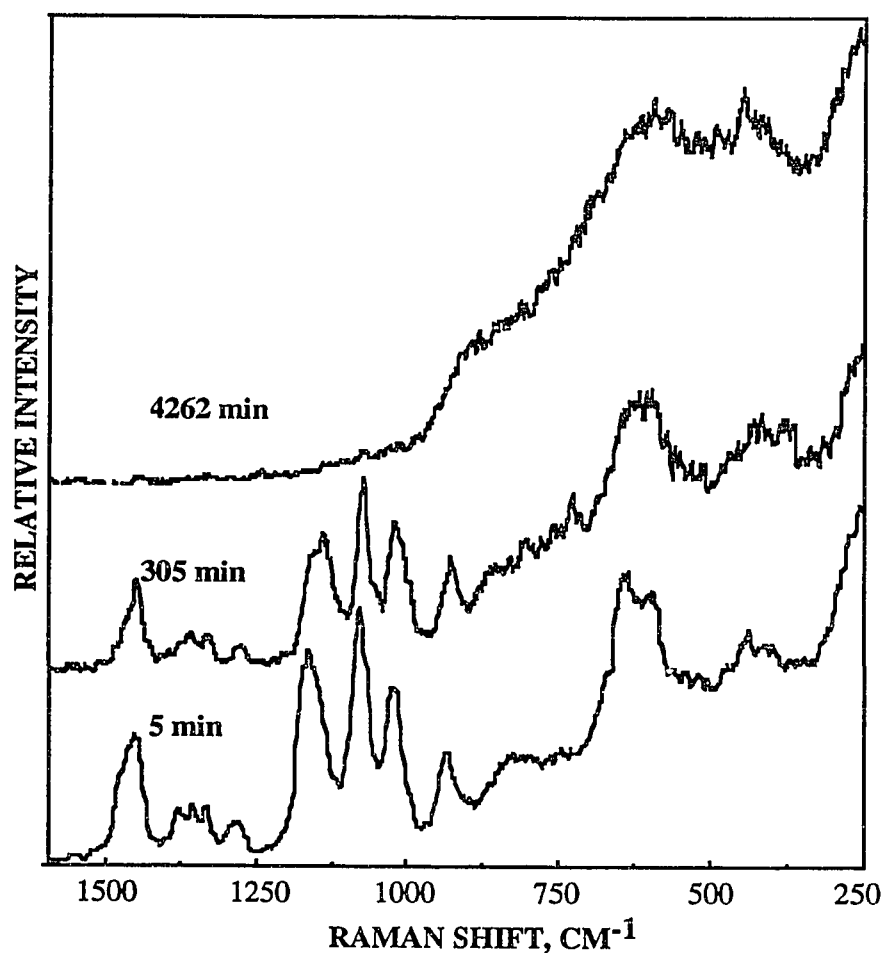


Figure 5.11 Raman spectra obtained at different times for an reacting TTE droplet in the wavenumber range 250-1000 cm^{-1} .

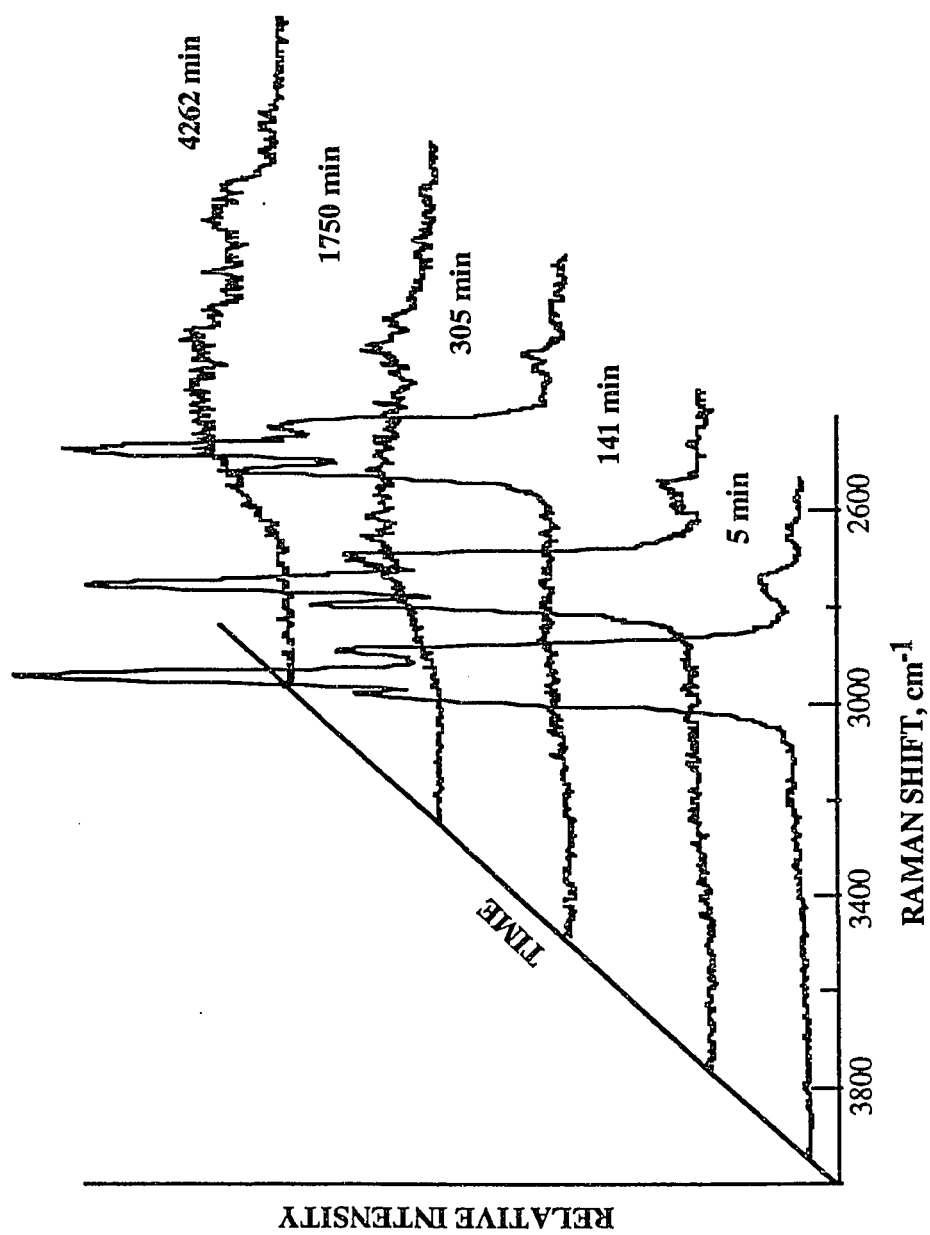


Figure 5.12 A series of Raman spectra obtained for an reacting TTE droplet in the wavenumber range 2500-4000 cm^{-1} .

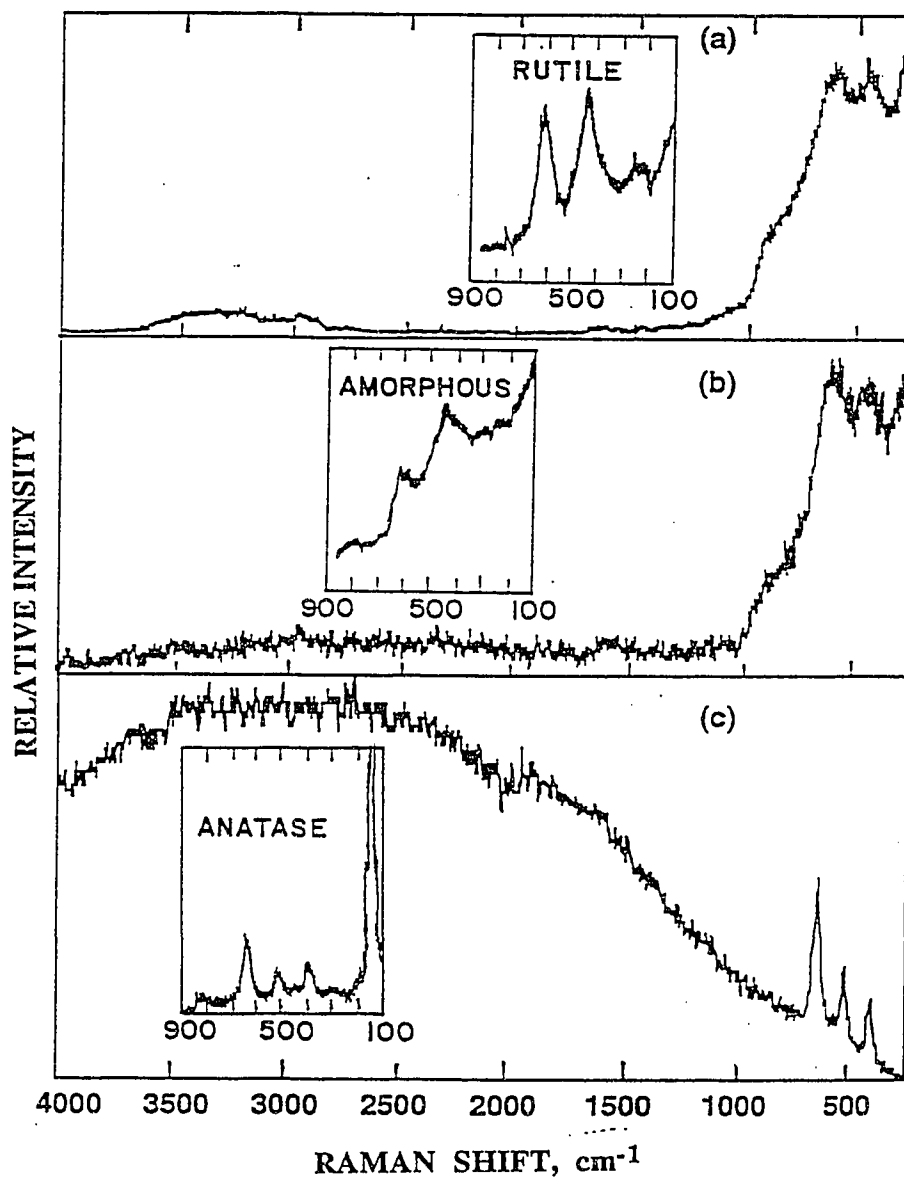


Figure 5.13 Raman spectra obtained during CO_2 laser heating for a reacting TTE microparticle compared with the results of She and Hsu for thin films of TiO_2 on a silicon substrate.

Besides the broad band in Fig. 5.13(c), there are well-defined peaks at 394, 516 and 633 cm^{-1} which can be observed after long-time heating. The three peaks are characteristic peaks for the anatase TiO_2 crystal. The Raman shifts agree with the values of 398, 515 and 640 cm^{-1} found by Balachandran and Eror (1982) for the anatase form of TiO_2 . They formed TiO_2 powder via slow evaporation of tetraisopropyl titanate, and found that the anatase form of TiO_2 commonly occurred at the lower temperature and the irreversible bulk transition from anatase form to rutile form occurred near 1023K.

The structural properties of amorphous titania films were also studied by She and Hsu (1988) using Raman spectroscopy. They obtained Raman spectra for 500 nm thick TiO_2 films having anatase, rutile and amorphous structures. The films were deposited on a silicon substrate. They found that an amorphous film with weak rutile structure recrystallizes into the anatase form above 325°C; recrystallization was found to be rapid above 400°C.

Traces of spectra of She and Hus are shown as inserts in Figs. 5.13a-c. The Raman data of the present study agrees well with their results. They found that the amorphous TiO_2 thin film almost transformed to the anatase form at temperature about 623 K. Based upon the study of She and Hus and of Balachandran and Eror, the temperature reached during the longer heating time was greater than 623 K, but less than 1023 K, for no characteristic Raman peaks associated with the rutile form TiO_2 were observed in the spectra. High power laser heating induced strong instability of the particle, so the study of the crystalline transition at much higher temperature could not be achieved in this work.

During the longer heating experiment the DC levitation voltage changed from 16.7 V to 9.8 V. The decrease in DC voltage may be due to the evaporation of water and, most likely, the evaporation of unreacted TTE from the microparticle during the heating.

5.5 Conclusion

The hydrolysis reaction of single TTE droplet was studied by means of elastic scattering and Raman spectra. The elastic scattering data showed that the reaction rate was significantly reduced after approximately 100s, and the reaction stopped after a thin shell of TiO_2 had formed. In order to determine the shell thickness and other properties, a "best fit" was made between the measured phase functions and the solution of Aden and Kerker. The determined shell density, refractive indices of shell and core are in agreement with values in the literature.

The TTE/water reaction at later times was also monitored by Raman measurements. Using electromagnetic heating, the crystalline transitions of the product TiO_2 were investigated. The Raman data for the coated microspheres agree with the bulk Raman measurements of TTE and ethanol made by Payne and Berlund. The TiO_2 formed at room temperature shows a mixture crystalline of amorphous and rutile forms. After long time heating, the amorphous/rutile crystalline forms transformed to the anatase structure which agrees with the results of She and Hsu for thin films of TiO_2 .

CHAPTER 6
MEASUREMENTS OF THE THERMOPHORETIC FORCE:
MICROSPHERES IN AIR

Measurements of the thermophoretic force (TF) were carried out for dioctyl phthalate (DOP) droplets, metal nickel, polystyrene latex (PSL) and silica glass spheres in air, helium and carbon dioxide, respectively. The results for microparticles in air are presented in this chapter. In the subsequent chapter the data for helium and carbon dioxide will be shown, and the effects on TF of the thermal properties of gas and particle, as well as other effects, will be discussed.

6.1 Experimental Materials

Theories of thermophoresis show that TF depends on the thermal conductivities of both particle (k_p) and gas (k_g) in the slip flow and the transition regimes, and on k_g only in the free-molecule regime. In addition to the study of the dependence of TF on Knudsen number in this research, attempts were also made to examine the effects of the thermal conductivities of gas and particle on the force. Therefore, materials with very different thermal conductivities were examined. Four materials were selected for the TF measurements. DOP was supplied by the Aldrich Chemical Company with a purity of 99.5%. DOP has an extremely low vapor pressure, which is confirmed by measurements of phase functions shown in section 6.3. It is critical to keep the size of the droplet constant while the force dependence on the Knudsen number is examined. Glass, PSL and nickel microparticles were supplied by the Duke Scientific Co.(Palo Alto, CA).

The physical properties of the four materials are summarized in Table 6.1. The thermal conductivities of DOP and PSL are very close, which are 0.125 W/m K and 0.122 W/m K respectively at $T = 298$ K. Glass and nickel spheres have thermal conductivities

0.8 W/m K and 90 W/m K, respectively, representing intermediate and very high k_p . In prior measurements, sodium chloride with $k_p = 6.0$ W/m K was used, but sodium chloride is a crystal whose shape is cubic or rectangular, and its density is not known accurately. Thus, nickel spheres with k_p nearly 15 times of that sodium chloride is better choice.

Table 6.1 Physical properties of the four materials: DOP, PSL, nickel and glass, together with three gases: helium, air and CO₂ at T = 298 K and 1 atmosphere pressure.

Materials	DOP	PSL	Nickel	Glass	CO ₂	Air	Helium
k (W/m s ⁻¹)	0.125	0.122	90.9	0.80	0.0105	0.0188	0.151
ρ (kg/m ³)	981	1105	8900	2450	1.79	1.17	0.163
Prandtl number					0.766	0.707	0.68
$\mu \times 10^7$, N s/m ²					148	184	198

(for air and CO₂, $k_{g, \text{tran}}$ are calculated from the viscosity μ using Eq. (3.9)).

Air, helium and carbon dioxide were chosen for the gases, and some of their relevant physical properties are listed in Table 6.1 for 298 K and atmospheric pressure. Helium is a monatomic gas having a relatively high thermal conductivity. Air is mainly a mixture of diatomic gases and the thermal conductivity is about one order of magnitude lower than that of helium. Carbon dioxide is a polyatomic gas with a linear molecular structure. The thermal conductivity of CO₂ is slightly lower than that of air. Combinations of the four types of particle with the three gases cover the thermal conductivity ratio range of $1.0 \times 10^{-4} \leq k_{g, \text{tran}}/k_p \leq 1.24$.

6.2 Experiments

Numerous measurements of the thermophoretic force were made in this research. The experimental conditions for air experiments are listed in Table 6.2. The experimental procedure was described in Chapter 4.

Table 6.2 Experimental conditions for particle/air thermophoretic force measurements.

Particle	Run Number	Radius μm	Charge Polarity	∇T_{∞} K/m
DOP	0409b	17.4	Positive	2710
	0501a	10.9	Positive	2560
	0510d	23.9	Positive	2140
	0510e	14.8	Positive	2150
	0518h	15.3	Positive	2100
	1011i	14.5	Negative	2730
	1025a	12.0	Negative	2730
PSL	0905a	10.9	Negative	2740
	0905b	10.9	Negative	2740
Glass	0927a	11.5	Negative	2740
	0927b	11.5	Negative	2740
Nickel	0726a	5.22	Negative	2830
	0728d	5.24	Negative	2800

Accurately sizing of the particle is critical since it is required in the calculation of the Knudsen number, $Kn = \lambda/a$, and in comparisons between theory and experiment. Here, λ is the mean free path of gas and a is the droplet radius. In this study, phase functions were used to determine the size of DOP, glass and PSL particles. The sizes of nickel spheres were determined by marginal stability measurements explained in Chapter 4. Figure 6.1

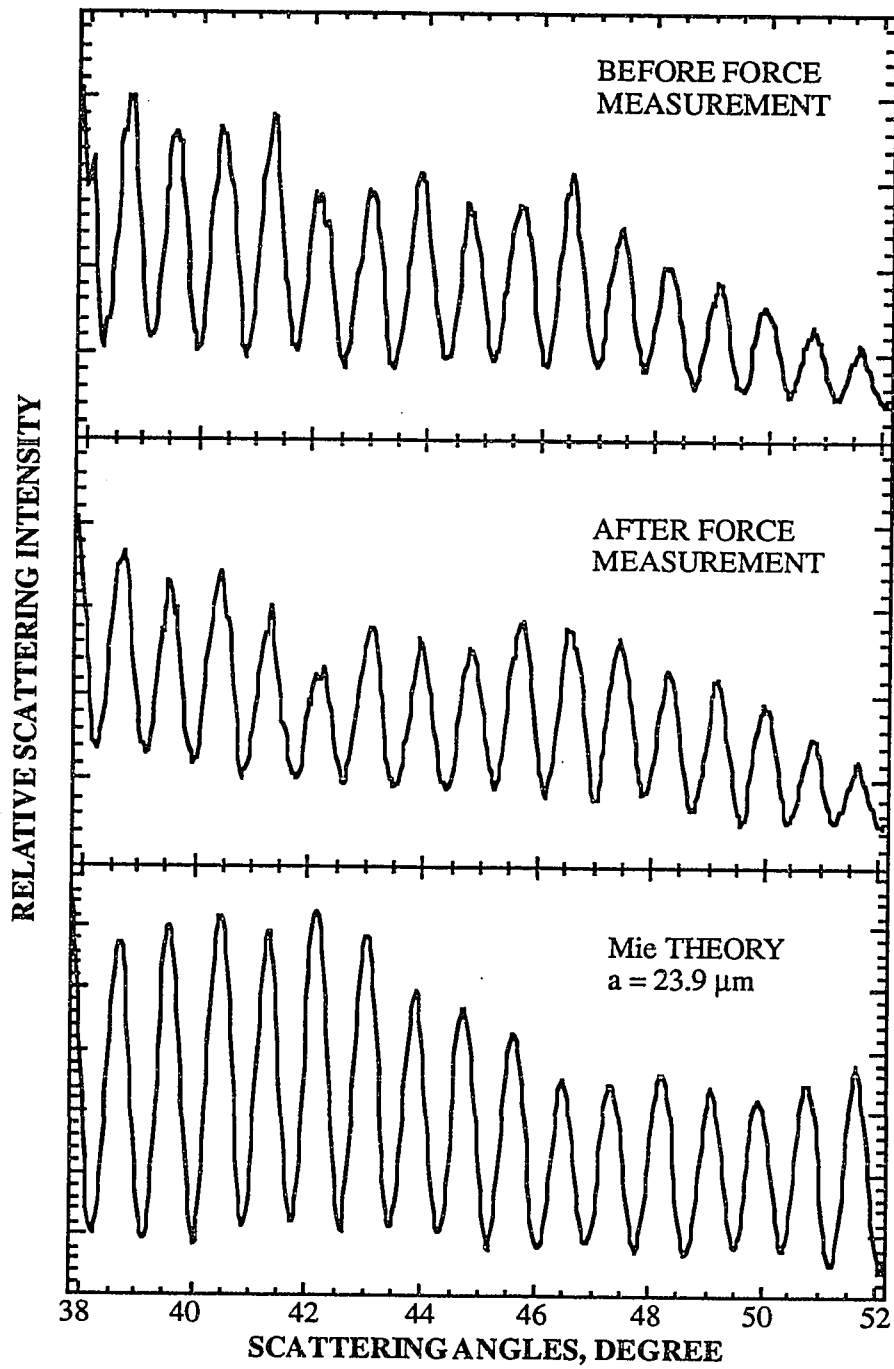


Figure 6.1 Experimental and theoretical phase functions for a DOP droplet with $a = 23.9 \mu\text{m}$.

shows the phase functions recorded before and after the force measurements for a DOP droplet. Also shown in the figure are results based on Mie theory for $a = 23.85 \mu\text{m}$ and $m = 1.486$ for DOP.

Note that the number of the peaks for the phase functions recorded before and after TF measurements are almost equal, which indicates that size variation of the DOP droplet through the experiment was negligible. The phase function for the solid PSL sphere is shown in Fig. 6.2. The data are noisy compared with those for the DOP droplet. The phase function was found to be an effective method to examine the shape of the particle. If the trapped solid particle is not spherical, highly irregular phase functions result, and they cannot be interpreted by means of Mie theory.

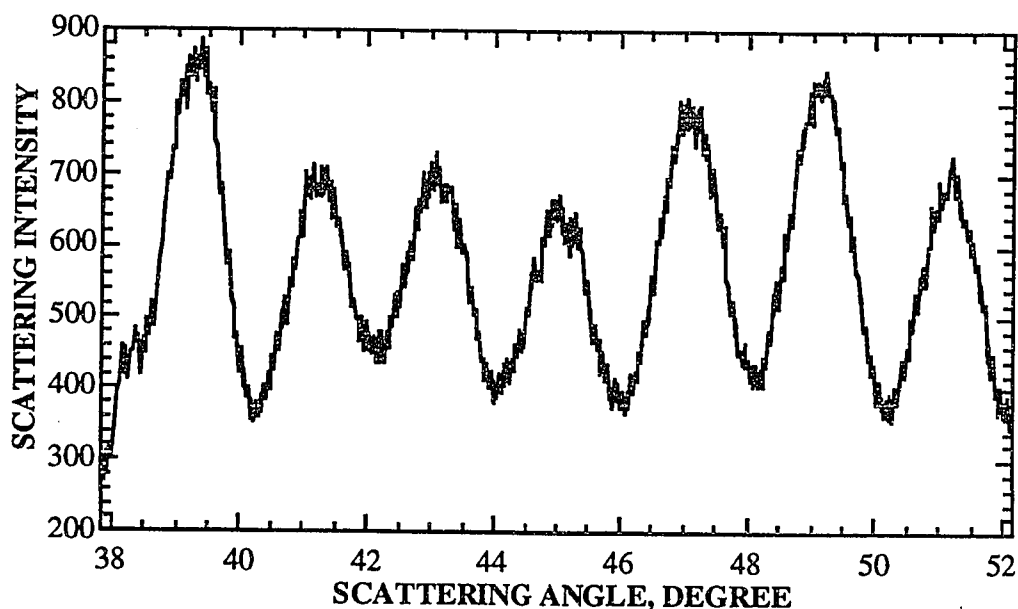


Figure 6.2 A measured phase function for a PSL sphere with $a = 10.56 \mu\text{m}$.

As mentioned in Chapter 4, the ratio of the thermophoretic force to the particle weight was obtained from the DC balancing voltage measurements. The governing equation can be written as

$$\frac{F_{th}}{mg} = \frac{V_{dc}}{V_{dc,0}} - 1 = \frac{\Delta V_{dc}}{V_{dc,0}}, \quad (6.1)$$

in which $V_{dc,0}$ is the voltage required to balance the particle weight, and V_{dc} is the measured voltage for a particle acted upon by the thermophoretic force. Representative raw data, plotted as F_{th}/mg versus Kn , that is, versus the reciprocal of the system pressure, are shown in Fig. 6.3 for five experiments using positively-charged DOP droplets of different sizes in air. The particle sizes and temperature gradients are listed in Table 6.2. The mean temperature of the chamber center was 298 ± 3 K for all the experiments.

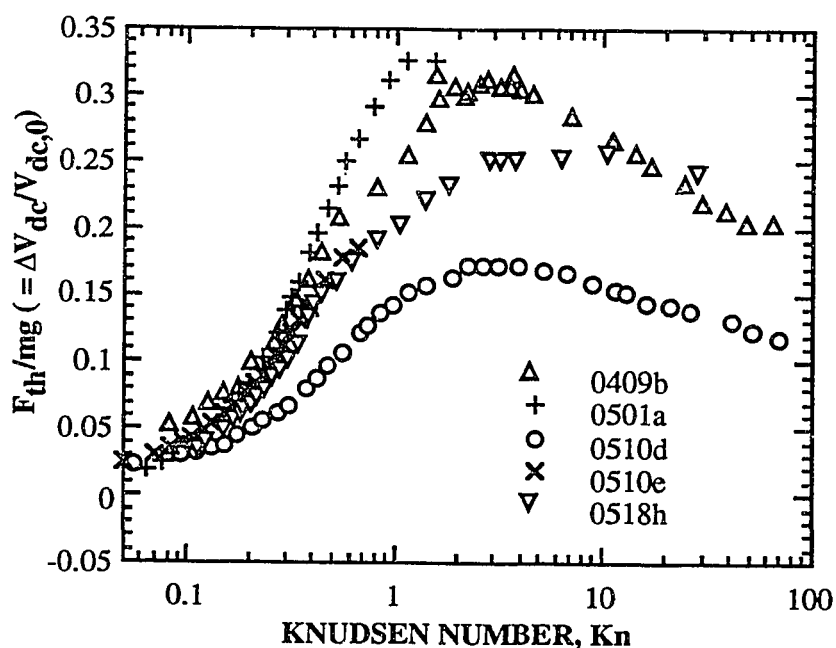


Figure 6.3 Ratio of the thermophoretic force to the particle weight for five DOP droplets levitated in air at 298 ± 3 K.

It can be seen that in air the maximum force reached is about one-third of the particle weight shown in Fig. 6.3. There appears to be a maximum in the thermophoretic force at

Kn~3. The maximum of the force in the transition regime is not expected from theoretical considerations, for the force should approach to the free-molecule limit as Kn becomes large. As shown later, the decrease of the thermophoretic force in the near free-molecule and free-molecule regimes is mainly due to temperature jumps at the heated and cooled surfaces, and to wall effects of the chamber.

6.3 Results and Discussion

Based upon various theoretical formula, the ratio of $F_{th}/a^2\sqrt{T_\infty}$ is expected to be a unique function of the Knudsen number for a specific gas/particle system. This is shown in Fig. 6.4, which is a replot of the same data from Fig. 6.3 in the form $F_{th}/a^2\sqrt{T_\infty}$. It can be seen that the normalization of the force substantially reduces the scatter in the data to a unique function of the Knudsen number.

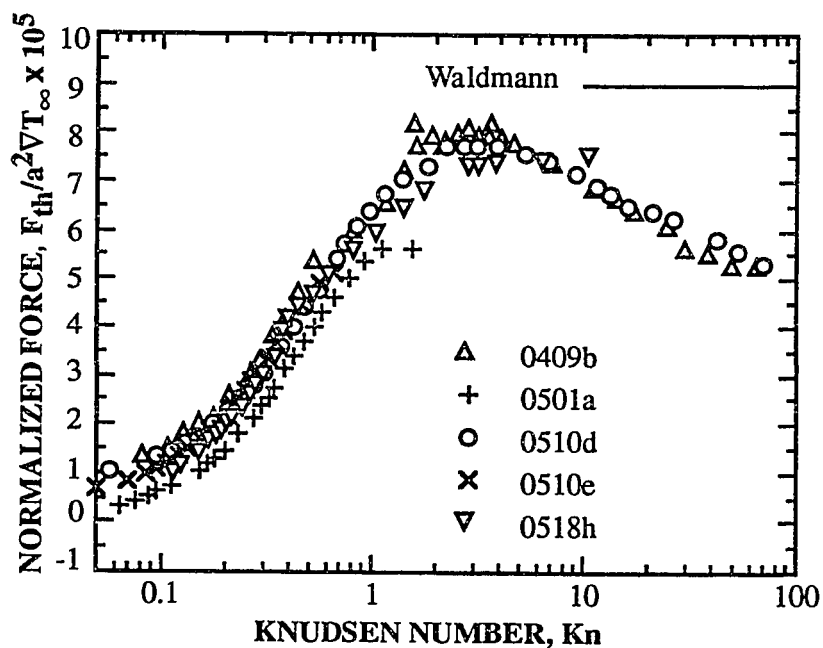


Figure 6.4 Data for the thermophoretic force (shown in Fig. 6.3) normalized by $a^2\sqrt{T_\infty}$ compared with Waldmann's theory for the free-molecule regime.

Also shown in the figure is the free molecule prediction of Waldmann (1959) given by Eq. (3.21). The asymptotic value determined from Eq. (3.21) is $F_{th}/a^2\nabla T_\infty = 9.028 \times 10^{-5}$ N/m K for air at 298 K, which is about 10% larger than the observed maximum.

It is not necessary to use all of the data in Fig. 6.4 in the following comparisons, so experiments 0501a and 0510d were selected as representative of the DOP/air data. They are replotted in Fig. 6.5 together with the data of Schmitt (1959) for silicone oil in argon and the data of Schadt and Cadle (1961) for tricresylphosphate (TCP) in air. Both sets of data were obtained with the modified Millikan apparatus reviewed in Chapter 3. The thermal conductivity ratio k_g/k_p was 0.135 and 0.099 for the experiments of Schmitt (1959) and Schadt and Cadle (1961), respectively, which are of the same order $O(10^{-1})$ as that for DOP droplets in air (0.158). Based upon theoretical expressions in the slip flow and transition regimes (Brock, 1962; 1967b), k_g/k_p has only a small effect on the thermophoretic force. Note that the data of Schmitt overlap with our data for experiment 0510a, but the few data points of Schadt and Cadle (1961) fall below most of the other data in Fig. 6.5.

6.3.1 Temperature Jump at the Thermal Plate Surfaces

The temperature jump at the surfaces of the cooled and heated plates results in the apparent decrease in the thermophoretic force shown in Figs. 6.3 to 6.5. In the data reduction the temperature gradients were calculated from the temperature difference between the cold and hot fluids, $(T_h - T_c)$, and the separation distance between the two plates, $2H$. Here, $2H = 26.6$ mm. As the mean free path of the gas approaches the separation distance of the plates, the temperature gradient at the center of the chamber deviates from the estimated value, for a temperature jump occurs near the plate surfaces. A second Knudsen number, $Kn_2 = \lambda/H$, should be taken into account in the data analysis as pointed out by Bakanov (1995). The first Knudsen number Kn is defined based upon the

particle radius, and the second is based upon the separation distance H . The radii of the DOP droplets were of the order of $10\ \mu\text{m}$, and for $H = 13.3\ \text{mm}$, $\text{Kn}_2 = a\text{Kn}/H \sim 10^{-3}\text{Kn}$, so the jump effects or slip effects are insignificant when $\text{Kn} < 1$ and $\text{Kn}_2 < 10^{-3}$, but for $\text{Kn} > 10$ the gas between the plates falls in the slip flow regime based on the plate spacing. As the mean free path increases further, molecular collisions with the walls of the chamber become significant, and it can be expected that the temperature gradient established with the heated and cooled plates becomes irrelevant at the lowest pressures studied. All of the experimental data show this effect.

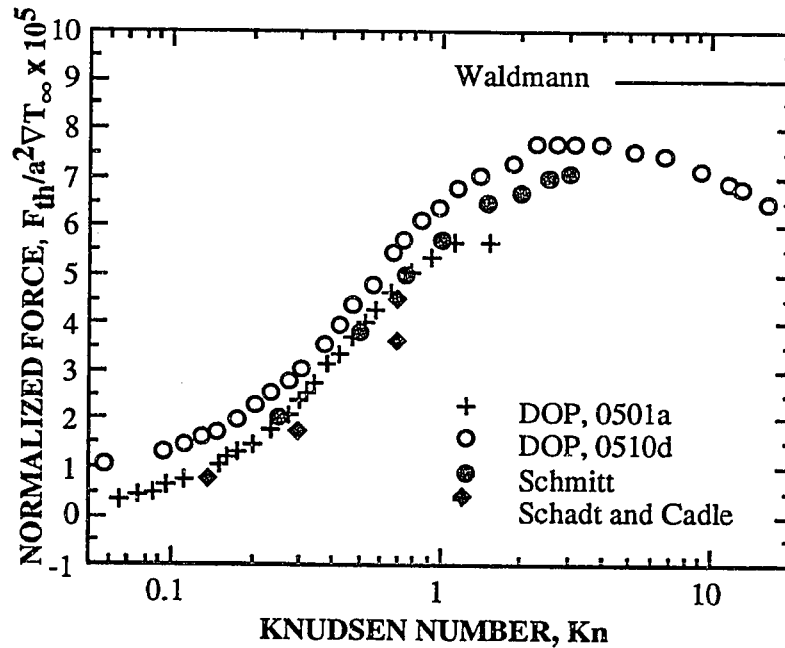


Figure 6.5 Comparison among the data for DOP in air, the data of Schmitt (1959) for silicone oil in argon, the data of Schadt and Cadle (1961) for tricresylphosphate in air, and the theory of Waldmann (1950) for the free-molecule regime.

Thus, as the chamber pressure decreases, two noncontinuum phenomena are involved in the data interpretation. One is related to the particle surface, and the other to the copper plate surfaces. The discontinuity boundary condition at the particle surface has

already been taken into account in the theoretical derivations for thermophoresis. Heat transfer between two parallel plates in the transition regime has been studied by a number of investigators. The results were reviewed by Devienne (1965) and Spring (1971).

Devienne proposed the following expression to correct the temperature gradient in the transition regime based upon the continuum value ∇T_∞ :

$$\nabla T_{Kn} = \frac{\nabla T_\infty}{(1 + 2C_t Kn_2)} = \frac{\nabla T_\infty}{(1 + 2C_t a Kn / H)}, \quad (6.2)$$

in which C_t is the temperature jump coefficient. Equation (6.2) indicates that in the transition regime the "effective" temperature gradient is lower than the continuum value, and one may regard the "effective" separation distance of plates as $(H + 2C_t Kn_2)$ instead of H , shown in Fig. 6.6.

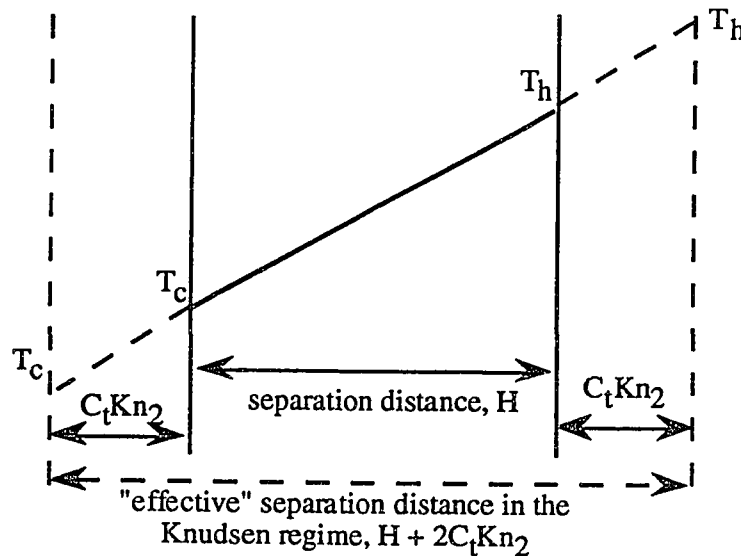


Figure 6.6 The schematics diagram showing the "effective" separation distance of two thermal plates in the transition regime.

The coefficient C_t , as discussed in Chapter 3, is related to the thermal accommodation coefficient, α_t . The appropriate relationship between them can be obtained from the solution of the Boltzmann equation. Based upon the linearized equation, Loyalka (1991) obtained the following relationship for the rigid-sphere gas molecules:

$$C_t = \frac{5\pi^{1/2}}{8} \frac{2 - \alpha_t}{\alpha_t} [(1 - \alpha_t) + 0.1134\alpha_t]. \quad (6.3)$$

Other expressions have been proposed based upon the BGK equations. Rigorous treatments are not available for polyatomic gas molecules with realistic interaction potentials, but Kennard (1938) proposed a relationship for polyatomic gases [see Eq. (3.14)]. For air at 298 K, Prandtl number, $Pr = 0.707$ and the ratio of specific heats γ (C_p/C_v) = 1.4, Eq. (3.14) can be written as:

$$C_t = \frac{2\gamma}{\gamma + 1} \frac{1}{Pr} \frac{2 - \alpha_t}{\alpha_t} = 1.65 \frac{2 - \alpha_t}{\alpha_t}. \quad (6.4)$$

Equation (6.4) was used to calculate the jump coefficient for air at the copper surfaces.

The theory and experimental results related to thermal accommodation coefficients, α_t , have been reviewed by Saxena and Joshi (1981). They tabulated the measurements of α_t for common gases on a number of surfaces, including the systems copper/air, copper/helium and copper/carbon dioxide. Springer (1971) pointed out that α_t depends on the surface type and its temperature as well as on the composition of any adsorbed gas. For air in contact with bronze, cast iron and aluminum surfaces he reported $\alpha_t \sim 0.99-0.97$, but $\alpha_t \sim 0.5$ for the nitrogen/platinum system. The sensitivity of α_t to the cleanness of the surface was addressed by Saxena and Joshi, stating "experimental α_t data on gas covered solid surfaces with controlled and reproducible surface conditions is important from an

engineering view point.... Data for adequately characterized solid surfaces are almost nonexistent and any experimental attempt to generate such data will be especially rewarding." For air molecules contacting a copper surface cleaned with an acid bath and dried with a heat gun, they reported $\alpha_t = 0.698$ at 243 K and pressure range 0.0002 to 0.004 mmHg corresponding to $2 \leq Kn_2 \leq 22$.

Assuming that the temperature gradients can be corrected according to Eq. (6.2), and the accommodation coefficient is allowed to vary, the normalized thermophoretic force can be adjusted upward. Figure 6.7 presents the adjusted TF for experiment 0501d with $\alpha_t = 0.25, 0.50$ and 1.0 . For $Kn < 3$, the correction is negligible for all of these accommodation coefficients, but it becomes significant for $Kn > 10$. The corrections based upon $\alpha_t = 0.25$ seems to overcorrect the data, and the adjustments corresponding to $\alpha_t = 0.5$ undercorrect the experimental results. A trial and error procedure indicated that the appropriate value of thermal accommodation coefficient was one-third. If we use this value to adjust the temperature gradient in the transition regime based upon the continuum value, the TF data approach a constant asymptotic value for $5 < Kn < 20$, but the force decreases for $Kn > 20$. Clearly, the wall effects of chamber, in addition to the slip effects, influence the thermophoretic force as the mean free path becomes large. In some measurements the thermophoretic forces were obtained at higher Kn number ($Kn > 200$), and the forces were found to be vanishingly small. This should be caused by the collisions of the gas molecules with the side walls of the chamber. The two "edge effects" can only be reduced by increasing the diameter of the heater and cooler and the separation distance between the thermal plates.

The value $\alpha_t = 1/3$ based upon the adjustments of TF is substantially lower than the previously reported accommodation coefficients for air and copper, but the values reported by Saxena and Joshi are for "clean" surfaces prepared by acid treatment. It is not clear what causes the difference in α_t . It is possible that the edge effects of the chamber

contribute to the relatively low α_t extracted from the adjustments of C_t , or the highly-oxidized and "dirty" copper surface in our experiments has an accommodation coefficient lower than a clean surface. Since the adjustments in the near-free molecule regime have little effect on the transition regime data, the primary findings of this research are not affected by the choice of α_t for the copper surface.

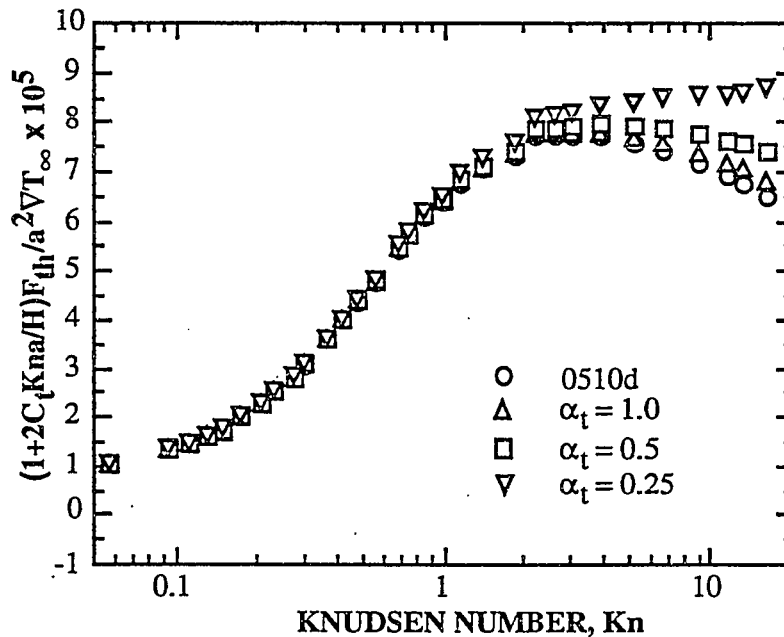


Figure 6.7 Experimental data for Run 0510d replotted as $(1+2C_tKn_2)F_{th}/a^2\nabla T_\infty$ versus Kn for three values of the thermal accommodation coefficient for the air/copper system.

6.3.2 Comparison among experiments and theory.

In the following comparison, the adjusted and normalized force, $(1+2C_tKn_2)F_{th}/(a^2\nabla T_\infty)$, based upon $\alpha_t = 1/3$ and Eqs. (6.2) and (6.4), will be used. Comparison is restricted to $Kn < 20$, for there is clearly an effect of the chamber wall on the data for large Kn .

The adjusted, and normalized, forces for the experiments 0501a are compared with the equations of Brock (1962), Dwyer (1967) and Phillips (1975) in Fig. 6.8. The thermal slip coefficient, C_{ts} , included in the equation of Brock (1962), was determined from the

relationship of Ivchenko and Yalamov (1971). The formula was shown in Eq. (3.10) and recommended by Talbot *et al.* (1980) to estimate C_{ts} . The accommodation coefficient for the particle/air system, α_t and α_m , were taken to be unity, which gives $C_{ts} = 1.17$, $C_t = 1.65$ and $C_m = 1.0$. Brock's solution is in reasonable agreement with the data in the transition regime ($0.1 < Kn < 1$), but it does not approach Waldmann's result for large Kn . The results of Phillips do not agree with the measurements for $Kn < 1.0$. The moment theory of Dwyer fails to predict the force in the slip flow regime and in the near free molecule regime. It is well known that the 13-moment method of Grad is inaccurate in the free-molecule regime, but the results of Dwyer even do not agree with the experimental results for low Kn .

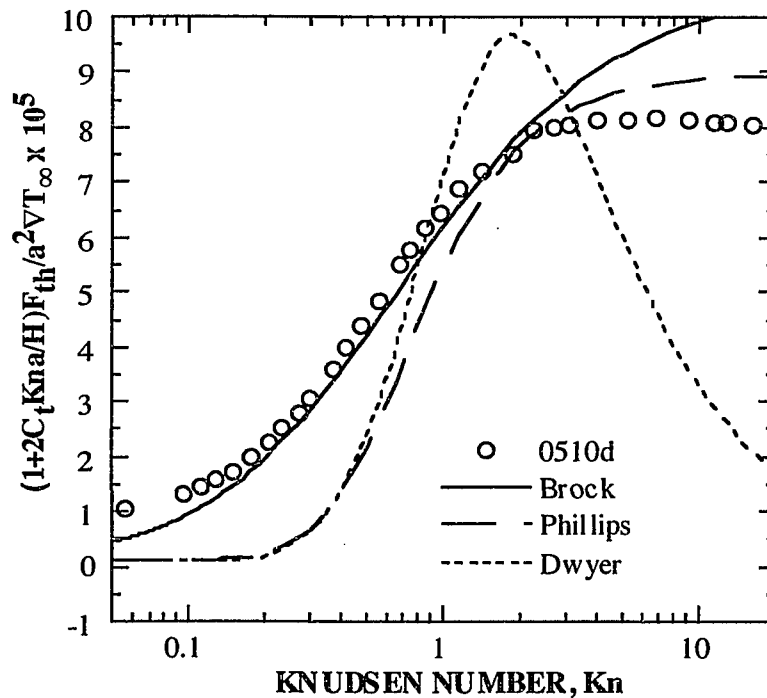


Figure 6.8 Comparison among experimental data of 0510d and the theories of Brock (1962), Dwyer (1967) and Phillips (1975) using unit accommodation coefficient for DOP/air.

Although one can adjust the values of the accommodation coefficient for DOP/air to attempt to get better agreement between theory and experiments, there is little need to do so, for the above three solutions were derived mainly for the slip flow regime, and rigorous theoretical results covering large Kn are available based upon the linearized Boltzmann equation. Those are the solutions of Loyalka (1992) for hard sphere molecules. He obtained numerical results for two thermal conductivity ratios, $k_g/k_p = 0.1$ and 0.01 . The results were found to depend on k_g/k_p weakly. This ratio for DOP droplets, glass, PSL and nickel spheres in air are respectively, 0.15 , 0.023 , 0.17 and 2.0×10^{-4} . In Fig. 6.9 the measurements for DOP/air and PSL/air are compared with the numerical results of Loyalka for $k_g/k_p = 0.1$. Also shown in the figure is the free-molecule limit of Waldmann. The agreement is good throughout the intermediate regime.

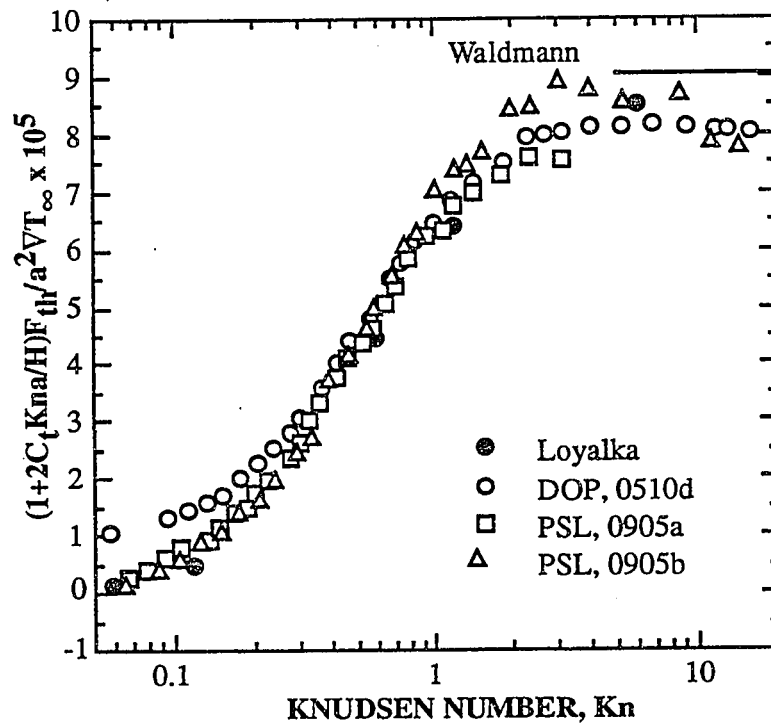


Figure 6.9 Comparison among the data for DOP and PSL spheres and the solutions of Loyalka (1992) for $k_g/k_p = 0.1$ and of Waldmann (1959).

Figure 6.10 compares the results for nickel and glass spheres in air with the solutions of Loyalka for $k_g/k_p = 0.01$ and also with Waldmann's asymptotic result. The agreement among the theoretical results of Loyalka and experiments are reasonably good in the transition regime. The data for nickel spheres scatter more than other data in the near free-molecule regime. Since nickel spheres have relatively larger masses than others ($\rho_{Ni} = 8900 \text{ kg/m}^3$), it is more difficult to balance the gravitational and thermophoretic forces by adjusting the DC voltage. For particles of low density, the oscillations resulting from an unbalanced vertical force can be seen easily through the microscope since the amplitudes were large, but the oscillations associated with nickel sphere had small amplitude and it was more difficult to balance the particle.

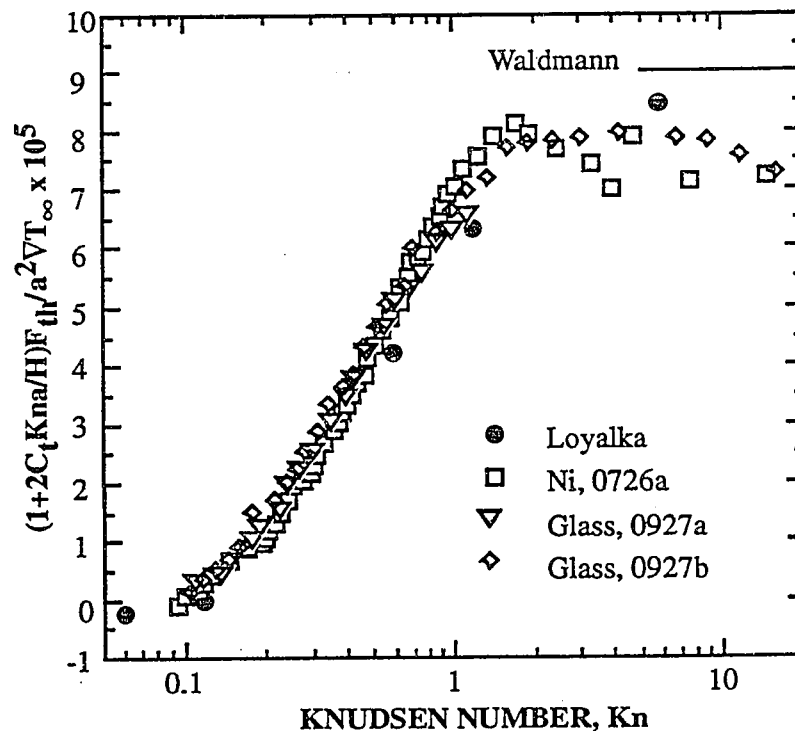


Figure 6.10 comparison among the data for glass and nickel spheres in air with the solutions of Loyalka (1992) for $k_g/k_p = 0.01$ and of Waldmann (1959).

The mean free path of air was determined from the relationship of Jeans (1925) for hard-sphere molecules

$$\lambda = \frac{1}{\sqrt{2}\pi\sigma^2} \frac{k_B T}{P}, \quad (6.5)$$

in which σ is the molecular diameter, k_B is the Boltzmann constant, and P and T are the system pressure and averaged system temperature. In theoretical analysis λ is normally defined by

$$\lambda = \frac{\mu}{0.499\rho\bar{c}}, \quad (6.6)$$

which is consistent with the definition by Eq. (6.5) based upon the kinetic theory of gases. In Eq. (6.6) μ is the gas viscosity, ρ is the gas density and \bar{c} is the mean speed of the gas defined by Eq. (3.22). The definition of Loyalka for λ is slightly different from (6.6), which is

$$\lambda = \frac{4k_B}{5P} \sqrt{\frac{mT}{2k_B}}. \quad (6.7)$$

For a monatomic gas, Eq. (6.7) can be rearranged to give

$$\lambda = \frac{2}{5} \left(\frac{2}{\pi}\right)^{1/2} \frac{1}{\pi\sigma^2} \frac{k_B T}{P}. \quad (6.8)$$

Figure 6.11 presents the normalized and adjusted data for DOP at $0.05 \leq Kn \leq 0.25$ together with the theories of Epstein (1929), Brock (1962) and Derjaguin and Yalamov

(1965). Unit accommodation coefficients were assumed for DOP/air in the theoretical solutions. It can be seen that Epstein's theory underpredicts most of the measurements, and the analysis of Derjaguin and Yalamov overpredicts the thermophoretic force. The solution of Brock is in good agreement with the data.

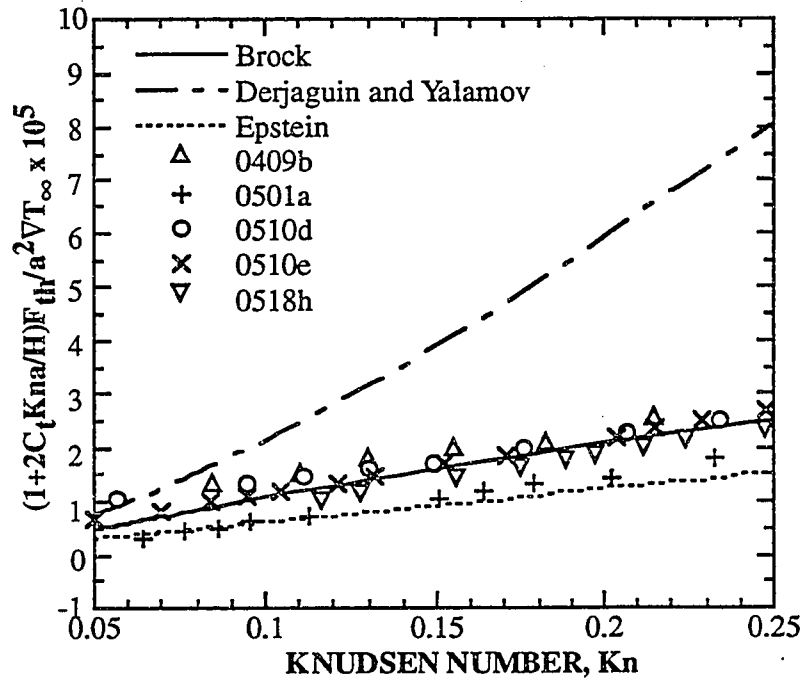


Figure 6.11 Data for DOP droplets in air in the slip flow regime compared with the solutions of Epstein (1929), Brock (1962) and Derjaguin and Yalamov (1965) using $\alpha_t = \alpha_m = 1.0$.

Two analytical formulas have been derived for the TF in the transition regime based on the BGK model: Brock (1967a) and Ivchenko and Yalamov (1970). In this regime, only the thermal accommodation coefficient enters into the solutions, so attempts were made to vary α_t in comparison. Figure 6.12 shows Brock's solutions for three α_t : 0.5, 0.75 and 1.0 together with the experimental data for DOP. Note that the theory gives a large negative forces for $Kn < 0.3$, but after that the analytical solution approaches the

experimental data, and eventually reaches the limit at large Kn . The agreement is reasonably good for $Kn > 1.0$. The data suggest that the value of α_t for DOP/air system lies in the range $0.75 \sim 1.0$.

The same comparison is made with Ivchenko and Yalamov's solution in Fig 6.13. The experimental data around $Kn = 2.0$ reasonably agree with the theoretical solution for $\alpha_t = 1.0$, but for $\alpha_t = 0.5$, and 0.75 , the theory always gives much higher forces than measured.

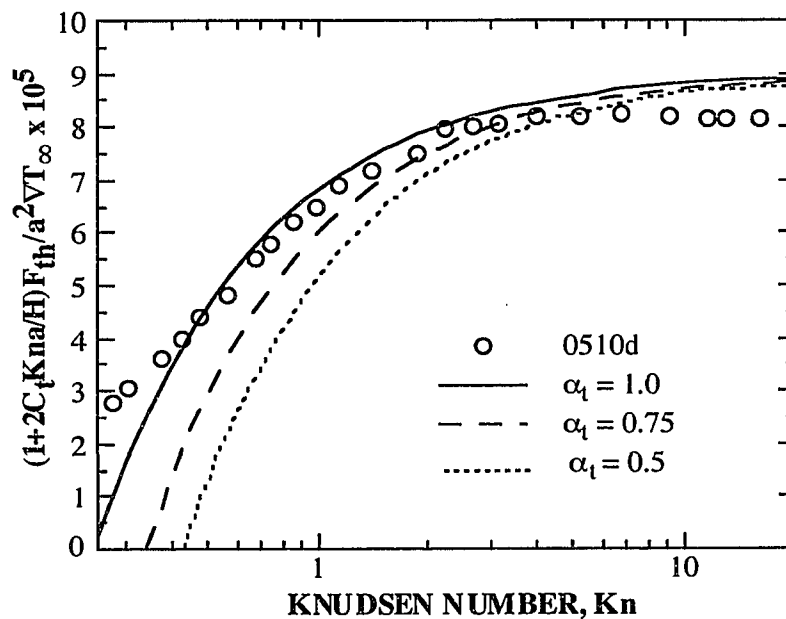


Figure 6.12. Adjusted and normalized force of experiment 0510d compared with the solutions of Brock (1967a) for the transition regime at $\alpha_t = 0.5, 0.75$ and 1.0 .

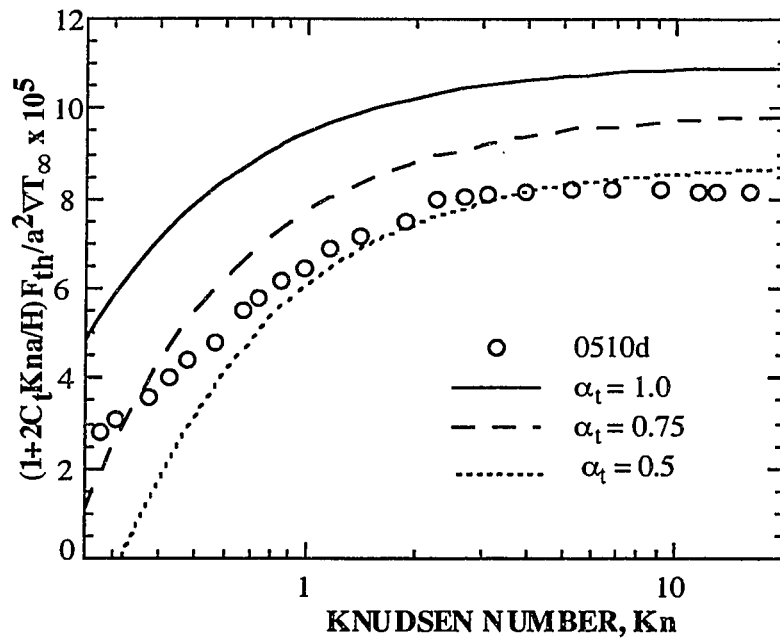


Figure 6.13 Adjusted and normalized force of experiment 0510d compared with the solutions of Ivchenko and Yalamov (1970) for $\alpha_t = 0.5, 0.75$ and 1.0 .

6.4 Conclusion

The thermophoretic force was determined for four type of microparticles in air over a wide range of Knudsen numbers. The force appears to decrease for $Kn > 3.0$. The decrease in TF at large Kn is caused by the temperature jump at the cooled and heated surfaces, and by the effects of the chamber wall. It is shown that the data in the near-free molecule regime can be adjusted upward using the relationship of Devienne to correct the temperature gradient. The thermal accommodation coefficient was found to be about 1/3 for copper/air system.

Most of the theoretical solutions were found to be inadequate to predict the thermophoretic force over the Knudsen range $0.01 < Kn < 10$, but Brock's slip flow theory for the near-continuum regime, and the more recent numerical results of Loyalka based upon the linearized Boltzmann equation, are in agreement with the experimental data in air.

CHAPTER 7

EFFECTS OF THE THERMAL PROPERTIES OF GAS AND PARTICLE ON THE THERMOPHORETIC FORCE

In the preceding chapter experimental results for the thermophoretic force (TF) for dioctyl phthalate (DOP) droplet, polystyrene latex (PSL), glass and metal nickel spheres in air were presented, and the data were employed to evaluate the various theories of TF. In this chapter the results for these materials in helium and carbon dioxide are shown together with additional data in air. The effects of thermal properties of gas and particle as well as other effects on the thermophoretic force will be discussed.

7.1 Effects of Temperature Jump

To illustrate the effects of temperature slip on the thermophoretic force, representative results for a PSL sphere in helium are shown in Figure 7.1 in the form $F_{th}/a^2\nabla T_\infty$ (without mention, the particle is assumed to be charged negatively in this discussion; the charge effects will be addressed later in this chapter). Note that the variation of TF in helium is similar to that in air. The normalized force $F_{th}/a^2\nabla T_\infty$ seems to reach a maximum at $Kn \sim 3.0$ and then decreases significantly as Kn increases. As explained before, the apparent decrease in F_{th} was caused by the temperature slip occurring near the copper plate surfaces as the gas mean free path became large. To illustrate the importance of these effects, the temperature gradient of the air was corrected using the relationship proposed by Devienne (1965) for heat transfer between flat plates in the intermediate Kn regime (see Eq. (6.2)). The thermal accommodation coefficient α_t , extracted from the TF adjustment in the near-free-molecule regime, was found to be about 1/3, which is significantly lower than the reported value $\alpha_t = 0.8-0.98$ by Spring (1971) for the copper/air system. To estimate α_t for the copper/helium system, a similar parametric study

was carried out to correct ∇T_∞ for helium in the transition regime. The adjusted force $F_{th}/(a^2\nabla T_{Kn})$ for $\alpha_t = 0.33$ and 0.05 are also shown in Fig. 7.1.

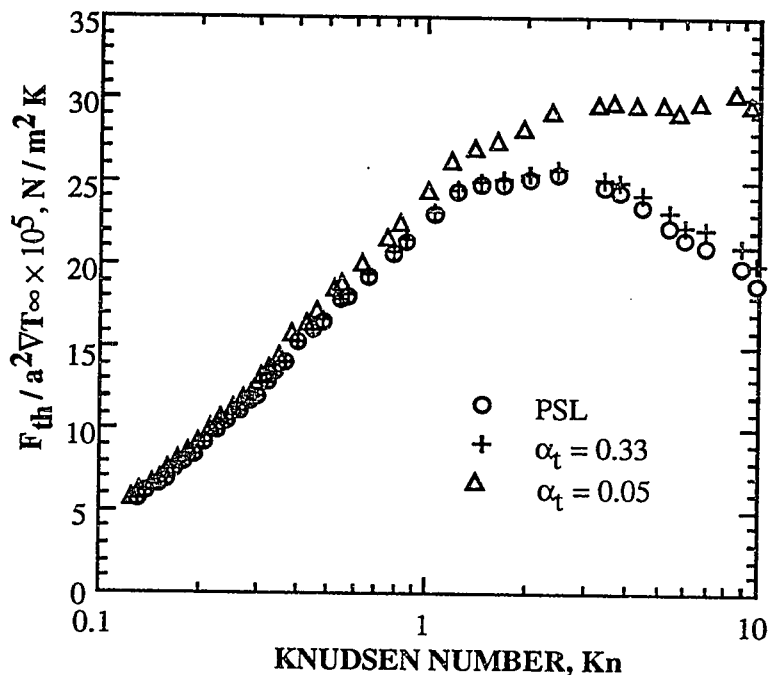


Figure 7.1 Thermophoretic force for a PSL sphere in helium normalized by $a^2\nabla T_\infty$ and replotted as $(1+2C_tKn_2)F_{th}/a^2\nabla T_\infty$ for $\alpha_t = 0.33$ and $\alpha_t = 0.05$, showing the effects of temperature slip.

For the copper/ CO_2 system, the adjustment to ∇T_∞ discussed above yielded $\alpha_t \approx 0.5$. The accommodation coefficient, reported by Saxena and Joshi (1981) for the copper/helium system, is 0.3-0.88 and 0.79-0.89 for CO_2 molecules contacting with copper surface. It is not clear what causes the difference in α_t . The accommodation coefficient for the "dirty" copper surface in the experiment may be actually lower than the values for a specially treated surface, since α_t is very sensitive to the surface condition. One must recognize that the values of α_t extracted depend on the relationship used for the calculation of C_t from α_t , and of ∇T_{Kn} from C_t . Although the extracted α_t in the three

gases are all lower than the reported data, simple corrections showed that the thermal accommodation coefficient increases with increasing molecule weight of gas, which qualitatively fall in agreement with Baule's theory of elastic collisions (1914) for α_t predictions.

It is noted the data for helium at $Kn < 1.0$ are not appreciably affected by adjustment of α_t , and the thermophoretic force almost reaches the free-molecule limit of Waldmann (1959) at $Kn \approx 3.0$ in all the results (see Fig. 7.2). To avoid misleading results caused by the adjustment, I shall focus my attention on the intermediate Kn regime and restrict the results presented to $Kn < 3.0$.

7.2 Comparison of Theory and Experiment

The results for glass and nickel spheres in helium are shown in Fig. 7.2 along with several theoretical solutions. The reported accommodation coefficient for glass and nickel surfaces in helium are respectively 0.365 and 0.385 at $T = 298$ K (Saxena and Joshi, 1981). In experiments the gas temperature at the chamber center was 298 ± 3 K, and the values of α_t reported by Saxena and Joshi were used in the equations of Brock (1967a) and Ivchenko and Yalamov (1970). Since the α_t for glass and nickel surfaces are quite close and the theoretical curves for them are almost overlapped, only the results for $\alpha_t = 0.365$ are showed in Fig. 7.2. It was noted that both solutions gave large negative F_{th} in the near-continuum regime and this was probably due to the errors involved in the BGK model (Loyalka, 1992). Brock's solution, which was derived from the BGK Boltzmann equation and should be valid in the transition regime, agrees with experimental results very well when Kn exceeds 0.2, but the results of Ivchenko and Yalamov overpredict the thermophoretic force over the entire range of Knudsen numbers.

The numerical solutions shown in Fig. 7.2 are of Sone and Aoki (1983), of Yamamoto and Ishihara (1988) and of Loyalka (1992). They are obtained from the

Boltzmann equation for diffuse gas/particle interaction, ($\alpha_t = 1.0$). Note that all the theoretical results fall below the experimental data. Loyalka's solution shown is for the thermal conductivity ratio $k_g/k_p = 0.01$, and the results of Sone and Aoki are based upon infinitesimally small k_g/k_p . The values of k_g/k_p are respectively 0.19 and 0.0017 for glass and nickel spheres in helium. The difference among the experiments and theory are apparently due to the fact that the thermal accommodation coefficients for glass and nickel in helium are significantly lower than unity as assumed in the theoretical computations. The effects of the accommodation coefficient on the thermophoretic force can be explored from the analytical solutions of Brock (1967a) and Ivchenko and Yalamov (1970); both indicate that the F_{th} increases with decreasing α_t for a given Kn. This is consistent with the experimental findings in this research.

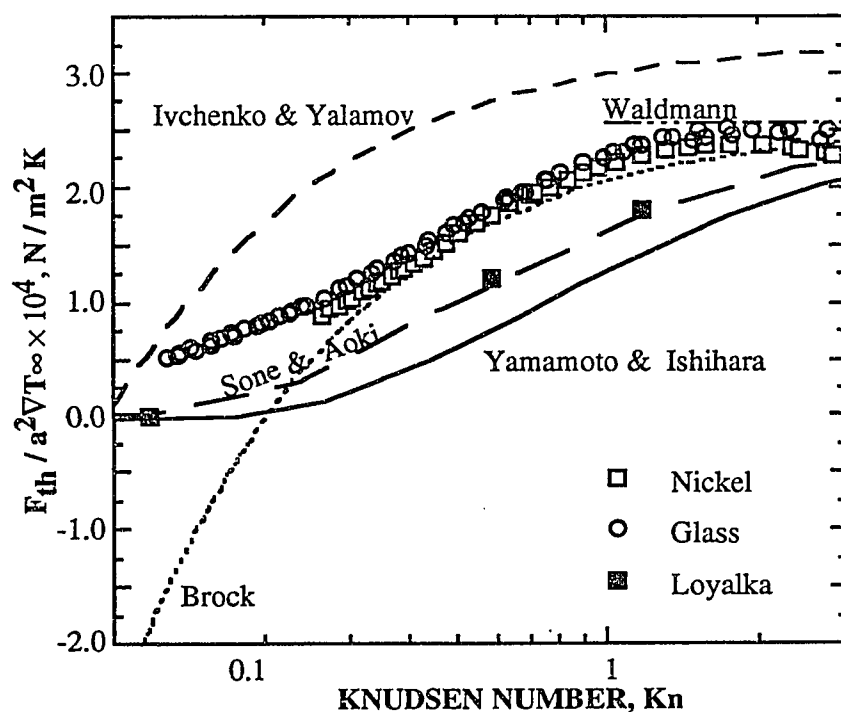


Figure 7.2 Comparison among experimental data for nickel and glass spheres in helium and various theoretical results for monatomic gas molecules.

As mentioned in the preceding chapter, the mean free path was estimated from the definition of Jean (1925), and the Knudsen numbers defined by various authors were corrected in the comparison.

The results of PSL and glass spheres in CO₂, similar to those in helium, are shown in Fig. 7.3. In this figure only the solutions of Brock (1967a), of Yamamoto and Ishihara, of Loyalka and of Waldmann are presented for comparison. Again, Brock's analytical solution reasonably agree with the experimental results for $Kn > 0.2$, and the numerical results of Loyalka for $k_g/k_p = 0.01$ fall on the data for glass spheres. The accommodation coefficient for glass in CO₂ was measured to be 0.45 at $T = 298$ K (Saxena and Joshi, 1981). The solution of Yamamoto and Ishihara (1988) reasonably agree with the experimental results for glass spheres at low Kn . The solution of Ivchenko and Yalamov, based upon $\alpha_t = 0.45$, was found to disagree with the experiments and is not presented in Fig. 7.3.

7.3 Effects of Temperature Gradient and Particle Size

In the theoretical considerations of thermophoresis, the temperature difference between the heated and cooled plates is assumed to be small compared with the mean temperature of gas. It ensures that the deviation of the molecular velocity distribution from the Maxwellian equilibrium distribution can be assumed sufficiently small so that the linearization of the Boltzmann equation is accurate. Also, the radiant heat transfer between the particle and the plate surface can be neglected. In these experiments the midplane temperature was always less than 310 K, and the maximum temperature difference between the heated and cooled plates was 77 K. The temperatures along the centers of two plates were measured by a small traversing K-type thermocouple. The results, presented in Fig. 4.14, demonstrate that the temperature gradient was linear and the radiant effects were insignificant under present experimental conditions.

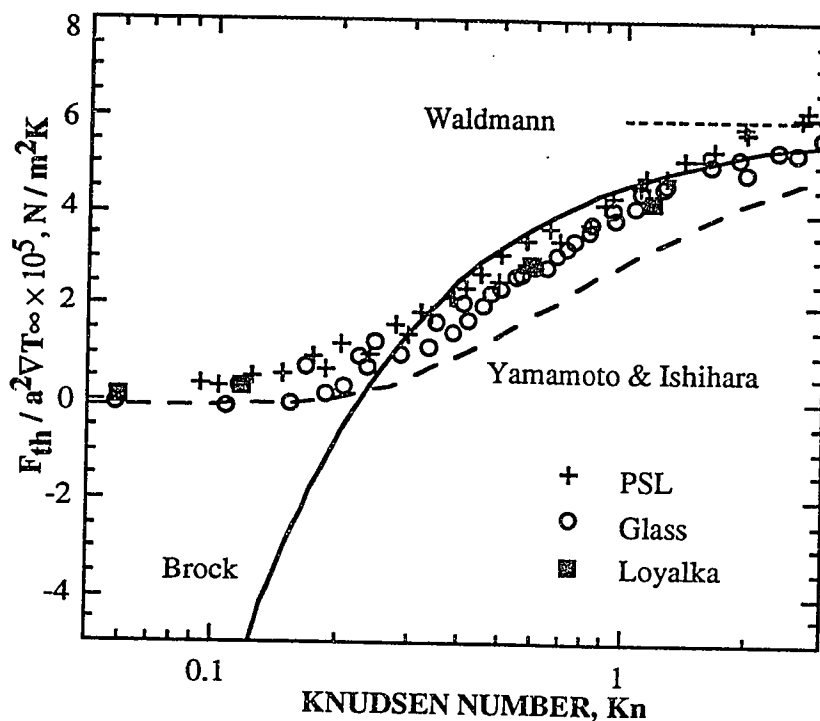


Figure 7.3 Comparison among experimental data for PSL and glass spheres in CO_2 and various theoretical results.

All the theoretical analyses of thermophoresis yield a linear dependence of F_{th} on ∇T_∞ and a^2 , although the derived dependences of F_{th} on Kn are complicated and vary significantly among available theories. These linear relationships were examined in this work. Figure 7.4 presents the results for PSL and glass spheres in air for various ∇T_∞ . The experimental data were obtained at constant pressure, and the Knudsen numbers determined from the experimental conditions were 0.52 and 2.05 for PSL and glass spheres, respectively. The results for PSL are compared with Brock's solution (1962) for the slip flow regime, and the data for the glass sphere are compared with Brock's theory (1967a) for intermediate Kn . The agreement among the theories and experiments is very good, and the linear dependence of F_{th} on ∇T_∞ is verified.

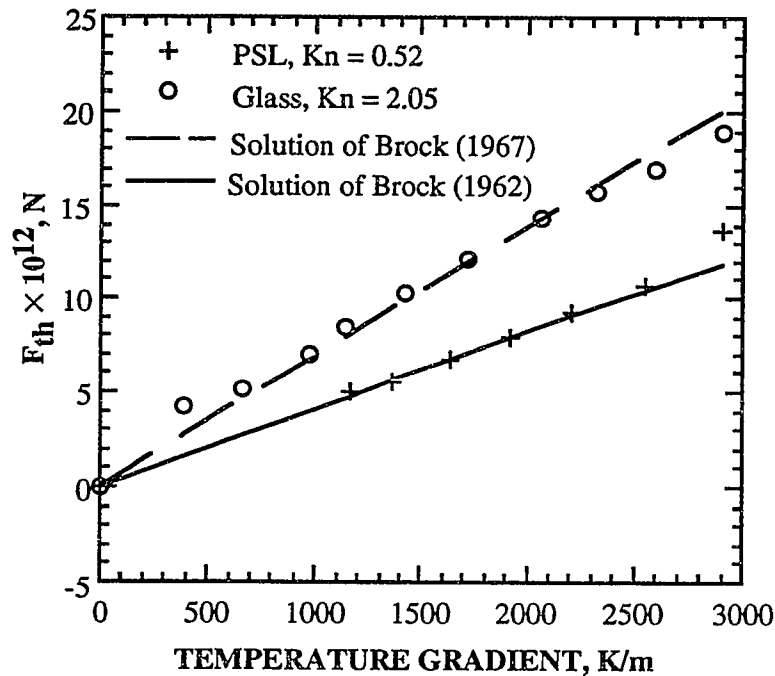


Figure 7.4 Effects of the temperature gradient on the thermophoretic force for glass and PSL spheres in helium compared with the solutions of Brock.

Figure 7.5 is a plot showing the linear dependence of F_{th} on a^2 . The experimental data were obtained for five positively-charged DOP droplets in air at Kn about 0.5. The droplet radii range from $10.9 \mu\text{m}$ to $23.9 \mu\text{m}$. The thermophoretic force was normalized by the gas temperature gradient ∇T_{∞} , for ∇T_{∞} varied in these measurements. It can be seen that the thermophoretic force varies linearly with a^2 , which is what theories predict.

7.4 Effects of Particle Thermal Conductivity

Theoretical predictions of TF for particles with high thermal conductivity were found to be low (Brock, 1962), and also negative TF was predicted by Sone and Aoki (1983), Loyalka (1992) and others in the near-continuum regime for them. The underprediction of

F_{th} was pointed out by Schadt and Cadle (1961) in their study of thermophoresis for mercury droplets and sodium chloride particles. They found that the measured F_{th} for mercury and NaCl were, respectively, about 30 and 50 times larger than Epstein's (1929) predictions. To reduce the disagreement, Jacobsen and Brock (1965) proposed a new solution for high k_p particles from the third approximation to the Boltzmann equation, but the final solution contains an unknown constant which must be determined from data fitting.

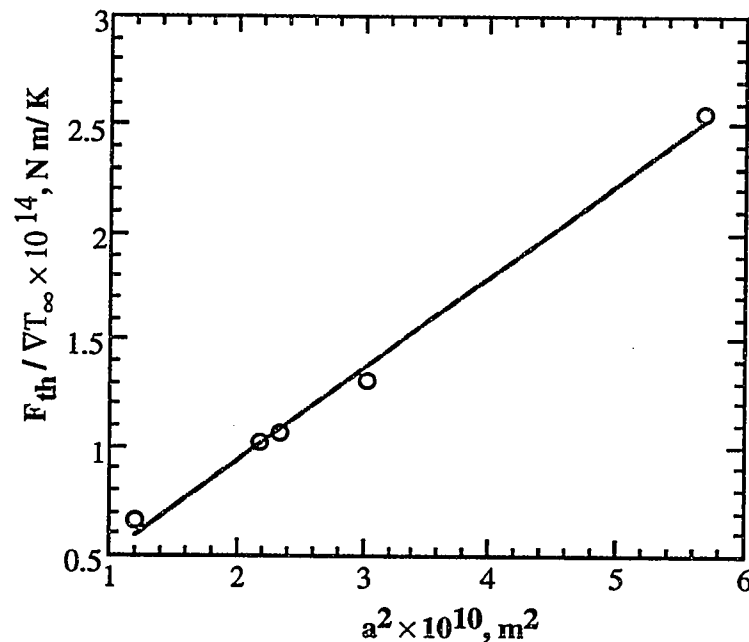


Figure 7.5 Effects of the particle radius on the thermophoretic force for DOP droplets in air.

Sodium chloride ($k_p = 6.0 \text{ W/m K}$) was used by Schadt and Cadle, by Jacobsen and Brock and by Prodi *et al.* (1979) to study the effects of k_p on the thermophoretic force. Crystalline sodium chloride has a cubic shape and the particles generated by atomizing the solution have unknown densities, so it is desirable to use spheres of known density.

Attempts were made to form a TiO_2 sphere having high k_p via a gas/droplet reaction as discussed in Chapter 5, but the particle produced was found to be inhomogeneous, so for high k_p , glass (0.8 W/m K) and nickel spheres (90.9W/m K) provided by Duke Scientific Corporation (Palo Alto, CA) were selected. For lower k_p particles, DOP (0.125 W/m K) and PSL (0.122 W/m K) were chosen.

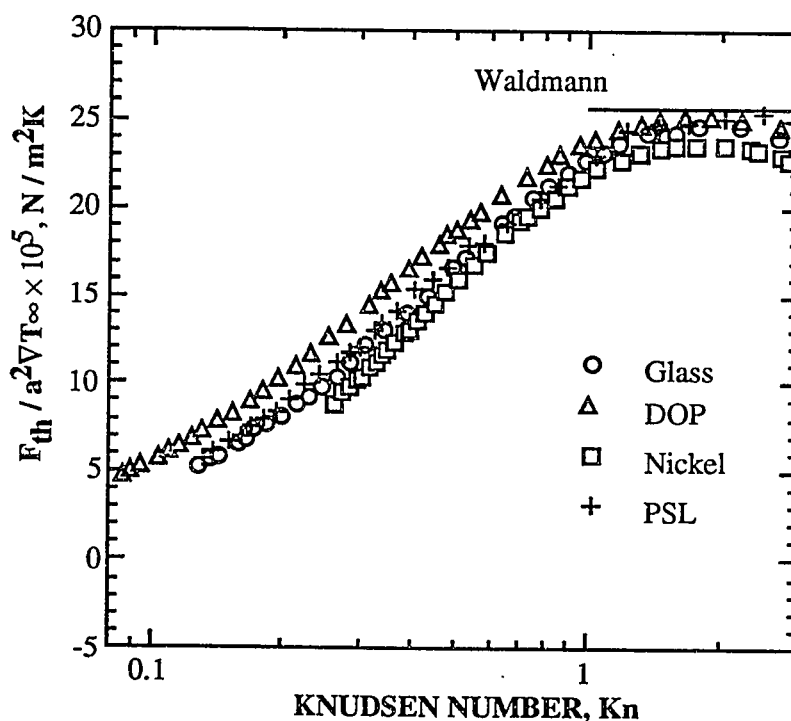


Figure 7.6 The thermophoretic force for DOP, PSL, glass and nickel spheres in helium.

The results for nickel, glass, PSL spheres and DOP droplets in helium are shown in Fig. 7.6 together with the free-molecule limit of Waldmann. The results indicate that the effects of k_p are small, for the variations of k_p cover almost three orders of magnitude, but only a slight difference in the normalized force can be identified from the results. The data for helium at small Kn, corresponding to pressures greater than 110 Torr could not be obtained because of the display limits of the vacuum gauge (110-0.01 Torr only). Similar

data for glass, PSL and DOP in CO₂ particles are presented in Fig. 7.7. Again, the results for glass and PSL almost overlapped, and the data for DOP droplets fall above those for the solid spheres. At large Kn the data scattered more around Waldmann's free-molecule limit.

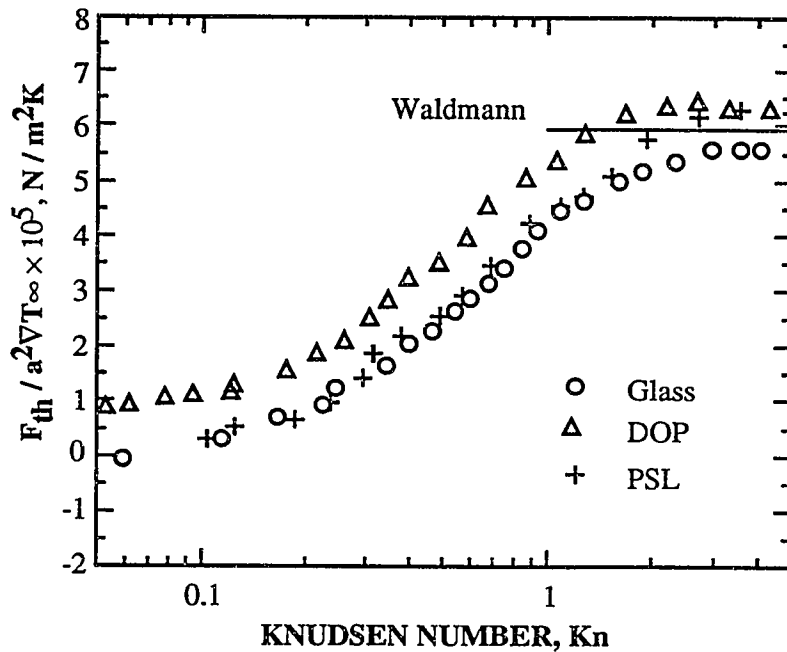


Figure 7.7 Thermophoretic force for DOP, PSL, glass and spheres in carbon dioxide.

The "negative" thermophoretic force, predicted by Sone and Aoki, by Loyalka and others, was not observed for glass and nickel spheres in air, helium and CO₂.

7.5 Effects of Gas Thermal Conductivity

Theoretical analyses of thermophoresis have usually been performed based upon a monatomic gas. For a polyatomic gas, molecular translation is usually regarded as the primary mechanism of energy and momentum transfer. For example, in Waldmann's analysis only the translational portion of the thermal conductivity of gas is taken into

consideration. In this study the thermophoretic force was measured in helium, air and CO₂ to explore the effects of the gas thermal conductivity on F_{th} .

Representative results for glass spheres in the three gases are presented in Fig. 7.8. Also shown in the figure are Waldmann's free-molecule limits for the three gases, which are respectively $F_{th}/a^2\nabla T_\infty = 9.025 \times 10^{-5} \text{ N/m}^2 \text{ K}$, $5.91 \times 10^{-5} \text{ N/m}^2 \text{ K}$ and $2.57 \times 10^{-4} \text{ N/m}^2 \text{ K}$ for air, CO₂ and helium. It can be seen that the normalized thermophoretic force is

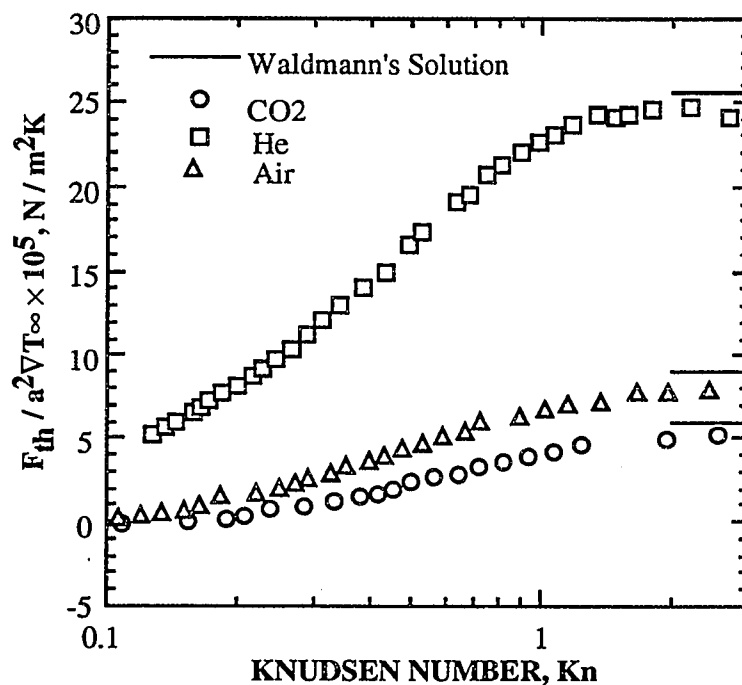


Figure 7.8 Effects of surrounding gas on the thermophoretic force for glass spheres.

strongly dependent on the gas thermal conductivity. At any given Knudsen number the force in helium is much higher than those in air and CO₂. For monatomic helium $k_{g,tran}$ is also its total thermal conductivity ($k_g = 0.151 \text{ W/m K}$ at $T = 298\text{K}$), and for air and CO₂ $k_{g,tran}$ was computed from the following kinetic relationship:

$$k_{g,tran} = \frac{15\mu}{4R}, \quad (7.1)$$

in which μ is the gas viscosity and R is the universal gas constant. The calculated $k_{g,tran}$ are 0.0188 W/mK and 0.0105 W/mK for air and CO₂, respectively, at $T = 298\text{K}$. They are nearly one order of magnitude lower than the $k_{g,tran}$ of helium. The viscosity data used were taken from Incropera and DeWitt (1990). The results for DOP droplets, PSL and nickel spheres in three gases are similar to those for the glass sphere.

7.6 Effects of Particle Charge

No theoretical analyses and no prior experiments on single particles have ever been carried out concerning how an electrical field influences the thermophoretic force, but Stratmann *et al.* (1988) and Cooper and his coworkers at IBM (Cooper *et al.*, 1989) theoretically investigated convective, diffusive, electrophoretic and thermophoretic mechanisms of particle deposition on electronic wafers. Chififu *et al.* (1987) studied the deposition velocities of PSL particles with an electrical potential applied to free-standing wafers, and Opiolka *et al.* (1994) showed that the thermophoretic deposition can be altered by an electric field. The electrostatic effects considered in these studies are for the particle/surface interaction rather than gas/surface interactions.

The effects of surface charge on the thermophoretic force were examined in this study. The polarity of the surface charge on DOP droplets and PSL spheres was altered by changing the polarity of the charging needle. The effects of surface charge are quite surprising and significant. Figures 7.9 and 7.10 present the results for DOP droplets in air and helium, respectively, and similar data for PSL spheres in helium are shown in Fig. 7.11. It can be seen that the charge effects are highly reproducible. In both gases the negatively-charged particles experienced a larger force than the positively-charged particles, and the force difference in helium was rather higher than that in air. It appears that the

thermophoretic force at large Kn for negatively charged particle approaches Waldmann's free-molecule limit, while the forces for the positively charged particle slightly fall below the asymptotic solution.

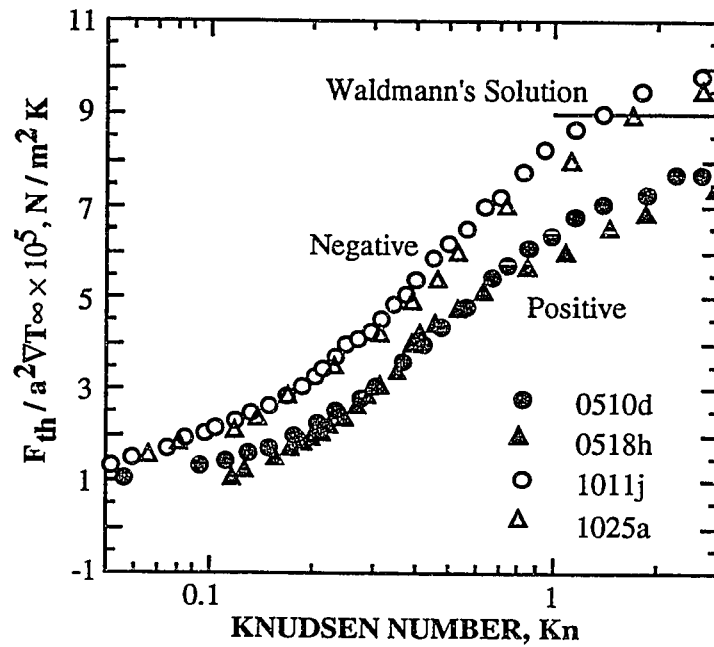


Figure 7.9 Effects of the charge polarity on the thermophoretic force for DOP droplets in air.

The coulombic surface charge q on a particle, trapped in the electrodynamic balance, can be estimated from the DC voltage, $V_{dc,0}$, required to balance the particle weight. A vertical force balance on a charged particle gives

$$mg = -qC_0 \frac{V_{dc,0}}{z_0}, \quad (7.2)$$

in which mg is the particle weight, which can be determined from the measured size and known density, z_0 is half of the distance of two electrodes ($z_0 = 1.5$ mm) and C_0 is a

geometric constant depending on the electrode configuration. The value of C_0 for the double-ring configurations were analyzed by Davis and Bridges (1994). For configurations similar to the one used in this work, they obtained approximately 0.8 ± 0.05 for C_0 . Using a value of 0.8 for C_0 , one may compute the total surface charge for the particles in the experiments, then the surface charge density can be estimated by the following relationship:

$$Q = \frac{q}{A} = -\frac{z_0 \rho_t g a^2}{3 C_0 V_{dc,0}}, \quad (7.3)$$

in which ρ_t is the density of the particle ($\rho_t = 981 \text{ kg/m}^3$ for DOP, and $\rho_t = 1050 \text{ kg/m}^3$ for PSL).

Table 7.1 Surface charge density for DOP droplets and PSL spheres

Particle	Experiment run	Charge polarity	a (μm)	$V_{dc,0}$ (volt)	$Q \times 10^6$ (C/m^2)
DOP	0510d	Positive	23.9	-33.90	8.48
	0518h	Positive	15.3	-17.26	10.7
	1011j	Negative	14.5	7.13	-24.5
	1025a	Negative	12.0	5.75	-25.1
	1011k	Negative	14.5	7.13	-24.5
	0519h	Positive	15.3	-17.26	10.7
PSL	1005c	Negative	10.9	3.30	-42.5
	0524j	Positive	10.7	-7.25	19.0

The calculated surface charge and charge density for DOP droplets and PSL spheres are summarized in Table 7.1 along with the particle radius and $V_{dc,0}$. For all the

measurements, the charge is of order 10^{-14} C, and the charge density is of order 10^{-5} C/m². The magnitude of the negative charge was generally about twice that of the positive charge for both DOP and PSL particles.

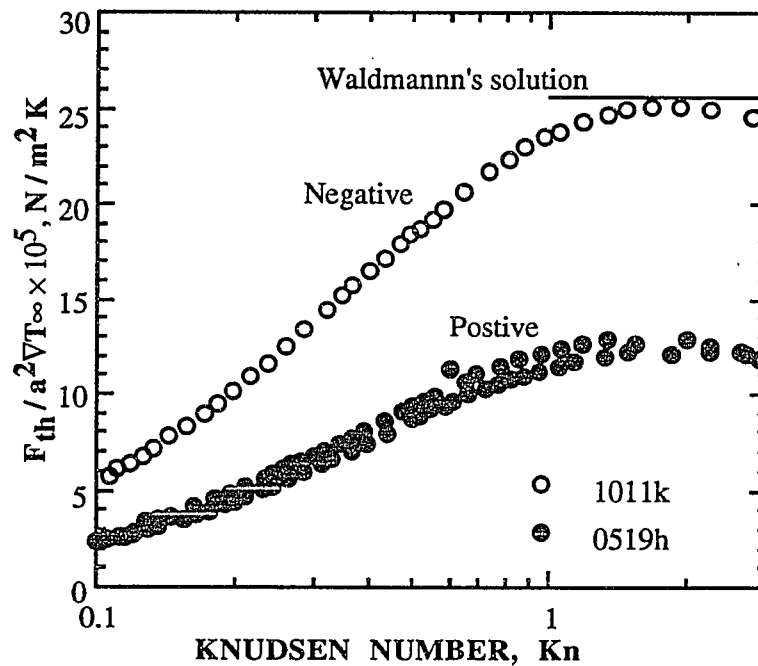


Figure 7.10 Effects of charge polarity on the thermophoretic force for DOP droplets in helium.

The electrostatic interaction between the particle and the gas molecules seems to influence the thermophoretic force exerted on the particle. Although helium has no permanent dipole moment, it appears that the electric field in the vicinity of the sphere induces a dipole moment. The electric field associated with a charged sphere is given by

$$\phi = \frac{q}{4\pi\epsilon r^2} \quad (7.4)$$

in which ϵ is the permittivity of free space, and r is the distance from the center of the sphere. The electric field estimated for one distance of the particle radius (typically $15 \mu\text{m}$) is of the order $2 \times 10^6 \text{ V/m}$, but the external DC field associated with the balancing voltage is typically of the order 3000 V/m , so it is possible that the strong static field near the particle surface affects the gas/particle interaction and consequently, affects the thermophoretic force.

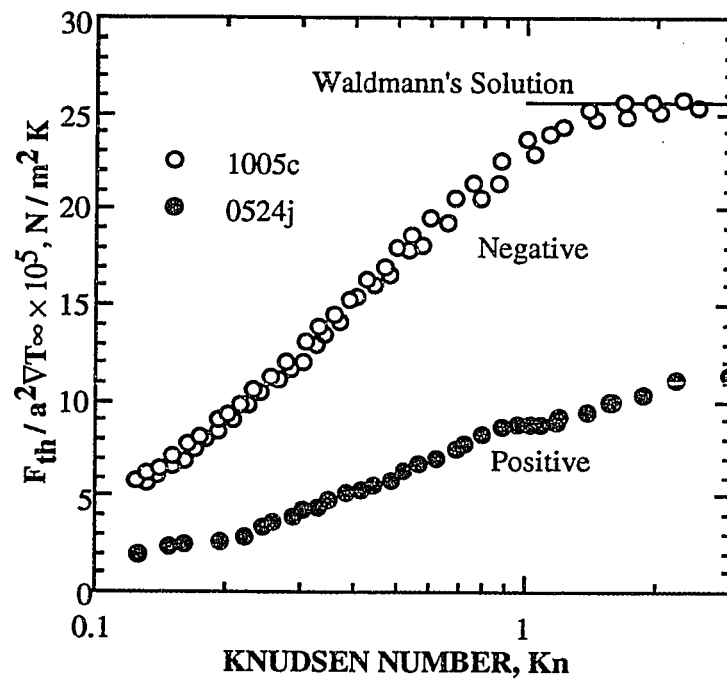


Fig 7.11 Effects of charge polarity on the thermophoretic force for PSL spheres in helium.

7.7 Conclusion

The thermophoretic force was measured for DOP droplets, PSL, glass and metal nickel spheres in air, helium and carbon dioxide over a wide range of Knudsen numbers. All the data appeared to decrease significantly for $\text{Kn} > 3$ due to the "temperature jump" effects at the copper plate surfaces, as well as the edge effects of the chamber wall at large

Kn. Corrections of the temperature gradient in the intermediate regime were made, and the extracted thermal accommodation coefficient for the copper/gas system were found to be significantly lower than reported values in literature.

The TF data at $Kn < 3.0$ were compared with the analytical solutions of Brock, and Ivchenko and Yalamov as well as several numerical solutions based upon the BGK Boltzmann equation. Ivchenko and Yalamov's theory disagrees with the experimental results in helium and CO_2 , and Brock's solution for the transition regime agrees with the data for $Kn > 0.2$. The experimental results in helium were found to be larger than all the numerical results for the diffuse gas/particle interaction, which indicates that the thermal accommodation coefficients for all particles in helium is much less than unity. The data for CO_2 agree with Loyalka's results, and the solution of Yamamoto and Ishiara (1988) reasonably agrees with the experimental data for low Kn.

The "negative" thermophoretic force, predicted by various investigators in the near-continuum regime, was not observed for glass and nickel particles with large thermal conductivity.

The measured thermophoretic force was found to vary linearly with respect to a^2 and ∇T_∞ which agrees with theoretical predictions. The effects of the particle thermal conductivity on F_{th} were found to be small, while the force was strongly dependent on the thermal conductivity of surrounding gas.

The effects of charge polarity on the thermophoretic force were found to be dramatic based upon the results for DOP droplets and PSL particles in air and helium. The negatively-charged particles appeared to receive larger TF than the positively-charged particle, also the force approaches to Waldmann's free-molecule limit at large Kn, but TF on the positively charged particles fall below the asymptotic solution at large Kn. The difference of force indicates that the application of surface charge can significantly alter the thermophoretic deposition on surfaces.

CHAPTER 8

AEROSOL EVAPORATION IN THE TRANSITION REGIME

Evaporation theories in the continuum, transition and free-molecule regimes as well as the related experimental studies have been reviewed in Chapter 2. It is shown that prior measurements for droplet evaporation in the transition regime are scarce and incomplete. More experimental work in the intermediate regime is required. This was made in this study using the apparatus developed for the thermophoretic force measurements. By electrostatically levitating single low-volatile dibutyl phthalate (DBP) droplets in air, the evaporation rates were measured from elastic scattering data at various pressures and temperatures. The experimental results are presented in this chapter. The evaporation rates determined at room temperature (297.7 K) were used to evaluate theories for the transition regime. In addition to the evaporation of single DBP droplets, two other experimental studies related to droplet evaporation are also discussed here. One is the measurements of the effects of polymethylmethacrylate (PMMA) polymer on the evaporation of DBP, and the other is the measurement of evaporation of industrial tin catalyst droplet by Raman spectra.

8.1 Evaporation of Single DBP Droplets in Air

Dibutyl phthalate (99.99+%) purchased from Aldrich Chemical Company was selected as the experimental material. The evaporation process of the low-volatility DBP is very slow, and the process can be treated isothermally. The results can be directly used to evaluate theories. Another purpose of studying DBP droplets is to provide the baseline data with which the effects of PMMA polymer on the evaporation of DBP can be examined.

A single DBP droplet was introduced and stabilized in the electrodynamic balance using the method discussed in Chapter 4. Before evaporation measurements were made, air flow was passed through the vacuum chamber to remove any accumulated DBP vapor from the chamber. Evaporation of DBP droplets at atmospheric pressure was studied by Bradley (1946) and Ray *et al.* (1979). The present measurements concentrated on low pressures ($P < 100$ Torr). In order to maintain the vapor concentration far from the droplet surface nearly zero, an on-line valve was slightly open to bleed some air through the top flange into the chamber at low pressures. Estimations based upon the vapor pressure determined by Ray *et al.* show that at room temperature, to fully saturate the vacuum chamber, complete evaporation of over ten thousand DBP droplets with a radius of $10\ \mu\text{m}$ is required. Thus, saturation effects in the present study should be insignificant.

Phase functions and resonance spectra (MDRs) were collected simultaneously in each experiment. Phase function data were incorporated to simplify the interpretation of the MDR data. Typical "raw" phase functions and MDRs for an evaporating DBP droplet are shown in Figs. 4.11 and 4.12, respectively, along with the Mie's solutions.

Since comparison among measurements and theories is usually made at certain Knudsen numbers, $\text{Kn} = \lambda/a$, in which λ is the mean free path of vapor and a is the droplet radius, evaporation measurements should be performed at a set of various pressures. At the same time the size should be controlled to vary slightly at any particular pressure. The latter can be conveniently achieved by means of the MDR measurements, since at a certain pressure the evaporation rate can be determined from two resonance peaks. The size change corresponding to two resonance peaks is about 0.8% for a $10\ \mu\text{m}$ DBP droplet (typical in these measurements), so the size can be treated as a constant. In order to reduce the error, a few resonance peaks (less than five) were normally recorded and used in the calculation of evaporation rate although two resonance peaks are sufficient. The averaged particle size was used to calculate Kn .

Figure 8.1 presents the change of radius for an evaporating DBP droplet at six different system pressures and a temperature of 297.7 K. It can be seen that the rate of size change, that is, the evaporation rate, increases with the decreasing system pressure until the free-molecule limit is reached.

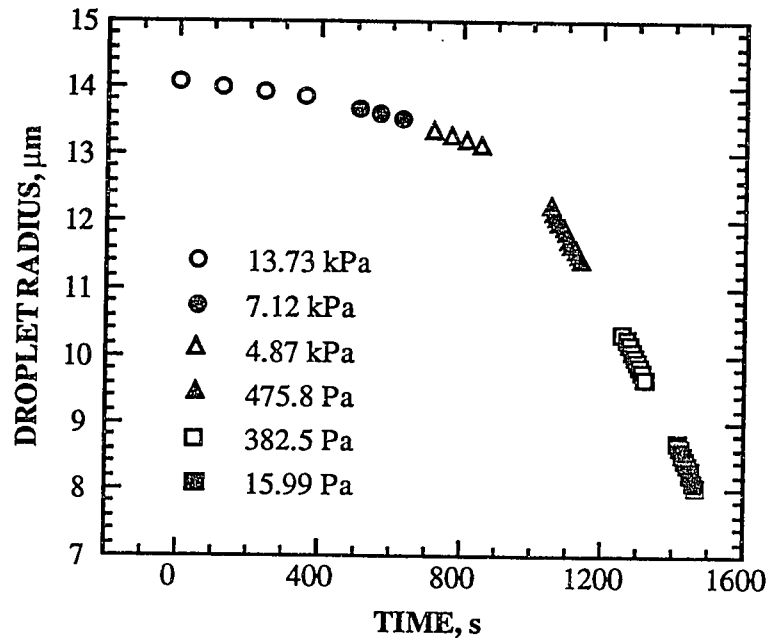


Figure 8.1 radii of an evaporating DBP droplet at six system pressures.

8.1.1 Estimation of Evaporation Rate

The evaporation rate or mass flux, defined by

$$J_k = -\rho_t \frac{da}{dt}, \quad (8.1)$$

can be determined from the rate of size change at a certain pressure, in which ρ is the droplet density. Based upon the evaporation theory of Maxwell, the evaporation rate in the continuum regime depends on the droplet size as given by Eqs. (3.28) to (3.29).

However, the size variation at one experimental pressure is negligible as explained above, so a plot of droplet radius versus time yields a straight line. This is shown in figure 8.2, which is a plot of the droplet radii determined from MDR data as a function of time at $P = 12.69$ kPa and $T = 296.4$ K. It can be seen that all the data points nearly fall on a straight line. The evaporation rate of DBP computed from the slope of line is 4.14×10^{-7} kg/m²s for $Kn = 0.0064$.

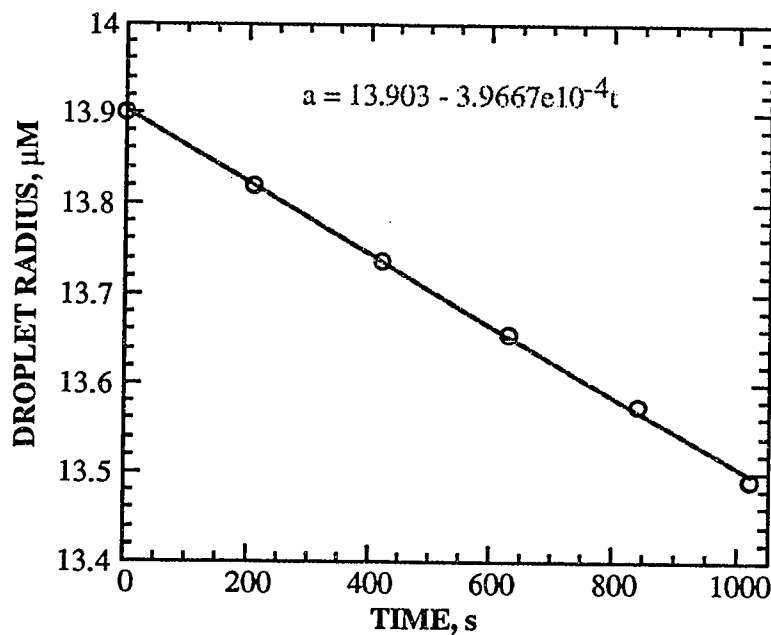


Figure 8.2 Plot of droplet radius versus time for an evaporating DBP droplet at $P = 12.69$ kPa ($Kn = 0.0064$) and $T = 296.4$ K, the slope is used to determine the evaporation rate.

The determination of evaporation rate in the free-molecule regime is straightforward since effusion theory predicts that the droplet radius varies linearly with time. Therefore, the evaporation rate at arbitrary Kn was determined by plotting the droplet radius versus time.

An alternative method for measuring the droplet radius or evaporation rate is to follow the change of DC levitation voltage during evaporation. This technique was used by Ray *et*

al. (1988) to study the evaporation of single dioctyl phthalate (DOP) droplets. In this study the DC voltage data for some experimental runs were recorded together with the phase functions and MDRs. Analyses of DC data can provide a consistent check on the measurements.

As shown in Chapter 4, if only the gravitational force acts on a particle, a vertical force balance will yield

$$m(t)g = -C_0q \frac{V_{dc}(t)}{z_0}, \quad (8.2)$$

in which $m(t)g$ is the particle weight, q is the charge on the droplet surface, C_0 is the geometric constant and z_0 is half of the separation distance between rings. Using $m(t) = 4\pi a(t)^3 \rho / 3$, one may rearrange Eq. (8.2) into

$$a(t) = k[V_{dc}(t)]^{1/3}, \quad (8.3)$$

in which $a(t)$ is the droplet radius at any time t , and k is given by

$$k = \left(\frac{3C_0q}{4\pi\rho_tgz_0} \right)^{1/3}. \quad (8.4)$$

Constant k includes the droplet charge which can be determined from the recorded DC voltage and the corresponding particle size measured from the elastic scattering data. Once the value of k is known, the particle size at any time can be obtained from the balancing DC voltage using Eq. (8.3), if surface charge is not lost in the experiment. The charge loss normally occurs for particles exposed to a UV light source, or occurs when Rayleigh instability limit of surface charge is reached during evaporation. As analyzed in Chapter 5, such charge loss normally does not happen under the experimental conditions of this study.

Figure 8.3 compares the radius of a DBP droplet determined from DC voltages, phase functions and MDRs as a function of time. The measurements based on phase functions and MDRs agree with each other very well, but the data based on the DC voltage is more scattered.

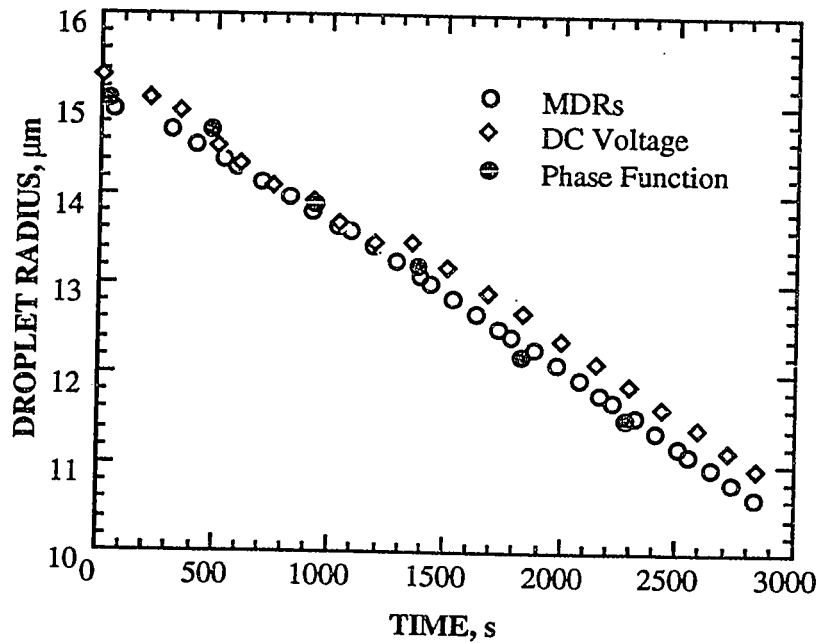


Figure 8.3 Comparison among the droplet radius of DBP determined from MDRs, DC voltage and phase function, respectively.

8.1.2 Determination of Vapor Pressure

The saturation vapor pressure, P_1^0 , can be determined by means of two methods. One is based upon the droplet size measurements in the continuum regime, and the other is based on measurements of the mass flux in the free-molecule regime. According to the diffusion theory of Maxwell (refer to Eqs. (3.28)-(3.29)), a plot of $a(t)^2$ versus time should yield a line whose slope, S_{ij} , includes the vapor pressure p_1^0 . Thus, p_1^0 can be determined from S_{ij} by

$$P_i^0 = -\frac{\rho_t R T_s}{2D_{ij}M_i} S_{ij} \quad (8.5)$$

in which R is gas constant, D_{ij} is the diffusivity of vapor i in the background gas j , M_i is the molecular weight of vapor, and T_s is the droplet surface temperature, which is approximately the bulk gas temperature for slow evaporation.

The vapor pressure can also be determined from the mass flux in the free-molecule regime. From Eq. (3.33) one may write P_i^0 by

$$P_i^0 = \frac{4RT_s}{\alpha_e \bar{c}_i M_i} J_{k, \text{fm}}, \quad (8.6)$$

in which α_e is the evaporation coefficient and \bar{c}_i is the mean speed of vapor defined by Eq. (3.22). The value of α_e was reported to be near unity for all liquids by various investigators (Paul, 1962; Mau, 1967; Bradley, 1949). This was also confirmed in the present study.

Davis and his associates (1974, 1978, 1981) obtained vapor pressures for DBP and several other organic from evaporation rate data using Eq. (8.5). Equation (8.6) was employed by Richardson *et al.* (1986) to determine the vapor pressure of sulfuric acid droplets, and by Tang and Munkelwitz (1991) for DOP and other organics. In those studies the evaporation coefficient was assumed unity. In present work the vapor pressures of DBP in the temperature range 263.3 - 302.0 K were determined by applying Eq. (8.6).

The vapor pressures estimated using Eq. (8.6) with $\alpha_t = 1.0$ are listed in Table 8.1 together with the droplet surface temperature and mass flux in the free-molecule regime, $J_{k, \text{fm}}$. Ray, Davis and Ravindran (1979) obtained vapor pressures for DBP in the temperature range 279.7-285.7 K and proposed a correlation, based upon their

measurements and reported data at higher temperatures (300~370 K), to predict the vapor pressure over a much wider range of temperature. The equation may be written as

$$\log p_i^0 = -\frac{4993}{T} + 14.342, \quad (8.7)$$

in which P_i^0 is in pascals. Although Eq. (8.7) broadly agrees with vapor pressure data over several orders of magnitude, it underpredicts the vapor pressure data measured by Ray *et al.*

Table 8.1. Measured mass flux and vapor pressure of DBP at different temperatures.

Particle	Temperature (K)	$J_{k, fm}$, Mass flux (kg/m ² s)	Vapor Pressure $\times 10^5$ (Pa)
0520s	263.3	2.32	5.15
0522t	264.5	2.90	6.45
0524v	267.4	5.65	12.6
0605h	278.0	17.1	39.0
0526z	282.0	23.7	54.5
0512a	286.2	42.0	97.2
0512c	297.7	122	288
0514d	297.8	138	326
0514e	297.7	130	307
0517g	297.7	126	298
0603a	302.0	177	422

The vapor pressures given in Table 8.1 are plotted in Fig. 8.4 together with the data of Ray *et al.* The new data show more scatter than those of Ray *et al.*, but the agreement

between the results are good. As mentioned above, Ray *et al.* computed the vapor pressure from Eq. (8.5), which did not require any assumption about the evaporation coefficient. The agreement shown in Fig. 8.4 suggests that the evaporation coefficient for DBP is unity. The vapor pressure data of the present work can be correlated by the equation

$$\log p_i^0 = -\frac{3900.5}{T} + 10.512, \quad (P_i^0 \text{ in Pa}) \quad (8.8)$$

which is also plotted in Fig. 8.4 by the solid line.

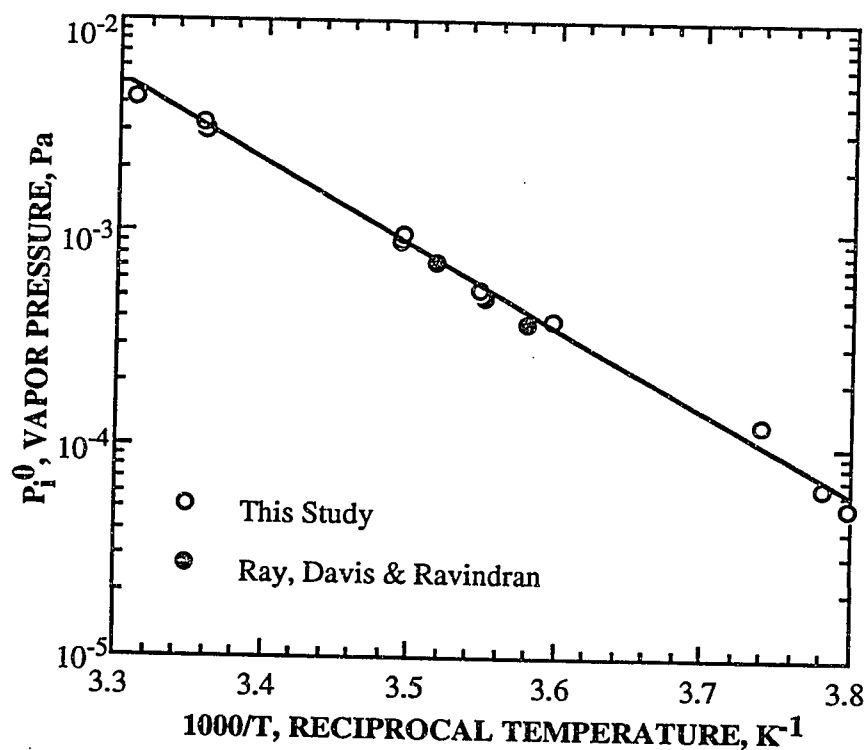


Figure 8.4 Comparison among the vapor pressures of DBP reported by Ray *et al.* (1979) and the results of this work estimated from the evaporation rate in the free-molecule regime.

The temperatures listed in Table 8.1 were measured by a 0.05 mm K-type thermocouple after the chamber had reached a thermal steady state at atmospheric pressure.

The thermocouple was fixed near the balance center where the droplet was trapped. During the experiment it was removed to avoid disturbing the electric field. Some uncertainty is expected to be involved in the temperature measurements since a small amount of air was bled into the chamber to remove any accumulated DBP vapor. If the air did not reach thermal equilibrium with the heat exchangers in the chamber, the measured temperature at atmospheric pressure would deviate from the actual droplet temperature. The scatter in the vapor pressures shown in Fig.8.4 may be attributed to the uncertainty in the droplet temperature. In order to reduce the uncertainty, the air introduced into the chamber should be kept at the same temperature as that of the particle.

8.1.3 Comparison between Experiment with Theory

It is convenient to compare theories and experiments based upon the mass flux ratio $J_k/J_{k,fm}$, in which J_k is the mass flux at any system pressure. According to the various theories of evaporation, this ratio should be a function of Kn. In the present work only the evaporation data at room temperature (297.7 K) were used to compare theory and experiment because of the uncertainty in droplet temperature at other temperatures. The data at room temperature should be accurate and reliable since the uncertainty was minimal at room temperature. During the experiments, the room temperature was found to fluctuate about one degree from earlier morning to late afternoon, so the thermal bath was used to circulate fluid through the heat exchangers in the chamber. The bath temperature was set at 297.7 K.

The mean free path of DBP vapor in air, λ_i , was calculated from the following relationship proposed by Jeans (1925) for rigid-sphere molecules

$$\lambda_i = [\pi(n_i\sigma_{ii}^2\sqrt{2} + n_j\sigma_{ij}\sqrt{1+M_i/M_j})]^{-1}, \quad (8.9)$$

where σ_{ii} and σ_{ij} are collision diameters for the like- and unlike-molecule interactions respectively, and n_i and n_j are the number densities of molecules i and j . The mean diameters estimated for air-air and DBP-DBP molecule interactions are, respectively, 3.62 and 8.29 Å, which gives the mean diameter $\sigma_{ij} = (\sigma_{ii} + \sigma_{jj})/2 = 5.96$ Å. For low-volatility DBP, n_i is much less than n_j , so the first term in Eq. (8.9) can be neglected. Using $n = P/k_B T$ where k_B is the Boltzmann constant, we may rewrite Eq. (8.9) as

$$\lambda_i = \frac{1}{\pi n_j \sigma_{ij} \sqrt{1 + M_i / M_j}} = 3.8802 \times 10^{-6} \frac{T}{P}, \quad (\lambda_i \text{ in m}) \quad (8.10)$$

in which P is the system pressure in Pa and T is the absolute temperature of system. The Knudsen number can be calculated using Eq. (8.10) for λ and the measured particle size, a .

An alternative approach to defining the mean free path has been used in the literature. This is based on the binary diffusivity of vapor molecules. The definitions among various theories are inconsistent, so it is necessary to establish a definitive relationship between λ_i and D_{ij} to adjust the Knudsen number. In the present study the theories of Fuchs and Sutugin (1970), Loyalka and his associates (1982, 1989) and Sitarski and Nowakowski (1979) were examined (all were reviewed in Chapter 3). The relationship for λ_i used by Fuchs and Sutugin was based on the simple kinetic theory of gases for hard sphere molecules,

$$\lambda_{i,D} = 3 \frac{D_{ij}}{\bar{c}_i}. \quad (8.11)$$

Loyalka and his associates applied the following formula for the mean free path,

$$\lambda_{i,L} = 2D_{ij} \left(\frac{m_i}{2k_B T} \right)^{1/2} = \frac{4}{\sqrt{\pi}} \frac{D_{ij}}{\bar{c}_i}. \quad (8.12)$$

Sitarski and Nowakowski defined the mean free path by

$$\lambda_{i,S-N} = \frac{32(1-\Delta) D_{ij}}{3\pi(1+Z) \bar{c}_i}, \quad (8.13)$$

in which $Z (= m_i/m_j)$ is the mass ratio of vapor molecule to the background gas molecule, and Δ is given by

$$\Delta = \frac{1}{10(1+Z)}. \quad (8.14)$$

The low-order diffusivity $D_{ij}^{(0)}$ for the rigid-sphere molecules can be written as

$$D_{ij}^{(0)} = \frac{3k_B^{3/2} [T^3(M_i + M_j) / 2M_i M_j]^{1/2}}{8\sqrt{2\pi} P \sigma_{ij}^2} \text{ in m}^2/\text{s}, \quad (8.15)$$

As pointed out by Hirschfelder, Curtiss and Bird (1954), only in the simple kinetic theory of gases is the mean free path directly related to the transport coefficient of diffusivity, thermal conductivity and viscosity. The first-order approximation for the binary diffusivity, $D_{ij}^{(1)}$, based upon the molecular interaction potential of Lennard-Jones, was given by Chapman and Cowling (1970),

$$D_{ij}^{(1)} = \frac{D_{ij}^{(0)}}{\Omega_{D,ij}}, \quad (8.16)$$

in which $\Omega_{D,ij}$ is the collision integral, a function of the dimensionless temperature $k_B T / \epsilon_{ij}$, where ϵ_{ij} is the Lennard-Jones molecular interaction parameter tabulated by Bird, Steward

and Lightfoot (1960) and others for common gases. The estimated value of $\Omega_{D,ij}$ for DBP in air is 1.36 at $T = 297.7$ K.

The binary diffusivity of DBP molecules in air can be determined from the measurements of mass fluxes in the continuum and free-molecule regimes. Based upon Eqs.(3.29) and (3.33), one may write

$$D_{ij} = \frac{a\bar{c}\alpha_e}{4} \frac{J_k}{J_{k,fm}}. \quad (8.17)$$

The diffusivities determined from two sets of experimental data using Eq. (8.17) are shown in Table 8.2 (in the calculation α_e is assumed to be unity). Also listed in the table are values estimated from Eqs. (8.15) and (8.16).

Table 8.2 Comparison among the diffusivities of DBP in air estimated from the flux measurements, and the values determined from theories.

Parameter	Case 1	Case 2
Pressure, Torr	102.97	53.42
Temperature, K	297.7	297.7
Particle size, μm	14.01	13.6
Measured $J_k/J_{k,fm}$	0.05445	0.1026
Knudsen Number	0.0058	0.0117
D_{ij} by Eq. (8.17), m^2/s	2.86×10^{-5}	5.25×10^{-5}
D_{ij} by Eq. (8.16), m^2/s	2.87×10^{-5}	5.53×10^{-5}
D_{ij} by Eq. (8.15), m^2/s	3.90×10^{-5}	7.52×10^{-5}

If the mean free path is approximated by Eq. (8.10), and if the diffusivity is calculated from Eq. (8.16), the mean free path may be written in the form

$$\lambda_i = \frac{32\Omega_{D,ij}}{3\pi(1+\frac{m_i}{m_j})} \frac{D_{ij}^{(1)}}{\bar{c}_i} = \frac{32}{3\pi(1+\frac{m_i}{m_j})} \frac{D_{ij}^{(0)}}{\bar{c}_i} \quad (8.18)$$

Equation (8.18) was employed to adjust the Knudsen numbers to be consistent with the various theories.

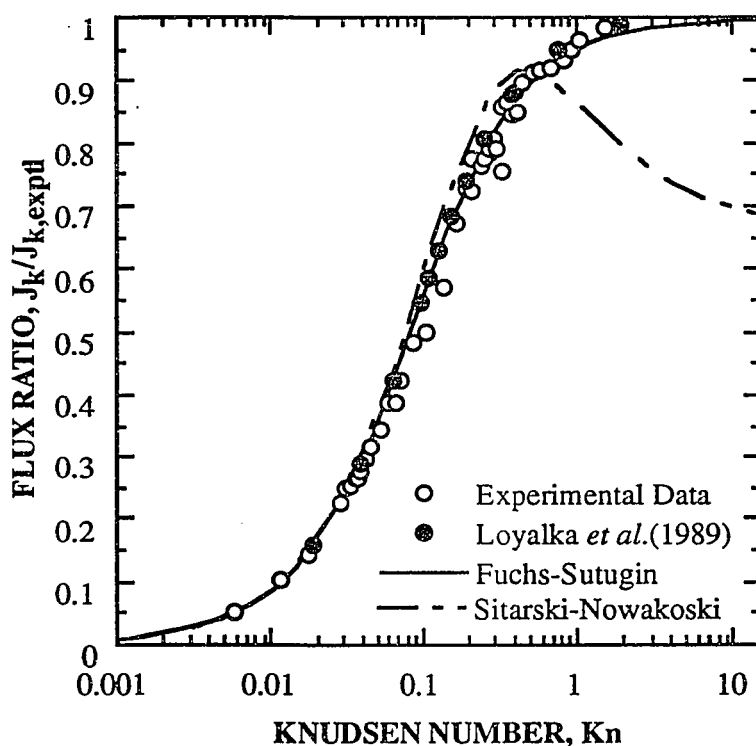


Figure 8.5 Flux ratio at various Kn based upon the measured flux in the free-molecule limit compared with the theories of Loyalka *et al.* (1989), Sitarski and Nowakowski (1979) and Fuchs and Sutugin (1970).

A comparison among experiment and theories is presented in Fig. 8.5. The data were based upon the measurements of four DBP droplets at 297.7 ± 0.1 K. The mass fluxes were normalized by the value in the free-molecule limit measured at the lowest pressure. Also shown in the figure are the solution of Fuchs-Sutugin (1970) for $Z \rightarrow 0$, the

numerical data of Loyalka *et al.* (1989) based upon $Z = 10$, and the 13-moment prediction by Sitarski and Nowakowski (1979) for $Z = 10$. For DBP in air, Z is close to 10. The interpolation formula of Loyalka (1982) is not included in the figure for it falls on the line representing the Fuchs-Sutugin equation. The agreement among the theories and experiments is good except for the moment solution of Sitarski and Nowakowski at larger Kn . At $0.1 < Kn < 0.4$, measurements slightly fall below the moment predictions and at large Kn the theory fails.

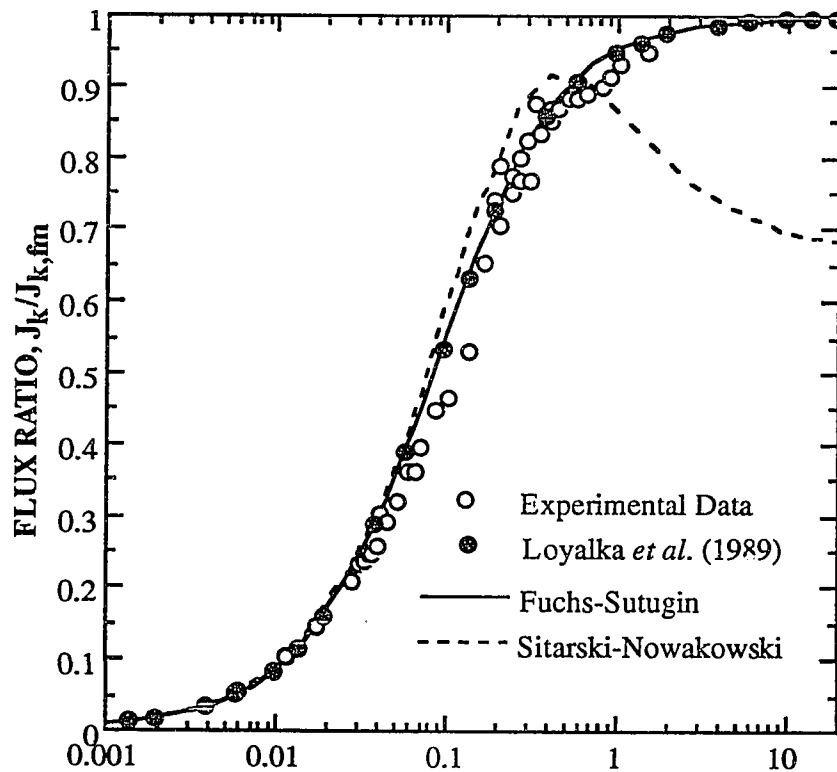


Figure 8.6 Flux ratio at various Kn based upon the flux calculated from Eq. (3.33) for the free-molecule limit compared with the theories of Loyalka *et al.* (1989), Sitarski and Nowakowski (1979) and Fuchs and Sutugin (1970).

A slightly different comparison among theory and experiment is made in Fig. 8.6. Instead of using the measured asymptotic mass flux, the value determined from Eq. (3.33)

using unity for the evaporation coefficient and the vapor pressure calculated using Eq. (8.8) was employed to normalize the mass flux. This comparison tends to reduce the scatter of data. The evaporation rate data in the transition regime fall slightly below the theoretical values.

The effect of the mass ratio, Z , on the evaporation rate was not examined in this work. Based upon the theoretical study of Loyalka *et al.* (1989) and Monchick and Reiss (1988), the effects are very small. It should be interesting to measure the evaporation rates in helium and carbon dioxide and compare the results to explore the effects of the surrounding gas.

8.2 Effects of PMMA Polymer on DBP Evaporation

The effects of PMMA polymer on the evaporation of DBP droplets were also examined in this study. A 5 wt% polymer solution was prepared by mixing the powder and DBP for about 24 hours. The solution was found to be highly viscous, and the micrometer size particles could not be generated by means of the electrified hypodermic needle. Thus, a dilute solution with 0.986 wt% polymer was then prepared. The evaporation of DBP leads to an increase in the polymer concentration since PMMA is non-volatile and remains in the particle during evaporation.

A single particle was trapped in the balance at atmosphere pressure, and a phase function was immediately collected to obtain the initial particle size, a_0 . The mass of polymer within the particle was determined from the initial concentration. The chamber was then evacuated. The size variations during pumping were followed by obtaining phase functions and MDRs. The recorded phase functions were similar to those for pure DBP component. The MDR data obtained at different times and at a temperature of 284 K are shown in Fig. 8.7. Compared with the data for the pure component shown in Fig. 4.16, the MDRs in Fig. 8.7 have slightly different features. The evaporation rate of a pure

component DBP droplet should be constant at any fixed pressure and temperature. In this case MDRs will be evenly distributed with respect to the time. However, in Fig. 8.7 peak spacing is seen to increase as evaporation proceeded. This indicated that the evaporation rate was greatly reduced as the polymer concentration increased.

The mass fluxes determined from the elastic scattering data are plotted in Fig. 8.8 for three temperatures as a function of the polymer concentration. The weight concentrations of polymer were computed by

$$W_t = \frac{a_0^3}{a(t)^3} W_{t,0}, \quad (8.19)$$

in which W_t is the polymer concentration at any time, t , with the particle radius, $a(t)$. $W_{t,0}$ is the initial weight concentration of polymer which is 0.986%. In the derivation of Eq. (8.19) the variation of particle density during evaporation was neglected for the polymer density is 1100 kg/m^3 , close to that of DBP ($\rho = 1043 \text{ Kg/m}^3$). The refractive index of PMMA polymer is unknown, so the index of DBP was assigned in the interpretation of MDR data for the binary-component particle. The highest concentration of polymer reached in the evaporation was less than 8 wt%, and some error may be involved in the use of the refractive index of DBP.

It can be seen that the mass flux was reduced significantly even at a concentration of 1 wt%. At 284 K the evaporation process was almost stopped as the concentration of PMMA reached 8 wt%. It is not clear how the polymer lowers the vapor pressure of DBP. In the binary evaporation study by Taflin *et al.* (1988), they found that the evaporation of water droplet was dramatically decreased once the concentration of SDS reached 10% of the critical micelle concentration (CMC). It is believed that a monolayer was formed at the surface which prohibited the water molecule escaping from the droplet surface. In present

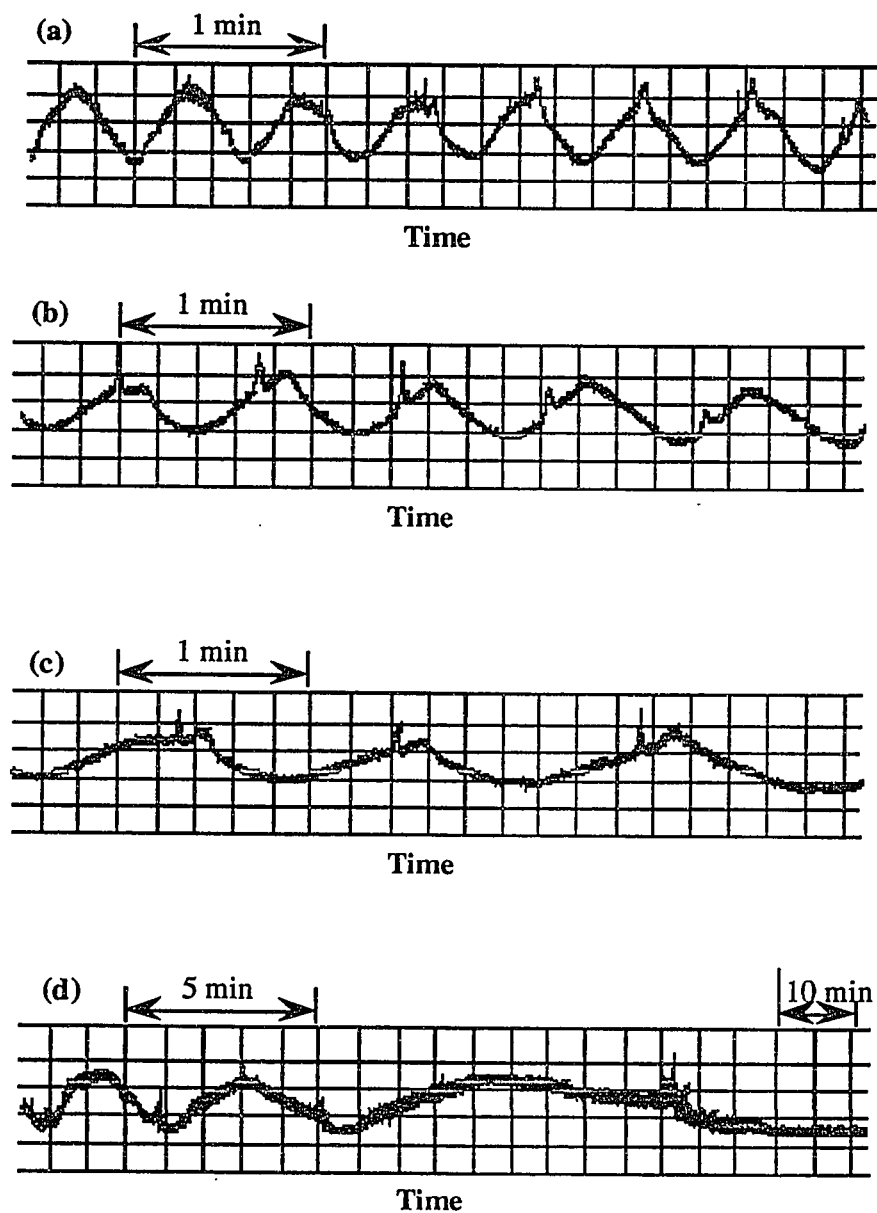


Figure 8.7 A sequence of resonance spectra obtained in the free-molecule regime and $T = 284$ K for an evaporating droplet, initially consisting of DBP and 0.986 wt% PMMA polymer.

experiment PMMA may precipitate and form a shell on the particle surface which prevents the evaporation of DBP molecules.

8.3 Evaporation Study of a Tin Catalyst Droplet.

Stannous octanoate (SNO) is a widely used commercial catalyst. It is used as a curing agent in vulcanizing silicones, and employed to stabilize rigid polyvinyl chloride and to manufacture rigid and flexible polyurethane foams (Diez *et al.*, 1988). Usually, it is produced by reacting stannous oxide (SnO) with an excess of 2-ethylhexanoic acid (EHA) according to the reaction,

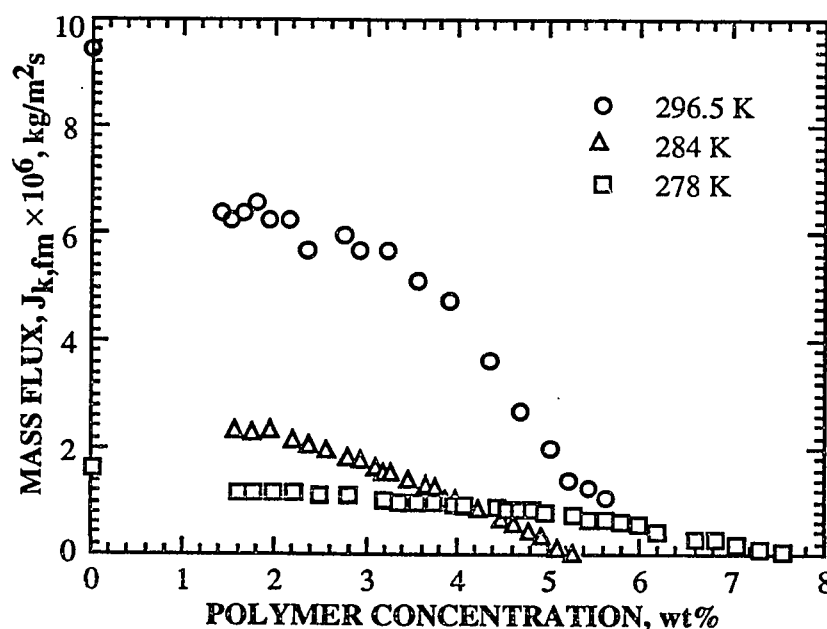
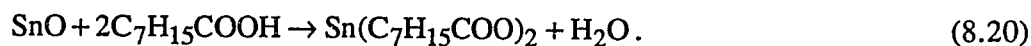


Figure 8.8 Mass flux measured in the free-molecule regime for evaporating droplets consisting of DBP and polymer at various weight concentrations of polymer and various temperatures.



The tin compound is a potentially hazardous material. The vapor pressures of SNO and EHA were measured at atmospheric pressure by Allen (Allen, 1992) using elastic scattering to follow the evaporation rate. Raman spectra were also used to explore the composition change during the evaporation process. Before this study no Raman data were available for SNO.

The chemicals EHA (99%) and SNO used in present study were supplied by Sandia National Laboratories. Measurements were made on the apparatus B, which was briefly described in Chapter 4.

The Raman spectrum for a microdroplet of EHA in the wavenumber range $1000\text{-}1800\text{ cm}^{-1}$ is shown in Fig 8.9 together with the bulk spectrum of EHA reported by Sadtler (1973). The agreement between them is reasonably good. The Raman data of the droplet are somewhat noisier than the bulk spectrum, which may be due to the low intensities of inelastic scattering signals from the small droplet. The Raman peak around 1650 cm^{-1} corresponds to the C = O bond, and the peaks at about 1450 cm^{-1} and 1300 cm^{-1} are associated with CH_2 bending and CH_2 wagging, respectively. The portion of the spectrum located near 1600 cm^{-1} in Fig. 8.9 for the microdroplet has a side peak at 1574 cm^{-1} , which corresponds to a weak laser line. Use of an optical filter can eliminate the weak laser line but decreases the signal-to-noise ratio of the Raman spectrum, so the argon-ion laser beam was not filtered. The normalized power of 488 nm line used was 1.0 W for these measurements.

A sequence of Raman spectra obtained at different times for an evaporating catalyst droplet is presented in Fig. 8.10. The evaporation process was studied over a long time interval, so the logarithm of the time in minutes is used in the figure. The actual times for the four spectra shown in Fig. 6.11 are 6, 74, 243 and 871 minutes, respectively. A distinct change can be observed in the spectra in the wavenumber region $1600\text{ - }1800\text{ cm}^{-1}$ as evaporation proceeded. In the earlier spectra a very small peak at $\sim 1700\text{ cm}^{-1}$ and a

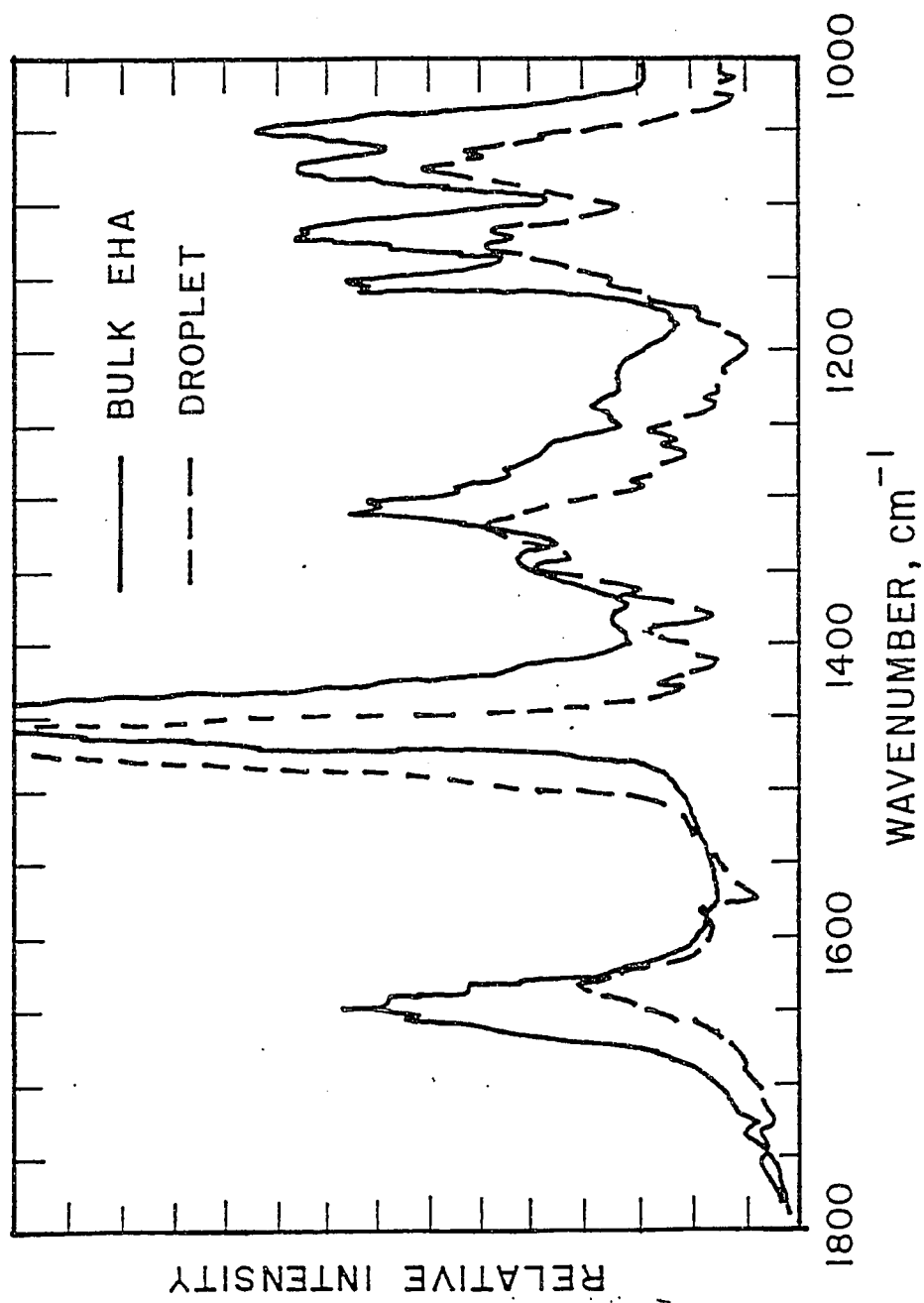


Figure 8.9 Comparison among the Raman spectrum of microdroplet of EHA and the spectrum of bulk sample by Sadtler (1973).

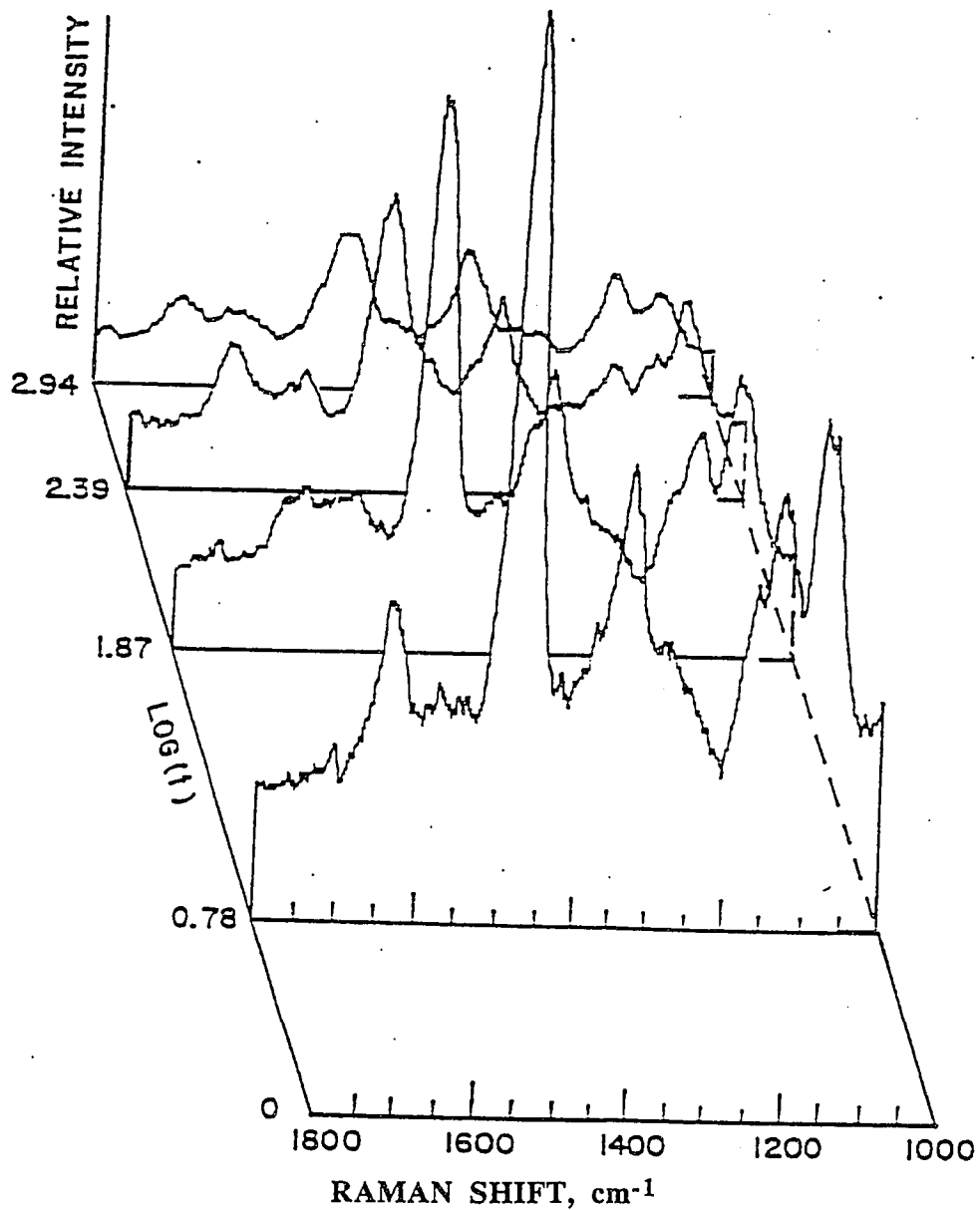


Figure 8.10 Raman spectra obtained at different time of evaporation for a droplet of catalysis consisting of EHA and SNO.

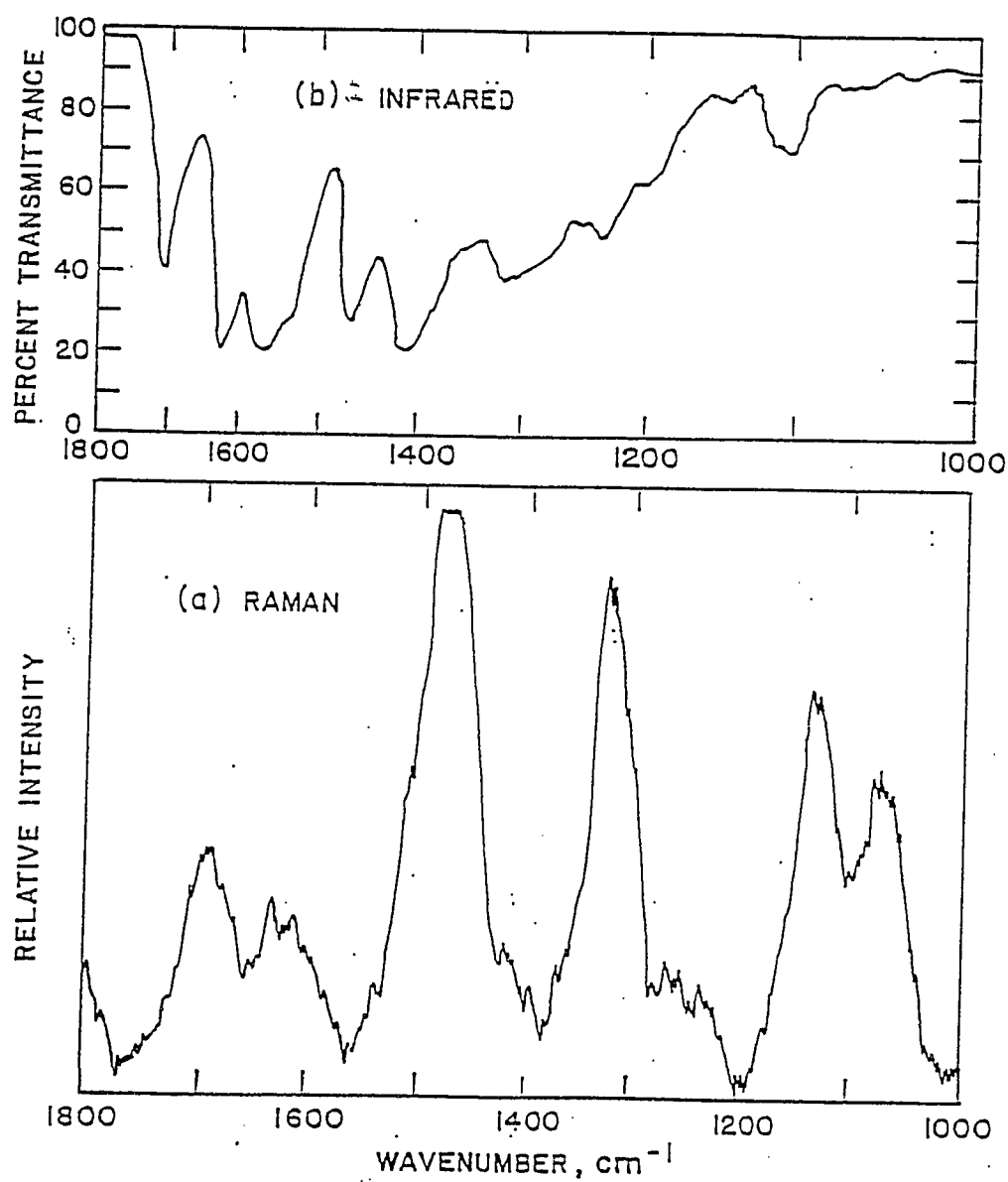


Figure 8.11 A Raman spectrum (a) for the remaining material of an evaporating droplet of tin catalysis and the infrared spectrum (b) for bulk SNO by Sadtler (1966).

relatively large peak at about 1635 cm^{-1} are shown, but after a few hours, the peak at 1635 cm^{-1} vanished. Instead, two peaks at 1610 and 1700 cm^{-1} became more pronounced. Comparison of the earlier spectra with the Raman data for an EHA droplet reveals that the catalysis droplet consisted mainly of EHA in the early stage of evaporation, but as EHA evaporated from the droplet, the Raman characteristics of the second component became dominant. The observed Raman spectra at later times should be that of SNO. The variation of DC levitation voltage confirmed that the catalysis droplet consisted of about 70 wt% EHA initially.

No Raman data are available in literature for bulk SNO, but the Raman spectrum obtained at the end of evaporation experiments can be compared with the infrared absorption spectrum for SNO taken from Sadtler (1966). Infrared absorption and Raman scattering are two complementary techniques for exploring molecular chemistry. The peaks at approximately 1330 , 1480 , 1600 and 1700 cm^{-1} appear in both spectra, indicating that the materials remaining in the droplet after long time evaporation were indeed SNO. Since spectroscopic grade SNO is not available, the Raman spectra for pure SNO droplet cannot be measured. Based upon the measurements for the catalyst droplet, the main differences between the Raman spectra for EHA and SNO lie in the wavenumber region $1550 - 1800\text{ cm}^{-1}$.

8.4 Conclusion

The evaporation rates of single DBP droplets in the transition regime were measured. The results fall in agreement with the theoretical solution of Fuchs and Sutugin and with the numerical results of Loyalka *et al.* for $Z = 10$. The theory of Sitarski and Nowakowski slightly overpredicts the rate in the range $0.04 < Kn < 0.4$ and fails for large Kn numbers. The vapor pressures at the temperature range $263\text{-}302\text{ K}$ were determined from the measured asymptotic mass flux. The new data agree with the results of Ray *et al.*, which

were estimated from droplet size change in the continuum regime. The evaporation coefficient of DBP in air was found to be approximately unity.

The effects of PMMA polymer on the mass flux of DBP were experimentally explored. It was found that the evaporation rates were reduced significantly even at the polymer concentration about 1 wt%.

The evaporation of toxic aerosol consisting of 2-ethylhexanoic acid and stannous octanoate was examined by the Raman spectroscopy. This is the first Raman spectra reported for SNO. The differences between Raman spectra for EHA and SNO were found to be in the wavenumber range 1550-1800 cm^{-1} .

CHAPTER 9

CONCLUSIONS

The main purpose of this research was to explore the phenomena associated with single microparticles using the light scattering techniques and DC levitation voltage measurements. Three processes have been investigated experimentally: gas/droplet reactions, the thermophoretic force and droplet evaporation in the Knudsen regime. These studies have been achieved using three electrodynamic balances (EDB) which have different functions, as summarized in Chapter 4. One balance was developed in this work for thermophoretic force and evaporation measurements. It coupled the double-ring electrodynamic balance with facilities for elastic scattering measurements, a vacuum system and constant temperature sources. It has been demonstrated that using this device one can obtain reproducible results for TF and evaporation rates in the Knudsen regime.

Measurements of the TF were carried out in helium, air and carbon dioxide for microdroplets of dioctyl phthalate (DOP) and microspheres of polystyrene latex (PSL), nickel and glass. It was found that the TF in each gas reached a maximum at $Kn \sim 3$, and beyond that the TF decreased instead of reaching the asymptotic solution as predicted by theories. The apparent decrease in TF was accounted for the "temperature jump" effect at the copper plates and for wall effects of the chamber. The "effective" temperature gradient was determined using the relationship of Devienne for heat transfer in the Knudsen regime. The thermal accommodation coefficients for copper in the three gases obtained by adjusting the temperature gradient were found to be significantly lower than values reported by Springer (1971), and by Saxena and Joshi (1981) for clean copper surfaces.

The experimental results of TF in three gases have good reproducibility. The results are not affected by the "slip" and wall effects in air and CO_2 for $Kn < 3.0$, and for $Kn < 1.0$ in helium. The data were used to evaluate various theories of thermophoresis in the

near-continuum and transition regimes. The results in air and CO₂ were found to agree well with Loyalka's (1992) results obtained by solving the linearized Boltzmann equation, and agree with Brock's (1962) hydrodynamic solution in the near-continuum regime. The moment solutions of Phillips and Dwyer are found to be inadequate to predict TF in air at any Kn. The analytical solutions of Brock (1967a) and of Ivchenko and Yalamov (1970) for TF in the transition were also examined using the data in air. It was found that Brock's theory reasonably agree with the data at $Kn > 0.3$, and the results of Ivchenko and Yalamov fall above the experimental results.

The experimental data in helium for four types of microparticles are somewhat higher compared with the numerical results of Loyalka (1992), of Yamamoto and Ishihara (1988) and of Sone and Aoki (1983), obtained for $\alpha_t = 1.0$. The assumption of diffuse gas/molecule interaction is unrealistic for helium molecules reflecting from various surface based upon prior studies (Saxena and Joshi, 1981). It is believed that the factor of α_t contributes to the disagreement between measurements and theories.

The effects of the thermal conductivity of the particle on the TF was found to be small, while the force depends strongly on the thermal conductivity of the gas. The charge effects on TF were investigated in this study for the first time. Negatively-charged particles were found to experience a larger force than those positively-charged.

The "negative" thermophoretic force, predicted by Sone and others for high thermal conductivity sphere at $Kn \sim 0.1$, was not observed in the experiments for glass and nickel spheres in the three gases used.

Evaporation measurements were performed on droplets of dibutyl phthalate (DBP) in air in the temperature range 263-302 K. The vapor pressures of DBP determined in this work from the mass flux in the free-molecule regime agree with the results of Ray *et al.* (1979), which are estimated from evaporation rates measured in the continuum regime. The agreement indicated that the evaporation coefficient of DBP in air is close to unity, as

assumed in the calculations. A new correlation was proposed to predict the vapor pressure of DBP over a wide temperature range. The evaporation rates at 297.7 K were used to evaluate vaporation theories for the Knudsen regime. It was found that the theories of Fuchs-Sutugin (1970) and of Loyalka *et al.* (1989) agree with the data, but the moment solution of Sitarski and Nowakowski (1979) does not predict the force correctly in the near-free molecule regime.

Elastic and Raman scattering were employed to follow the reaction between a droplet of titanium ethoxide and water vapor. The reaction leads to the formation of a coated microsphere, consisting of a TTE core and a TiO_2 shell. It was demonstrated that one can determine the shell thickness and refractive indices of the core and shell by comparing the recorded light scattering data with the scattering theory of Aden and Kerker for coated spheres. Very little work has been done to use Raman scattering to study dynamic processes. In this work Raman spectroscopy was used to follow the reaction, and it is shown that the change of chemical components within the particle during reaction can be monitored by Raman spectroscopy.

Further study on the effects of surface charge on the thermophoretic force should be interesting, since it is possible to vary the thermal deposition process by applying different charges on the particle surface.

LIST OF REFERENCES

- Aardahl, C. L. and E. J. Davis, "Gas/Aerosol chemical reaction in the NaOH-SO₂-H₂O system", submitted to *Appl. Spectros.* (1995).
- Abramowitz, M. and I. A. Stegun, Handbook of Mathematical Functions, U.S. Government Printing Office, Washington, D.C., 1964.
- Aden, A. L. and Kerker, M. "Scattering of electromagnetic waves from two concentric spheres", *J. Appl. Phys.*, **22**:1242 (1951).
- Allen, T. M., "Heat and mass transfer studies of single microparticles via elastic and inelastic light scattering", Ph. D. Dissertation, University of Washington, Seattle, WA, 1992.
- Annis, B. K., "Thermal creep in gases", *J. Chem. Phys.*, **57**:2898 (1972).
- Arnold, S., and L. M. Folan "Spherical void electrodynamic levitator", *Rev. Sci. Instrum.* **58**:1732 (1987).
- Ashkin, A., "Acceleration and trapping of particles by radiation pressure", *Phys. Rev. Lett.*, **24**:156 (1970).
- Ashkin, A., and J. M. Dziedzic, "Feedback stabilization of optically levitated particles", *Appl. Phys. Lett.*, **30**:202 (1977).
- Bakanov, S. P. "Future direction for experiments in thermophoresis: a commentary", *J. Aerosol Sci.*, **26**:1 (1995).
- Bakanov, S. P., "Thermophoresis in gases at small Knudsen number", *Aerosol Sci. Tech.* **15**:77 (1991).
- Bakanov, S. P. and B. V. Derjaguin, *Koll. Zh.* **21**:365 (1959).
- Balachandran, U. and N. G. Eror, "Raman spectra of titanium dioxide", *J. Solid State Chem.*, **42**:276 (1982).
- Baule, B., *Ann Physk*, **44**:145 (1914).
- Bhatnagar, P. L., E. P. Gross and M. Krook, "A model of collision processes in gases", *Phys. Rev.*, **94**, 511 (1954).
- Bhagavavtam, S., Scattering of light and Raman effect, Chemical Publishing Co. Inc., New York, 1942.
- Bird, R. B., W. E. Stewart and E. N. Lightfoot, Transport Phenomena, Wiley, New York, 1960.
- Bohren, C. F., and D. R. Huffman, Absorption and Scattering of Light by Small Particles, Wiley and Sons, New York, 1983.

- Bradley, G. S., M. G. Evans and R. W. Whytlaw-Gray, "The rate of evaporation of droplet: Evaporation and diffusion coefficients, and vapor pressure of dibutyl phthalate and butyl stearate", *Proc. Roy. Soc.*, **186A**:368 (1946).
- Bradley, G. S. and A. D. Shellard "The rate of evaporation of droplet III: Evaporation and rates of evaporation of straight-chain paraffin hydrocarbons", *Proc. Roy. Soc.*, **198A**:239 (1949).
- Brock, J. R., "The thermal force in the transition Regime", *J. Colloid Interface Sci.*, **23**:448 (1967a).
- Brock, J. R., "On radiometer force", *J. Colloid Interface Sci.*, **25**: 564 (1967b).
- Brock, J. R., "Highly nonequilibrium evaporation of moving particles in the transition region of Knudsen number", *J. Colloid Interface Sci.*, **24**: 344 (1967c).
- Brock, J. R., "On the theory of thermal forces acting on aerosol particles", *J. Colloid Interface Sci.*, **17**:768 (1962).
- Buehler, M. F., "Raman spectroscopy of levitated microparticles", Ph. D. Dissertation, University of Washington, Seattle, WA, 1991.
- Buehler, M. F., T. M. Allen and E. J. Davis, "Microparticle Raman spectroscopy of multicomponent aerosols", *J. Colloid Interface Sci.*, **146**:79 (1991).
- Cawood, W. "Dispersed system in gases: Dust, Smoke and Fog", PP. 1068, Faraday Society General Discussions, Gurney and Jackson, London, 1936.
- Chapman, S. and T. G. Cowling, Mathematical Theory of Non-Uniform Gases, Cambridge Univ. Press, Cambridge, 1953.
- Chew, H., P. J. McNulty and M. Kerker, "Model for Raman and fluorescent scattering by molecules embedded in small particles", *Phys. Rev. A*, **13**:396 (1976).
- Chew, H., M. Sculley, M. Kerker, P. J. McNulty and D. D. Cooke, "Raman and fluorescent scattering by molecules embedded in small particles: results for coherent optical processes", *J. Opt. Soc. America*, **68**:1686 (1978).
- Chirifu, S., S. Sakata, M. Inoue, T. Yoshida and T. Okada, "Study of aerosol deposition on wafer surface (part 1): experimental analysis", Proc. 5th Symp. Aerosol Sci. & Tech., Japan Association of Aerosol Science and Technology, Tsukuba, Japan, pp. 102-105, 1987.
- Chylek, P., V. Ramaswamy, A. Ashkin and J. M. Dziedzic, "Simultaneous determination of refractive index and size of spherical dielectric particles from light scattering data", *Appl. Opt.* **22**:2302 (1983).
- Conwell, P. R., P. W. Barber and C. K. Rushforth, "Resonant spectra of dielectric spheres", *J. Opt.Soc. America: A*, **1**:62 (1984).

- Cooper, D. W., M. H. Peters and R. J. Miller, "Predicted deposition of submicrometer particles due to diffusion and electrostatics in viscous axisymmetric stagnation-point flow", *Aerosol Sci. Tech.*, **11**:133 (1989).
- Davis, E. J. and M. A. Bridges, "The Rayleigh limit of charge revisited: light scattering from exploding droplets", *J. Aerosol Sci.*, **25**:1179 (1994).
- Davis, E. J., "Microchemical engineering: the physics and chemistry of the microparticle", in Advances in Chemical Engineering, Vol. **18**, Academic Press, New York, PP. 1-94, (1992).
- Davis, E. J., and E. Chorbajian, "The measurement of evaporation rates of submicron aerosol droplets", *Ind. Eng. Chem. Fundam.*, **13**:272 (1974).
- Davis, E. J., and R. Periasamy, "Light scattering and aerodynamic size measurements for homogeneous and inhomogeneous microspheres", *Langmuir*, **1**:373 (1985).
- Davis, E. J., P. Ravindran and A. K. Ray, "Single aerosol particle studies", *Advances in Colloid and Interface Science*, **15**:1 (1981).
- Davis, E. J., Ray, A. K. and Chang, R., "Experimental determination of aerosol evaporation rates at large and small Knudsen number", *A.I.ChE. Symposium Series* **175**, 74:190 (1978).
- Davis, E. J., and A. K. Ray, "Determination of diffusion coefficients by submicron droplet evaporation", *J. Chem. Phys.*, **67**:414 (1977).
- Davis, L. A. and Adair III, T. W., "Thermal force on a sphere", *J. Chem. Phys.*, **62**: 2278 (1975).
- Debye, P., "Der Lichtdruck auf Kugeln von beliebigem Material", *Ann. Physik*, **30**:57 (1909).
- Derjaguin, B. V. and Yu. Yalamov, "Theory of thermophoresis of large aerosol particles", *J. Colloid Sci.*, **20**:555 (1965).
- Derjaguin, B. V. and Storozhilova, A. I. and Ya. I. Rabinovicj, "Experimental verification the theory of thermophoresis of aerosol particles", *J. Colloid Interface Sci.*, **21**: 35 (1966).
- Derjaguin, B. V. and Yalamov, Yu., "The theory of thermophoresis and diffuphoresisi on aerosol particle and their experimental application" In International Review in Aerosol Physics and Chemistry, Vol. 3, Edit by G. M. Hidy and J. R. Brock, 1972.
- Derjaguin, B. V., Y. I. Rabinovich, A. I. Storozhilova and G. I. Shcherbina,, "Measurement of the coefficient of thermal slip of gases and the thermophoresis velocity of large size aerosol particles", *J. Colloid Interface Sci.*, **57**:451 (1976).
- Devienne, F.M., "Heat transfer in the rarefied gases" in *Advances in Heat Transfer*. Vol. **2**, Academic Press, New York, pp. 272-352 (1965).

- Diez, F. V., H. Sastre and J. Coca, "Effect of the operating conditions on the preparation of stannous octanoate from stannous oxide", *Ind. Eng. Chem. Res.*, **27**:845 (1988).
- Dwyer, H. A., "Thirteen moment theory of the thermal force on a spherical particle", *Phys. Fluids*, **10**:976 (1967).
- Einstein, A., *Z. Phys.*, **27**:1 (1924).
- Epstein, P. S., "Zur Theorie des Radiometers", *Z. Physik* **54**:537 (1929).
- Foss, W. and E. J. Davis, "Formation of coated aerosol particles by simultaneously diffusion and chemical reaction", *J. Aerosol Sci.*, **25**:33 (1994).
- Foss, W., W. Li, T. M. Allen, D. S. Blair and E. J. Davis, "Studies of toxic aerosols via elastic and inelastic light scattering," *Aerosol Sci. Tech.*, **18**:187 (1993).
- Freiberg, J. E. and S. E. Schwartz, "Oxidation of SO₂ in aqueous droplets: mass-transport limitation in laboratory studies and the ambient atmosphere", *Atmospheric Environment*, **15**:1145 (1981).
- Frickel, R. H., R. E. Shaffer and J. B. Stamatoff, "Chambers for the electrodynamic containment of charged aerosol particles", Report No. ARCSL-TR-77041, Chemical Systems Laboratory, Aberdeen Proving Ground, Maryland, 1978.
- Fuchs, N. A., *Phys. Z. Sowjet*, **6**:224 (1934)
- Fuchs, N. A. and A. G. Sutugin, Highly Dispersed Aerosols, Ann Arbor Science Publishers, Ann Arbor, 1970.
- Fulton, J., Master's Thesis, University of Washington, Seattle, WA, 1985.
- Gorelov, S. L., *MZHG*, **5**:178, in Russian (1976).
- Gucker, F. T., and J. J. Egan, "Measurement of the angular variation of light scattered from single aerosol droplets", *J. Colloid Interface Sci.*, **16**:68 (1961).
- Hansen, A. D. A., Benner, W. H. and Novakov, T. "sulfur dioxide oxidation in laboratory clouds", *Atmos. Environ.*, **25A**:2521 (1991).
- Hartung, W. H. and Avedisian, C. T., "On the electrodynamic balance", *Proc. Roy. Soc. London A*, **427**:237 (1992).
- Hightower, R. L., C. B. Richardson, H. B. Lin, J. D. Eversole and A. J. Campillo "Measurements of scattering of light from layered microparticles", *Opt. Lett.* **9**:946 (1988).
- Hirschfelder, J. O., C. F. Curtiss and R. B. Bird, "Molecular theory of gases and liquids", Wiley, New York, 1954.
- Hirsh, G and E. Oskam, Electrical breakdown of gases, Edited by J. M. Meek and J. D. Craggs, John Wiley and Sons, New York, 1978.

- Incropera, F. P. and D. P. De Witt, Fundamentals of Heat and Mass Transfer, John Wiley and Sons, New York, 1990.
- Ingebretsen, B. J. and E. Matijević, "Kinetics of hydrolysis of metal aerosol droplets in the presence of water vapor", *J. Colloid Interface Sci.*, **100**:1 (1984).
- Ingebretsen, B. J. and E. Matijević, "Preparation of uniform colloidal dispersions by chemical reactions in aerosols—2. Spherical particles of aluminum hydrous oxide", *J. Aerosol Sci.*, **11**:271 (1980)
- Ivchenko, I. N. and Yu. I. Yalamov, "Thermophoresis of aerosol particles in the nearly free molecular regime", *SSSR, Mek. Zhi. GAZa*, Vol. **5**:3 (1970).
- Ivchenko, I. N. and Yu. I. Yalamov, "A hydrodynamic method for the calculation of the rate of thermophoresis of Moderately large involatile aerosol particles", *Russ. J. of Phys. Chem.*, **45**:317 (1971).
- Jacobsen, S. and J. R. Brock, "The thermal force on spherical sodium chloride aerosols", *J. Colloid Sci.*, **20**:544 (1965).
- Jeans, J. H. The Dynamical Theory of Gases, Cambridge University Press, Cambridge, 1925.
- Jeans, J., The Dynamical Theory of Gases, Dover Publications, New York, 1954.
- Kelly, G. E. and Senegers, J. V., "droplet growth in a dilute vapor", *J. Chem. Phys.*, **61**:2800 (1974).
- Kennard, E. H., Kinetic Theory of Gases, McGraw-Hill, New York, 1938.
- Kerker, M., The Scattering of Light and Other Electromagnetic Radiation, Academic Press, New York, 1969.
- Kerker, M., and S. D. Druger, "Raman and fluorescent scattering by molecules embedded in spheres with radii up to several multiples of the wavelength", *Appl. Opt.* **18**:1172 (1979).
- Kerker, M., P. J. McNulty, M. Sculley, H. Chew and D. D. Cooke, "Raman and fluorescent scattering by molecules embedded in small particles: numerical results for incoherent optical processes", *J. Opt. Soc. America*, **68**:1676 (1978).
- Kousaka, Y., K. Okuyama, S. Nishio, and T. Yoshida, "Experimental study of thermophoresis of aerosol particles", *J. Chem. Eng. Jpn.* **9**:147 (1976).
- Langmuir I., *Phys. Rev.* **12**:368 (1918).
- Law, W. S., "Motion of a sphere in a rarefied gas: drag and thermophoresis", Ph. D. Dissertation, University of Missouri-Columbia, Columbia, MO, 1985.

- Lea, K. C. and S. K. Loyalka, "Motion of a sphere in a rarefied gas" *Phys. Fluids*, **25**:1550 (1982).
- Lettieri, T. R., and R. E. Preston, "Observation of sharp resonances in the spontaneous Raman spectrum of a single optically levitated microdroplet", *Optics Communications*, **54**:349 (1985).
- Li, W., S. D. Rassat, W. R. Foss and E. J. Davis, "Formation and properties of aerocolloidal TiO₂-coated microspheres produced by alkoxide droplet reaction", *J. Colloid Interface Sci.*, **162**:267.
- Long, D. A., Raman Spectroscopy, McGraw-Hill International Book Co., New York, 1977.
- Lorenz, L., *Videnskab. Selskab. Skrifter*, **6**:1 (1890).
- Loyalka, S. K., "Thermophoretic force on a single particle-I. Numerical solution of the linearized Boltzmann equation", *J. Aerosol Sci.*, **23**:291 (1992).
- Loyalka, S. K. "Temperature jump: rigid-sphere gas with arbitrary gas/surface interaction", *Nuclear Sci. Eng.* **108**: 69 (1991).
- Loyalka, S. K., Hamoodi, S. A. and R. V. Tompson, "Isothermal condensation on a spherical particle", *Phys. Fluids A*, **1**:358 (1989).
- Loyalka, S. K., "Thermophoretic force on a single particle-I. Numerical solution of the linearized Boltzmann equation", *J. Aerosol Sci.*, **23**:291 (1992).
- Loyalka, S. K., "Condensation on a spherical droplet", *J. Chem. Phys.*, **58**:354 (1973).
- Loyalka, S. K., "Condensation on a spherical droplet, II", *J. Colloid Interface Sci.*, **87**:216 (1982).
- Mason, E. A. and S. Chapman, "Motion of small suspended particles in nonuniform gases", *J. Chem. Phys.* **36**:627 (1962).
- Matijević, E., Q. Zhong and R. E. Partch, "Preparation of uniform colloidal dispersion by chemical reactions in aerosols. VI. silica/titania composite particles", *Aerosol Sci. Tech.* **22**:162 (1995).
- Mau, J. R., "Evaporation coefficient of liquid", *Ind. Eng. Chem. Fundam.*, **6**:504 (1967).
- Maxwell, J. C., in The Scientific Papers of Clerk Maxwell, W. D. Niven, ed., Cambridge University Press, London, 1890.
- Mie, G., "Optics of turbid media", *Ann. Physik*, **25**:377 (1908).
- Monchick, L. and H. Reiss, "Studies of evaporation of small drops", *J. Chem. Phys.* **22**:831 (1954).
- Monchick, L. and R. Blackmore, "A variation calculation of the rate of evaporation of small droplets", *J. Aerosol Sci.* **19**:273 (1988).

- Nagel, S. R., MacChesney, J. B. and Walker, K. L., "An overview of the modified chemical vapor deposition (MCVD) process and performance", *IEEE J. Quan. Elec.*, **18**:459 (1982).
- Ohwada, T. and Sone, Y., "Analysis of thermal stress slip flow and negative thermophoresis using the Boltzmann equation for hard-sphere molecules. *Eur. J. Mech. B/Fluids* **11**:389 (1992).
- Opiolka, S., F. Schmidt and H. Fissan, "Combined effects of electrophoresis and thermophoresis on particle deposition onto flat surfaces", *J. Aerosol Sci.*, **25**:665 (1994).
- Ostrach, S., "Natural convection in enclosures" in *Advances in Heat Transfer*, Vol. 8, Edit by P. H. James and F. I. Thomas, pp 161-227, 1972.
- Owen, J. F., P. W. Barber, P. B. Dorain and R. K. Chang, "Enhancement of fluorescence induced by microstructure resonances of a dielectric fiber", *Phys. Rev. Lett.* **47**:1075 (1981a).
- Owen, J. F., R. K. Chang and P. W. Barber, "Internal electric field distributions of a dielectric cylinder at resonance wavelengths", *Opt. Lett.* **6**:540 (1981b).
- Owen, J. F., R. K. Chang and P. W. Barber, "Morphology-dependent resonances in Raman scattering, fluorescence emission, and elastic scattering from microparticles", *Aerosol Sci.Tech.* **1**:293 (1982).
- Paranjpe, M. K., "The convection and variation of temperature near a hot surface", *Proc. Indian Acad. Sci.*, **4a**:423 (1936).
- Paul, B., "Compilation of evaporation coefficients", *Am. Rocket Soc. J.*, **32**:1321 (1962).
- Paul, W., O. Osberghaus and E. Fischer, *Forschungsber. Wirtsch. Verkerminiseriums*, Nordheim-Westfalan, No. 415 (1958).
- Paul, W., and M. Raether, "Das Elektrische Massenfilter", *Z. Phys.*, **140**:262 (1955).
- Payne, M. J. and K. A. Berglund, "Raman spectroscopic studies of titanium alkoxides using UV excitation", *Mat. Res. Soc. Symp. Proc.*, **73**:627 (1986).
- Phillips, W. F., "Thermal force on spherical particles in a rarefied gas", *Phys. Fluid*, **15**:999 (1972).
- Phillips, W. F., "Motion of aerosol particles in a temperature gradients", *Phys. Fluids*, **18**:144 (1975).
- Prasinis, E. P. and T. T. Kodas, "Manufacturing of materials by aerosol processes" in *Aerosol Measurement*, Ed. by K. Willeke and P. A. Baron, Van Nostrand Reinhold, New York, PP. 721-746, 1993.
- Preston, R. E., T. R. Lettieri and H. G. Semerjian, "Characterization of single levitated droplets by Raman spectroscopy", *Langmuir*, **1**:365 (1985).

- Prodi, F. and Sanranchiara, G., "Measurements of thermophoretic velocities of aerosol particles in the transition region", *J. Aerosol Sci.*, **10**:421 (1979).
- Prodi, F. and F. Tampieri, "Problems in the measurement of thermophoretic velocities of aerosol particles. *J. Aerosol Sci.* **19**:167 (1988).
- Raman, C. V., and K. S. Krishnan, "A new type of secondary radiation", *Nature*, **121**:501 (1928).
- Rassat, S. D., "Raman spectroscopic investigation of gas-solid reaction of single microparticles", Ph. D. Dissertation, University of Washington, Seattle, WA, 1994
- Ray, A. K., R. D. Johnson and A. Souryi, "Dynamic behavior of single glycerol droplets in humid air streams", *Langmuir*, **5**:133 (1989).
- Ray, A. K., J. Lee and H. L. Tilley, "Direct measurements of evaporation rates of single droplets at large Knudsen number", *Langmuir*, **4**:631 (1988).
- Ray, A. K., A. Souryi, E. J. Davis and T. M. Allen, "The precision of light scattering techniques for measuring optical parameters of microspheres", *Appl. Opt.*, **30**:3974 (1991).
- Ray, A. K., E. J. Davis and Ravindran, P., "Determination of ultralow vapor pressures by submicro droplet evaporation ", *J. Chem. Phys.*, **71**:582 (1979).
- Richardson, C. B., H-B. Lin, R. McGraw and I. N. Tang, "Growth rate measurements for single suspended droplets using the optical resonance method", *Aerosol Sci. Tech.*, **5**:103 (1986).
- Richardson, C. B., R. L. Hightower and A. L. Pigg, "Optical measurement of the evaporation of sulfuric acid droplets", *Appl. Opt.*, **25**:1226 (1986).
- Richardson, C. B., and J. F. Spann, "Measurement of the water cycle in a levitated ammonium sulfate particle", *J. Aerosol Sci.*, **15**:563 (1984).
- Rosenblatt, P. and K. V. LaMer, "Motion of a particle in a temperature gradient", *Phys. Rev.*, **70**: 856 (1946).
- Rubel, G. O., and J. W. Gentry, "Investigation of the reaction between single aerosol acid droplets and ammonia gas", *J. Aerosol Sci.*, **15**:661 (1984).
- Rubel, G. O., and M. E. Milham, "Determination of vapor pressure/molecular weight correlations from droplet evaporation data", *Chem. Eng. Sci.* **39**:1043 (1984).
- Rubel, G. O., and J. W. Gentry, "Onset of particle crystallization resulting from acid droplet ammonia gas reactions", *J. Aerosol Sci.*, **17**:397 (1986).
- Rubel, G. O., and J. W. Gentry, "Onset of particle crystallization resulting from acid droplet ammonia gas reactions", *J. Aerosol Sci.*, **18**:23 (1987).

- Sadtler Standard Spectra, Raman Spectra, Sadtler Research Laboratory, Philadelphia, 1973.
- Sadtler Standard Spectra, Standard Infrared Grating Spectra, Sadtler Research Laboratory, Philadelphia, 1966.
- Sahni, D. C., "Effect of a black sphere on the flux distribution in an infinite moderator", *J. Nucl. Energy*, **20**:915 (1966).
- Saxena, S. C. and R. K. Joshi, "Part A: thermal accommodation coefficient" in Thermal Accommodation and Adsorption Coefficients of Gases, Ed. by Y. S. Touloukian and C. Y. Joshi, McGraw-Hill, New York, pp 3-308, 1981.
- Schadt, C. F. and R. D. Cadle, "Thermal force on aerosol particles", *J. Phys. Chem.*, **65**:1689 (1961).
- Schmitt, K. H., "Untersuchungen an schwebstoffteilchen im temperaturfeld", *Z. Naturforsch.* **14a**:870 (1959).
- Schweiger, G., "Raman scattering on single aerosol particles and on flowing aerosols: a review", *J. Aerosol Sci.*, **21**:483 (1990b).
- She, C. Y. and L. S. Hsu, "Probing structure properties of amorphous films with Raman spectroscopy", in NBS Special Publication, 746:383 (1988).
- Sherman, F. S., in Rarefied Gas Dynamics, Ed. by L. Talbot, Academic Press, New York, 1963.
- Sitarski, M. and Nowakowski, B., "Condensation rate of trace vapor on Knudsen aerosols from the solution of the Boltzmann equation", *J. Colloid Interface Sci.*, **73**:152 (1979).
- Smekal, A., *Naturwissenschaften*, **11**:873 (1923).
- Smirnov, V. *Trudy tsent. aero-gidrodin. Inst.* No. 92, 1968.
- Sloane, C. S., and Elmoursi, A. A., "Conf. Record 1987 IEEE Industry Applications Mtg., Part II, P. 1568, IEEE Publ. Services, New York, 1987.
- Sone, Y., "Flow induced by thermal stress in rarefied gas", *Phys. Fluids*, **15**:1418 (1972).
- Sone, Y. and K. Aoki, "Negative thermophoresis: Thermal stress slip flow around a spherical particle in a rarefied gas", In Rarefied gas dynamics, 489 (1980).
- Sone, Y. and K. Aoki., "A similarity solution of the linearized Boltzmann equation with application to thermophoresis of a spherical particle", *J. DE Mecan. Theo. et Appl.*, **2**:3 (1983).
- Springer, G. S., "Heat transfer in the rarefied gases" in Advances in Heat Transfer, Vol. 7, Academic Press, New York, pp.163-218 (1971).

- Spring, G. S., "Thermal force on a particles in the transition regime", *J. Colloid Interface Sci.*, **34**: 215 (1970).
- Stratmann, F., T. W. Peterson and H. Fissan, "Particle deposition onto a flat surface from a point particle source", 1988 IES Proceedings, pp 417-422 (1988).
- Straubel, H. and H. Straubel, "Investigation of freely suspended single particles producing crystals and turbidity during chemical reactions", *J. Aerosol Sci.*, **13**:220 (1982).
- Straubel, H. and H. Straubel, "Investigation of chemical reactions of aerosols", *J. Aerosol Sci.*, **15**:220 (1984).
- Straubel, H., *Z. Aerosolforschung und Therapie*, **4**:385 (1955).
- Taflin, D. C., "Interpretation of Microdroplet Mass Transfer Phenomena by Optical Resonance Spectroscopy", Ph. D. Dissertation, University of Washington, Seattle, WA, 1988.
- Taflin, D. C., and E. J. Davis, "A study of aerosol chemical reactions by optical resonance spectroscopy", *J. Aerosol Sci.*, **21**:73 (1990).
- Taflin, D. C., S. H. Zhang, T. M. Allen and E. J. Davis, "Measurement of droplet interfacial phenomena by light-scattering techniques," *AIChE Journal*, **34**:1310 (1988).
- Talbot, L. and R. K. Cheng, R. W. Schfer and D. R. Willis, "Thermophoresis of particles in a heated boundary layer", *J. Fluid Mech.* **101**:737 (1980).
- Tang, I. N., H. R. Munkelwitz, and N. Wang, "Water activity measurements with single suspended droplets: NaCl-H₂O and KCl-H₂O systems", *J. Colloid Interface Sci.*, **114**:409 (1986).
- Tang, I. N., and H. R. Munkelwitz, "Determination of vapor pressure from droplet evaporation kinetics", *J. Colloid Interface Sci.*, **141**:109 (1991).
- Thurn, R., and W. Kiefer, "Observation of structural resonances in the Raman spectra of optically levitated dielectric microspheres", *J. Raman Spectros.*, **15**:411 (1984).
- Thurn, R., and W. Kiefer, "Structural resonances observed in the Raman spectra of optically levitated liquid droplets", *Appl. Opt.* **24**:1515 (1985).
- Tong, N. T., "Experiments on photophoresis and thermophoresis", *J. Colloid Interface Sci.*, **51**:143 (1975).
- van de Hulst, Light Scattering by Small Particles, Dover, New York, 1981; First Published by John Wiley and Sons, New York, 1957.
- Visca, M. and Matijević, E. J., "Preparation of uniform colloidal dispersions by chemical reaction in aerosols, I. spherical particles of titanium dioxide" *J. Colloid Interface Sci.*, **68**:308 (1979).

- Waldmann, L. "die Kräfte eines inhomogenen Gases auf kleine suspendierte Kugeln", *Z. Naturforsch*, **14a**:589 (1959).
- Wagner, P. E., "Aerosol growth by condensation" in *Aerosol Physics II*, Ed. by W. H. Marlow, Springer-Verlag, New York, PP. 129-178, 1982.
- Waldmann, L. (1959) "Über die Kräfte eines inhomogenen Gases auf kleine suspendierte Kugeln", *Z. Naturforsch* **14a**, 589-599.
- Walker, K. L., Geyling, F. T. and Nagel, S. R., "Thermophoretic deposition of small particles in the modified chemical vapor deposition (MCVD) process", *J. Amer. Ceram. Soc.*, **63**:552 (1980).
- Weast, R. C., *CRC Handbook of Chemistry and Physics*, CRC Press, Boca Raton, 1984.
- Weiss-Wrana, K., "Optical properties of interplanetary dust: comparison with light scattering by larger meteoritic and terrestrial grains", *Astronomy and Astrophysics*, **126**:240 (1983).
- Wildmann, J. F. and E. J. Davis, "Photochemical initialized polymerization of single microparticles", *Colloid & Polymer Sci.*, submitted for publication (1995).
- Williams, M. M. R., "The thermophoretic force between a sphere and a plane surface", *J. Colloid Interface Sci.*, **122**:110 (1988).
- Williams, M. M. R., "The influence of a plane boundary on the thermophoretic force in the Knudsen regime", *J. Colloid Interface Sci.*, **117**:193 (1987).
- Williams, M. M. R. and Loyalka, S. K., *Aerosol Science and Theory and Practice*, Pergamon Press, New York, 1991.
- Wiscombe, W. J., "Improved Mie scattering algorithms", *Appl. Opt.* **19**:1505 (1980).
- Wright, P. G., "On the discontinuity involved in diffusion across an interface (the Δ of Fuchs)", *Discuss. Faraday Soc.*, **30**:100 (1960)
- Wuerker, R. F., H. Shelton and R. V. Langmuir, "Electrodynamic containment of charged particles", *J. Appl. Phys.*, **30**:342 (1959).
- Wyatt, P. J., and D. T. Phillips, "A new instrument for the study of individual aerosol particles", *J. Colloid Interface Sci.*, **39**:125 (1972).
- Yamamoto, K. and Ishihara, Y., "Thermophoresis of a spherical particle in a rarefied gas of a transition regime", *Phys. Fluids*, **31**: 3618 (1988)
- Zhang, S. C. and G. L. Messing, "Synthesis of solid, spherical zirconia particles by spray pyrolysis", *J. Amer. Ceram. Soc.*, **73**:61 (1990).

APPENDIX A
SCHEMATICS OF MAIN VACUUM CHAMBER

Top view of the main vacuum chamber constructed for the thermophoretic force measurements was shown in Fig. 4.10. Here, a vertical view of the main chamber is presented in Fig. A1, and the schematic diagrams of the mating flanges for ports 7 and 8 are shown in Fig. A2 and A3, respectively.

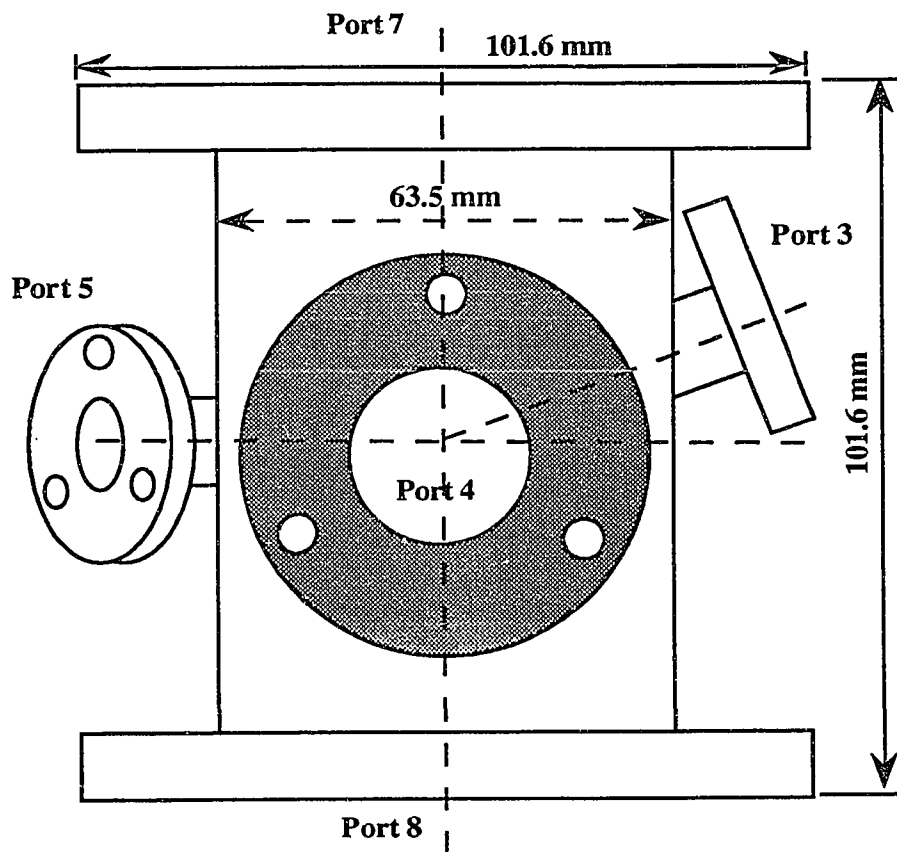


Figure A1. A front view of the vacuum chamber used for the measurements of the thermophoretic force and evaporation rates in the Knudsen regime.

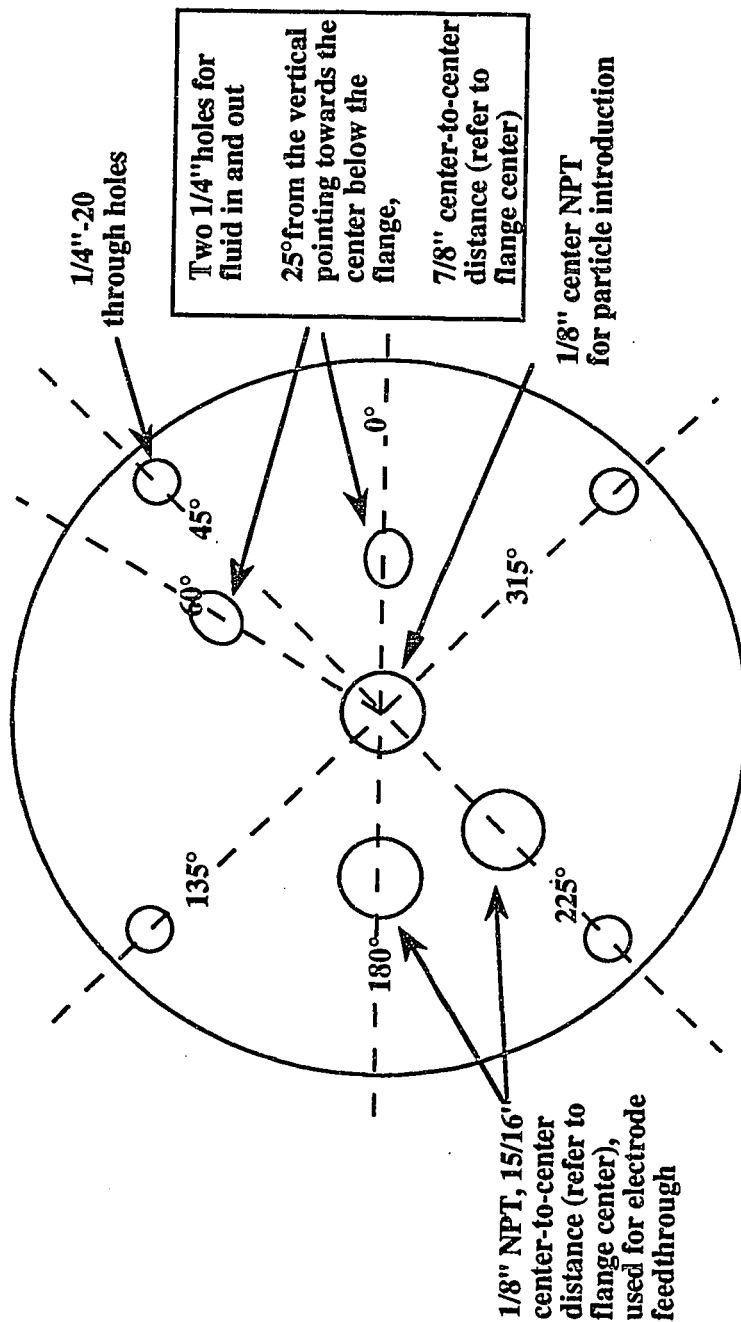


Figure A2 A diagram for the mating flange for Port 7 showing the holes for electrical feedthrough, and inlet and outlet ports for constant temperature fluids.

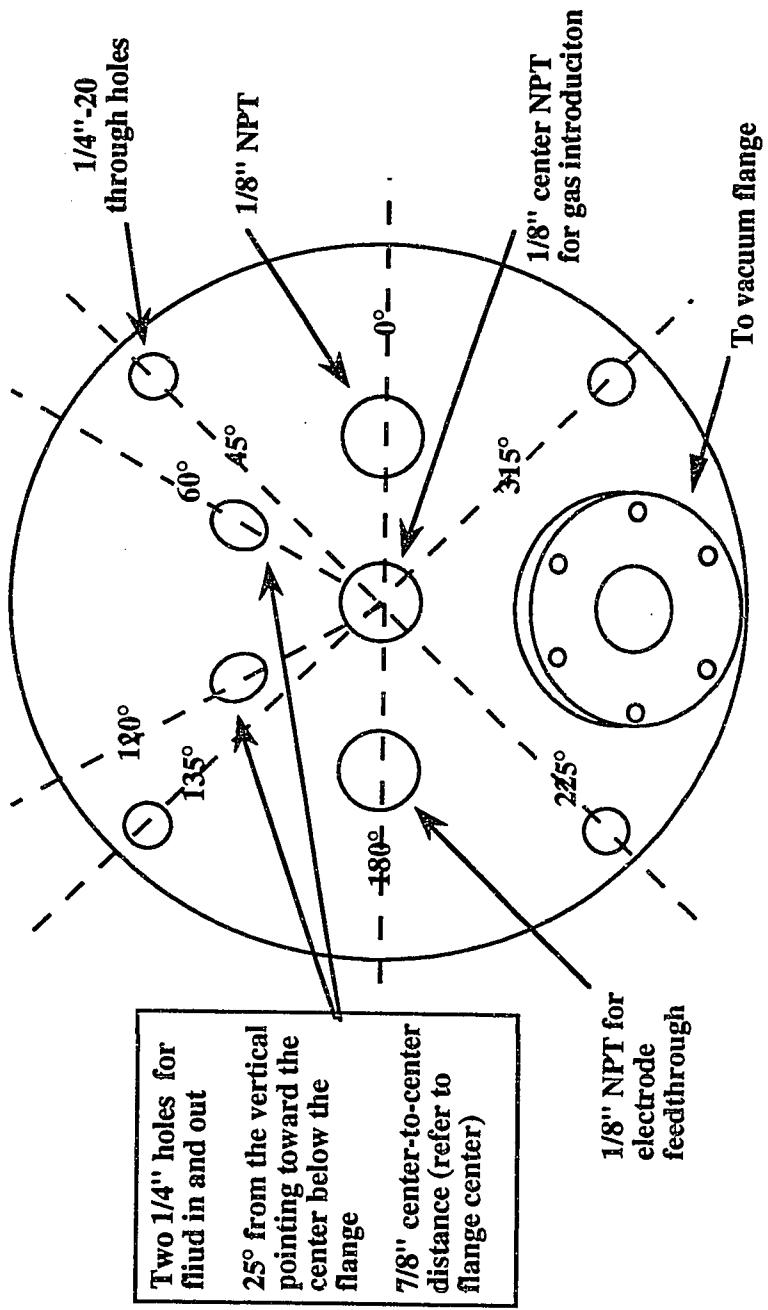


Figure A3 A diagram for the mating flange for Port 8 showing the holes for electrical feedthrough, and inlet and outlet ports for constant temperature fluids.

APPENDIX B

PROGRAM MIE_COATED_OPTIMUM1.FOR

This program is written to perform a "best fit" between recorded elastic light scattering data and the theoretical solution of Aden and Kerker (*Appl. Phys.*, **22**:1242; 1951) for a coated sphere. The program reads the experiment data and normalize them, then varies the shell thickness and core size, and calculate the light scattering intensity at individual values of core and shell thickness. Finally, the program calculate the difference of scattering intensity between the normalized theoretical solutions and the experimental data. The values of core and shell corresponding to the minimum rms was the optimum results.

For a coated particle, four parameters are involved which are the core size, shell thickness, and refractive indices of core and shell. Before you run the program, you need to specify the variation range of the core, shell, or the range of refractive indices. The presented program shows how to vary the core size and shell thickness based upon the known refractive indices. The same program can also be used to find the "optimum" values of refractive indices of core and shell with small change, suppose the core size and shell are known. The program is recommended to calculate scattering intensity for a sphere with relatively thin shell compared with the core size. For thick shell, some variables are overflowed during the calculation.

There are two input data files. "MIEINPT.DAT" includes the data for size parameter and refractive indices, and also includes the data required in the shell density calculation (the calculation method of shell density was discussed in Chapter 5). The other input file is the experimental data files containing the recorded light scattering data. If the experiment data are noisy, they can be smoothed by a FFT program. The output file of the FFT process is then taken as the experiment data file for input.

C

C ***** INPUT VARIABLES*****

C

C NPT: number of points used in the calculation of scattering intensity at a given

C scattering angle regime

C NPTY: number of points used to specify the stepsize of variation of particle size

C parameter
 C NPTX: number of points used to specify the stepsize of variation of core size
 C parameter
 C XSTART: starting value of core size parameter
 C XEND: ending value of core size parameter
 C YSTART: starting value of particle size parameter
 C YEND: ending value of particle size parameter
 C REFRE1: real part of the refractive index of core
 C REFIM1: imaginary part of the refractive index of core
 C REFRE2: real part of the refractive index of shell
 C REFIM2: imaginary part of the refractive index of shell
 C THETA1: initial value of light scattering angle, theta
 C THETA2: ending value of light scattering angle, theta
 C (THETA2 should be specified larger than THETA1)
 C PHI: polarization angle (for example: vertical polarization, PHI = 90 degree
 C and PHI = 45 degree for unpolarized light)
 C
 C *****OUTPUT VARIABLES*****
 C
 C THETA(I): scattering angle, theta
 C RICAI(I): scattering intensity at angle Theta (I) based upon the optimum values of
 C core size and shell thickness which the program obtained.

 COMPLEX*16 REF1,REF2,REF21,S1(30,30,256),S2(30,30,256)
 COMPLEX*16 XX1(30),XX2(30),YY2(30),X1,X2,Y2
 COMPLEX*16 CHI0X2,CHI1X2,CHINX2,CHI0Y2,CHI1Y2,CHINY2,
 1 CHIPX2,CHIPY2
 COMPLEX*16 D0X1,D1X1,D0X2,D1X2,D0Y2,D1Y2
 COMPLEX*16 XI0Y,XI1Y,XINY
 COMPLEX*16 ANCAP,BNCAP,DNBAR,GNBAR,AN,BN,CRACK,BRACK,
 1 AMESS1,AMESS2,AMESS3,AMESS4
 REAL*8 Y,YY(30),PSI1Y,PSI0Y,PSINY,CHI0Y,CHI1Y,CHINY,FN,RN,CN,DEL
 REAL*8 TEMP1(30),TEMP2(30)
 CHARACTER*20 FILOPT,FILEXP
 CHARACTER*72 DUMMY

C

```

DIMENSION PI0(256),PI1(256),PI(256),TAU(256),AMU(256)
DIMENSION THETA(256),THETAR(256),DUMMY1(256),DUMMY2(256)
DIMENSION RICAL(30,30,256),RIEXP(256),VARSUM(30,30)

```

C

```

OPEN(UNIT = 5,FILE= 'MSIZE.DAT', STATUS = 'OLD')
READ(5,*)REFRE1,REFIM1
READ(5,*)REFRE2,REFIM2
READ(5,*)XSTART,XEND
READ(5,*)YSTART,YEND
READ(5,*)THETA1,THETA2
READ(5,*)NPT,NPTX,NPTY,PHI
READ(5,*)SLOPE,VOLT,B
READ(5,5)FILEXP
READ(5,5)FILOPT
5 FORMAT(A20)

```

C the experimental input file includes four lines of header, so they are read by DUMMY

```

OPEN(UNIT=8,FILE=FILEXP,STATUS='OLD')
READ(8,6)DUMMY
READ(8,6)DUMMY
READ(8,6)DUMMY
READ(8,6)DUMMY
6 FORMAT(A72)
READ(8,*)(DUMMY1(I),DUMMY2(I), I=1,63)
READ(8,*)(THETA(I),RIEXP(I), I=1,NPT)

OPEN(UNIT=14, FILE=FILOPT, STATUS='NEW')
WRITE(14,*)NPT
WRITE(14,20)XSTART,XEND,YSTART,YEND
WRITE(14,25)REFRE1,REFIM1,REFRE2,REFIM2
20 FORMAT(2X,'CORE SIZE X=',F6.2,'-',F6.2,2X,'COATED SIZE
1 Y=',F6.2,'-',F6.2)
25 FORMAT(2X,'M1=',F6.4,'+i*',F6.4,1X,'M2=',F6.4,

```

```
1'+i*',F6.4/8X,'SCATTERING ANGLE    INTENSITY')
```

C calculate $\sin^2\phi$ and $\cos^2\phi$

```
SPHISQ=SIND(PHI)**2
```

```
CPHISQ=1.0-SPHISQ
```

C calculate the stepsize of theta and terms to be used in the series summation NSTOP

```
DEL=1.0D-8
```

```
THETAS=(THETA2-THETA1)/(NPT-1)
```

```
DO 30 I=1,NPT
```

```
  THETA(I)=THETA1+(I-1)*THETAS
```

```
  THETAR(I)=THETA(I)*3.1415926/180
```

```
  AMU(I)=COS(THETAR(I))
```

```
30 CONTINUE
```

```
YSTOP=YEND+4.0*YEND**0.3333+2.0
```

```
NSTOP=YSTOP
```

```
REF1=CMPLX(REFRE1,REFIM1)
```

```
REF2=CMPLX(REFRE2,REFIM2)
```

```
REF21=REF2/REF1
```

C stepsize for core and particle size parameter

```
DO 35 I=1,NPTX
```

```
  TEMP1(I)=XSTART+(I-1)*(XEND-XSTART)/(NPTX-1)
```

```
  XX1(I)=TEMP1(I)*REF1
```

```
  XX2(I)=TEMP1(I)*REF2
```

```
35 CONTINUE
```

```
DO 37 I=1,NPTY
```

```
  TEMP2(I)=YSTART+(I-1)*(YEND-YSTART)/(NPTY-1)
```

```
  YY(I)=TEMP2(I)
```

```
  YY2(I)=TEMP2(I)*REF2
```

```
37 CONTINUE
```

```
C initialize variable values
DO 40 K=1,NPTY
  DO 40 J=1,NPTX
    DO 40 I=1,NPT
      S1(K,J,I)=DCMPLX(0.0,0.0)
      S2(K,J,I)=DCMPLX(0.0,0.0)
40 CONTINUE

DO 42 K=1,NPTY
  DO 42 J=1,NPTX
    VARSUM(K,J)=0
42 CONTINUE

C finding the maximum scattering intensity of the experimental data
RMAX=1.0E-38
RAVEXP=0.0
DO 44 I=1,NPT
  RMAX=MAX(RMAX,RIEXP(I))
  RAVEXP=RAVEXP+RIEXP(I)
44 CONTINUE
RAVEXP=RAVEXP/NPT
DO 110 I=1,NPT
  RIEXP(I)=RIEXP(I)/RAVEXP
110 CONTINUE

C start K-loop (varying the overall particle size)

DO 4000 K=1,NPTY
  Y2=YY2(K)
  Y=YY(K)

C start J-loop (varying the core size)

DO 3000 J=1,NPTX
```

```

X1=XX1(J)
X2=XX2(J)
CHI0X2=-CDSIN(X2)
CHI1X2=CDCOS(X2)
CHI0Y=-DSIN(Y)
CHI1Y=DCOS(Y)
CHI0Y2=-CDSIN(Y2)
CHI1Y2=CDCOS(Y2)
D0X1=CDCOS(X1)/CDSIN(X1)
D0X2=CDCOS(X2)/CDSIN(X2)
D0Y2=CDCOS(Y2)/CDSIN(Y2)
PSI0Y=DCOS(Y)
PSI1Y=DSIN(Y)
XI0Y=DCMPLX(PSI0Y,-CHI0Y)
XI1Y=DCMPLX(PSI1Y,-CHI1Y)
DO 45 I=1,NPT
    PI0(I)=0.0
    PI1(I)=1.0
45  CONTINUE

```

C start N-Loop

```

N=1
IFLAG=0
2000 CN=N
    FN=(2.0*CN+1.0)/(CN*(CN+1.0))
    RN=2.0*CN-1.0
    CHINY=RN*CHI1Y/Y-CHI0Y
    PSINY=RN*PSI1Y/Y-PSI0Y
    XINY=DCMPLX(PSINY,-CHINY)
    D1X1=1.0/(CN/X1-D0X1)-CN/X1
    D1X2=1.0/(CN/X2-D0X2)-CN/X2
    D1Y2=1.0/(CN/Y2-D0Y2)-CN/Y2
    CHINX2=RN*CHI1X2/X2-CHI0X2
    CHINY2=RN*CHI1Y2/Y2-CHI0Y2

```

CHIPX2=CHI1X2-CN*CHINX2/X2
 CHIPY2=CHI1Y2-CN*CHINY2/Y2

C calculate the coefficients A_n and B_n (see Chapter 2 for definition of A_n and B_n)

ANCAP=REF21*D1X1-D1X2
 ANCAP=ANCAP/(REF21*D1X1*CHINX2-CHIPX2)
 ANCAP=ANCAP/(CHINX2*D1X2-CHIPX2)
 BRACK=ANCAP*(CHINY2*D1Y2-CHIPY2)
 BNCAP=REF21*D1X2-D1X1
 BNCAP=BNCAP/(REF21*CHIPX2-D1X1*CHINX2)
 BNCAP=BNCAP/(CHINX2*D1X2-CHIPX2)
 CRACK=BNCAP*(CHINY2*D1Y2-CHIPY2)
 AMESS1=BRACK*CHIPY2
 AMESS2=BRACK*CHINY2
 AMESS3=CRACK*CHIPY2
 AMESS4=CRACK*CHINY2
 IF(CDABS(AMESS1).GT.DEL*CDABS(D1Y2)) GOTO 100
 IF(CDABS(AMESS2).GT.DEL) GOTO 100
 IF(CDABS(AMESS3).GT.DEL*CDABS(D1Y2)) GOTO 100
 IF(CDABS(AMESS4).GT.DEL) GOTO 100
 BRACK=0
 CRACK=0
 IFLAG=1
 100 DNBAR=D1Y2-BRACK*CHIPY2
 DNBAR=DNBAR/(1.0-BRACK*CHINY2)
 GNBAR=D1Y2-CRACK*CHIPY2
 GNBAR=GNBAR/(1.0-CRACK*CHINY2)
 AN=(DNBAR/REF2+CN/Y)*PSINY-PSI1Y
 AN=AN/((DNBAR/REF2+CN/Y)*XINY-XI1Y)
 BN=(REF2*GNBAR+CN/Y)*PSINY-PSI1Y
 BN=BN/((REF2*GNBAR+CN/Y)*XINY-XI1Y)

C start theta-loop

```

DO 200 I=1,NPT
  PI(I)=PI1(I)
  TAU(I)=CN*AMU(I)*PI(I)-(CN+1)*PI0(I)
  S1(K,J,I)=S1(K,J,I)+FN*(AN*PI(I)+BN*TAU(I))
  S2(K,J,I)=S2(K,J,I)+FN*(AN*TAU(I)+BN*PI(I))
200 CONTINUE

```

C exchange the coefficients

```

CHI0Y=CHI1Y
CHI1Y=CHINY
CHI0X2=CHI1X2
CHI1X2=CHINX2
CHI0Y2=CHI1Y2
CHI1Y2=CHINY2
D0X1=D1X1
D0X2=D1X2
D0Y2=D1Y2
PSI0Y=PSI1Y
PSI1Y=PSINY
XI1Y=DCMPLX(PSI1Y,-CHI1Y)
DO 250 I=1,NPT
  PI1(I)=(2*CN+1.0)/CN*AMU(I)*PI(I)
  PI1(I)=PI1(I)-(CN+1.0)*PI0(I)/CN
  PI0(I)=PI(I)
250 CONTINUE

```

N=N+1

IF(N-1-NSTOP)2000,1000,1000

1000 RLARGE=1.0E-38

C calculate the intensity and find the maximum value

RAVCAL=0.0

DO 300 I=1,NPT

```

    RICAL(K,J,I)=S1(K,J,I)*DCONJG(S1(K,J,I))*SPHISQ
    RICAL(K,J,I)=RICAL(K,J,I)+S2(K,J,I)*DCONJG(S2(K,J,I))*CPHISQ
    RAVCAL=RAVCAL+RICAL(K,J,I)
    IF(LEQ.1)THEN RLARGE=RICAL(K,J,I)
    RLARGE=MAX(RLARGE,RICAL(K,J,I))
300 CONTINUE

```

```

    RATIO=RLARGE/RMAX
    RAVCAL=RAVCAL/NPT
    DO 310 I=1,NPT
        RICAL(K,J,I)=RICAL(K,J,I)/RAVCAL
310 CONTINUE

```

```

C   calculate rms (root mean square)
    DO 320 I=1,NPT
C   RICAL(K,J,I)=RICAL(K,J,I)/RATIO
    VAR=(RICAL(K,J,I)-RIEXP(I))**2
    VARSUM(K,J)=VARSUM(K,J)+VAR
320 CONTINUE
    VARSUM(K,J)=VARSUM(K,J)/NPT

```

```

C   stop the J-Loop
3000 CONTINUE
C   stop the K-Loop
4000 CONTINUE

```

```

    SMALL=1.0E38

```

```

C   find the minimum rms and the corresponding values of core and particle sizes

```

```

    DO 550 K=1,NPTY
        DO 550 J=1,NPTX
            SMALL=MIN(SMALL,VARSUM(K,J))
550 CONTINUE
    TEMP3=0.

```

```

DO 610 K=1,NPTY
  DO 600 J=1,NPTX
    TEMP3=SMALL-VARSUM(K,J)
    IF(TEMP3.EQ.0)THEN
      NOPY=K
      NOPX=J
      ROPMY=TEMP2(NOPY)
      ROPMX=TEMP1(NOPX)
    ENDIF
600 CONTINUE
610 CONTINUE

C  OPEN(UNIT=14,FILE=FILOPT,STATUS='NEW')
  DO 650 I=1,NPT
    WRITE(14,700)THETA(I),RICAL(NOPY,NOPX,I)
    WRITE(15,700)THETA(I),RIEXP(I)
700 FORMAT(F8.2,F12.5)
650 CONTINUE
    WRITE(14,660)NOPY,NOPX
660 FORMAT(2X,'OPTIMUM POINT FOR Y=',I4,', FOR X=',I4)
    WRITE(14,670)ROPMY,ROPMX
670 FORMAT(' OPTIMUM FITTING DATA IS:Y=',F7.2,' X=',F7.2)
    WRITE(14,680)VARSUM(NOPY,NOPX)
680 FORMAT(' THE MINIMUM VARIATION IS:VARSUM=',F13.7)

C  calculate shell density

```

```

CPI=3.1415926
Y=ROPMY*0.6328/2/CPI
X=ROPMX*0.6328/2/CPI
DENS0=1088
DENS0=DENS0*SLOPE*VOLT/Y**3-0.002435*B/Y**2
DENS1=DENS0*Y**3-DENS0*X**3
DENS1=DENS1/(Y**3-X**3)
THICK=Y-X

```

```
VOLUME=4/3*CPI*(Y**3-X**3)
TMOLAR=VOLUME*DENS1/79.0
450  FORMAT(1X,'THICK=',F8.3,' DENSITY=',F12.3)
460  FORMAT(1X,' NUMBER OF MOLAR=',F12.3)
      WRITE(14,450)THICK,DENS1
      WRITE(14,460)TMOLAR

      STOP
      END
```

APPENDIX C
RAW DATA FOR THE MEASURED THERMOPHORETIC FORCE

Appendix C lists the raw data related to the figures shown in Chapter 6 and 7 for the thermophoretic force. It includes the recorded system pressure and DC voltage. The thermophoretic force, F_{th} , calculated from DC voltage as well as the Knudsen number estimated from the system pressure and particle radius are also included. Only the normalized force by $a^2 \nabla T_\infty$ are presented here. The normalized and adjusted force, $(1+2C_t Kna/H)F_{th}/a^2 \nabla T_\infty$, are not shown due to the space limitation, but they can be calculated from the data presented using Eq. (6.2) and (6.4).

Table C1. Thermophoretic force data for system **DOP/air** and Run **0409b**Droplet radius: 17.4 μm

Temperature of hot plate: 333.9 K

Temperature of cold plate: 261.9 K

Initial DC voltage, $V_{dc,0}$: 14.12 volt

Surface charge polarity: positive

Related figures: 6.3, 6.4, 6.11

Pressure (Pa)	Kn	V_{dc} (volt)	$\nabla V_{dc}/V_{dc,0}$	F_{th} (N)	$F_{th}/(a^2\nabla T_{\infty})$ (N/m ² K)
26831	0.0145	14.4	0.02	4.23E-12	5.15E-06
12836	0.0303	14.49	0.026	5.59E-12	6.8E-06
8037.4	0.0483	14.57	0.032	6.8E-12	8.28E-06
4571.8	0.085	14.85	0.052	1.1E-11	1.34E-05
3505.5	0.1108	14.94	0.058	1.24E-11	1.51E-05
2972.4	0.1307	15.1	0.069	1.48E-11	1.8E-05
2495.2	0.1557	15.21	0.077	1.65E-11	2E-05
2130	0.1824	15.26	0.081	1.72E-11	2.1E-05
1806.1	0.2151	15.51	0.098	2.1E-11	2.56E-05
1412.9	0.2749	15.73	0.114	2.43E-11	2.96E-05
1292.9	0.3004	15.91	0.127	2.71E-11	3.29E-05
1119.6	0.3469	16.17	0.145	3.1E-11	3.77E-05
973.01	0.3992	16.38	0.16	3.42E-11	4.16E-05
841.06	0.4618	16.67	0.181	3.85E-11	4.69E-05
705.1	0.5509	17.05	0.208	4.43E-11	5.39E-05
459.85	0.8447	17.36	0.229	4.9E-11	5.96E-05
322.56	1.2042	17.69	0.253	5.4E-11	6.57E-05
263.91	1.4718	18.03	0.277	5.91E-11	7.19E-05
227.93	1.7042	18.3	0.296	6.32E-11	7.69E-05
238.59	1.628	18.57	0.315	6.73E-11	8.18E-05
191.94	2.0237	18.43	0.305	6.52E-11	7.93E-05
175.68	2.211	18.32	0.297	6.35E-11	7.72E-05
167.01	2.3257	18.38	0.302	6.44E-11	7.83E-05
148.48	2.6159	18.45	0.307	6.55E-11	7.96E-05
132.89	2.9229	18.51	0.311	6.64E-11	8.07E-05
116.76	3.3266	18.43	0.305	6.52E-11	7.93E-05
104.9	3.7028	18.43	0.305	6.52E-11	7.93E-05
102.5	3.7895	18.56	0.314	6.71E-11	8.17E-05
92.37	4.2051	18.4	0.303	6.47E-11	7.87E-05
79.707	4.8731	18.35	0.3	6.39E-11	7.78E-05
52.649	7.3775	18.12	0.283	6.05E-11	7.36E-05
33.856	11.473	17.85	0.264	5.64E-11	6.86E-05
25.991	14.944	17.73	0.256	5.46E-11	6.64E-05
21.726	17.878	17.59	0.246	5.25E-11	6.38E-05

15.195	25.562	17.42	0.234	4.99E-11	6.07E-05
12.396	31.334	17.19	0.217	4.64E-11	5.65E-05
9.5968	40.474	17.11	0.212	4.52E-11	5.5E-05
7.5975	51.125	16.98	0.203	4.32E-11	5.26E-05
5.7314	67.77	16.98	0.203	4.32E-11	5.26E-05

Table C2. Thermophoretic force data for system **DOP/air** and Run **0501a**.Particle radius: 10.9 μm

Temperature of hot plate: 331.5 K

Temperature of cool plate: 263.5K

Initial DC voltage, $V_{dc,0}$: 7.07 volt

Surface charge polarity: positive

Related figures: 6.3, 6.4, 6.5, 6.11

Pressure (Pa)	Kn	V_{dc} (volt)	$\nabla V_{dc}/V_{dc,0}$	F_{th} (N)	$F_{th}/(a^2\nabla T_{\infty})$ (N/m ² K)
13734.1	0.0447	7.11	0.0057	2.99E-13	9.77E-07
12837.1	0.0478	7.14	0.0099	5.23E-13	1.71E-06
9503.54	0.0646	7.2	0.0184	9.72E-13	3.17E-06
8045.35	0.0763	7.25	0.0255	1.35E-12	4.4E-06
7117.66	0.0862	7.28	0.0297	1.57E-12	5.13E-06
6447.21	0.0952	7.33	0.0368	1.94E-12	6.35E-06
5438.21	0.1128	7.37	0.0424	2.24E-12	7.33E-06
4078.66	0.1504	7.5	0.0608	3.21E-12	1.05E-05
3745.43	0.1638	7.56	0.0693	3.66E-12	1.2E-05
3430.87	0.1788	7.61	0.0764	4.04E-12	1.32E-05
3033.67	0.2022	7.66	0.0835	4.41E-12	1.44E-05
2637.8	0.2326	7.8	0.1033	5.46E-12	1.78E-05
2265.92	0.2708	7.93	0.1216	6.43E-12	2.1E-05
2065.99	0.297	8.04	0.1372	7.25E-12	2.37E-05
1919.37	0.3197	8.11	0.1471	7.77E-12	2.54E-05
1799.41	0.341	8.19	0.1584	8.37E-12	2.74E-05
1603.47	0.3826	8.35	0.181	9.57E-12	3.13E-05
1452.86	0.4223	8.45	0.1952	1.03E-11	3.37E-05
1306.24	0.4697	8.59	0.215	1.14E-11	3.71E-05
1172.95	0.5231	8.71	0.232	1.23E-11	4.01E-05
1059.65	0.579	8.83	0.2489	1.32E-11	4.3E-05
930.361	0.6595	8.96	0.2673	1.41E-11	4.62E-05
793.072	0.7736	9.13	0.2914	1.54E-11	5.03E-05
666.447	0.9206	9.27	0.3112	1.64E-11	5.37E-05
545.154	1.1255	9.38	0.3267	1.73E-11	5.64E-05
397.203	1.5447	9.38	0.3267	1.73E-11	5.64E-05

Table C3. Thermophoretic force data for system DOP/air and Run 0510d.

Particle radius: 23.9 μm

Temperature of hot plate: 324.5 K

Temperature of cold plate: 267.6 K

Initial DC voltage, $V_{dc,0}$: 33.9 volt

Surface charge polarity: positive

Related figures: 6.3, 6.4, 6.5, 6.8, 6.11

Pressure (Pa)	Kn	V_{dc} (volt)	$\nabla V_{dc}/V_{dc,0}$	F_{th} (N)	$F_{th}/(a^2\nabla T_{\infty})$ (N/m ² K)
13089.026	0.0213	34.6	0.0206	1.13E-11	9.29E-06
10116.671	0.0275	34.6	0.0206	1.13E-11	9.29E-06
6759.1092	0.0412	34.7	0.0236	1.29E-11	1.06E-05
4914.3829	0.0567	34.7	0.0236	1.29E-11	1.06E-05
2945.6974	0.0946	34.9	0.0295	1.61E-11	1.33E-05
2495.1789	0.1117	35	0.0324	1.78E-11	1.46E-05
2141.9618	0.1301	35.1	0.0354	1.94E-11	1.59E-05
1863.3868	0.1496	35.2	0.0383	2.1E-11	1.72E-05
1586.1447	0.1757	35.4	0.0442	2.42E-11	1.99E-05
1346.2237	0.207	35.6	0.0501	2.74E-11	2.26E-05
1191.6079	0.2339	35.8	0.056	3.07E-11	2.52E-05
1014.3329	0.2748	36	0.0619	3.39E-11	2.79E-05
918.36447	0.3035	36.2	0.0678	3.71E-11	3.05E-05
753.08553	0.3701	36.6	0.0796	4.36E-11	3.58E-05
662.44868	0.4207	36.9	0.0885	4.84E-11	3.98E-05
585.14079	0.4763	37.2	0.0973	5.33E-11	4.38E-05
495.83684	0.5621	37.5	0.1062	5.81E-11	4.78E-05
413.19737	0.6745	38	0.1209	6.62E-11	5.44E-05
378.54211	0.7362	38.2	0.1268	6.94E-11	5.7E-05
327.89211	0.85	38.5	0.1357	7.42E-11	6.1E-05
282.57368	0.9863	38.7	0.1416	7.75E-11	6.37E-05
242.58684	1.1489	39	0.1504	8.23E-11	6.77E-05
198.60132	1.4033	39.2	0.1563	8.55E-11	7.03E-05
149.28421	1.8669	39.4	0.1622	8.88E-11	7.3E-05
123.95921	2.2483	39.7	0.1711	9.36E-11	7.69E-05
103.96579	2.6807	39.7	0.1711	9.36E-11	7.69E-05
89.303947	3.1208	39.7	0.1711	9.36E-11	7.69E-05
70.643421	3.9452	39.7	0.1711	9.36E-11	7.69E-05
53.315789	5.2274	39.6	0.1681	9.2E-11	7.56E-05
41.319737	6.745	39.5	0.1652	9.04E-11	7.43E-05
30.656579	9.091	39.3	0.1593	8.72E-11	7.16E-05
23.992105	11.616	39.1	0.1534	8.39E-11	6.9E-05

21.326316	13.068	39	0.1504	8.23E-11	6.77E-05
17.327632	16.084	38.8	0.1445	7.91E-11	6.5E-05
13.328947	20.909	38.7	0.1416	7.75E-11	6.37E-05
10.663158	26.137	38.6	0.1386	7.59E-11	6.23E-05
6.6644737	41.819	38.3	0.1298	7.1E-11	5.84E-05
5.3315789	52.274	38.1	0.1239	6.78E-11	5.57E-05
3.9986842	69.698	37.9	0.118	6.46E-11	5.31E-05

Table C4. Thermophoretic force data for system **DOP/air** and Run **0510e**.

Particle radius: 14.8 μm

Temperature of hot plate: 324.8 K

Temperature of cool plate: 267.6 K

Initial DC voltage, $V_{dc,0}$: 15.75 volt

Particle charge polarity: positive

Related figures: 6.3, 6.4, 6.11

Pressure (Pa)	Kn	V_{dc} (volt)	$\nabla V_{dc}/V_{dc,0}$	F_{th} (N)	$F_{th}/(a^2\nabla T_{\infty})$ (N/m ² K)
13831	0.0326	16.03	0.018	2.31E-12	4.93E-06
11300	0.0399	16.07	0.02	2.65E-12	5.63E-06
9027.7	0.05	16.13	0.024	3.14E-12	6.69E-06
6453.9	0.0699	16.22	0.03	3.89E-12	8.27E-06
5363.6	0.0842	16.31	0.036	4.63E-12	9.86E-06
4762.4	0.0948	16.37	0.039	5.13E-12	1.09E-05
4321.2	0.1045	16.44	0.044	5.7E-12	1.21E-05
3730.8	0.121	16.52	0.049	6.37E-12	1.36E-05
3418.9	0.132	16.6	0.054	7.03E-12	1.5E-05
2968.4	0.1521	16.71	0.061	7.94E-12	1.69E-05
2652.5	0.1702	16.81	0.067	8.76E-12	1.87E-05
2211.3	0.2041	16.99	0.079	1.03E-11	2.18E-05
2098	0.2152	17.08	0.084	1.1E-11	2.34E-05
1971.4	0.229	17.17	0.09	1.17E-11	2.5E-05
1823.4	0.2476	17.27	0.097	1.26E-11	2.68E-05
1695.4	0.2662	17.39	0.104	1.36E-11	2.89E-05
1554.2	0.2904	17.51	0.112	1.45E-11	3.1E-05
1408.9	0.3204	17.65	0.121	1.57E-11	3.34E-05
1295.6	0.3484	17.81	0.131	1.7E-11	3.63E-05
1175.6	0.384	17.96	0.14	1.83E-11	3.89E-05
991.67	0.4552	18.28	0.161	2.09E-11	4.45E-05
811.73	0.5561	18.53	0.177	2.3E-11	4.89E-05
691.77	0.6525	18.66	0.185	2.41E-11	5.12E-05

Table C5. Thermophoretic force data for system **DOP/air** and Run **0518h**Particle radius: 15.3 μm

Temperature of hot plate: 324.8 K

Temperature of cold plate: 268.8 K

Initial DC voltage, $V_{dc,0}$: 16.57 volt

Surface charge polarity: positive

Related figures: 6.3, 6.4, 6.11

Pressure (Pa)	Kn	V_{dc} (volt)	$\nabla V_{dc}/V_{dc,0}$	F_{th} (N)	$F_{th}/(a^2\nabla T_{\infty})$ (N/m ² K)
3737.4	0.11687	17.14	0.034	4.99E-12	1.01E-05
3409.5	0.12811	17.22	0.039	5.7E-12	1.15E-05
2797.7	0.15613	17.37	0.048	7.01E-12	1.42E-05
2495.2	0.17506	17.49	0.056	8.06E-12	1.63E-05
2316.6	0.18856	17.57	0.06	8.76E-12	1.77E-05
2209.9	0.19766	17.61	0.063	9.11E-12	1.84E-05
2060.7	0.21197	17.69	0.068	9.81E-12	1.98E-05
1946	0.22446	17.77	0.072	1.05E-11	2.13E-05
1763.4	0.2477	17.87	0.078	1.14E-11	2.3E-05
1619.5	0.26972	18.03	0.088	1.28E-11	2.59E-05
1506.2	0.29001	18.13	0.094	1.37E-11	2.76E-05
1382.2	0.31602	18.25	0.101	1.47E-11	2.98E-05
1226.3	0.35621	18.44	0.113	1.64E-11	3.31E-05
1113	0.39247	18.78	0.133	1.94E-11	3.92E-05
1053	0.41483	18.91	0.141	2.05E-11	4.15E-05
943.69	0.46287	19.04	0.149	2.16E-11	4.38E-05
810.4	0.539	19.21	0.159	2.31E-11	4.68E-05
689.11	0.63387	19.43	0.173	2.51E-11	5.07E-05
510.5	0.85565	19.72	0.19	2.76E-11	5.58E-05
398.54	1.09603	19.92	0.202	2.94E-11	5.94E-05
295.9	1.47618	20.21	0.22	3.19E-11	6.45E-05
234.59	1.862	20.4	0.231	3.36E-11	6.79E-05
147.95	2.95236	20.7	0.249	3.62E-11	7.32E-05
131.96	3.31022	20.7	0.249	3.62E-11	7.32E-05
109.3	3.99649	20.72	0.25	3.64E-11	7.35E-05
66.645	6.55424	20.75	0.252	3.66E-11	7.41E-05
39.987	10.9237	20.8	0.255	3.71E-11	7.5E-05

Table C6 Thermophoretic force data for system **DOP/air** and Run **OT94A**.Particle radius: 12.0 μm

Temperature of hot plate: 334.7 K

Temperature of cold plate: 262.1 K

Initial DC voltage, $V_{dc,0}$: 5.75 volt

Surface charge ploarity: negative

Related figure: 7.9

Pressure (Pa)	Kn	V_{dc} (volt)	$\nabla V_{dc}/V_{dc,0}$	F_{th} (N)	$F_{th}/(a^2\nabla T_{\infty})$ (N/m ² K)
14627	0.0385	6.11	0.0626	4.33E-12	1.11E-05
12001	0.0469	6.16	0.0713	4.93E-12	1.26E-05
8349.3	0.0674	6.24	0.0852	5.89E-12	1.51E-05
6811.1	0.0826	6.33	0.1009	6.97E-12	1.78E-05
4753.1	0.1184	6.41	0.1148	7.94E-12	2.03E-05
4028	0.1397	6.49	0.1287	8.9E-12	2.28E-05
3268.3	0.1722	6.66	0.1583	1.09E-11	2.8E-05
2429.9	0.2316	6.87	0.1948	1.35E-11	3.44E-05
1778.1	0.3166	7.09	0.233	1.61E-11	4.12E-05
1430.2	0.3936	7.33	0.2748	1.9E-11	4.86E-05
1202.3	0.4682	7.48	0.3009	2.08E-11	5.32E-05
1050.3	0.5359	7.68	0.3357	2.32E-11	5.94E-05
753.09	0.7474	8.01	0.393	2.72E-11	6.95E-05
497.17	1.1322	8.33	0.4487	3.1E-11	7.94E-05
327.89	1.7166	8.64	0.5026	3.47E-11	8.89E-05
206.6	2.7245	8.81	0.5322	3.68E-11	9.41E-05

Table C7. Thermophoretic force data for system **DOP/air** and **Run1011j** (also called "SE94I6")

Particle radius: 14.5 μm

Temperature of hot plate: 334.7 K

Temperature of cold plate: 262.1 K

Initial DC voltage, $V_{dc,0}$: 7.13 volt

Surface charge ploarity: negative

Related figure: 7.9

Pressure (Pa)	Kn	V_{dc} (volt)	$\nabla V_{dc}/V_{dc,0}$	F_{th} (N)	$F_{th}/(a^2\nabla T_{\infty})$ (N/m ² K)
14321	0.0326	7.39	0.0365	4.44E-12	7.79E-06
11943	0.039	7.45	0.0449	5.46E-12	9.58E-06
10923	0.0427	7.52	0.0547	6.65E-12	1.17E-05
9026.4	0.0517	7.57	0.0617	7.51E-12	1.32E-05
7888.1	0.0591	7.62	0.0687	8.36E-12	1.47E-05
6162	0.0757	7.7	0.0799	9.72E-12	1.71E-05
5479.5	0.0851	7.78	0.0912	1.11E-11	1.95E-05

4825.1	0.0966	7.8	0.094	1.14E-11	2.01E-05
4441.2	0.105	7.84	0.0996	1.21E-11	2.13E-05
3892.1	0.1198	7.9	0.108	1.31E-11	2.31E-05
3550.8	0.1313	7.95	0.115	1.4E-11	2.46E-05
3101.6	0.1503	8.01	0.1234	1.5E-11	2.64E-05
2768.4	0.1684	8.07	0.1318	1.6E-11	2.81E-05
2508.5	0.1859	8.15	0.1431	1.74E-11	3.05E-05
2309.9	0.2019	8.22	0.1529	1.86E-11	3.26E-05
2179.3	0.214	8.28	0.1613	1.96E-11	3.44E-05
2015.3	0.2314	8.37	0.1739	2.12E-11	3.71E-05
1874.1	0.2488	8.46	0.1865	2.27E-11	3.98E-05
1720.8	0.271	8.5	0.1921	2.34E-11	4.1E-05
1583.5	0.2945	8.55	0.1992	2.42E-11	4.25E-05
1464.9	0.3183	8.64	0.2118	2.58E-11	4.52E-05
1346.2	0.3464	8.75	0.2272	2.76E-11	4.85E-05
1239.6	0.3761	8.82	0.237	2.88E-11	5.06E-05
1161	0.4016	8.93	0.2525	3.07E-11	5.39E-05
1023.7	0.4555	9.09	0.2749	3.34E-11	5.87E-05
930.36	0.5012	9.2	0.2903	3.53E-11	6.2E-05
821.06	0.5679	9.31	0.3058	3.72E-11	6.53E-05
735.76	0.6337	9.46	0.3268	3.97E-11	6.98E-05
667.78	0.6982	9.54	0.338	4.11E-11	7.22E-05
566.48	0.8231	9.72	0.3633	4.42E-11	7.76E-05
493.17	0.9455	9.88	0.3857	4.69E-11	8.23E-05
403.87	1.1545	10.03	0.4067	4.95E-11	8.68E-05
333.22	1.3993	10.14	0.4222	5.13E-11	9.01E-05
261.25	1.7848	10.29	0.4432	5.39E-11	9.46E-05
175.94	2.6501	10.4	0.4586	5.58E-11	9.79E-05

Table C8. Thermophoretic force data for system **DOP/helium** and Run **1011k** (also called "**SE94I2**")

Particle radius: 14.45 μm

Temperature of hot plate: 334.7 K

Temperature of cold plate: 262.1 K

Initial DC voltage, $V_{dc,0}$: 7.13 volt

Surface charge polarity: negative

Related figures: 7.6, 7.10

Pressure (Pa)	Kn	V_{dc} (volt)	$\nabla V_{dc}/V_{dc,0}$	F_{th} (N)	$F_{th}/(a^2VT_{\infty})$ (N/m ² K)
11941	0.1062	9.05	0.2693	3.28E-11	5.75E-05
11406	0.1112	9.16	0.2847	3.46E-11	6.08E-05
10767	0.1178	9.27	0.3001	3.65E-11	6.41E-05

10059	0.1261	9.39	0.317	3.86E-11	6.77E-05
9534.2	0.133	9.54	0.338	4.11E-11	7.22E-05
8822.4	0.1438	9.74	0.3661	4.45E-11	7.82E-05
8074.7	0.1571	9.89	0.3871	4.71E-11	8.26E-05
7382.9	0.1718	10.11	0.418	5.08E-11	8.92E-05
6920.4	0.1833	10.32	0.4474	5.44E-11	9.55E-05
6353.9	0.1996	10.51	0.4741	5.77E-11	0.000101
5822.1	0.2179	10.76	0.5091	6.19E-11	0.000109
5366.2	0.2364	11.01	0.5442	6.62E-11	0.000116
4874.4	0.2602	11.31	0.5863	7.13E-11	0.000125
4455.9	0.2847	11.58	0.6241	7.59E-11	0.000133
3968	0.3197	11.93	0.6732	8.19E-11	0.000144
3686.8	0.3441	12.22	0.7139	8.68E-11	0.000152
3477.5	0.3648	12.37	0.7349	8.94E-11	0.000157
3191	0.3975	12.63	0.7714	9.38E-11	0.000165
2960.4	0.4285	12.86	0.8036	9.77E-11	0.000172
2725.8	0.4654	13.11	0.8387	1.02E-10	0.000179
2592.5	0.4893	13.29	0.864	1.05E-10	0.000184
2460.5	0.5155	13.4	0.8794	1.07E-10	0.000188
2313.9	0.5482	13.57	0.9032	1.1E-10	0.000193
2175.3	0.5831	13.74	0.9271	1.13E-10	0.000198
1972.7	0.643	14.04	0.9691	1.18E-10	0.000207
1727.4	0.7343	14.37	1.0154	1.23E-10	0.000217
1555.5	0.8155	14.6	1.0477	1.27E-10	0.000224
1446.2	0.8771	14.8	1.0757	1.31E-10	0.00023
1295.6	0.9791	14.97	1.0996	1.34E-10	0.000235
1203.6	1.0539	15.08	1.115	1.36E-10	0.000238
1070.3	1.1852	15.26	1.1403	1.39E-10	0.000243
938.36	1.3518	15.38	1.1571	1.41E-10	0.000247
857.05	1.4801	15.44	1.1655	1.42E-10	0.000249
755.75	1.6785	15.49	1.1725	1.43E-10	0.00025
659.78	1.9226	15.5	1.1739	1.43E-10	0.000251
561.15	2.2605	15.44	1.1655	1.42E-10	0.000249
457.18	2.7746	15.33	1.1501	1.4E-10	0.000246

Table C9. Thermophoretic force data for system **DOP/helium** and Run **0519h** (also called "MA94H2")

Particle radius: 15.3 μm

Temperature of hot plate: 322.2 K

Temperature of cold plate: 268.9 K

Initial DC voltage, $V_{dc,0}$: 17.26 volt

Surface charge polarity: positive

Related figures: 7.10

Pressure (Pa)	Kn	V _{dc} (volt)	$\nabla V_{dc}/V_{dc,0}$	F _{th} (N)	F _{th} /(a ² ∇T _∞) (N/m ² K)
12684	0.1	18.63	0.0794	1.15E-11	2.45E-05
12083	0.105	18.69	0.0829	1.2E-11	2.56E-05
11222	0.113	18.8	0.0892	1.3E-11	2.75E-05
10563	0.12	18.89	0.0944	1.37E-11	2.91E-05
9810.1	0.129	19	0.1008	1.46E-11	3.11E-05
9318.3	0.136	19.07	0.1049	1.52E-11	3.24E-05
8172	0.155	19.32	0.1194	1.73E-11	3.68E-05
7705.5	0.165	19.45	0.1269	1.84E-11	3.91E-05
7168.3	0.177	19.58	0.1344	1.95E-11	4.15E-05
6644.5	0.191	19.76	0.1448	2.1E-11	4.47E-05
6331.3	0.2	19.87	0.1512	2.2E-11	4.66E-05
5987.4	0.212	19.99	0.1582	2.3E-11	4.88E-05
5444.9	0.233	20.21	0.1709	2.48E-11	5.27E-05
5203.6	0.244	20.34	0.1784	2.59E-11	5.5E-05
4785.1	0.265	20.58	0.1924	2.79E-11	5.93E-05
4442.5	0.286	20.8	0.2051	2.98E-11	6.33E-05
4089.3	0.31	20.98	0.2155	3.13E-11	6.65E-05
3842.7	0.33	21.13	0.2242	3.26E-11	6.92E-05
3496.2	0.363	21.39	0.2393	3.47E-11	7.38E-05
3234.9	0.392	21.62	0.2526	3.67E-11	7.79E-05
2903	0.437	21.95	0.2717	3.95E-11	8.38E-05
2553.8	0.497	22.37	0.2961	4.3E-11	9.13E-05
2452.5	0.517	22.45	0.3007	4.37E-11	9.28E-05
2328.6	0.545	22.64	0.3117	4.53E-11	9.62E-05
2166	0.586	22.78	0.3198	4.64E-11	9.87E-05
2070	0.613	22.94	0.3291	4.78E-11	0.000102
1911.4	0.664	23.1	0.3384	4.91E-11	0.000104
1746.1	0.726	23.31	0.3505	5.09E-11	0.000108
1652.8	0.767	23.41	0.3563	5.17E-11	0.00011
1542.2	0.823	23.58	0.3662	5.32E-11	0.000113
1442.2	0.88	23.65	0.3702	5.38E-11	0.000114
1340.9	0.946	23.81	0.3795	5.51E-11	0.000117
1204.9	1.053	23.95	0.3876	5.63E-11	0.00012
1109	1.144	24.1	0.3963	5.75E-11	0.000122
961.02	1.32	24.26	0.4056	5.89E-11	0.000125
850.39	1.492	24.41	0.4143	6.01E-11	0.000128
683.78	1.855	24.39	0.4131	6E-11	0.000127
558.48	2.271	24.46	0.4171	6.06E-11	0.000129
467.85	2.711	24.33	0.4096	5.95E-11	0.000126

Table C10. Thermophoretic force data for system **DOP/helium** and Run **0519h** (also called "MA94H3").

Particle radius: 15.3 μm

Temperature of hot plate: 322.2 K

Temperature of cold plate: 268.9 K

Initial DC voltage, $V_{dc,0}$: 17.84 volt

Surface charge polarity: positive

Related figure: 7.10

Pressure (Pa)	Kn	V_{dc} (volt)	$\nabla V_{dc}/V_{dc,0}$	F_{th} (N)	$F_{th}/(a^2\nabla T_{\infty})$ (N/m ² K)
10976	0.115	19.46	0.0908	1.32E-11	2.8E-05
10510	0.1201	19.61	0.0992	1.44E-11	3.06E-05
9943.4	0.1269	19.86	0.1132	1.64E-11	3.49E-05
9338.3	0.1351	19.95	0.1183	1.72E-11	3.65E-05
8755.8	0.1441	20.09	0.1261	1.83E-11	3.89E-05
7722.8	0.1634	20.35	0.1407	2.04E-11	4.34E-05
6961.7	0.1813	20.62	0.1558	2.26E-11	4.81E-05
6449.9	0.1957	20.79	0.1654	2.4E-11	5.1E-05
5954	0.212	21.01	0.1777	2.58E-11	5.48E-05
5424.9	0.2326	21.27	0.1923	2.79E-11	5.93E-05
5165	0.2443	21.39	0.199	2.89E-11	6.14E-05
4933	0.2558	21.57	0.2091	3.04E-11	6.45E-05
4742.4	0.2661	21.67	0.2147	3.12E-11	6.62E-05
4523.8	0.279	21.77	0.2203	3.2E-11	6.8E-05
4218.6	0.2991	21.98	0.2321	3.37E-11	7.16E-05
4002.7	0.3153	22.13	0.2405	3.49E-11	7.42E-05
3730.8	0.3383	22.3	0.25	3.63E-11	7.71E-05
3481.5	0.3625	22.52	0.2623	3.81E-11	8.09E-05
3268.3	0.3861	22.74	0.2747	3.99E-11	8.47E-05
2936.4	0.4298	23.07	0.2932	4.26E-11	9.04E-05
2693.8	0.4685	23.38	0.3105	4.51E-11	9.58E-05
2539.2	0.497	23.5	0.3173	4.61E-11	9.79E-05
2405.9	0.5245	23.7	0.3285	4.77E-11	0.000101
2271.3	0.5556	23.85	0.3369	4.89E-11	0.000104
2100.6	0.6008	24.7	0.3845	5.58E-11	0.000119
1935.4	0.6521	24.28	0.361	5.24E-11	0.000111
1851.4	0.6816	24.52	0.3744	5.44E-11	0.000116
1623.5	0.7773	24.81	0.3907	5.67E-11	0.000121
1482.2	0.8514	24.99	0.4008	5.82E-11	0.000124
1323.6	0.9535	25.18	0.4114	5.97E-11	0.000127
1190.3	1.0602	25.34	0.4204	6.1E-11	0.00013
1069	1.1805	25.51	0.4299	6.24E-11	0.000133
938.36	1.3449	25.64	0.4372	6.35E-11	0.000135
818.4	1.542	25.5	0.4294	6.23E-11	0.000132
631.79	1.9974	25.62	0.4361	6.33E-11	0.000135
559.82	2.2543	25.4	0.4238	6.15E-11	0.000131
479.84	2.63	25.24	0.4148	6.02E-11	0.000128

439.86	2.8691	25	0.4013	5.83E-11	0.000124
--------	--------	----	--------	----------	----------

Table C11. Thermophoretic force data for system DOP/CO₂ and Run OT94CParticle radius: 13.8 μm

Temperature of hot plate: 334.7 K

Temperature of cold plate: 262.0 K

Initial DC voltage, $V_{dc,0}$: 6.0 volt

Surface charge polarity: negative

Related figure: 7.7

Pressure (Pa)	Kn	V_{dc} (volt)	$\nabla V_{dc}/V_{dc,0}$	F_{th} (N)	$F_{th}/(a^2\nabla T_{\infty})$ (N/m ² K)
5899.4	0.054	6.24	0.04	4.28E-12	8.17E-06
4991.7	0.0638	6.26	0.043	4.64E-12	8.85E-06
3982.7	0.08	6.3	0.05	5.35E-12	1.02E-05
3305.6	0.0964	6.31	0.052	5.53E-12	1.06E-05
2544.5	0.1252	6.33	0.055	5.88E-12	1.12E-05
2525.8	0.1262	6.37	0.062	6.6E-12	1.26E-05
1763.4	0.1807	6.45	0.075	8.02E-12	1.53E-05
1439.5	0.2214	6.54	0.09	9.63E-12	1.84E-05
1184.9	0.2689	6.6	0.1	1.07E-11	2.04E-05
1013	0.3146	6.72	0.12	1.28E-11	2.45E-05
886.38	0.3595	6.81	0.135	1.44E-11	2.76E-05
783.74	0.4066	6.94	0.157	1.68E-11	3.2E-05
639.79	0.498	7.02	0.17	1.82E-11	3.47E-05
530.49	0.6007	7.15	0.192	2.05E-11	3.92E-05
459.85	0.6929	7.32	0.22	2.35E-11	4.49E-05
359.88	0.8854	7.46	0.243	2.6E-11	4.97E-05
291.9	1.0916	7.56	0.26	2.78E-11	5.31E-05
241.25	1.3208	7.7	0.283	3.03E-11	5.79E-05
185.27	1.7199	7.81	0.302	3.23E-11	6.16E-05
139.95	2.2768	7.85	0.308	3.3E-11	6.3E-05
114.63	2.7798	7.88	0.313	3.35E-11	6.4E-05
93.303	3.4152	7.84	0.307	3.28E-11	6.26E-05
71.976	4.4271	7.83	0.305	3.26E-11	6.23E-05
50.65	6.2911	7.71	0.285	3.05E-11	5.82E-05
37.321	8.5379	7.6	0.267	2.85E-11	5.45E-05
27.991	11.384	7.49	0.248	2.66E-11	5.07E-05
22.659	14.062	7.32	0.22	2.35E-11	4.49E-05
18.661	17.076	7.09	0.182	1.94E-11	3.71E-05
14.662	21.733	7.04	0.173	1.85E-11	3.54E-05
13.329	23.906	6.91	0.152	1.62E-11	3.1E-05
10.663	29.883	6.77	0.128	1.37E-11	2.62E-05

Table C12. Thermophoretic force data for system PSL/air and Run 0905a.

Particle radius: 10.9 μm

Temperature of hot plate: 334.9 K

Temperature of cold plate: 261.9 K

Initial DC voltage, $V_{dc,0}$: 3.3 volt

Surface charge polarity: negative

Related figures: 6.9

Pressure (Pa)	Kn	V_{dc} (volt)	$\nabla V_{dc}/V_{dc,0}$	F_{th} (N)	$F_{th}/(a^2\nabla T_{\infty})$ (N/m ² K)
9133	0.0676	3.35	0.015	8.49E-13	2.6E-06
7846.8	0.0787	3.38	0.024	1.36E-12	4.16E-06
6669.8	0.0926	3.42	0.036	2.04E-12	6.24E-06
5819.4	0.1061	3.45	0.045	2.55E-12	7.8E-06
4643.8	0.133	3.48	0.055	3.06E-12	9.36E-06
4169.3	0.1481	3.52	0.067	3.74E-12	1.14E-05
3649.5	0.1692	3.57	0.082	4.58E-12	1.4E-05
3301.6	0.1871	3.59	0.088	4.92E-12	1.51E-05
3073.7	0.2009	3.64	0.103	5.77E-12	1.77E-05
2752.4	0.2244	3.68	0.115	6.45E-12	1.98E-05
2221.9	0.2779	3.75	0.136	7.64E-12	2.34E-05
2060.7	0.2997	3.8	0.152	8.49E-12	2.6E-05
1890	0.3267	3.88	0.176	9.85E-12	3.02E-05
1706.1	0.362	3.94	0.194	1.09E-11	3.33E-05
1464.9	0.4216	4.02	0.218	1.22E-11	3.74E-05
1331.6	0.4638	4.09	0.239	1.34E-11	4.11E-05
1171.6	0.5271	4.14	0.255	1.43E-11	4.37E-05
1062.3	0.5813	4.19	0.27	1.51E-11	4.63E-05
966.35	0.6391	4.27	0.294	1.65E-11	5.04E-05
865.05	0.7139	4.33	0.312	1.75E-11	5.36E-05
783.74	0.788	4.42	0.339	1.9E-11	5.82E-05
666.45	0.9266	4.49	0.361	2.02E-11	6.19E-05
566.48	1.0902	4.51	0.367	2.05E-11	6.29E-05
515.83	1.1972	4.59	0.391	2.19E-11	6.71E-05
434.52	1.4212	4.63	0.403	2.26E-11	6.92E-05
338.56	1.8241	4.69	0.421	2.36E-11	7.23E-05
265.25	2.3283	4.74	0.436	2.44E-11	7.49E-05
198.6	3.1096	4.72	0.43	2.41E-11	7.38E-05
149.28	4.1368	4.66	0.412	2.31E-11	7.07E-05
117.29	5.265	4.65	0.409	2.29E-11	7.02E-05
99.967	6.1776	4.62	0.4	2.24E-11	6.86E-05
83.972	7.3543	4.6	0.394	2.21E-11	6.76E-05

67.978	9.0848	4.51	0.367	2.05E-11	6.29E-05
50.65	12.193	4.5	0.364	2.04E-11	6.24E-05
34.655	17.82	4.44	0.345	1.94E-11	5.93E-05

Table C13 Thermophoretic force data for system PSL/ air and Run 0905b

Particle radius: 10.9 μm

Temperature of hot plate: 334.9 K

Temperature of cold plate: 261.9 K

Initial DC voltage, $V_{dc,0}$: 3.3 volt

Surface Charge Polarity: negative

Related figures: 6.9

Pressure (Pa)	Kn	V_{dc} (volt)	$\nabla V_{dc}/V_{dc,0}$	F_{th} (N)	$F_{th}/(a^2\nabla T_{\infty})$ (N/m ² K)
9194.3	0.067	3.33	0.0091	5.09E-13	1.56E-06
6945.7	0.089	3.38	0.0242	1.36E-12	4.16E-06
5794.1	0.107	3.41	0.0333	1.87E-12	5.72E-06
4829.1	0.128	3.47	0.0515	2.89E-12	8.84E-06
4048	0.153	3.5	0.0606	3.4E-12	1.04E-05
3408.2	0.181	3.57	0.0818	4.58E-12	1.4E-05
2889.7	0.214	3.61	0.0939	5.26E-12	1.61E-05
2492.5	0.248	3.68	0.1152	6.45E-12	1.98E-05
2072.7	0.298	3.77	0.1424	7.98E-12	2.44E-05
1775.4	0.348	3.82	0.1576	8.83E-12	2.7E-05
1532.8	0.403	4.01	0.2152	1.21E-11	3.69E-05
1292.9	0.478	4.1	0.2424	1.36E-11	4.16E-05
1099.6	0.562	4.19	0.2697	1.51E-11	4.63E-05
1013	0.61	4.25	0.2879	1.61E-11	4.94E-05
878.38	0.703	4.36	0.3212	1.8E-11	5.51E-05
783.74	0.788	4.46	0.3515	1.97E-11	6.03E-05
694.44	0.889	4.5	0.3636	2.04E-11	6.24E-05
590.47	1.046	4.64	0.4061	2.28E-11	6.97E-05
497.17	1.242	4.71	0.4273	2.39E-11	7.33E-05
445.19	1.387	4.72	0.4303	2.41E-11	7.38E-05
385.21	1.603	4.76	0.4424	2.48E-11	7.59E-05
302.57	2.041	4.9	0.4848	2.72E-11	8.32E-05
253.25	2.439	4.9	0.4848	2.72E-11	8.32E-05
197.27	3.131	4.98	0.5091	2.85E-11	8.74E-05
153.28	4.029	4.94	0.497	2.78E-11	8.53E-05
113.3	5.451	4.89	0.4818	2.7E-11	8.27E-05
69.311	8.91	4.88	0.4788	2.68E-11	8.22E-05
53.316	11.58	4.7	0.4242	2.38E-11	7.28E-05
41.32	14.95	4.66	0.4121	2.31E-11	7.07E-05

Table C14. Thermophoretic force data for system PSL/CO₂ and Run SE94H2Particle radius: 10.91 μm

Temperature of hot plate: 334.9 K

Temperature of cold plate: 261.9 K

Initial DC voltage, $V_{dc,0}$: 3.3 volt

Surface charge polarity: negative

Related figures: 7.3

Pressure (Pa)	Kn	V_{dc} (volt)	$\nabla V_{dc}/V_{dc,0}$	F_{th} (N)	$F_{th}/(a^2\nabla T_{\infty})$ (N/m ² K)
14549	0.0278	3.33	0.0091	5.09E-13	1.56E-06
4313.2	0.0938	3.37	0.0212	1.19E-12	3.64E-06
2761.8	0.1465	3.41	0.0333	1.87E-12	5.72E-06
2303.2	0.1756	3.48	0.0545	3.06E-12	9.36E-06
1991.3	0.2031	3.53	0.0697	3.91E-12	1.2E-05
1459.5	0.2771	3.61	0.0939	5.26E-12	1.61E-05
1200.9	0.3368	3.65	0.1061	5.94E-12	1.82E-05
1069	0.3784	3.72	0.1273	7.13E-12	2.18E-05
993.01	0.4073	3.76	0.1394	7.81E-12	2.39E-05
903.7	0.4476	3.82	0.1576	8.83E-12	2.7E-05
810.4	0.4991	3.9	0.1818	1.02E-11	3.12E-05
699.77	0.578	3.96	0.2	1.12E-11	3.43E-05
613.13	0.6597	4.01	0.2152	1.21E-11	3.69E-05
489.17	0.8268	4.03	0.2212	1.24E-11	3.8E-05
430.53	0.9395	4.14	0.2545	1.43E-11	4.37E-05
359.88	1.1239	4.21	0.2758	1.55E-11	4.73E-05
291.9	1.3856	4.28	0.297	1.66E-11	5.1E-05
249.25	1.6227	4.32	0.3091	1.73E-11	5.3E-05
207.93	1.9452	4.39	0.3303	1.85E-11	5.67E-05
153.28	2.6387	4.45	0.3485	1.95E-11	5.98E-05

Table C15. Thermophoretic force data for system PSL/CO₂ and Run SE94H5Particle radius: 10.91 μm

Temperature of hot plate: 334.9 K

Temperature of cold plate: 261.9 K

Initial DC voltage, $V_{dc,0}$: 3.3 volt

Surface charge polarity: negative

Related figures: 7.3, 7.7

Pressure (Pa)	Kn	V _{dc} (volt)	$\nabla V_{dc}/V_{dc,0}$	F _{th} (N)	F _{th} /(a ² ∇T _∞) (N/m ² K)
3934.7	0.1028	3.36	0.0182	1.02E-12	3.12E-06
3258.9	0.1241	3.4	0.0303	1.7E-12	5.2E-06
2150	0.1881	3.43	0.0394	2.21E-12	6.76E-06
1699.4	0.238	3.49	0.0576	3.23E-12	9.88E-06
1363.6	0.2966	3.57	0.0818	4.58E-12	1.4E-05
1274.2	0.3174	3.66	0.1091	6.11E-12	1.87E-05
1055.7	0.3831	3.72	0.1273	7.13E-12	2.18E-05
819.73	0.4934	3.79	0.1485	8.32E-12	2.55E-05
705.1	0.5736	3.86	0.1697	9.51E-12	2.91E-05
583.81	0.6928	3.96	0.2	1.12E-11	3.43E-05
454.52	0.8899	4.11	0.2455	1.38E-11	4.21E-05
371.88	1.0876	4.17	0.2636	1.48E-11	4.52E-05
319.89	1.2644	4.21	0.2758	1.55E-11	4.73E-05
263.91	1.5326	4.28	0.297	1.66E-11	5.1E-05
209.26	1.9328	4.41	0.3364	1.88E-11	5.77E-05
147.95	2.7337	4.48	0.3576	2E-11	6.14E-05

Table C16. Thermophoretic force data for system PSL/helium and Run 1005c (also called "SE94H6")

Particle radius: 10.91 μm

Temperature of hot plate: 334.9 K

Temperature of cold plate: 261.9 K

Initial DC voltage, V_{dc,0}: 3.30 volt

Surface charge polarity: negative

Related figures: 7.6, 7.11

Pressure (Pa)	Kn	V _{dc} (volt)	$\nabla V_{dc}/V_{dc,0}$	F _{th} (N)	F _{th} /(a ² ∇T _∞) (N/m ² K)
13654	0.1313	4.4	0.333	1.87E-11	5.72E-05
12904	0.139	4.48	0.358	2E-11	6.14E-05
11960	0.1499	4.57	0.385	2.16E-11	6.6E-05
11228	0.1597	4.63	0.403	2.26E-11	6.92E-05
10637	0.1686	4.74	0.436	2.44E-11	7.49E-05
9960.7	0.18	4.84	0.467	2.61E-11	8.01E-05
9312.9	0.1926	4.92	0.491	2.75E-11	8.42E-05
8638.5	0.2076	5.05	0.53	2.97E-11	9.1E-05
7965.4	0.2251	5.2	0.576	3.23E-11	9.88E-05
7380.2	0.243	5.31	0.609	3.41E-11	0.000105

6713.8	0.2671	5.44	0.648	3.63E-11	0.000111
6279.3	0.2856	5.55	0.682	3.82E-11	0.000117
5924.7	0.3027	5.61	0.7	3.92E-11	0.00012
5508.9	0.3255	5.79	0.755	4.23E-11	0.000129
5270.3	0.3403	5.89	0.785	4.4E-11	0.000135
4863.7	0.3687	6.02	0.824	4.62E-11	0.000141
4438.5	0.404	6.25	0.894	5.01E-11	0.000153
4038.7	0.444	6.38	0.933	5.23E-11	0.00016
3733.4	0.4803	6.49	0.967	5.42E-11	0.000166
3334.9	0.5377	6.74	1.042	5.84E-11	0.000179
3111	0.5764	6.78	1.055	5.91E-11	0.000181
2731.1	0.6566	7	1.121	6.28E-11	0.000192
2296.6	0.7808	7.26	1.2	6.72E-11	0.000206
2088.6	0.8586	7.4	1.242	6.96E-11	0.000213
1720.8	1.0421	7.71	1.336	7.49E-11	0.000229
1472.8	1.2175	7.98	1.418	7.95E-11	0.000243
1243.6	1.442	8.06	1.442	8.08E-11	0.000247
1061	1.6902	8.07	1.445	8.1E-11	0.000248
883.71	2.0292	8.13	1.464	8.2E-11	0.000251
725.09	2.4731	8.17	1.476	8.27E-11	0.000253

Table C17. Thermophoretic force data for system PSL/helium and Run1005C (also called "SE94H7")

Particle radius: 10.91 μm

Temperature of hot plate: 334.9 K

Temperature of cold plate: 261.9 K

Initial DC voltage, $V_{dc,0}$: 3.30 volt

Surface charge polarity: negative

Related figures: 7.6, 7.11

Pressure (Pa)	Kn	V_{dc} (volt)	$\nabla V_{dc}/V_{dc,0}$	F_{th} (N)	$F_{th}/(a^2\nabla T_{\infty})$ (N/m ² K)
14441	0.1242	4.42	0.3394	1.9E-11	5.82E-05
13577	0.1321	4.49	0.3606	2.02E-11	6.19E-05
12770	0.1404	4.55	0.3788	2.12E-11	6.5E-05
11905	0.1506	4.66	0.4121	2.31E-11	7.07E-05
11000	0.163	4.8	0.4545	2.55E-11	7.8E-05
10338	0.1735	4.86	0.4727	2.65E-11	8.11E-05
9415.6	0.1905	5.03	0.5242	2.94E-11	9E-05
8862.4	0.2023	5.1	0.5455	3.06E-11	9.36E-05

8277.3	0.2166	5.2	0.5758	3.23E-11	9.88E-05
7706.8	0.2327	5.34	0.6182	3.46E-11	0.000106
7005.7	0.256	5.46	0.6545	3.67E-11	0.000112
6467.2	0.2773	5.61	0.7	3.92E-11	0.00012
5832.7	0.3074	5.81	0.7606	4.26E-11	0.000131
5411.6	0.3314	5.96	0.8061	4.52E-11	0.000138
5034.3	0.3562	6.08	0.8424	4.72E-11	0.000145
4623.8	0.3878	6.23	0.8879	4.97E-11	0.000152
4210.6	0.4259	6.43	0.9485	5.31E-11	0.000163
3828.1	0.4684	6.57	0.9909	5.55E-11	0.00017
3552.2	0.5048	6.75	1.0455	5.86E-11	0.000179
3273.6	0.5478	6.87	1.0818	6.06E-11	0.000186
2976.4	0.6025	7.05	1.1364	6.37E-11	0.000195
2617.8	0.685	7.26	1.2	6.72E-11	0.000206
2364.6	0.7584	7.41	1.2455	6.98E-11	0.000214
2056.7	0.8719	7.62	1.3091	7.33E-11	0.000225
1796.7	0.9981	7.86	1.3818	7.74E-11	0.000237
1580.8	1.1344	7.91	1.397	7.83E-11	0.00024
1299.6	1.3799	8.16	1.4727	8.25E-11	0.000253
1067.6	1.6796	8.22	1.4909	8.35E-11	0.000256
923.7	1.9414	8.22	1.4909	8.35E-11	0.000256
778.41	2.3037	8.24	1.497	8.39E-11	0.000257

Table C18. Thermophoretic force data for system PSL/helium and Run 0524j (also called "MA94J")

Particle radius: 10.7 μm

Temperature of hot plate: 328 K

Temperature of cold plate: 268.1 K

Initial DC voltage, $V_{dc,0}$: 7.19 volt

Surface charge polarity: positive

Related figure: 7.11

Pressure (Pa)	Kn	V_{dc} (volt)	$\nabla V_{dc}/V_{dc,0}$	F_{th} (N)	$F_{th}/(a^2\nabla T_{\infty})$ (N/m ² K)
14386	0.12722	7.78	0.0821	4.31E-12	1.68E-05
12276	0.14909	7.87	0.0946	4.96E-12	1.94E-05
11304	0.1619	7.9	0.0987	5.18E-12	2.02E-05
9355.6	0.19563	7.94	0.1043	5.47E-12	2.13E-05
8120	0.22539	8.04	0.1182	6.2E-12	2.42E-05
7437.6	0.24608	8.19	0.1391	7.3E-12	2.85E-05
7032.4	0.26025	8.25	0.1474	7.74E-12	3.02E-05
6280.6	0.2914	8.33	0.1586	8.32E-12	3.24E-05
5951.4	0.30753	8.44	0.1739	9.12E-12	3.56E-05

5494.2	0.33311	8.5	0.1822	9.56E-12	3.73E-05
5224.9	0.35028	8.59	0.1947	1.02E-11	3.98E-05
4754.4	0.38495	8.7	0.21	1.1E-11	4.3E-05
4391.9	0.41672	8.76	0.2184	1.15E-11	4.47E-05
4094.7	0.44697	8.82	0.2267	1.19E-11	4.64E-05
3697.5	0.49499	8.92	0.2406	1.26E-11	4.92E-05
3465.5	0.52812	9.06	0.2601	1.37E-11	5.32E-05
3205.6	0.57094	9.15	0.2726	1.43E-11	5.58E-05
2889.7	0.63335	9.25	0.2865	1.5E-11	5.86E-05
2596.5	0.70488	9.39	0.306	1.61E-11	6.26E-05
2489.8	0.73506	9.49	0.3199	1.68E-11	6.55E-05
2271.3	0.80581	9.61	0.3366	1.77E-11	6.89E-05
2040.7	0.89686	9.73	0.3533	1.85E-11	7.23E-05
1882	0.97245	9.78	0.3602	1.89E-11	7.37E-05
1754.1	1.04339	9.78	0.3602	1.89E-11	7.37E-05
1663.5	1.10024	9.78	0.3602	1.89E-11	7.37E-05
1530.2	1.19608	9.81	0.3644	1.91E-11	7.46E-05
1508.8	1.21299	9.88	0.3741	1.96E-11	7.65E-05
1307.6	1.39969	9.98	0.388	2.04E-11	7.94E-05
1143.6	1.60035	10.13	0.4089	2.15E-11	8.37E-05
1155.6	1.58374	10.13	0.4089	2.15E-11	8.37E-05
975.68	1.87582	10.23	0.4228	2.22E-11	8.65E-05
817.06	2.23997	10.46	0.4548	2.39E-11	9.31E-05
613.13	2.985	10.55	0.4673	2.45E-11	9.56E-05

Table C19. Thermophoretic force data for system nickel/air and Run 0726a

Particle radius: 5.22 μm

Temperature of hot plate: 338.4 K

Temperature of cold plate: 263.2K

Initial DC voltage, $V_{dc,0}$: 24.87 volt

Surface charge polarity; negative

Related figures: 6.10

Pressure (Pa)	Kn	V_{dc} (volt)	$V_{dc}/V_{dc,0}$	F_{th} (N)	$F_{th}/(a^2VT_\infty)$ (N/m ² K)
13014	0.1002	24.9	0.0012	6.29E-14	8.15E-07
11692	0.1115	24.93	0.0024	1.26E-13	1.63E-06
10988	0.1186	24.97	0.004	2.1E-13	2.72E-06
10291	0.1267	25.02	0.006	3.14E-13	4.08E-06
8866.4	0.147	25.12	0.0101	5.24E-13	6.79E-06
7724.1	0.1688	25.19	0.0129	6.7E-13	8.7E-06
6723.1	0.1939	25.23	0.0145	7.54E-13	9.78E-06
6616.5	0.197	25.26	0.0157	8.17E-13	1.06E-05
6420.6	0.203	25.31	0.0177	9.22E-13	1.2E-05

6020.7	0.2165	25.35	0.0193	1.01E-12	1.3E-05
5703.5	0.2286	25.42	0.0221	1.15E-12	1.49E-05
5354.2	0.2435	25.5	0.0253	1.32E-12	1.71E-05
5135.6	0.2538	25.59	0.029	1.51E-12	1.96E-05
4702.5	0.2772	25.62	0.0302	1.57E-12	2.04E-05
4475.9	0.2913	25.67	0.0322	1.68E-12	2.17E-05
4334.6	0.3007	25.71	0.0338	1.76E-12	2.28E-05
4221.3	0.3088	25.78	0.0366	1.91E-12	2.47E-05
3984	0.3272	25.85	0.0394	2.05E-12	2.66E-05
3677.5	0.3545	25.93	0.0426	2.22E-12	2.88E-05
3500.2	0.3724	25.99	0.045	2.35E-12	3.04E-05
3392.2	0.3843	26.05	0.0474	2.47E-12	3.21E-05
3258.9	0.4	26.1	0.0495	2.58E-12	3.34E-05
3099	0.4207	26.16	0.0519	2.7E-12	3.51E-05
2975	0.4382	26.24	0.0551	2.87E-12	3.72E-05
2827.1	0.4611	26.29	0.0571	2.98E-12	3.86E-05
2709.8	0.4811	26.4	0.0615	3.21E-12	4.16E-05
2557.8	0.5097	26.47	0.0643	3.35E-12	4.35E-05
2423.2	0.538	26.56	0.068	3.54E-12	4.59E-05
2263.3	0.576	26.65	0.0716	3.73E-12	4.84E-05
2066	0.631	26.74	0.0752	3.92E-12	5.08E-05
2050	0.6359	26.83	0.0788	4.11E-12	5.33E-05
1934	0.674	26.9	0.0816	4.25E-12	5.52E-05
1871.4	0.6966	26.99	0.0852	4.44E-12	5.76E-05
1759.4	0.7409	27.02	0.0864	4.5E-12	5.84E-05
1706.1	0.7641	27.06	0.0881	4.59E-12	5.95E-05
1626.1	0.8017	27.13	0.0909	4.74E-12	6.14E-05
1551.5	0.8402	27.21	0.0941	4.9E-12	6.36E-05
1456.9	0.8948	27.28	0.0969	5.05E-12	6.55E-05
1418.2	0.9192	27.33	0.0989	5.15E-12	6.69E-05
1347.6	0.9674	27.42	0.1025	5.34E-12	6.93E-05
1268.9	1.0273	27.47	0.1045	5.45E-12	7.07E-05
1195.6	1.0903	27.58	0.109	5.68E-12	7.37E-05
1050.3	1.2412	27.65	0.1118	5.82E-12	7.56E-05
927.69	1.4052	27.78	0.117	6.1E-12	7.91E-05
761.08	1.7128	27.85	0.1198	6.24E-12	8.1E-05
674.44	1.9329	27.79	0.1174	6.12E-12	7.94E-05
534.49	2.439	27.7	0.1138	5.93E-12	7.69E-05
390.54	3.338	27.6	0.1098	5.72E-12	7.42E-05
331.89	3.9279	27.45	0.1037	5.41E-12	7.01E-05
277.24	4.7021	27.78	0.117	6.1E-12	7.91E-05
169.28	7.7011	27.49	0.1053	5.49E-12	7.12E-05
87.971	14.819	27.52	0.1066	5.55E-12	7.2E-05

Table C20. Thermophoretic force data for system nickel/helium and Run SE94C
Particle radius: 5.46 μm

Temperature of hot plate: 334.7 K
 Temperature of cold plate: 262.1 K
 Initial DC voltage, $V_{dc,0}$: 19.11 volt
 Surface charge polarity: negative
 Related figure: 7.2, 7.6

Pressure (Pa)	Kn	V_{dc} (volt)	$\nabla V_{dc}/V_{dc,0}$	F_{th} (N)	$F_{th}/(a^2\nabla T_{\infty})$ (N/m ² K)
13632	0.263	21.4	0.12	7.15E-12	8.78E-05
13120	0.273	21.57	0.129	7.68E-12	9.43E-05
12579	0.285	21.66	0.133	7.96E-12	9.77E-05
12057	0.297	21.76	0.139	8.27E-12	1.02E-04
11771	0.304	21.82	0.142	8.46E-12	1.04E-04
11267	0.318	21.96	0.149	8.9E-12	1.09E-04
10854	0.33	22.04	0.153	9.15E-12	1.12E-04
10503	0.341	22.15	0.159	9.49E-12	1.17E-04
10211	0.351	22.21	0.162	9.68E-12	1.19E-04
9806.1	0.365	22.32	0.168	1E-11	1.23E-04
9383.6	0.382	22.45	0.175	1.04E-11	1.28E-04
9155.7	0.391	22.51	0.178	1.06E-11	1.30E-04
8767.8	0.408	22.63	0.184	1.1E-11	1.35E-04
8421.2	0.425	22.75	0.19	1.14E-11	1.40E-04
7994.7	0.448	22.91	0.199	1.19E-11	1.46E-04
7554.8	0.474	23.08	0.208	1.24E-11	1.52E-04
7061.7	0.507	23.27	0.218	1.3E-11	1.59E-04
6528.5	0.548	23.5	0.23	1.37E-11	1.68E-04
6115.3	0.586	23.69	0.24	1.43E-11	1.76E-04
5575.5	0.642	23.97	0.254	1.52E-11	1.86E-04
5103.7	0.702	24.15	0.264	1.57E-11	1.93E-04
4954.4	0.723	24.23	0.268	1.6E-11	1.96E-04
4625.1	0.774	24.34	0.274	1.63E-11	2.00E-04
4269.3	0.839	24.49	0.282	1.68E-11	2.06E-04
3993.4	0.897	24.65	0.29	1.73E-11	2.12E-04
3713.4	0.964	24.77	0.296	1.77E-11	2.17E-04
3409.5	1.05	24.91	0.304	1.81E-11	2.22E-04
3017.7	1.187	25.04	0.31	1.85E-11	2.27E-04
2725.8	1.314	25.15	0.316	1.89E-11	2.31E-04
2444.5	1.465	25.23	0.32	1.91E-11	2.35E-04
2253.9	1.589	25.27	0.322	1.92E-11	2.36E-04
2026	1.767	25.27	0.322	1.92E-11	2.36E-04
1747.4	2.049	25.27	0.322	1.92E-11	2.36E-04
1538.2	2.328	25.23	0.32	1.91E-11	2.35E-04
1480.8	2.418	25.18	0.318	1.89E-11	2.33E-04
1318.2	2.716	25.12	0.314	1.88E-11	2.30E-04
1264.9	2.831	25.03	0.31	1.85E-11	2.27E-04

Table C21 Thermophoretic force data for system glass/air and Run 0927a.

Particle radius: 11.5 μm

Temperature of hot plate: 335.1 K

Temperature of cold plate: 262.2 K

Initial DC voltage, $V_{dc,0}$: 24.87 volt

Surface charge polarity: negative

Related figure: 6.10

Pressure (Pa)	Kn	V_{dc} (volt)	$\nabla V_{dc}/V_{dc,0}$	F_{th} (N)	$F_{th}/(a^2\nabla T_\infty)$ (N/m ² K)
5118.3	0.1149	14.89	0.0068	1.03E-12	2.85E-06
4157.3	0.1415	14.94	0.0101	1.54E-12	4.27E-06
3181.6	0.1848	15.14	0.0237	3.6E-12	9.97E-06
2932.4	0.2005	15.22	0.0291	4.42E-12	1.23E-05
2476.5	0.2375	15.32	0.0358	5.44E-12	1.51E-05
2309.9	0.2546	15.47	0.046	6.98E-12	1.94E-05
2088.6	0.2815	15.56	0.0521	7.91E-12	2.19E-05
1880.7	0.3127	15.67	0.0595	9.04E-12	2.51E-05
1603.5	0.3667	15.85	0.0717	1.09E-11	3.02E-05
1420.9	0.4139	16	0.0818	1.24E-11	3.45E-05
1318.2	0.4461	16.1	0.0886	1.35E-11	3.73E-05
1187.6	0.4952	16.26	0.0994	1.51E-11	4.19E-05
1025	0.5737	16.41	0.1095	1.66E-11	4.62E-05
922.36	0.6376	16.56	0.1197	1.82E-11	5.04E-05
822.4	0.7151	16.64	0.1251	1.9E-11	5.27E-05
735.76	0.7993	16.73	0.1312	1.99E-11	5.53E-05
643.79	0.9134	16.9	0.1427	2.17E-11	6.01E-05
567.81	1.0356	16.98	0.1481	2.25E-11	6.24E-05
495.84	1.186	17.06	0.1535	2.33E-11	6.47E-05

Table C22. Thermophoretic force data for glass/air and Run 0927b

Particle radius: 11.5 μm

Temperature of hot plate: 335.1 K

Temperature of cold plate: 262.2 K

Initial DC voltage, $V_{dc,0}$: 24.87 volt

Surface charge polarity: negative

Related figures: 6.10

Pressure (Pa)	Kn	V _{dc} (volt)	$\nabla V_{dc}/V_{dc,0}$	F _{th} (N)	F _{th} /(a ² ∇T _∞) (N/m ² K)
5404.9	0.1088	14.83	0.0027	4.109E-13	1.14E-06
4825.1	0.12187	14.9	0.0074	1.13E-12	3.13E-06
4311.9	0.13638	14.97	0.0122	1.849E-12	5.13E-06
3838.7	0.15319	15.03	0.0162	2.465E-12	6.84E-06
3505.5	0.16775	15.1	0.021	3.184E-12	8.83E-06
3145.6	0.18694	15.31	0.0352	5.341E-12	1.43E-05
2612.5	0.2251	15.39	0.0406	6.163E-12	1.71E-05
2324.6	0.25297	15.49	0.0473	7.19E-12	1.99E-05
2132.6	0.27574	15.56	0.0521	7.909E-12	2.19E-05
1994	0.29491	15.67	0.0595	9.039E-12	2.51E-05
1776.7	0.33097	15.79	0.0676	1.027E-11	2.85E-05
1624.8	0.36193	15.96	0.0791	1.202E-11	3.33E-05
1439.5	0.40851	16.06	0.0859	1.305E-11	3.62E-05
1326.2	0.4434	16.14	0.0913	1.387E-11	3.85E-05
1203.6	0.48858	16.3	0.1021	1.551E-11	4.3E-05
1091.6	0.53869	16.42	0.1102	1.674E-11	4.65E-05
982.34	0.59862	16.55	0.119	1.808E-11	5.02E-05
859.72	0.68401	16.66	0.1264	1.921E-11	5.33E-05
793.07	0.74149	16.87	0.1406	2.137E-11	5.93E-05
638.46	0.92106	16.97	0.1474	2.239E-11	6.21E-05
565.15	1.04053	17.09	0.1555	2.363E-11	6.55E-05
495.84	1.18599	17.22	0.1643	2.496E-11	6.93E-05
415.86	1.41406	17.28	0.1684	2.558E-11	7.1E-05
345.22	1.70342	17.46	0.1805	2.743E-11	7.61E-05
293.24	2.00539	17.48	0.1819	2.763E-11	7.67E-05
235.92	2.49258	17.49	0.1826	2.773E-11	7.69E-05
185.27	3.174	17.49	0.1826	2.773E-11	7.69E-05
133.29	4.41187	17.49	0.1826	2.773E-11	7.69E-05
81.307	7.23257	17.41	0.1771	2.691E-11	7.47E-05
62.646	9.38695	17.36	0.1738	2.64E-11	7.32E-05
47.984	12.2552	17.23	0.165	2.506E-11	6.95E-05
34.655	16.9687	17.07	0.1542	2.342E-11	6.5E-05

Table C23. Thermophoretic force data for system glass/helium and Run JA95Y1

Particle radius: 10.65 μm

Temperature of hot plate: 337.5 K

Temperature of cold plate: 265.1 K

Initial DC voltage, V_{dc,0}: 10.18 volt

Surface charge polarity: negative

Related figure: 7.2,7.6

Pressure (Pa)	Kn	V _{dc} (volt)	$\nabla V_{dc}/V_{dc,0}$	F _{th} (N)	F _{th} /(a ² ∇T _∞) (N/m ² K)
14522	0.128	11.75	0.132	1.61E-11	5.20E-05
13618	0.1364	11.87	0.144	1.75E-11	5.66E-05
12984	0.1431	11.93	0.149	1.82E-11	5.88E-05
11797	0.1575	12.11	0.167	2.03E-11	6.57E-05
11252	0.1651	12.19	0.174	2.12E-11	6.87E-05
10794	0.1721	12.31	0.186	2.26E-11	7.33E-05
10139	0.1833	12.41	0.196	2.38E-11	7.71E-05
9375.6	0.1982	12.51	0.205	2.5E-11	8.09E-05
8577.2	0.2166	12.7	0.224	2.72E-11	8.81E-05
8100	0.2294	12.81	0.234	2.85E-11	9.23E-05
7594.8	0.2447	12.95	0.248	3.01E-11	9.76E-05
7003	0.2653	13.1	0.262	3.19E-11	1.03E-04
6499.2	0.2859	13.33	0.284	3.46E-11	1.12E-04
5983.4	0.3105	13.57	0.307	3.74E-11	1.21E-04
5432.9	0.342	13.82	0.331	4.03E-11	1.31E-04
4814.4	0.3859	14.08	0.356	4.33E-11	1.40E-04
4286.6	0.4335	14.33	0.381	4.63E-11	1.50E-04
3786.8	0.4907	14.75	0.421	5.12E-11	1.66E-04
3512.2	0.529	14.93	0.438	5.33E-11	1.73E-04
2935	0.6331	15.42	0.486	5.9E-11	1.91E-04
2720.4	0.683	15.54	0.497	6.05E-11	1.96E-04
2476.5	0.7503	15.82	0.524	6.37E-11	2.07E-04
2289.9	0.8114	15.97	0.539	6.55E-11	2.12E-04
2056.7	0.9034	16.19	0.56	6.81E-11	2.21E-04
1870.1	0.9936	16.35	0.575	6.99E-11	2.27E-04
1719.4	1.0806	16.46	0.586	7.12E-11	2.31E-04
1576.8	1.1784	16.62	0.601	7.31E-11	2.37E-04
1370.2	1.3561	16.76	0.615	7.47E-11	2.42E-04
1244.9	1.4925	16.74	0.613	7.45E-11	2.41E-04
1172.9	1.5841	16.78	0.617	7.5E-11	2.43E-04
1038.3	1.7895	16.86	0.624	7.59E-11	2.46E-04
839.72	2.2127	16.88	0.626	7.62E-11	2.47E-04
693.11	2.6808	16.71	0.61	7.42E-11	2.40E-04

Table C24. Thermophoretic force data for system glass/CO₂ and Run SE95F1

Particle radius: 10.11 μm

Temperature of hot plate: 334.7 K

Temperature of cold plate: 262 K

Initial DC voltage, V_{dc,0}: 8.73 volt

Surface charge polarity: negative

Related figure: 7.3, 7.7

Pressure (Pa)	Kn	V _{dc} (volt)	$\nabla V_{dc}/V_{dc,0}$	F _{th} (N)	F _{th} /(a ² ∇T _∞) (N/m ² K)
3776.1	0.1156	8.8	0.008	8.34E-13	2.99E-06
2611.1	0.1671	8.9	0.0195	2.03E-12	7.25E-06
1936.7	0.2253	8.95	0.0252	2.62E-12	9.39E-06
1775.4	0.2458	9.02	0.0332	3.46E-12	1.24E-05
1270.2	0.3435	9.12	0.0447	4.65E-12	1.66E-05
1078.3	0.4047	9.21	0.055	5.72E-12	2.05E-05
926.36	0.4711	9.26	0.0607	6.32E-12	2.26E-05
806.4	0.5411	9.35	0.071	7.39E-12	2.65E-05
723.76	0.6029	9.4	0.0767	7.98E-12	2.86E-05
642.46	0.6792	9.46	0.0836	8.7E-12	3.12E-05
578.48	0.7543	9.53	0.0916	9.53E-12	3.41E-05
519.83	0.8394	9.61	0.1008	1.05E-11	3.76E-05
463.85	0.9407	9.69	0.11	1.14E-11	4.1E-05
399.87	1.0913	9.77	0.1191	1.24E-11	4.44E-05
346.55	1.2592	9.81	0.1237	1.29E-11	4.61E-05
273.24	1.597	9.9	0.134	1.39E-11	4.99E-05
233.26	1.8707	9.94	0.1386	1.44E-11	5.16E-05
186.61	2.3384	9.98	0.1432	1.49E-11	5.33E-05
147.95	2.9494	10.04	0.1501	1.56E-11	5.59E-05

Table C25. Thermophoretic force data for system glass/CO₂ and Run SE95F2

Particle radius: 10.11 μm

Temperature of hot plate: 334.7 K

Temperature of cold plate: 262 K

Initial DC voltage, V_{dc,0}: 8.73 volt

Surface charge polarity: negative

Related figures: 7.3

Pressure (Pa)	Kn	V _{dc} (volt)	$\nabla V_{dc}/V_{dc,0}$	F _{th} (N)	F _{th} /(a ² ∇T _∞) (N/m ² K)
2829.7	0.1542	8.72	-0.001	-1.2E-13	-4.3E-07
2320.6	0.188	8.77	0.0046	4.77E-13	1.71E-06
2092.6	0.2085	8.81	0.0092	9.53E-13	3.41E-06
1850.1	0.2359	8.9	0.0195	2.03E-12	7.25E-06
1548.8	0.2817	8.96	0.0263	2.74E-12	9.81E-06
1310.2	0.333	9	0.0309	3.22E-12	1.15E-05
1143.6	0.3816	9.07	0.0389	4.05E-12	1.45E-05

1047.7	0.4165	9.13	0.0458	4.77E-12	1.71E-05
958.35	0.4553	9.2	0.0538	5.6E-12	2.01E-05
875.71	0.4983	9.29	0.0641	6.67E-12	2.39E-05
773.08	0.5644	9.36	0.0722	7.51E-12	2.69E-05
674.44	0.647	9.4	0.0767	7.98E-12	2.86E-05
606.47	0.7195	9.49	0.0871	9.06E-12	3.24E-05
527.83	0.8267	9.58	0.0974	1.01E-11	3.63E-05
462.51	0.9435	9.64	0.1042	1.08E-11	3.88E-05
407.87	1.0699	9.7	0.1111	1.16E-11	4.14E-05
349.22	1.2495	9.8	0.1226	1.28E-11	4.57E-05
222.59	1.9604	9.87	0.1306	1.36E-11	4.86E-05
170.61	2.5577	9.96	0.1409	1.47E-11	5.25E-05
117.29	3.7202	10.03	0.1489	1.55E-11	5.55E-05
95.968	4.5469	10.03	0.1489	1.55E-11	5.55E-05

VITA

Name: Wanguang Li

Date of Birth: April 14, 1968

Place of Birth: Hunan, People's Republic of China

Education:

Ph. D. in Chemical Engineering, University of Washington, Seattle, 1995

B. S. in Chemical Engineering, East China Institute of Technology, Nanjing, 1990

Publications:

Li, W. and Davis, E. J. (1995). "Aerosol evaporation in the transition regime," submitted for publication in *Aerosol Sci. Technology*.

Li, W. and Davis, E. J. (1995). "The effects of gas and particle properties on the thermophoretic force," *J. Aerosol Sci.*, 26 (7), 1063-1083.

Li, W. and Davis, E. J. (1995). "Thermophoretic force measurements on a single aerosol particle using electrodynamic levitation," *J. Aerosol Sci.*, 26 (7), 1085-1099.

Li, W., S. D. Rassat, W. R. Foss and E. J. Davis (1994). "Formation and properties of aerocolloidal TiO₂-coated microspheres produced by alkoxide droplet reaction," *J. Colloid Interf. Sci.*, 162 (2), 267-278.

W. R. Foss, W. Li, T. M. Allen, D. S. Blair and E. J. Davis (1993). "Studies of toxic aerosols via elastic and inelastic light scattering," *Aerosol Sci. Technology*, 18, 187-201.

Conference Papers:

Li, W and Davis, E. J. (1995) "Effects of thermal properties on the thermophoretic force," Paper at 14th annual meeting, American Association of Aerosol Research, Pittsburgh, PA, Oct. 10-15.

Rassat, S. D., W. Li and E. J. Davis (1994), "Thermophoretic force measurements on single microparticles levitated in an electrodynamic balance," NASA Graduate Student Research Program 1994 Annual Symposium, Washington, DC, May 11-13.

Davis, E. J., Foss, W. R. and Li, W. (1993). "Formation of coated particle via gas/liquid chemical reaction," Paper at the 12th Annual meeting, American Association of Aerosol Research, Oak Brook, IL, Oct. 11-15.

Rassat, S. D., W. Li and E. J. Davis (1993), "Thermophoretic force measurements on single microparticles levitated in an electrodynamic balance," NASA Graduate Student Research Program 1993 Annual Symposium, Washington, DC, May 11-13.

Davis, E.J., Foss, W. R. and Li, W. (1992). "A study of toxic aerosol evaporation via elastic scattering," Paper presented at the 18th AIChE meeting, Miami Beach.